Geotechnical Special Publication No. 176

Analysis of Asphalt Pavement Materials and Systems

EMERGING METHODS

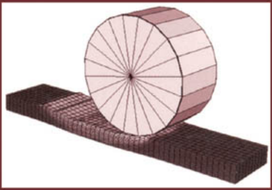

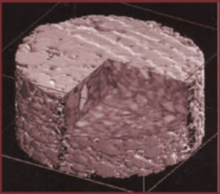

EDITED BY
Linbing Wang and Eyad Masad

GEOTECHNICAL SPECIAL PUBLICATION NO. 176

ANALYSIS OF ASPHALT PAVEMENT MATERIALS AND SYSTEMS

EMERGING METHODS

PROCEEDINGS OF THE SYMPOSIUM
ON THE MECHANICS OF FLEXIBLE PAVEMENTS

June 25–30, 2006
Boulder, Colorado

SPONSORED BY
Pavements Committee of the Geo-Institute of the American Society of Civil Engineers

The Inelastic Committee and the Granular Materials Committee of the ASCE Mechanics Division

EDITED BY
Linbing Wang
Eyad Masad

Published by the American Society of Civil Engineers

Library of Congress Cataloging-in-Publication Data on file.

American Society of Civil Engineers
1801 Alexander Bell Drive
Reston, Virginia, 20191-4400

www.pubs.asce.org

Any statements expressed in these materials are those of the individual authors and do not necessarily represent the views of ASCE, which takes no responsibility for any statement made herein. No reference made in this publication to any specific method, product, process, or service constitutes or implies an endorsement, recommendation, or warranty thereof by ASCE. The materials are for general information only and do not represent a standard of ASCE, nor are they intended as a reference in purchase specifications, contracts, regulations, statutes, or any other legal document. ASCE makes no representation or warranty of any kind, whether express or implied, concerning the accuracy, completeness, suitability, or utility of any information, apparatus, product, or process discussed in this publication, and assumes no liability therefore. This information should not be used without first securing competent advice with respect to its suitability for any general or specific application. Anyone utilizing this information assumes all liability arising from such use, including but not limited to infringement of any patent or patents.

ASCE and American Society of Civil Engineers—Registered in U.S. Patent and Trademark Office.

Photocopies and reprints.
You can obtain instant permission to photocopy ASCE publications by using ASCE's online permission service (www.pubs.asce.org/authors/RightslinkWelcomePage.html). Requests for 100 copies or more should be submitted to the Reprints Department, Publications Division, ASCE, (address above); email: permissions@asce.org. A reprint order form can be found at www.pubs.asce.org/authors/reprints.html.

Copyright © 2007 by the American Society of Civil Engineers. All Rights Reserved.
ISBN 13: 978-0-7844-0924-4
ISBN 10: 0-7844-0924-2
Manufactured in the United States of America.

14 13 12 11 10 09 08 07   1 2 3 4 5

Preface

This special publication includes 13 papers on characterization, modeling and simulation of asphalt concrete and subgrade, addressing some timely issues in mechanics of flexible pavements. They include four papers on modeling and simulations of asphalt concrete by incorporating the microscopic structures of the material, the interactions between aggregates, mastics and voids, and the use of Finite Element Method (FEM) and Discrete Element Method (DEM); two papers on the continuum approaches including nonlinear viscoelastic analysis and temperature dependency; two papers on laboratory characterization of asphalt concrete; three papers on the characterization of subgrade soil resilient modulus, incorporation of nonlinear soil behavior into pavement analysis, and the evaluation of the effect of using geogrid; and one paper on pavement evaluation.

Each paper published in this GSP was evaluated by peer reviewers and the editors. The review comments were sent to the authors and they have been addressed to the reviewers and the editors' satisfaction. The ASCE Geo-Institute Pavements Committee and the reviewers are sincerely acknowledged for their time and efforts.

The papers in this GSP include eight papers that were presented in the symposium on Mechanics of Flexible Pavements at the 15th U.S. National Congress of Theoretical and Applied Mechanics, held at Boulder, Colorado, June 25-30 2006 and five papers submitted for publication only. The symposium was supported by the Geo-Institute Pavements Committee, the Inelastic Committee and the Granular Materials Committee of the ASCE Mechanics Division.

The editors of this GSP would like to thank the Board of Governors of the Geo Institute for their approving the symposium and the special publication.

Linbing Wang, Virginia Tech
Eyad Masad, Texas A & M University

January 10, 2007

Geotechnical Special Publications

1 *Terzaghi Lectures*
2 *Geotechnical Aspects of Stiff and Hard Clays*
3 *Landslide Dams: Processes, Risk, and Mitigation*
7 *Timber Bulkheads*
9 *Foundations & Excavations in Decomposed Rock of the Piedmont Province*
11 *Dynamic Response of Pile Foundations-Experiment, Analysis and Observation*
14 *Geotechnical Aspects of Karst Terrains*
15 *Measured Performance Shallow Foundations*
16 *Special Topics in Foundations*
17 *Soil Properties Evaluation from Centrifugal Models*
18 *Geosynthetics for Soil Improvement*
19 *Mine Induced Subsidence: Effects on Engineered Structures*
21 *Hydraulic Fill Structures*
22 *Foundation Engineering*
23 *Predicted and Observed Axial Behavior of Piles*
24 *Resilient Moduli of Soils: Laboratory Conditions*
25 *Design and Performance of Earth Retaining Structures*
27 *Geotechnical Engineering Congress*
28 *Detection of and Construction at the Soil/Rock Interface*
29 *Recent Advances in Instrumentation, Data Acquisition and Testing in Soil Dynamics*
32 *Embankment of Dams-James L. Sherard Contributions*
33 *Excavation and Support for the Urban Infrastructure*
34 *Piles Under Dynamic Loads*
35 *Geotechnical Practice in Dam Rehabilitation*
37 *Advances in Site Characterization: Data Acquisition, Data Management and Data Interpretation*
39 *Unsaturated Soils*
40 *Vertical and Horizontal Deformations of Foundations and Embankments*
41 *Predicted and Measured Behavior of Five Spread Footings on Sand*
42 *Serviceability of Earth Retaining Structures*
43 *Fracture Mechanics Applied to Geotechnical Engineering*
44 *Ground Failures Under Seismic Conditions*
45 *In Situ Deep Soil Improvement*
46 *Geoenvironment 2000*
47 *Geo-Environmental Issues Facing the Americas*
48 *Soil Suction Applications in Geotechnical Engineering*
49 *Soil Improvement for Earthquake Hazard Mitigation*
50 *Foundation Upgrading and Repair for Infrastructure Improvement*
51 *Performance of Deep Foundations Under Seismic Loading*
52 *Landslides Under Static and Dynamic Conditions-Analysis, Monitoring, and Mitigation*
53 *Landfill Closures-Environmental Protection and Land Recovery*
54 *Earthquake Design and Performance of Solid Waste Landfills*
55 *Earthquake-Induced Movements and Seismic Remediation of Existing Foundations and Abutments*
56 *Static and Dynamic Properties of Gravelly Soils*
57 *Verification of Geotechnical Grouting*
58 *Uncertainty in the Geologic Environment*
59 *Engineered Contaminated Soils and Interaction of Soil Geomembranes*
60 *Analysis and Design of Retaining Structures Against Earthquakes*
61 *Measuring and Modeling Time Dependent Soil Behavior*
62 *Case Histories of Geophysics Applied to Civil Engineering and Public Policy*
63 *Design with Residual Materials: Geotechnical and Construction Considerations*
64 *Observation and Modeling in Numerical Analysis and Model Tests in Dynamic Soil-Structure Interaction Problems*
65 *Dredging and Management of Dredged Material*
66 *Grouting: Compaction, Remediation and Testing*
67 *Spatial Analysis in Soil Dynamics and Earthquake Engineering*
68 *Unsaturated Soil Engineering Practice*
69 *Ground Improvement, Ground Reinforcement, Ground Treatment: Developments 1987-1997*
70 *Seismic Analysis and Design for Soil-Pile-Structure Interactions*
71 *In Situ Remediation of the Geoenvironment*
72 *Degradation of Natural Building Stone*
73 *Innovative Design and Construction for Foundations and Substructures Subject to Freezing and Frost*

74 *Guidelines of Engineering Practice for Braced and Tied-Back Excavations*
75 *Geotechnical Earthquake Engineering and Soil Dynamics III*
76 *Geosynthetics in Foundation Reinforcement and Erosion Control Systems*
77 *Stability of Natural Slopes in the Coastal Plain*
78 *Filtration and Drainage in Geotechnical/Geoenvironmental Engineering*
79 *Recycled Materials in Geotechnical Applications*
80 *Grouts and Grouting: A Potpourri of Projects*
81 *Soil Improvement for Big Digs*
82 *Risk-Based Corrective Action and Brownfields Restorations*
83 *Design and Construction of Earth Retaining Systems*
84 *Effects of Construction on Structures*
85 *Application of Geotechnical Principles in Pavement Engineering*
86 *Big Digs Around the World*
87 *Jacked Tunnel Design and Construction*
88 *Analysis, Design, Construction, and Testing of Deep Foundations*
89 *Recent Advances in the Characterization of Transportation Geo-Materials*
90 *Geo-Engineering for Underground Facilities*
91 *Special Geotechnical Testing: Central Artery/Tunnel Project in Boston, Massachusetts*
94 *Performance Confirmation of Constructed Geotechnical Facilities*
95 *Soil-Cement and Other Construction Practices in Geotechnical Engineering*
96 *Numerical Methods in Geotechnical Engineering: Recent Developments*
97 *Innovations and Applications in Geotechnical Site Characterization*
98 *Pavement Subgrade, Unbound Materials, and Nondestructive Testing*
99 *Advances in Unsaturated Geotechnics*
100 *New Technological and Design Developments in Deep Foundations*
101 *Slope Stability 2000*
102 *Trends in Rock Mechanics*
103 *Advances in Transportation and Geoenvironmental Systems Using Geosynthetics*
104 *Advances in Grouting and Ground Modification*
105 *Environmental Geotechnics*
106 *Geotechnical Measurements: Lab & Field*
107 *Soil Dynamics and Liquefaction 2000*
108 *Use of Geophysical Methods in Construction*
109 *Educational Issues in Geotechnical Engineering*
110 *Computer Simulation of Earthquake Effects*
111 *Judgment and Innovation: The Heritage and Future of the Geotechnical Engineering Profession*
112 *Soft Ground Technology*
114 *Soils Magic*
115 *Expansive Clay Soils and Vegetative Influence on Shallow Foundations*
116 *Deep Foundations 2002: An International Perspective on Theory, Design, Construction, and Performance*
117 *Discrete Element Methods: Numerical Modeling of Discontinua*
118 *A History of Progress: Selected U.S. Papers in Geotechnical Engineering*
119 *Soil Behavior and Soft Ground Construction*
120 *Grouting and Ground Treatment*
121 *Probabilistic Site Characterization at the National Geotechnical Experimentation Sites*
122 *Sinkholes and the Engineering and Environmental Impacts of Karst*
123 *Recent Advances in Materials Characterization and Modeling of Pavement Systems*
124 *GeoSupport 2004: Drilled Shafts, Micropiling, Deep Mixing, Remedial and Specialty Foundation Systems*
125 *Current Practices and Future Trends in Deep Foundations*
126 *Geotechnical Engineering for Transportation Projects*
127 *Recycled Materials in Geotechnics*
128 *Soil Constitutive Models: Evaluation, Selection, and Calibration*
129 *Advances in Designing and Testing Deep Foundations*
130 *Advances in Pavement Engineering*
131 *Contemporary Issues in Foundation Engineering*
132 *Advances in Deep Foundations: In Memory of Michael W. O'Neill*
133 *Earthquake Engineering and Soil Dynamics*
134 *Soil Dynamics Symposium in Honor of Professor Richard D. Woods*
135 *Erosion of Soils and Scour of Foundations*
136 *Innovations in Grouting and Soil Improvement*

137 *Legal and Liability Issues in Geotechnical Engineering*
138 *Site Characterization and Modeling*
139 *Calibration of Constitutive Models*
140 *Slopes and Retaining Structures Under Seismic and Static Conditions*
141 *International Perspectives on Soil Reinforcement Applications*
142 *Waste Containment and Remediation*
143 *Geomechanics: Testing, Modeling, and Simulation*
144 *Sinkholes and the Engineering and Environmental Impacts of Karst*
145 *Seismic Performance and Simulation of Pile Foundations in Liquefied and Laterally Spreading Ground*
146 *Asphalt Concrete: Simulation, Modeling and Experimental Characterization*
147 *Unsaturated Soils 2006*
148 *Advances in Unsaturated Soil, Seepage, and Environmental Geotechnics*
149 *Site and Geomaterial Characterization*
150 *Soil and Rock Behavior and Modeling*
151 *Advances in Earth Structures: Research to Practice*
152 *Ground Modification and Seismic Mitigation*
153 *Foundation Analysis and Design: Innovative Methods*
154 *Pavement Mechanics and Performance*
155 *Underground Construction and Ground Movement*
156 *Geomechanics II: Testing, Modeling, and Simulation*
157 *Computer Applications in Geotechnical Engineering*
158 *Contemporary Issues in Deep Foundations*
159 *Case Studies in Earth Retaining Structures*
160 *Dynamic Response and Soil Properties*
161 *Embankments, Dams, and Slopes: Lessons from the New Orleans Levee Failures and Other Issues*
162 *Problematic Soils and Rocks and In Situ Characterization*
163 *Geoenvironmental Engineering*
164 *Innovative Applications of Geophysics in Civil Engineering*
165 *Geosynthetics in Reinforcement and Hydraulic Applications*
166 *Educational Activities in Geotechnical Engineering*
167 *Geotechnics of Soil Erosion*
168 *Grouting for Ground Improvement: Innovative Concepts and Applications*
169 *Soil and Material Inputs for Mechanistic-Empirical Pavement Design*
170 *Probabilistic Applications in Geotechnical Engineering*
171 *Advances in Shallow Foundations*
172 *Soil Improvement*
173 *Advances in Measurement and Modeling of Soil Behavior*
174 *Designing Our Underground Space*
175 *Field Measurements in Geomechanics 2007*

Contents

STRESS CONCENTRATION FACTOR AS A PERFORMANCE INDICATOR FOR ASPHALT MIXES

Linbing Wang[1], P.E., Member, ASCE. Yongping Wang[2], Qingbin Li[3]
and Gerardo Flintsch[4]

ABSTRACT: This paper presents some recent developments in using Finite Element Method (FEM) and the 3D microstructure of asphalt concrete reconstructed from x-ray tomography imaging to evaluate its performance. Asphalt concrete is modeled as a material composed of an effective solid and void. The stress concentration factor and its distributions are computed and correlated to the overall resistance of the mixtures against rutting and fatigue, and the internal structural quantities. The correlation of the stress concentration factor with the field performance of the WesTrack mixes indicates that mixes with large stress concentration factors, as expected, may be more prone to rutting and fatigue cracking than those with smaller stress concentration factors.

INTRODUCTION

Asphalt concrete is a heterogeneous medium comprised of three constituents of aggregates, binder and voids. The three constituents have significantly different properties. Traditional methods treat this material as a homogeneous continuum. Correspondingly, characterization of asphalt concrete is mainly in the scheme of homogeneous continuum. This treatment is valid for averaged quantities such as total

---

[1] Associate Professor, Department of Civil and Environmental Engineering, Virginia Tech, Blacksburg, VA 24061.

[2] Graduate Research Assistant, Department of Civil and Environmental Engineering, Virginia Tech, Blacksburg, VA 24061.

[3] Professor, Institute of Hydraulic Structures, Department of Hydraulic Engineering, Tsinghua University Beijing, 100084, P.R. China.

[4] Associate Professor, Department of Civil and Environmental Engineering, Virginia Tech, Blacksburg, VA

deformation and overall stiffness, but encounters difficulties in dealing with localized deformations such as rutting, and cracking initiation and propagation. The localized phenomena are sensitive to the microstructure of the material and the properties of the constituents. With recent developments in microstructure characterization and especially the X-ray Computerized Tomography (XCT) technique (Shashidhar, 1999; Wang et al, 2001; Wang et al., 2003; Tashman et al, 2002), the three-dimensional (3D) microstructure of asphalt concrete can be characterized, allowing a better understanding of the localized phenomena. For example, a cylindrical asphalt concrete specimen subjected to a uniform axial tension on the boundary could be only considered subject to a uniform tension on every cross section, if no microstructural information could be incorporated. Nevertheless, the stress in the specimen is significantly localized and related to the void size and spatial distributions, the relative stiffness of aggregates and binder/mastics, and the aggregate shape and configuration. Due to the complicated microstructure, the stress in any specific location within the specimen could be either shielded (smaller than the stress on the boundary) or magnified (larger than the stress on the boundary). The localized phenomena would take place at locations where either the constituent is soft or the stress is significantly magnified (stress concentration). A study to assess how stress concentration and/or strain localization are affected by mix characteristics, such as gradation, would provide some insightful information on the performance of the mix.

Among the three constituents, voids have the most distinct features from binder and aggregates as voids can be assumed to have zero stiffness. If aggregates coated with asphalt binder are considered as an effective solid, asphalt concrete can be modeled as a material consisting of only the effective solids and voids. However, the simplification would not be true if the void structure of asphalt concrete is not considered. Without microstructural considerations, it would make no difference for two mixes of different gradations but of the same asphalt content and the same void content. The void structure is related to the aggregate gradation as well as the compaction methods and efforts. It was discovered that the void size distribution might be a mirror image of the aggregate gradation and carry the information of mix design. Figure 1 presents the aggregate gradation and the void size distribution of the three mixes of the WesTrack project (Epps, 1997). The similarity between the aggregate gradation and the corresponding void size distribution indicates that void size distribution carries the effect of aggregate gradation and is a comprehensive indicator of the mixture's internal structure.

The properties of the effective solid are also important. The effective solid is composed of the aggregates coated with asphalt binder. Theoretically, it should be a viscoelastic or a viscoplastic material. At low temperature or under fast loading and small stress conditions, the effective solid may be modeled as an elastic material. These simplifications reduce the asphalt concrete microstructure to an elastic continuum weakened by the randomly distributed air voids related to mix characteristics (although certain percentage air void, i.e. 4%, is required to avoid bleeding or plastic mixes, above that level, a mix will be weakened more with larger air void content). With these simplifications, the localized stress distributions in an asphalt concrete specimen, subject to a uniform boundary stress, could be conveniently computed.

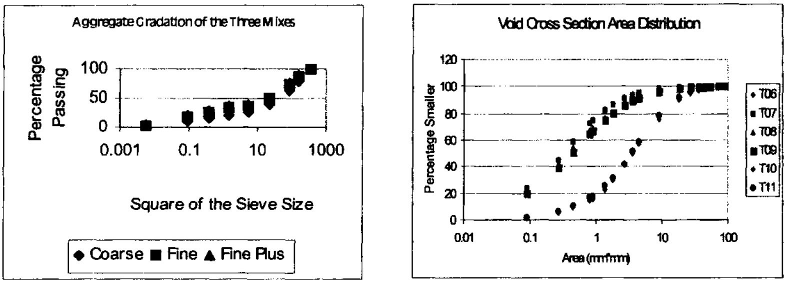

a. Aggregate Gradation **b. Void Size Distribution**

FIG. 1 Relation between Aggregate Gradation and Void Size Distribution (T06, T07, Fine Mix ; T08, T09, Fine Plus Mix; T10, T11, Coarse Mix)

The effective solid can be considered as a homogeneous medium. Therefore it is anticipated that the yielding and cracking initiation would most likely start at those points where the stress concentration is severe. The severity of the stress concentration may provide an assessment of the rationality of the structure of the mix although it doesn't require the characterization of the mix for the entire deformation process under different magnitudes of loading and at different temperatures. A better mix should have less severe stress concentration or strain localization regardless of the magnitude of stress and temperature.

The paper presents the development of FEM simulation of the internal stress distribution of asphalt concrete subject to a uniform external tensile stress or compressive stress. The simulation makes use of the actual 3D void structure obtained from X-ray tomography imaging. A simple parameter, the stress concentration factor is defined as an indicator of a mixture's potential performance. The stress concentration factor is correlated with the internal structure and the field performance of the three mixes of the WesTrack project. The correlations indicate that the stress concentration factor may provide a promising indicator of mixture performance.

IMPLICATION OF EMBEDDED VOIDS TO STRESS CONCENTRATIONS

Figure 2 presents a simple case: an elastic plate weakened by a single cavity. The plate is subjected to a uniformly distributed tensile stress on two boundaries. The elasticity solution indicates that the largest stress is at the edge of the void, and the ratio between the largest stress and the uniform far field stress on the boundaries, the stress concentration factor S_c, equals to (Wu, 1987):

$$S_c = (1 + 2\frac{a}{b}) \tag{1}$$

Where *a* and *b* are the lengths of the semi-axis of the ellipsis.

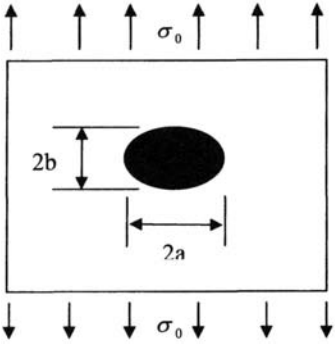

FIG. 2 Void Shape and Stress Concentration Factor

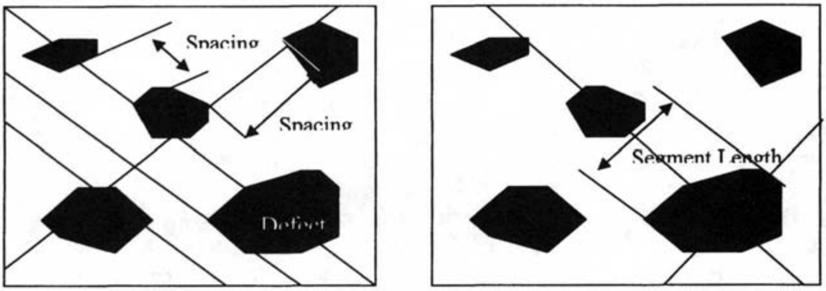

a. Mean Solid Path is the Average Spacing among the Cracked Surfaces or Voids in Different Orientations

b. Average Size of Defect is the Average Segment Length in Different Orientations of All the Defects or Voids

FIG.3 Damaged /Void Surfaces, Spacing among the Surfaces and Definitions of Mean Solid Path and Average Size of Defect

METHODOLOGY

In this study, the randomly distributed void structure is obtained from x-ray tomography imaging. X-ray tomography imaging is an effective tool to characterize the 3D microstructure, defects, and inhomogeneity of materials. Interested readers are referred to (Kak, 1999) for more details about its mechanisms. Figure 4 graphically illustrates the procedures used for this study. Figure 4.a presents a 3D rendering of an asphalt concrete core obtained through x-ray tomography imaging, where a series of slices of images were stacked. Figure 4.b presents the plane view of a small block of the inside of the core. Simulation will be performed on such blocks randomly sampled from the core so that the boundary effect at the specimen edges can be eliminated and the computational time reduced. Figure 4.c presents the binary counterpart of the block presented in Figure 4.b, where voids and the effective solid are respectively represented as black and white. It should be noted that an image is actually the visualization of an array showing the intensities of pixels, the smallest element in the image. Figure 5 presents the image overlapped by the pixel grid. For each pixel, its coordinates (X, Y) are recorded. If black represents voids, the pixels that have pixel values of zero are void pixels and their locations can be determined.

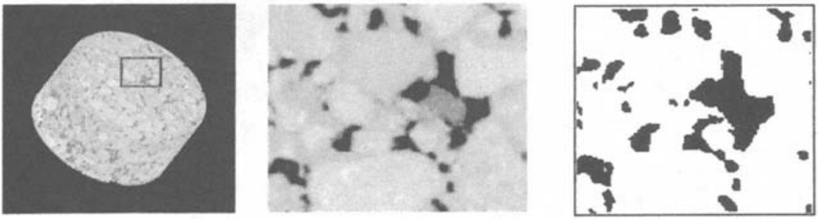

a. 3D Rendering **b. Plane View of A Block** **c.Binary Counterpart of b**

FIG. 4 Illustration of the Procedure

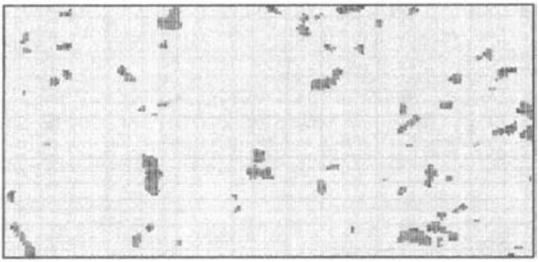

FIG. 5 Randomly Distributed Voids Overlapped with Pixel Grids

A method was developed to abstract coordinates of voids from the binary tomography images and the structure of the material is represented as an assemble of voxels (Wang, 1999, 2003). A voxel is the corresponding volume element in three-dimensional (3D) space for a pixel in 2D space. Figure 6a presents one such 3D voxel grid. The voxel in this study is not cubic. It is a rectangular with XY (12) cross sections represented as pixels (square). The Z (3) dimension takes the spacing of the slices. Each voxel is modeled as an eight-node element. The simulation follows two steps. Step one simulates the case when the uniform voxel grid is subject to a uniformly distributed tensile stress at the boundary (Figure 6a). Step two simulates the removal of the void voxels (Figure 6b). The stress concentration factor is defined as the ratio between the maximum tensile stress and the uniformly distributed tensile stress on the boundaries.

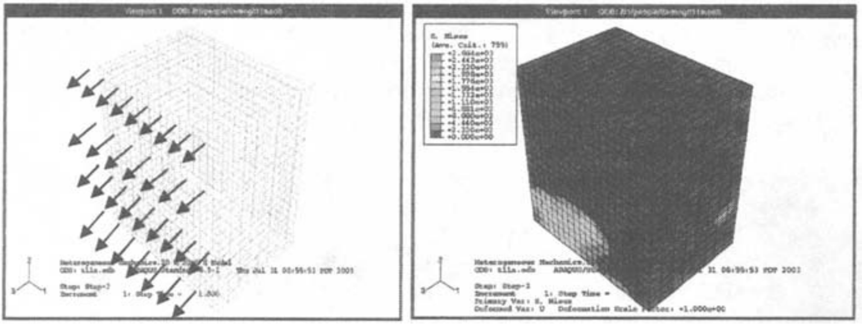

a. Step One: Sampled Block Subjected to Uniaxial Tension

b: Step Two: Removal of the Randomly Distributed Voids

FIG. 6 Illustration of the Voxel Concept and the Two Step Simulation

In this study, the size of each element (voxel) is 0.29X0.29X1.8mm. For the problem studied, 50X50X10=25000 elements, representing a rectangular block of 15X15X18 mm^3 were used for the simulation. This selection addresses both representativeness and computational time. Too small size simulation may cause numerical instability. Larger size simulation can be achieved but at much slower speed. For the purpose of this study, many blocks from a specimen are sampled for the simulation so that a statistical evaluation of the stress concentration factors can be obtained, and the inhomogeneous void structure or the mix's structure can be evaluated.

Simulation Results

The above method was applied to the evaluation of the stress concentration factors of the three mixes: the coarse mix, the fine mix and the fine plus mix of the WesTrack project.

Figure 6b also presents the distribution of the Von Mises stresses of one of the simulations, where clearly the effective shear stress (the Von Mises stress) around the voids is much larger. The mean stress concentration factors for the three mixes are presented in Figure 7. Clearly, the coarse mix has the largest stress concentration factor while the fine mix has the smallest stress concentration factor with the fine plus mix in the middle. It should be noted that the total air void contents of the three mixes are the same. So the significant differences in stress concentration factor should be the result of the void size and spatial distributions that reflect the aggregate gradation and compaction effects. If the stress concentration factor is used to rank the performance of the three mixes, they will give a consistent ranking with the field performance (Epps, 1997).

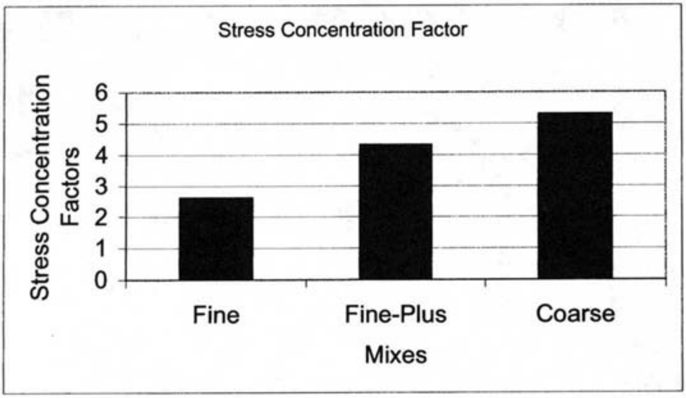

FIG. 7 Mean Stress Concentration Factors of the Three Mixes

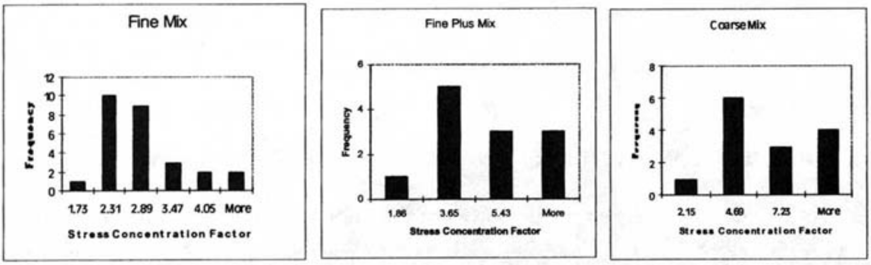

FIG. 8 Distributions of the Stress Concentration Factors of the Three Mixes

Statistical Analysis

The simulation is performed on a number of randomly sampled blocks from one specimen for each mix. Table 1 presents the statistics of the stress concentration factors including the minimums, maximums, the means and the standard deviations, while Figure 8 presents the histograms of the stress concentration factors for the three mixes. The Student t-tests indicate that the coarse mix and the fine mix are significantly different; the fine mix and fine plus mix are significantly different; but the coarse mix and the fine plus mix are not significantly different. In addition the standard deviations of the stress concentration factor for the three mixes also indicate that the coarse mix has the largest variation, indicating more significant inhomogeneity of its void structure.

TABLE 1. Statistics of Stress Concentration Factors

Mixes (1)	Max (2)	Min (3)	Mean (4)	STDEV (5)
Fine	4.625	1.73	2.609	0.583
Fine-Plus	7.213	1.863	4.186	2.694
Coarse	9.768	2.148	5.295	6.079
T-Test	t Stat.		P(T<=t) one-tail	
Fine& Fine-Plus	-3.177		0.0036	
Fine & Coarse	-3.977		0.00069	
Fine-Plus & Coarse	-1.367		0.0925	

Other Boundary Conditions

Obviously, the uni-axial tension analysis is only one measure of the stress concentration factors. Due to the factor that stress concentration is also related to the orientation of the irregularly shaped voids, the stress concentration factor due to the extension/compression in other orientations should also be evaluated. In addition, the mix's response to shear forces on the boundary may better differentiate the structures in terms rutting. These studies are currently in progress and will be presented in a separate paper. Nevertheless, a better mixture structure should have a smaller stress concentration factor in terms of any of the rational stress boundary conditions.

CORRELATION WITH INTERNAL STRUCTURAL QUANTITIES

As mentioned in the previous sections, the stress concentration factor should be related to the void size and spatial distributions, including the mean solid path among the voids, and the void size /spacing ratio etc. It would be interesting to investigate whether these internal structure quantities are related to the stress concentration factors. In previous studies, Wang et al (2001; 2003) quantified the internal structure parameters, including the effective damage, the mean solid path among the voids, and the ratio between the average size and the mean solid path using a stereology-based method. This section presents these correlations. For completeness of the paper, the implications of these terms are briefly explained as follows.

Void Area Fraction and Effective Damage Parameter

Figure 9a and Equations (2) and (3) illustrate the concept of effective stress. In Figure 9a, if the cross-section has no or some void area, the stresses are respectively equal to

$$\sigma_n = \frac{F}{A} \tag{2}$$

$$\sigma_e = \frac{F}{A - A_v} = \frac{F}{A}\frac{1}{1-\varphi} = \sigma_n \frac{1}{1-\varphi} \tag{3}$$

Where F is the total force applied normal to the cross-section; A is the cross-section area; A_v is the area of air voids contained in A; σ_n is the nominal normal stress; σ_e is the effective stress; and φ is the area fraction of voids ($\varphi = \frac{A_v}{A}$, in continuum damage mechanics, this parameter is named as damage scalar).

Generally, the area fractions of air voids in different orientations at the same point are different. In some orientations, the area fractions may be significantly larger than those in other orientations. Representation of this orientational variation of the area fractions requires the use of a second order tensor φ_{ij}. In continuum damage mechanics it is named as damage tensor (Voyiadjis, 1999). Its typical application can be found in the following equation (Murakami, 1988).

$$\bar{\sigma}_{ij} = M_{ijkl}\sigma_{kl} \tag{4}$$

where $\bar{\sigma}_{ij}$ and σ_{kl} are the effective stress tensor and Cauchy stress tensor respectively, while M_{ijkl} is a symmetric fourth rank tensor-the damage effect tensor. By using their vector formats of the tensors, Murakami (1988) showed that:

$$M=(I-\varphi)^{-1} \tag{5}$$

where I is the second-rank identity tensor, and φ is the damage tensor.

Voyiadjis and Kattan (1999) also introduced an effective damage term $\varphi = \sqrt{\varphi_1^2 + \varphi_2^2 + \varphi_3^2}$ to represent the overall damage. Wang et al (2003) quantified this term for the mixes of the WesTrack project. Figure 10a presents the correlation between the effective damage and the stress concentration factor. The correlation is very well. Nevertheless, more data points are needed to verify this correlation.

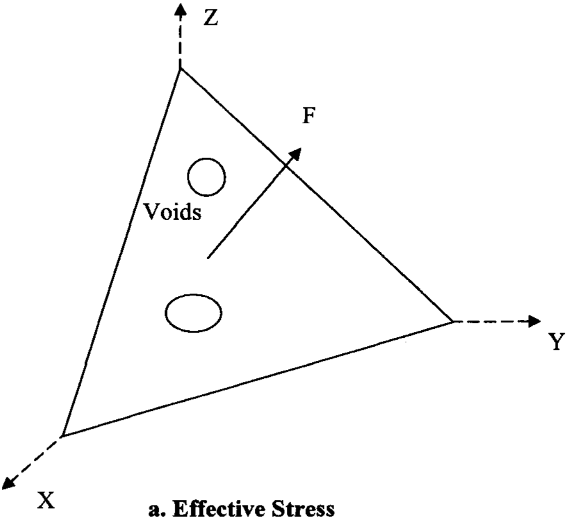

a. Effective Stress

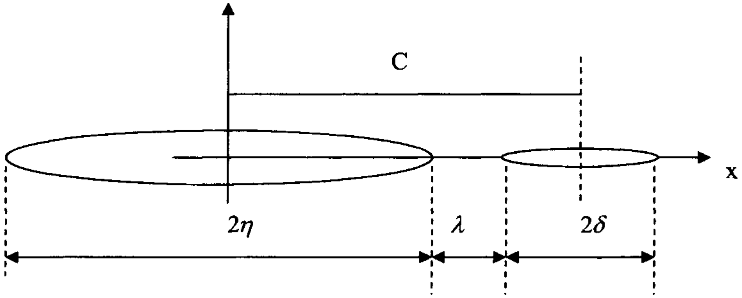

b. Spacing/Size Ratio

FIG. 9 Illustration of Effective Stress and Spacing Size Ratio

Mean Solid Path

Figure 3 illustrates several interacting cavities as well as the definitions of mean solid path and the average size of defects (voids, in this study). When the two cavities are far away, their interaction is negligible. However, when the two cavities are close, they will interact with each other to further weaken the material. The spacing between the two voids is an indication of the strength of interaction and is an important parameter (Lacy, 1997; 1999). As the distribution of the average spacing among the voids and/or damaged surfaces is usually not isotropic, tensors are needed to represent these distributions. For correlation analysis, only the mean solid path is used. Figure 10b presents the correlation between the mean solid path and the stress concentration factor. The correlation is also very well and makes sense. Again, more data points are needed to verify this correlation.

Spacing-Size Ratio

The size of and the spacing between voids/defects are important variables in non-local damage theories. For modeling applications, the size of cracks or voids and the average spacing among the cracks offer two relevant parameters that are related to performance. Chudnovsky et al (1987a; 1987b) developed a simple model addressing the interaction of two cracks, in which the two important model parameters are the spacing between the two crack tips and the sizes of the cracks. Figure 9b presents the configuration of two interacting cracks. The stress intensity (Mode I) of the large crack is affected by the adjacent cracks. The ratio $\frac{K_1^{eff}}{K_1^0}$ (where K_1^{eff} is the effective stress intensity of a crack when subjected to the influence of the adjacent crack while K_1^0 is the stress intensity without the influence of adjacent cracks) decreases with the increase of λ/δ, which is equivalent to that the larger the crack size and/or the smaller the spacing, the larger the effective stress intensity. Therefore, under the same external loading, the material with smaller λ/δ should have a larger stress intensity factor. Equations (6) and (7) present the relation between the effective stress intensity and the crack configuration parameters illustrated in Figure 9b.

$$\frac{K_1^{eff}}{K_1^0} = \frac{1}{1-q} \tag{6}$$

$$q = \frac{1}{\sqrt{2(\delta/\eta + \lambda/\eta)}} \int_{-1}^{1} \sqrt{\frac{1+t}{1-t}} \left(\frac{1}{\sqrt{1-(\frac{\delta}{\eta})^2/(t - C^2/\eta^2)}} - 1 \right) dt \tag{7}$$

Figure 10c presents the correlation between the spacing/size factor and the stress concentration factor. The correlation is also very good. However, additional data points are required to verify this correlation.

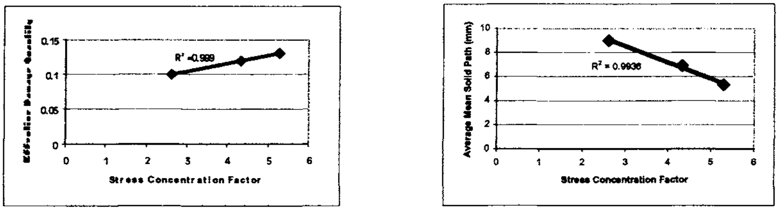

a. Effective Damage Quantity **b. Average Mean Solid Path**

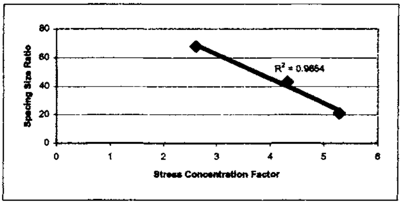

c. Spacing Size Ratio

FIG. 10 Stress Concentration Factor with Internal Structural Quantities

CONCLUSION

The stress concentration factor may present a simple performance indicator for asphalt mixes against both rutting and fatigue. Additional study to consider the mixture as a three-constituent composite with binder or mastics modeled as viscoelastic material is recommended. The stress concentration factor is well correlated to the internal structure parameters such as effective damage, mean solid path, and the spacing size ratio. The internal structure parameters, by mechanics theories, are related to material properties and may serve as good internal variables for modeling and simulation. Additional data shall be needed to widely verify the presented relations and test validity of using the stress concentration factor as a performance indicator. However, the good correlations between the stress concentration factor and the internal structure parameters and the field performance indicate that stress concentration factor may serve as a promising simple performance indicator for asphalt concrete.

ACKNOWLEDGEMENT

Research funding provided by the Board of Regents of Louisiana is sincerely acknowledged.

REFERENCES

Chudnovsky, A., Dolgopolsky, A. and Kachanov, M. (1987a). "Elastic Interaction of a Crack with a Microcrack Array-I. Formulation of the Problem and General Form of the Solution." *Int. J. Solids and Structures*, 23(1), 1-10.

Chudnovsky, A., Dolgopolsky, A. and Kachanov, M. (1987b). "Elastic Interaction of a Crack with a Microcrack Array-II. Elastic Solution for Two Crack Configurations (Piecewise Constant and Linear Approximations)." *Int. J. Solids and Structures*, 23(1), 11-21.

Epps, Jon, Monismith, C. L. and Seeds, S. B. (1997). "Westrack Full-Scale Test Track: Interim Findings." http://www.westrack.com/isap.pdf

Kak, A.C. and Slaney, M. (1999). "Principles of Computerized Tomographic Imaging." IEEE Press.

Lacy, T.E., McDowell, D.L, Willice, P.A. and Talreja, R. (1997). "On Representation of Damage Evolution in Continuum Damage Mechanics." *International Journal of Damage Mechanics*, 6, 62-95.

Lacy, T.E., McDowell, D.L, Willice, P.A. and Talreja, R. (1999). "Gradient Concept for Evolution of Damage." *Mechanics of Materials*, 31, 831-860.

Murakami, S. (1988). "Mechanical modeling of material damage". *J. Appl. Mech.*, 55, 280-286.

Shashidhar, N. (1999). "X-ray tomography of asphalt concrete." *Transportation Research Record*, 1681, 186-192.

Tashman, L; Masad, E; D'Angelo, J; Bukowski, J; Harman, T (2002). "X-Ray Tomography to Characterize Air Void Distribution in Superpave Gyratory Compacted Specimens." *International Journal of Pavement Engineering*. 3 (1), 19-28.

Voyiadjis, G. Z., and Kattan, P. (1999). "Advances in Damage Mechanics: Metals and Metal Matrix Composites." 542 p., Elsevier, Oxford.

Wang, L.B. (1999). "3D FEM Simulation for WesTrack Mixes from X-ray Tomography Images." *Research Report*, School of Civil and Environmental Engineering, Georgia Institute of Technology.

Wang, L.B., Frost, J.D. and Shashidhar, N. (2001). "Microstructure Study of Westrack Mixes from X-ray Tomography Images." *TRR*, 1767, 85-94.

Wang, L.B., Frost, J.D., Voyiadjis, G. and Harman, T.P. (2003). "Quantification of Damage Parameters Using X-ray Tomography Images." *Journal of Mechanics of Materials*, 35, 777-790.

Wang, L.B. (2003). "Enhancing Rutting Performance of Flexible Pavements (Characterization of Asphalt Concrete Using X-ray Computerized Tomography." FHWA MIHE.

Wang, L.B. (2003). "Stress Concentration Factor of Poroelastic Material by FEM Simulation and X-ray Tomography Imaging." *ASCE Engineering Mechanics Conference*, Seattle, WA.

Wu, J. L. (1987). "Elasticity." Tongji University Press.

Aggregate Effect on Asphalt Mixture Properties by Modeling Particle-to-Particle Interaction

Zhanping You[1], William G. Buttlar[2], and Qingli Dai[3]

ABSTRACT: A number of researchers have studied aggregate characteristics including elongation, flatness, and other shapes that are believed to affect asphalt mixture properties such as internal resistance, rutting resistance, tensile strength, and complex modulus etc. However, the aggregate modulus also affects the asphalt mixture modulus significantly, which has not been taken into consideration. In this paper, the effect of aggregate particle-to-particle interaction was studied through numerical modeling using the discrete element modeling (DEM) approach. The individual material phases (e.g., aggregates and mastic) were modeled with clusters of discrete elements based upon laboratory testing of the individual phases. For a given set of material parameters for each phase, the degree of particle-to-particle contact in an asphalt mixture was found to have a profound influence on overall mixture modulus. A parametric investigation of aggregate modulus revealed that the contribution of aggregate modulus to overall mixture modulus was very significant. Pending further experimental verification on asphalt mixtures, this finding may shed new light on the importance of aggregate stiffness on overall mixture properties.

INTRODUCTION

A number of researchers have studied aggregate characteristics including elongation, flatness, etc., which have been found to affect asphalt mixture properties such as resistance to permanent deformation, tensile strength, and complex modulus. The effect of aggregate characteristics on the behavior of asphalt mixtures, using both static and repeated load triaxial tests, were studied for three types of coarse aggregates (Gandhi and Gallaway 1970). It was found that the aggregate shape and

---

[1] Tomasini Assistant Professor, Ph.D., P.E., Department of Civil and Environmental Engineering, Michigan Technological University, 1400 Townsend Drive, Houghton, Michigan, 49931-1295, zyou@mtu.edu

[2] Associate Professor, Ph.D., P.E., Department of Civil and Environmental Engineering, University of Illinois at Urbana-Champaign, IL 61801, buttlar@uiuc.edu

[3] Visiting Assistant Professor, School of Technology and Department of Mechanical Engineering-Engineering Mechanics, 1400 Townsend Drive, Houghton, MI 49931, qingdai@mtu.edu

surface characteristics played an important role in the behavior of asphalt mixtures under both static and dynamic loading conditions. The flat and elongated coarse aggregate affects the field compaction of hot-mix asphalt (Aho et al. 2001). The aggregate shape also affects the wear resistance of asphalt pavement (Alkio and Vuorinen 1996).

In order to study the effect of aggregate gradation variation on asphalt concrete mix properties (Elliott et al. 1991), mixtures with five gradations were tested. It was found that the fine-coarse and coarse-fine gradation variations had the greatest impact on mix properties (e.g., creep modulus, split tensile strength, and resilient modulus). In order to study the coarse aggregate effects on an asphalt mixture, researchers also investigated the effects of coarse aggregate content on the resistance of stone matrix asphalt (SMA) mixtures to moisture damage, aging, and low-temperature cracking (Stuart and Mogawer 1995). Researchers also investigated the effect of coarse aggregate morphology on the resilient modulus of hot-mix asphalt (Pan et al. 2005). Although the changes in aggregate gradation did not significantly affect the relationship between the coarse aggregate morphology and the resilient modulus, decreasing the nominal maximum aggregate size from 19 mm to 9.5 mm indicated an increasing positive influence of aggregate morphology on the resilient modulus of asphalt mixes.

In studies of *Portland cement concrete*, the concrete modulus of elasticity has been related to the aggregate type and specific gravity (Yazdani et al. 2005). In a related study, four types of aggregate were used to investigate the effect of aggregate type on the elastic modulus of concrete (Alexander and Milne 1995). It was found that the influence of these mix variables on short-term stress-strain behavior and concrete elastic modulus, E, was dependent on aggregate and cement type. Andesite and dolomite yielded considerably stiffer concretes than granite or quartzite. Silica fume produced concretes of similar or slightly greater modulus than the ordinary Portland cement (OPC), but slag and fly ash reduced modulus, particularly at early ages, on an equal strength or water-cement ratio basis. (Hansen 1965) derived an equation to calculate modulus of elasticity from its components (i.e., mortar and paste).

Due to the lower stiffness of asphalt binder relative to hardened cement paste, one would intuitively expect aggregate modulus to play an even larger role in the modulus of asphalt concrete mixtures. However, this topic has not received much attention in the literature (You 2003). This paper presents a numerical modeling study (clustered DEM approach) supported with laboratory testing results aimed at investigating the role of aggregate content, connectivity, and modulus on overall asphalt mixture stiffness.

ASPHALT MIXTURE SPECIMEN PREPARATION AND LABORATORY TESTS

An experimental program was developed to serve two main purposes: 1) to measure the complex modulus (E*) of a sand-mastic mixture (asphalt plus fine aggregate), which was a required input to the clustered DEM model (described below), and 2) to obtain E* of the HMA mixture, which was used to assess and to calibrate the numerical model. Uniaxial compression testing and hollow cylinder testing of mixture and sand mastic specimens were conducted to measure the complex moduli

(E*). A 9.5-mm (nominal maximum aggregate size) mixture was used in this study. Gyratory specimens were used to produce uniaxial compression specimens and hollow cylinder tensile test (HCT) specimens. The sand mastic (1.18-mm nominal maximum aggregate size) had around 14% asphalt content, by weight of the mixture. The sand mixture was prepared using a specially designed aluminum molds to create uniaxial compression and HCT specimens. Complex moduli used in this portion of the study were measured at three temperatures, -20, -10, and 0°C, and four frequencies, 0.1, 1, 5, and 10Hz. In the test, cyclic loads were carefully applied to keep the response in a linear visco-elastic range (Airey et al. 2003).

MICROSTRUCTURE MODELING OF THE MIXTURE

The discrete element method has received considerable attention in the past 20 years after its gradual development for studies in rock mechanics (Cundall 1971; Cundall 2000). During this time, the DEM method has been extended to many other fields. The modeling procedure used in this study adopted a clustered DEM, or *microfabric* approach (Buttlar and You 2001). A unique feature of this approach is the cohesive and adhesive strength for asphalt concrete. Biaxial compressive modulus prediction using the discrete element modeling approach has been recently demonstrated (You and Buttlar 2004) to match or exceed the predictive capabilities of empirical modulus prediction models. A hollow cylinder tensile test was modeled to predict mixture tensile modulus (You and Buttlar 2005). It was found that the two dimensional (2D) clustered DEM provided very good estimates of mixture dynamic modulus across a range of loading temperatures and frequencies without calibration.

In the clustered DEM modeling approach, various material phases (e.g., aggregates, mastic) are modeled with clusters of discrete elements. Aggregate and mastic modulus are significant input parameters in these models, which are obtained by converting the macro-modulus obtained from laboratory tests to micro-modulus in the DEM models. A significant model feature is that the cohesive strength of individual aggregates and the mastic can be considered, along with the adhesion at the aggregate-mastic interface (You and Buttlar 2005, 2006; and Dai and You 2007). In addition, aggregate-aggregate interactions are considered in the DEM approach using detailed morphological information (aggregate shape, contact, force chain structure, etc.).

EFFECTS OF FINE AGGREGATE THROUGH COMPRESSIVE TEST

In order to examine the effect of fine aggregate on the complex modulus of the asphalt mixture, four discrete element models were prepared for each image of a mixture specimen. Figure 1 shows the four DE models. In the model with an aggregate concentration ratio c=0.40, the aggregate size is larger than 2.36mm (No. 8 sieve), where the degree of particle-to-particle contact is relatively low. This work can be done in the image process by filtering, using a defined subroutine. If the aggregate is filtered with threshold of 1.18mm (No. 16 sieve), the aggregate concentration ratio is 0.47 as shown in figure, where the degree of particle-to-particle contact is relatively higher. When the aggregate is filtered with a threshold of 0.6mm (No. 30 sieve), the aggregate concentration ratio is found to be 0.51. The aggregate concentration ratio becomes 0.52 when the finest aggregate particles in the image are passed through a 0.3mm sieve (No. 50 sieve). Note that the DE models shown in this figure are from the same specimen image. The difference is the aggregate contents in the model. The main similarity is that the coarse aggregate structure is the same, i.e., all the models include the same aggregate internal 2D structure with minimum aggregate size of 2.36mm.

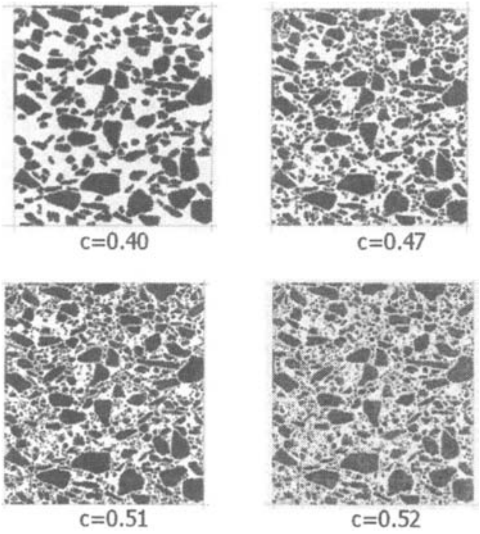

Figure 1. Discrete elements of the aggregate skeletons with four different degrees of particle-to-particle contact for a 9.5mm mixture

The four models create a network of contact force chains in the aggregate skeleton structure (i.e., internal structure or aggregate-aggregate interlock) during the DEM simulation, which increases with increasing aggregate content (and therefore increasing aggregate contact, sometimes expressed in terms of coordination number, or number of contacts per particle). In all the models, the sand mastic moduli were kept at the same level, i.e., the measured value across a range of loading frequencies and test temperatures.

In order to compare the effect of aggregate contact within a fine aggregate structure on the complex modulus of the asphalt mixture, the four discrete element models were simulated. Figure 2 shows the DEM predictions for this fine mixture (9.5mm nom maximum aggregate size) using a uniaxial compression DEM simulation. Among the four curves, the curve for aggregate concentration ratio of 0.52 yields the highest prediction and the 0.41 concentration ratio yields the lowest prediction for any mastic modulus. As expected, for a specific test temperature and loading frequency, the mixture modulus prediction is dependent on the aggregate microstructure. When the aggregate structure includes more aggregate-aggregate contacts or aggregate interaction, the mixture yields higher modulus. Comparing the model with 0.40 and 0.47 aggregate concentration ratios, there is a modulus increase of 15% when 7% fine aggregate is included in the mixture, when the mastic modulus is 1GPa. For a similar case, when the mixture includes 11% more fines, the mixture modulus increased by 18%. It should be noted that when even 1% more fines are included, the mixture modulus increases by almost 4%. If the mastic modulus is 7.5GPa (at a lower temperature), when the aggregate concentration ratio increased from 0.40 to 0.41, 0.47, and 0.52, respectively, the mixture modulus increased by 12%, 17%, and 19%, respectively.

Figure 2 also shows the DEM prediction compared with laboratory measurements versus sand mastic modulus. For the model with an aggregate volume concentration ratio c=0.47, the average prediction difference is 11%, compared with 16% predicted from the model with a 0.40 concentration ratio. For the model with aggregate volume concentration ratio of 0.51, the average prediction difference is 10% between the prediction and the measurements. Based upon a paired t-test, there is a 95% confidence interval (-0.70, 2.38) for the mean difference between the DEM predictions (c=0.51) and the measurements. Therefore, there is a 95% confidence that the mean difference between prediction and the measurements across a range of temperatures and frequencies is statistically insignificant.

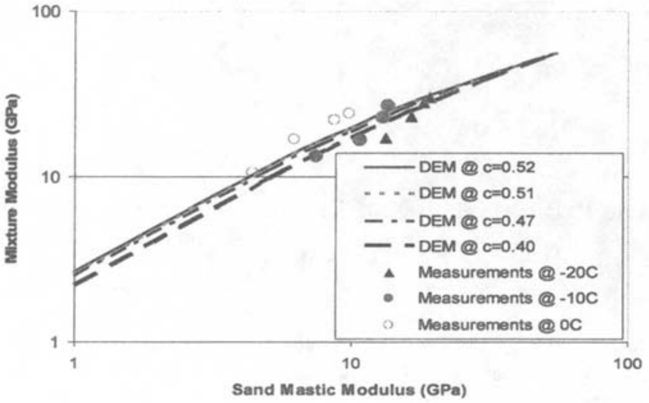

Figure 2. DEM predictions of the mixture when aggregate modulus is fixed and sand mastic modulus varies

For the model with an aggregate volume concentration ratio of 0.52, the average prediction difference is 10%. Again, the model prediction is much better than the model with c=0.40 (with low degree of particle-to-particle contact). There is a 95% confidence interval (-1.02, 2.06) for the mean difference. Therefore, the statistical analysis results indicate that the prediction from this model is acceptable and is the best among the four models.

The objective of the examples given here is to aid in the understanding of the important stiffening effect of aggregate-aggregate contact and aggregate volume concentration, as well as aggregate gradation effect. Due to the length limitation, it is very difficult to give a detailed explanation of other results and findings. When a 3D model is used in the near future, it is possible that the prediction will be further improved.

EFFECT OF AGGREGATE MODULUS

In order to study the effect of aggregate modulus to the mixture modulus, the model in Figure 2 (c=0.51) was used. When a fixed mastic modulus of 5.27GPa, aggregate modulus was varied from 1 to 120GPa. For this specific model, the mixture modulus prediction is shown in Figure 3. It can be found that when the aggregate modulus increases from 40 to 80 GPa, the mixture modulus increases 12%; when aggregate modulus increases from 20 to 120 GPa, mixture modulus increases 80%. Obviously, when stiffer aggregate is used, a stiffer mixture is expected. However, many studies such as the recent, well-known predictions (Witczak et al. 2001; Christensen et al. 2003) for asphalt mixture do not consider the aggregate modulus effect. It should be noted that the modulus of aggregate is very difficult to measure. Researchers at University of Illinois measured the modulus of limestone from a local quarry and found there was more than a two-fold difference in aggregate modulus for the aggregate sources from different depths in the quarry (You 2003).

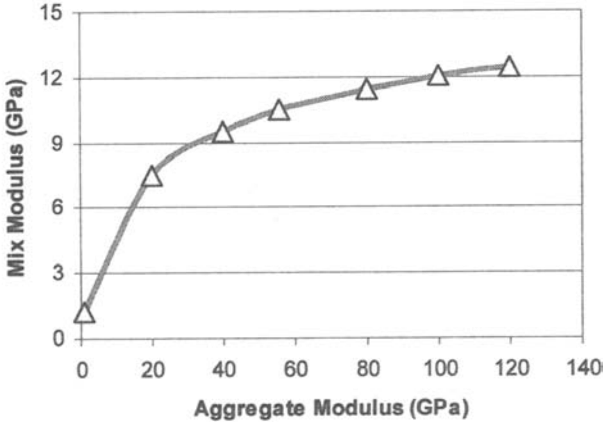

Figure 3. Aggregate modulus effect to mixture modulus when aggregate modulus varies and sand mastic modulus is fixed

SUMMARY AND CONCLUSION

In this paper, the effect of aggregate particle-to-particle interaction was modeled and the mixture moduli were predicted using the discrete element modeling approach. In this approach, the material phases (aggregates and mastic) were modeled with clusters of discrete elements with different properties. The moduli of the aggregate and mastic were among the input parameters. A compressive test was simulated considering the heterogeneity of asphalt mixture. When the degree of particle-to-particle contact in an asphalt mixture increased, a higher mixture modulus was predicted. Aggregate modulus sensitivity analysis showed that the aggregate modulus contribution to mixture modulus can be significant. It is anticipated that ongoing 3D imaging and modeling efforts will have lead further improvement in mixture property and behavior predictions, and will provide detailed insight towards the roles of coarse and fine aggregates, their gradation, and other morphological characteristics in the behavior of asphalt mixtures.

REFERENCES

Aho, B. D., W. R. Vavrik and S. H. Carpenter (2001). Effect of Flat and Elongated Coarse Aggregate on Field Compaction of Hot-Mix Asphalt, Transportation Research Board.

Airey, G. D., B. Rahimzadeh and A. C. Collop (2003). "Viscoelastic linearity limits for bituminous materials." Materials and Structures/Materiaux et Constructions **36**(264): 643-647.

Alexander, M. G. and T. I. Milne (1995). Influence of Cement Blend and Aggregate Type on Stress-Strain Behavior and Elastic Modulus of Concrete, American Concrete Institute.

Alkio, R. and J. Vuorinen (1996). The Effect of Aggregate Shape on the Wear Resistance of Asphalt Pavement : A Study With Field Test Slabs: Wear Results Of The First Winter, Tielaitos, Tielaitoksen Selvityksia.

Buttlar, W. G. and Z. You (2001). "Discrete Element Modeling of Asphalt Concrete: A Micro-Fabric Approach." Journal of the Transportation Board, National Research Council, Washington, D.C. **1757**.

Christensen, D. W., T. Pellien and R. F. Bonaquist (2003). "Hirsch Models for Estimating the Modulus of Asphalt Concrete." J. Assoc. Asphalt Paving Tech. **72**: 97-121.

Cundall, P. A. (1971). A Computer Model for Simulating Progressive Large Scale Movements in Blocky Rock Systems. Proceedings of the Symposium of the International Society of Rock Mechanics, Nancy, France.

Cundall, P. A. (2000). "A Discontinuous Future for Numerical Modelling in Geomechanics?" Geotech. Eng **149**(1): 41-47.

Dai, Q. and You, Z (2007), Prediction of Creep Stiffness of Asphalt Mixture with Micromechanical Finite Element and Discrete Element Models, Journal of

Engineering Mechanics, American Society of Civil Engineers (ASCE), Volume 133, Issue 2.

Elliott, R. P., M. C. Ford, M. Ghanim and Y. F. Tu (1991). Effect of Aggregate Gradation Variation on Asphalt Concrete Mix Properties, Transportation Research Board.

Gandhi, P. M. and B. M. Gallaway (1970). The Effect of Aggregate Characteristics on The Behavior of Asphalt Mixtures Under Static and Dynamic Loading Conditions, American Society for Testing and Materials.

Hansen, T. C. (1965). Influence of Aggregate and Voids on Modulus of Elasticity of Concrete Cement Mortar and Cement Paste. Journal Proceedings, ACI.

Pan, T., E. Tutumluer and S. H. Carpenter (2005). Effect of Coarse Aggregate Morphology on the Resilient Modulus of Hot-Mix Asphalt, Transportation Research Board.

Stuart, K. D. and W. S. Mogawer (1995). Effect of Coarse Aggregate Content on Stone Matrix Asphalt Durability and Low-Temperature Cracking, Transportation Research Board.

Witczak, M. W., M. Bari and M. M. Quayum (2001). Sensitivity of Simple Performance Test Dynamic Modulus |E*|. N.-S. C4bReport. Tempe, AZ., Arizona State University, Department of Civil and Environmental Engineering.

Yazdani, N., B. McKinnie and S. Haroon (2005). Aggregate-Based Modulus of Elasticity for Florida Concrete, Transportation Research Board.

You, Z. (2003). Development of a Micromechanical Modeling Approach to Predict Asphalt Mixture Stiffness Using Discrete Element Method. Department of Civil and Environmental Engineering. University of Illinois at Urbana-Champaign. Ph.D. dissertation: 512.

You, Z. and W. G. Buttlar (2004). "Discrete Element Modeling to Predict the Modulus of Asphalt Concrete Mixtures." Journal of Materials in Civil Engineering, ASCE **16**(2): 140-146.

You, Z. and W. G. Buttlar (2005). "Application of Discrete Element Modeling Techniques to Predict the Complex Modulus of Asphalt–Aggregate Hollow Cylinders Subjected to Internal Pressure." Journal of the Transportation Research Board, National Research Council, **1929**: 218-226.

You, Z. and W. G. Buttlar (2006), Micromechanical Modeling Approach to Predict Compressive Complex Moduli of Asphalt Mixture Using Distinct Element Method, Journal of the Transportation Research Board, National Research Council, Washington, D.C., No. **1970**, pp 73-83.

Investigation of Linear and Damage-Coupled Viscoelastic Properties of Sustainable Asphalt Mixture Using a Micromechanical Finite Element Approach

Qingli Dai [1] and Zhanping You [2]

Abstract

This paper presents a microstructure-based finite element model by incorporating elastic aggregates and viscoelastic sand mastic. The microstructure-based finite element (FE) approach was used to predict the linear and damage-coupled viscoelastic properties of reclaimed asphalt mixture. The two-dimensional (2D) microstructure of asphalt mixture was obtained from the scanned image of a smoothly sawn surface of a reclaimed asphalt pavement (RAP) mixture specimen. In the microstructure, the sketches of highly irregular aggregates were converted into polygons. The whole microstructure model was divided into highly irregular aggregate and sand mastic subdomains. The finite element mesh was generated within each subdomain. The deformation of the aggregate and mastic subdomains was connected through the sharing boundary nodes. Linear and damage-coupled viscoelastic finite element model was developed with displacement-based incremental formulation. The linear and damage-coupled viscoelastic simulation was conducted on the image sample of test specimen under different sinusoidal force loading frequencies. The uniaxial compression simulation results showed creep deformation constant cyclic force loading amplitude and damage-coupled viscoelastic responses have larger creep deformation. Simulations under different loading frequencies found compression strain deceases with loading frequencies due to less relaxation time.

Introduction

A sustainable asphalt mixture is designed to consider the economic, societal, and environmental factors through life cycle analysis. The use of reclaimed asphalt pavement (RAP) material has been considered as sustainable asphalt mixtures and has obtained varying degrees of success in the United States. The asphalt pavement recycling methods include hot mix recycling, hot in-place recycling, cold in-place recycling and full depth reclamation. Hot mix recycling is the predominant method of structural recycling and the mix design procedure is basically similar as the one for new mixtures with the additional requirement for asphalt pavement analysis (Roberts et al. 1996). A recycled mixture should be designed to produce an asphalt material having the same properties as that in a new one. The aged asphalt binder must be mixed with the new asphalt binder or recycling agent to provide the overall desired binder properties. Recent study have reported

---

[1] Visiting Assistant Professor, School of Technology and Department of Mechanical Engineering-Engineering Mechanics, Michigan Technological University, Houghton, 1400 Townsend Drive, MI 49931. qingdai@mtu.edu

[2] Tomasini Assistant Professor, Dept. of Civil and Environmental Engineering, Michigan Technological University, 1400 Townsend Drive, Houghton, MI 49931. zyou@mtu.edu

investigations of the performance of Superpave asphalt mixtures incorporating RAP (McDaniel and Shah 2003) and mechanical properties of RAP (Picado-Santos et al. 2004). However, there still exists uncertainty on proper recycling processes and on the subsequent performance of the recycled product.

Asphalt mixture is a composite material of graded aggregates bound with mastic (asphalt binder plus fine aggregates and fines). Recycling processes further complicate the mechanical behavior by introducing additional variation of these constituents, and by adding several ageing/time-dependent effects. For such materials, the macro properties depend on many micro phenomena that occur at the aggregate/mastic level. A fundamental knowledge of the material behavior is needed to understand and explain recycling issues, and a micromechanical model would be an excellent tool to establish such basic mechanisms.

Asphalt mixture were investigated by non-interaction particle micromechanics models without specified geometry (Buttlar and Roque 1996; Buttlar and Roque 1997; Hashin and Shtrikman 1963; Schapery 1969; Voigt 1889), as well as, with specified geometry (Buttlar et al. 1999; Christensen and Lo 1979; Hashin 1965; Shashidhar et al. 1996). A two-dimensional (2D) micro-fabric discrete element model (MDEM) concept was developed and calibrated to predict the stiffness of asphalt mixtures (You and Buttlar 2004; You and Buttlar 2005; You and Buttlar 2006).

Finite element modeling of asphalt concrete microstructure potentially allows accurate modeling of aggregate and mastic complex constitutive behaviors and microstructure geometries. Research work has been conducted using finite element techniques (Bahia et al. 1999; Bazant 1990; Budhu et al. 1997; Guddati et al. 2002; Kose et al. 2000; Mora 1992; Mustoe and Griffiths 1998; Papagiannakis et al. 2002; Sepehr et al. 1994; Stankowski 1990). In addition, an equivalent lattice network approach was applied, where the local interaction between neighboring particles was modeled with a special frame-type finite element (Dai and Sadd 2004; Dai et al. 2005; Sadd et al. 2004b; Sadd et al. 2004c). A mixed finite element approach was developed to study asphalt mixture by using continuum elements for the effective asphalt mastic and rigid body defined with rigid elements for each aggregate (Dai et al. 2006). A unified approach for the rate-independent and rate-dependent damage behavior has been developed using Schapery's nonlinear viscoelastic model. Properties of the continuum elements are specified through a user material subroutine within the ABAQUS code and this allows linear and damage-coupled viscoelastic constitutive behavior of the mastic cement to be incorporated. In these models, the microstructure of real asphalt materials is simulated with idealized elliptical aggregate and rectangular effective mastic zone (Dai 2004). Using image processing and ellipse fitting methods, particle dimensions and locations were determined from digital photographs of the sample's surface microstructure. The objectives of this study are 1) develop a microstructure-based finite element model by incorporating elastic aggregates with viscoelastic sand mastic 2) numerically investigate the linear and damage-coupled viscoelastic behavior of reclaimed asphalt mixture.

Microstructure of asphalt mixture

In this study, the two-dimensional (2D) microstructure of asphalt mixture was obtained by optically scanning smoothly sawn asphalt mixture test specimens. A high-resolution scanner was used to obtain grayscale images from the sections (You and

Buttlar 2006). Image processing technique was used to converted the image into many-sided polygons using a custom developed macro program to define the microstructure of asphalt mixture (Buttlar and You 2001). The average of the polygon diameter was chosen as a threshold to determine which aggregates would be "retained" on a given sieve (the rest of the aggregates would be "passed" the given sieve), although some other measurement parameters were also attempted in analyzing the gradation of the aggregates (You 2003). The polygons used in the micromechanical model were filtered as coarse aggregates. In the model of the asphalt mixture, the coarse aggregates retained on 2.36mm sieve (No. 8) were counted in the subdomain of aggregate. The fine aggregates passing 2.36mm were filtered as sand mastic. Elastic properties of aggregates were measured and applied to aggregate subdomain, and viscoelastic mastic properties were also calibrated with mastic creep tests (Dai and You 2007). Finite element simulation was conducted to predict the global mixture behavior by combining aggregate and mastic properties.

FE Incremental Formulation for Linear Viscoelastic Behavior

The linear constitutive behavior for this Maxwell-type model can be expressed as a hereditary integral

$$\sigma_{ij} = E_\infty \varepsilon_{ij} + \int_0^t E_t \frac{d\varepsilon_{ij}(\tau)}{d\tau} d\tau, \tag{1}$$

where E_t is the transient modulus changing with time, and expressed with a Prony series

$$E_t = \sum_{m=1}^{M} E_m e^{-\frac{(t-\tau)}{\rho_m}}, \text{ and } \rho_m = \frac{\eta_m}{E_m} \tag{2}$$

In these equations, E_m, η_m and ρ_m are the spring constant, dashpot viscosity and relaxation time respectively for the m^{th} Maxwell element.

The reduced time (effective time) is defined by using time-temperature superposition principle as

$$\xi(t) = \int_0^t \frac{1}{\alpha_T} d\tau \tag{3}$$

where the term $\alpha_T = \alpha_T(T(\tau))$ is a temperature-dependent time-scale shift factor.

Three-dimensional behavior can be formulated with uncoupled volumetric and deviatoric stress-strain relations. A displacement-based incremental finite element modeling scheme with constant strain rate over each increment was developed in the following format:

$$\Delta\sigma = K \cdot \Delta\varepsilon + \Delta\sigma^R \tag{4}$$

Where $\Delta\sigma$ and $\Delta\varepsilon$ are incremental stress and strain, K is the incremental stiffness and $\Delta\sigma^R$ is the residue stress vector.

The incremental formulation of the volumetric behavior is obtained with constant volumetric strain rate $R_{kk} = \frac{\Delta\varepsilon_{kk}}{\Delta\xi}$,

$$\Delta\sigma_{kk} = 3\left[K_\infty + \sum_{m=1}^{N} \frac{K_m \rho_m}{\Delta\xi}\left(1 - e^{-\frac{\Delta\xi}{\rho_m}}\right)\right]\Delta\varepsilon_{kk} + \Delta\sigma_{kk}^R \tag{5}$$

where K_∞ and K_m are bulk moduli, and the residual part $\Delta\sigma_{kk}^R$ can be expressed in a recursive relation with the history variable S_m,

$$\Delta\sigma_{kk}^R = \sum_{m=1}^{M} -\left(1-e^{-\frac{\Delta\xi}{\rho_m}}\right) S_m(\xi_n), \text{ and } S_m(\xi_n) = 3K_m R_{kk}\rho_m\left(1-e^{-\frac{\Delta\xi}{\rho_m}}\right) + S_m(\xi_{n-1})e^{-\frac{\Delta\xi}{\rho_m}} \qquad (6)$$

For the initial increment, the history variable $S_m(\xi_1)$ equals to $3K_m R_{kk}\rho_m\left(1-e^{-\frac{\Delta\xi}{\rho_m}}\right)$ and is similar to the following formulations.

The formulation of the deviatoric behavior with deviatoric stress $\hat{\sigma}_{ij} = \sigma_{ij} - \frac{1}{3}\sigma_{kk}\delta_{ij}$ and strain $\hat{\varepsilon}_{ij} = \varepsilon_{ij} - \frac{1}{3}\varepsilon_{kk}\delta_{ij}$ is obtained with constant deviatoric strain rate $\hat{R}_{ij} = \frac{\Delta\hat{\varepsilon}_{ij}}{\Delta\xi}$,

$$\Delta\hat{\sigma}_{ij} = 2\left[G_\infty + \sum_{m=1}^{N}\frac{G_m\rho_m}{\Delta\xi}\left(1-e^{-\frac{\Delta\xi}{\rho_m}}\right)\right]\Delta\hat{\varepsilon}_{ij} + \Delta\hat{\sigma}_{ij}^R \qquad (7)$$

and the residual part $\Delta\hat{\sigma}_{ij}^R$ can be expressed in the recursive relation

$$\Delta\hat{\sigma}_{ij}^R = \sum_{m=1}^{N} -\left(1-e^{-\frac{\Delta\xi}{\rho_m}}\right) S_m(\xi_n), \text{ and } S_m(\xi_n) = 2G_m\hat{R}_{ij}\rho_m\left(1-e^{-\frac{\Delta\xi}{\rho_m}}\right) + S_m(\xi_{n-1})e^{-\frac{\Delta\xi}{\rho_m}} \qquad (8)$$

Normal incremental stresses can be formulated with combination of volumetric and deviatoric behaviors, while shear incremental stresses can be obtained from deviatoric behaviors. Once the incremental stress components are developed, the incremental stiffness terms can be calculated and then the incremental 3D linear viscoelastic behavior was formulated as

$$\begin{bmatrix}\Delta\sigma_{xx}\\ \Delta\sigma_{yy}\\ \Delta\sigma_{zz}\\ \Delta\sigma_{xy}\\ \Delta\sigma_{yz}\\ \Delta\sigma_{zx}\end{bmatrix} = \begin{bmatrix} K_1 & K_2 & K_2 & 0 & 0 & 0\\ \cdot & K_1 & K_2 & 0 & 0 & 0\\ \cdot & \cdot & K_1 & 0 & 0 & 0\\ \cdot & \cdot & \cdot & K_3 & 0 & 0\\ \cdot & \cdot & \cdot & \cdot & K_3 & 0\\ \cdot & \cdot & \cdot & \cdot & \cdot & K_3 \end{bmatrix}\begin{bmatrix}\Delta\varepsilon_{xx}\\ \Delta\varepsilon_{yy}\\ \Delta\varepsilon_{zz}\\ \Delta\varepsilon_{xy}\\ \Delta\varepsilon_{yz}\\ \Delta\varepsilon_{zx}\end{bmatrix} + \begin{bmatrix}\Delta\sigma_{kk}^R + \Delta\hat{\sigma}_{xx}^R\\ \Delta\sigma_{kk}^R + \Delta\hat{\sigma}_{yy}^R\\ \Delta\sigma_{kk}^R + \Delta\hat{\sigma}_{zz}^R\\ \Delta\hat{\sigma}_{xy}^R\\ \Delta\hat{\sigma}_{yz}^R\\ \Delta\hat{\sigma}_{zx}^R\end{bmatrix} \qquad (9)$$

where

$$\begin{aligned} K_1 &= \left[K_\infty + \sum_{m=1}^{N}\frac{K_m\rho_m}{\Delta\xi}\left(1-e^{-\frac{\Delta\xi}{\rho_m}}\right)\right] + \frac{4}{3}\left[G_\infty + \sum_{m=1}^{N}\frac{G_m\rho_m}{\Delta\xi}\left(1-e^{-\frac{\Delta\xi}{\rho_m}}\right)\right]\\ K_2 &= \left[K_\infty + \sum_{m=1}^{N}\frac{K_m\rho_m}{\Delta\xi}\left(1-e^{-\frac{\Delta\xi}{\rho_m}}\right)\right] - \frac{2}{3}\left[G_\infty + \sum_{m=1}^{N}\frac{G_m\rho_m}{\Delta\xi}\left(1-e^{-\frac{\Delta\xi}{\rho_m}}\right)\right]\\ K_3 &= 2\left[G_\infty + \sum_{m=1}^{N}\frac{G_m\rho_m}{\Delta\xi}\left(1-e^{-\frac{\Delta\xi}{\rho_m}}\right)\right] \end{aligned} \qquad (10)$$

FE Incremental Formulation for Damage-Coupled Viscoelastic Behavior

Reclaimed asphalt mixture has damage-coupled viscoelastic behavior. The original Schapery nonlinear viscoelastic model (Schapery 1969) was given as

$$\sigma(\xi) = h_e E_\infty \varepsilon(\xi) + \int_0^\xi h_1 E_t(\xi - \xi') \frac{d(h_2 \varepsilon(\xi'))}{d\xi'} d\xi' \tag{11}$$

This model incorporates three different nonlinear parameters: h_e is the nonlinear factor of the relaxed elastic modulus E_∞, h_1 measures the nonlinearity effect in the transient modulus E_t, and h_2 accounts for the loading rate effect.

Following form (11), a rate-independent damage-coupled viscoelastic model is proposed by replacing two nonlinear parameters h_e and h_1 with damage variables which would be expressed with damage evolution functions (Assume h_2=1 to neglect rate-dependent damage behavior in this study).

$$\sigma(\xi) = h_e(\varepsilon_{\max}) E_\infty \varepsilon(\xi) + \int_0^\xi h_1(\varepsilon_{\max}) E_t(\xi - \xi') \frac{d(\varepsilon(\xi'))}{d\xi'} d\xi' \tag{12}$$

where h_e and h_1 are the elastic and viscoelastic damage variables for the rate-independent failure behavior. These variables are functions of the maximum strain $\varepsilon_{\max}$, which is defined as the maximum value over the past history up to the current time ξ,

$$\varepsilon_{\max} = \max(\varepsilon(\xi')),\ \xi' \in [0, \xi] \tag{13}$$

The elastic damage variable $h_e = 1 - \Omega$ measures the relaxed elastic stiffness reduction, and can be described by using the inelastic damage evolution law in Sadd et al.(Sadd et al. 2004a; Sadd et al. 2004b),

$$h_e(\varepsilon_{\max}) = e^{-b\frac{\varepsilon_{\max}}{\varepsilon_0}} \tag{14}$$

where the material parameters ε_0 and b are related to the softening strain and damage evolution rate respectively.

The viscoelastic variable h_1 measures the damage effect in the transient modulus, and is chosen with the following exponential form by (Simo and Ju 1987),

$$h_1(\varepsilon_{\max}) = \beta + (1 - \beta) \frac{1 - e^{-\left(\frac{\varepsilon_{\max}}{\varepsilon_0}\right)}}{\varepsilon_{\max} / \varepsilon_0},\ \beta \in [0, 1] \tag{15}$$

The variable h_1 will reduce from 1 to β as the maximum strain $\varepsilon_{\max}$ increases, and ε_0 is also the softening stain.

Following the previous formulation procedures, the incremental formulation of the volumetric behavior is obtained with constant volumetric strain rate $R_{kk} = \frac{\Delta\varepsilon_{kk}}{\Delta\xi}$,

$$\Delta\sigma_{kk} = 3\left[K_\infty h_e(\varepsilon_{\max}^{kk}) + \sum_{m=1}^{N} h_1(\varepsilon_{\max}^{kk}) \frac{K_m \rho_m}{\Delta\xi} \left(1 - e^{-\frac{\Delta\xi}{\rho_m}}\right)\right] \Delta\varepsilon_{kk} + \Delta\sigma_{kk}^R \tag{16}$$

and the residual part $\Delta\sigma_{kk}^R$ can be expressed in a recursive relation with the history variable S_m,

$$\Delta\sigma_{kk}^{R}=\sum_{m=1}^{M}-\left(1-e^{-\frac{\Delta\xi}{\rho_m}}\right)S_m(\xi_n),\text{ and } S_m(\xi_n)=3K_m h_1\left(\varepsilon_{\max}^{kk}\right)R_{kk}\rho_m\left(1-e^{-\frac{\Delta\xi}{\rho_m}}\right)+S_m(\xi_{n-1})e^{-\frac{\Delta\xi}{\rho_m}} \tag{17}$$

For the deviatoric behavior, the formulation of the deviatoric behavior is obtained with constant deviatoric strain rate $\hat{R}_{ij}=\dfrac{\Delta\hat{\varepsilon}_{ij}}{\Delta\xi}$,

$$\Delta\hat{\sigma}_{ij}=2\left[G_\infty h_e\left(\varepsilon_{\max}^{e}\right)+\sum_{m=1}^{N}h_1\left(\varepsilon_{\max}^{e}\right)\frac{G_m\rho_m}{\Delta\xi}\left(1-e^{-\frac{\Delta\xi}{\rho_m}}\right)\right]\Delta\hat{\varepsilon}_{ij}+\Delta\hat{\sigma}_{ij}^{R} \tag{18}$$

where $\varepsilon_{\max}^{e}$ is the maximum equivalent strain, and the equivalent strain $\varepsilon_e=\sqrt{\frac{3}{2}\hat{\varepsilon}_{ij}\hat{\varepsilon}_{ij}}$. And the residual part $\Delta\hat{\sigma}_{ij}^{R}$ can be expressed in the recursive relation

$$\Delta\hat{\sigma}_{ij}^{R}=\sum_{m=1}^{N}-\left(1-e^{-\frac{\Delta\xi}{\rho_m}}\right)S_m(\xi_n),\text{ and } S_m(\xi_n)=2G_m h_1\left(\varepsilon_{\max}^{e}\right)\hat{R}_{ij}\rho_m\left(1-e^{-\frac{\Delta\xi}{\rho_m}}\right)+S_m(\xi_{n-1})e^{-\frac{\Delta\xi}{\rho_m}} \tag{19}$$

Similarly, the incremental stress components can be developed from volumetric and deviatoric behaviors. The incremental 3D damage-coupled viscoelastic behavior can be formulated as

$$\begin{bmatrix}\Delta\sigma_{xx}\\ \Delta\sigma_{yy}\\ \Delta\sigma_{zz}\\ \Delta\sigma_{xy}\\ \Delta\sigma_{yz}\\ \Delta\sigma_{zx}\end{bmatrix}=\begin{bmatrix}K_{d1} & K_{d2} & K_{d2} & 0 & 0 & 0\\ \cdot & K_{d1} & K_{d2} & 0 & 0 & 0\\ \cdot & \cdot & K_{d1} & 0 & 0 & 0\\ \cdot & \cdot & \cdot & K_{d3} & 0 & 0\\ \cdot & \cdot & \cdot & \cdot & K_{d3} & 0\\ \cdot & \cdot & \cdot & \cdot & \cdot & K_{d3}\end{bmatrix}\begin{bmatrix}\Delta\varepsilon_{xx}\\ \Delta\varepsilon_{yy}\\ \Delta\varepsilon_{zz}\\ \Delta\varepsilon_{xy}\\ \Delta\varepsilon_{yz}\\ \Delta\varepsilon_{zx}\end{bmatrix}+\begin{bmatrix}\Delta\sigma_{kk}^{R}+\Delta\hat{\sigma}_{xx}^{R}\\ \Delta\sigma_{kk}^{R}+\Delta\hat{\sigma}_{yy}^{R}\\ \Delta\sigma_{kk}^{R}+\Delta\hat{\sigma}_{zz}^{R}\\ \Delta\hat{\sigma}_{xy}^{R}\\ \Delta\hat{\sigma}_{yz}^{R}\\ \Delta\hat{\sigma}_{zx}^{R}\end{bmatrix} \tag{20}$$

With these terms:

$$\begin{aligned}\frac{\partial\Delta\sigma_{xx}}{\partial\Delta\varepsilon_{xx}}&=\left[K_\infty h_e\left(\varepsilon_{\max}^{e}\right)+\sum_{m=1}^{N}h_1\left(\varepsilon_{\max}^{e}\right)\frac{K_m\rho_m}{\Delta\xi}\left(1-e^{-\frac{\Delta\xi}{\rho_m}}\right)\right]\\ &\quad+\frac{4}{3}\left[G_\infty h_e\left(\varepsilon_{\max}^{e}\right)+\sum_{m=1}^{N}h_1\left(\varepsilon_{\max}^{e}\right)\frac{G_m\rho_m}{\Delta\xi}\left(1-e^{-\frac{\Delta\xi}{\rho_m}}\right)\right]=K_{d1}\\ \frac{\partial\Delta\sigma_{xx}}{\partial\Delta\varepsilon_{yy}}&=\left[K_\infty h_e\left(\varepsilon_{\max}^{e}\right)+\sum_{m=1}^{N}h_1\left(\varepsilon_{\max}^{e}\right)\frac{K_m\rho_m}{\Delta\xi}\left(1-e^{-\frac{\Delta\xi}{\rho_m}}\right)\right]\\ &\quad-\frac{2}{3}\left[G_\infty h_e\left(\varepsilon_{\max}^{e}\right)+\sum_{m=1}^{N}h_1\left(\varepsilon_{\max}^{e}\right)\frac{G_m\rho_m}{\Delta\xi}\left(1-e^{-\frac{\Delta\xi}{\rho_m}}\right)\right]=K_{d2}\\ \frac{\partial\Delta\sigma_{xy}}{\partial\Delta\varepsilon_{xy}}&=2\left[G_\infty h_e\left(\varepsilon_{\max}^{e}\right)+\sum_{m=1}^{N}h_1\left(\varepsilon_{\max}^{e}\right)\frac{G_m\rho_m}{\Delta\xi}\left(1-e^{-\frac{\Delta\xi}{\rho_m}}\right)\right]=K_{d3}\end{aligned} \tag{21}$$

The linear and damage-coupled viscoelastic models were defined in the ABAQUS user material subroutines for mastic subdomains. A displacement-based time-dependent finite element analysis was conducted by integrating elastic aggregate and linear and damage-coupled viscoelastic mastic to predict the global behavior of asphalt mixture.

Micromechanical Finite Element Simulation of Reclaimed Asphalt Mixture

As mentioned previously, reclaimed asphalt materials (similar as the regular hot mix asphalt) composed of very irregular aggregates and complex distributed mastic. The microstructures were divided into different aggregate and mastic subdomains. The finite element mesh was generated within the subdomains (aggregates and mastic) and along the subdomain boundaries. Fig. 1 shows the finite element meshes in the aggregates and mastic subdomains of a specimen surface. Finite elements in the neighboring subdomains share the nodes on irregular boundaries, and therefore the displacements of neighboring subdomains were connected through the shared nodes.

After the FE model has been developed, uniaxial compression test was simulated. For the compression simulation, the x- and y- displacements of the nodes on the bottom layer and the x- displacements of the nodes on the top layer were constrained. The sinusoidal cyclic force loading was evenly divided and imposed on nodes of the top layer. The evaluated Maxwell model parameters for asphalt mastic and elastic modulus of aggregates were inputted for predicting global viscoelastic properties. In the simulation, axial strain was calculated by dividing the average vertical displacement of top particles with the initial height of the undeformed specimen, and axial stress was obtained by dividing the constant loading force on the top layer with the specimen initial cross-section area.

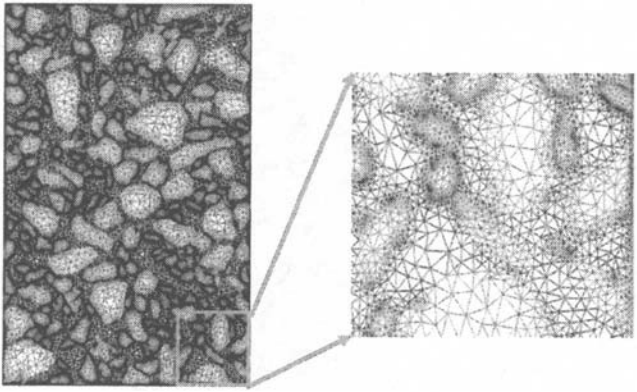

Fig. 1. The FEM meshes for the aggregate and mastic subdomains

Cyclic loading Simulation and Results

Sinusoidal cyclic force loading was imposed to the computational specimen to conduct uniaxial compression simulation under the different frequencies (0.1 Hz, 1 Hz, 5 Hz and 10 Hz). The laboratory tests of elastic aggregate (rock) and linear viscoelastic mastic were conducted to provide material input parameters for the FE models. The aggregate modulus takes a typical modulus of 55.5GPa for the limestone. The evaluate Maxwell model for reclaimed asphalt mastic includes one spring and four Maxwell elements in parallel ($E_\infty = 59.7MPa$, $E_1 = 5710.6MPa$, $\tau_1 = 26.2s$, $E_2 = 2075.1MPa$,

$\tau_2 = 311.9s$, $E_3 = 1449MPa$, $\tau_3 = 1678.8s$, $E_4 = 734.9MPa$, $\tau_1 = 19952.6s$). Model damage parameters were chosen as $b = 1$, $\beta = 0.3$, and softening strain $\varepsilon_0 = 0.2$ for the simulation.

Fig. 2 shows the cyclic simulation under the frequency of 0.1 Hz. The simulation was conducted with elastic aggregate and linear/damage-coupled viscoelastic mastic properties. In the figures, the black curve is the imposed compression stress loading with left-hand axial scales, and the magenta color indicates the strain response with right-hand axial scales. For better illustration, the final several cycles were magnified in the right-side figures for each frequency. The figures show the increasing creep compression strain along the loading time for the constant force loading magnitude. Comparing results (a) and (b) using linear and damage-coupled viscoelastic mastic properties, it shows viscoelastic damage behavior increases the sample creep deformation under the constant cyclic force loading. From the results of different loading frequencies, it was found that the uniaxial compression strain responses decease with the loading frequencies due to the less relaxation time. An ongoing experimental test plan will be conducted to verify the simulation results.

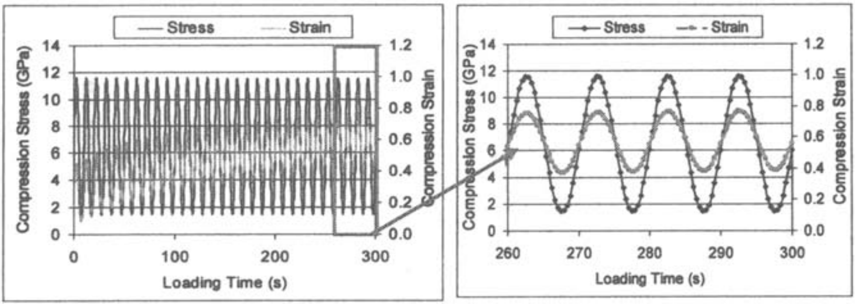

(a) Linear viscoelastic mastic

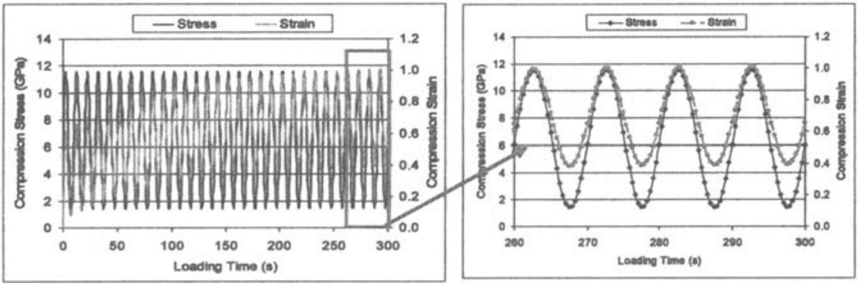

(b) Damage-coupled viscoelastic mastic

Fig. 2. The FEM simulation results under sinusoidal loading at a frequency of 0.1Hz

Summaries and Conclusions

The micromechanical Finite Element (FE) model by incorporating elastic aggregates and linear/damage-coupled viscoelastic mastic has been used to simulate viscoelastic behavior of a sustainable asphalt mixture -reclaimed asphalt mixture. The 2D microstructure of reclaimed asphalt mixture was obtained by optically scanning the smoothly sawn surface of asphalt specimens. In the microstructure, aggregates and sand mastic were divided into different subdomains. Finite element mesh was generated within each aggregate and sand mastic subdomain. Then the linear/damage-coupled viscoelastic mastic with specified properties defined in an ABAQUS user subroutine was combined with elastic aggregates to simulate global linear and damage-coupled viscoelastic behavior of reclaimed asphalt mixtures. Simulation results under a loading frequency showed the viscoelastic creep behavior under the constant loading magnitude. The damage-coupled viscoelastic mixture generated larger creep deformation comparing the linear behavior. Comparison under different loading frequencies found the compression strain decreases with frequencies due to less relaxation time. Simulation results indicate the developed finite element models are capable for complex viscoelastic behavior of reclaimed asphalt mixture. Further study will be extended to the three-dimensional micromechanical simulation.

References

Bahia, H., Zhai, H., Bonnetti, K., and Kose, S. (1999). "Nonlinear viscoelastic and fatigue properties of asphalt binders." *J. Assoc. Asphalt Paving Tech.*, 68, 1-34.

Bazant, Z. P., Tabbara, M.R., Kazemi, Y., Pijaudier-Cabot, G. (1990). " Random particle simulation of damage and fracture in particulate or fiber-reinforced composites. ." Damage Mechanics in Engineering Materials, Trans. ASME, AMD.

Budhu, M. S., Ramakrishnan, and Frantziskonis, G. "Modeling of Granular Materials: A Numerical Model Using Lattices, Mechanics of Deformation and Flow of Particulate Materials." *McNu Conference,Trans. ASCE,* Northwestern Univ.

Buttlar, W. G., Bozkurt, D., Al-Khateeb, G. G., and Waldhoff, A. S. (1999). *Understanding asphalt mastic behavior through micromechanics (with discussion and closure),* Transportation Research Board.

Buttlar, W. G., and Roque, R. "Evaluation of empirical and theoretical models to determine asphalt mixture stiffnesses at low temperatures." Baltimore, MD, USA, 99-141.

Buttlar, W. G., and Roque, R. (1997). *Effect of asphalt mixture master compliance modeling technique on thermal cracking performance evaluation using superpave,* University of Washington, Seattle.

Buttlar, W. G., and You, Z. (2001). "Discrete Element Modeling of Asphalt Concrete: A Micro-Fabric Approach." *Journal of the Transportation Board, National Research Council, Washington, D.C.*, 1757.

Christensen, R. M., and Lo, K. H. (1979). "Solutions for Effective Shear Properties in Three Phase Sphere and Cylinder Models." *J. Mech. Phys. Solids*, 27, 315-330.

Dai, Q. (2004). "Micromechanical Modeling of Constitutive and Damage Behavior of Heterogeneous Asphalt Materials," University of Rhode Island.

Dai, Q., and Sadd, M. H. (2004). "Parametric model study of microstructure effects on damage behavior of asphalt samples." *International Journal of Pavement Engineering*, 5(1), 19-30.

Dai, Q., Sadd, M. H., and Parameswaran V. Shukla A. (2005). "Prediction of damage behaviors in asphalt materials using a micromechanical finite-element model and image analysis." *Journal of Engineering Mechanics*, 131(7), 668-677.

Dai, Q., Sadd, M. H., and You, Z. (2006). "A Micromechanical Finite Element Model for Viscoelastic Creep and Viscoelastic Damage Behavior of Asphalt Mixture." *International Journal for Numerical and Analytical Methods in Geomechanics*, 30, 1135–1158.

Dai, Q. and You, Z (2007), Prediction of Creep Stiffness of Asphalt Mixture with Micromechanical Finite Element and Discrete Element Models, Journal of Engineering Mechanics, American Society of Civil Engineers (ASCE), Volume 133, Issue 2, pp. 163-173.

Guddati, M. N., Feng, Z., and Kim, R. (2002). "Toward a micromechanics-based procedure to characterize fatigue performance of asphalt concrete." *Transportation Research Record*(1789), 121-128.

Hashin, Z. (1965). "Viscoelastic Behaviour of Heterogeneous Media." *In Journal of Applied Mechanics, Trans. ASME,*, 9, 630-636.

Hashin, Z., and Shtrikman, S. (1963). "A Variational Approach to the Theory of the Elastic Behaviour of Multiphase Materials." *J. Mech. Phys. Solids*, Vol. 11, 137.

Kose, S., Guler, M., Bahia, H. U., and Masad, E. (2000). "Distribution of Strains within Asphalt Binders in HMA Using Image and Finite Element Techniques." *J. Trans. Res. Record National Research Council, Washington, D.C.*, 1728(21-27).

McDaniel, R. S., and Shah, A. (2003). *Use of reclaimed asphalt pavement (rap) under superpave specifications (with discussion)*, Association of Asphalt Paving Technologists.

Mora, P. "A Lattice Solid Model for Rock Rheology and Tectonics." *The Seismic Simulation Project Tech.*, Institut de Physique du Globe, Paris, 3-28.

Mustoe, G. G. W., and Griffiths, D. V. "An Equivalent Model Using Discrete Element Method(DEM), ." *Proc. 12th ASCE Engineering Mechanics Conf.*, La Jolla, CA.

Papagiannakis, A. T., Abbas, A., and Masad, E. (2002). "Micromechanical analysis of viscoelastic properties of asphalt concretes." *Transportation Research Record*(1789), 113-120.

Picado-Santos, L. G., Oliveira, J. R. M., and Pereira, P. A. A. (2004). "Mechanical Characterisation of Hot Mix Recycled Materials." *International Journal of Pavement Engineering*, 5(4), pp 211-220.

Roberts, F. L., Kandhal, P. S., Brown, E. R., Lee, D. Y., and Kennedy, T. W. (1996). "Hot Mix Asphalt Materials, Mixture Design and Construction. Second Edition." NAPA Research and Education Foundation, 603 p.

Sadd, M. H., Dai, Q., and Parameswaran, V. (2004a). "Microstructural simulation of asphalt materials: Modeling and experimental studies." *Journal of Materials in Civil Engineering*, 16(2), 107-115.

Sadd, M. H., Dai, Q., Parameswaran, V., and Shukla, A. (2004b). "Microstructural simulation of asphalt materials: Modeling and experimental studies." *Journal of Materials in Civil Engineering*, 16(2), 107-115.

Sadd, M. H., Dai, Q., Parameswaran, V., and Shukla, A. (2004c). "Simulation of Asphalt Materials Using Finite Element Micromechanical Model with Damage Mechanics." *Transportation Research Record*(1832), 86-95.

Schapery, R. A. (1969). "On the characterization of nonlinear viscoelastic materials." *Polymer Engineering and Science*, 9(4), 295-310.

Sepehr, K., Svec, O. J., Yue, Z. Q., and El Hussein, H. M. "Finite element modelling of asphalt concrete microstructure." Udine, Italy, 225.

Shashidhar, N., Needham, S. P., Chollar, B. H., and Romero, P. (1996). "Prediction of the performance of mineral fillers in stone matrix asphalt." *J. Assoc. Asphalt Paving Tech.*, 222-251.

Simo, J. C., and Ju, J. W. (1987). "Strain- and Stress-Based Continuum Damage Models - I. Formulation." *International Journal of Solids and Structures*, 23(7), 821-840.

Stankowski , T. (1990). "Numerical Simulation of Failure in Particle Composite, Computers and Structures." *Computers and Structures, Great Britain*, 44(1/2), 460.

Voigt, W. (1889). *Ueber die Beziehung zwischen den beiden Elasticitatsconstanten isotroper Korper.*

You, Z. (2003). "Development of a Micromechanical Modeling Approach to Predict Asphalt Mixture Stiffness Using Discrete Element Method," University of Illinois at Urbana-Champaign, published by UMI, a Bell & Howell Information Company, Ann Arbor, MI.

You, Z., and Buttlar, W. G. (2004). "Discrete Element Modeling to Predict the Modulus of Asphalt Concrete Mixtures." *Journal of Materials in Civil Engineering, ASCE*, 16(2), 140-146.

You, Z., and Buttlar, W. G. (2005). "Application of Discrete Element Modeling Techniques to Predict the Complex Modulus of Asphalt–Aggregate Hollow Cylinders Subjected to Internal Pressure." *Journal of the Transportation Research Board, National Research Council*, 1929, 218-226.

You, Z., and Buttlar, W. G. (2006). "Micromechanical Modeling Approach to Predict Compressive Dynamic Moduli of Asphalt Mixture Using the Distinct Element Method." *Journal of the Transportation Research Board, National Research Council, Washington, D.C.*, No. 1970, 73-83.

Estimation of the Stiffness of Asphalt Mastics Using Hirsch Model

Cristian Druta[1], Linbing Wang[2], George Z. Voyiadjis[3] and Chris Abadie[4]

ABSTRACT: Mastic properties are very important to the performance of asphalt concrete. Fine and coarse aggregates are usually not directly interacting with asphalt binder but with mastics. Permanent deformation and fatigue cracking tend to occur in the mastics and the interfaces between mastic and aggregate. Mastics demonstrate much more complicated behavior than asphalt binder including permanent deformation, non-linearity, and temperature sensitivity. Two important mastic properties include its shear modulus and permanent deformation. Too low stiffness may lead to high potential of rutting while too high stiffness may lead to cracking. This study targets at estimating the shear stiffness of mastics using the complex shear modulus of binder and the Hirsch model based on binder modulus and the volumetric composition of filler. Predictions of the mastics shear moduli using Hirsch model were compared with experimental measurements at different temperatures and frequencies and show very good agreement. The study also indicates that Time-Temperature superposition algorithms are applicable to mastics for different volume fractions of mineral fillers.

INTRODUCTION

Mineral fillers have commonly been used in asphalt mixtures to fill the voids between the larger aggregate particles (Chen 1996, Jo et al. 1998, Jo and Kim 2001). Generally, aggregates passing the No. 200 sieve are called filler (Ishai and Craus 1996, Anderson and Marasteanu 1999) and are used in percentages by volume in the mix designs. In fact, if a core of asphalt concrete is observed in cross section, three components can be visually observed are aggregate (coarse and fine), air voids, and mastic (Vacin et al. 1997, Buttlar et al. 1998). The asphalt cement occurs not as asphalt alone, but is intimately mixed with mineral fillers forming the mastic. Such a distribution points to the important role played by the mastic in the workability and performance of asphalt concrete.

---

[1] Postdoctoral Research Assistant, Virginia Tech University, Department of Civil and Environmental Eng., Blacksburg VA 24061, cdruta1@lsu.edu
2 Associate Professor, Virginia State University, Department of Civil and Environmental Eng.,Blacksburg VA 24061, Tel. (540)231-5262, wangl@vt.edu
3 Boyd Professor, Louisiana State University, Baton Rouge LA 70803, Tel. (225)578-8668
4 Materials Administrator, Louisiana Transportation Research Center, 4101 Gourrier Avenue
Baton Rouge LA 70808, Tel. (225)767-9109, chrisabadie@dotd.la.gov

Although several studies have been reported in the asphalt literature, a good correlation between any measured physical property and the stiffening of asphalt by mineral fillers has not been reported yet (Smith and Hesp 2000; Uddin 1999). This may be attributed to the fact that the stiffening potential of mineral fillers is a complex function of several factors such as average particle size, gradation, shape of the particles, presence of agglomerates, degree of dispersion, and asphalt-filler interface properties. Also, some of these properties interact with each other in complex ways - for example, the degree of dispersion is related to asphalt-filler interface properties; and the presence of agglomerates is dependent upon the average particle size and also the asphalt-filler interface properties (Anderson and Chrismer 1984, Jiang et al. 1997).

OBJECTIVES

There were two major objectives for this study. The first objective was to estimate the influence of type and amount of mineral fillers on mechanical properties of asphalt mastics through dynamic rheometer testing (DSR). One binder and three types of fillers were mixed at five volume fractions and tested at three temperatures. For the interpretation of the results, "master curves" technique was employed in order to determine a correlation between the binder and the mastics using these test results. The second objective was to estimate the complex modulus of mastics by using binder complex modulus from the DSR testing and the volumetric composition of the mineral fillers through Hirsch model.

MATERIALS

Fillers

Three fillers were used in this study and they were: Donna Fill, Limestone and Granite. All the fillers were used to form the mastics in five volume fractions: 5, 10, 15, 20, and 30% (bulk material).

Donna Fill, also known as nepheline syenite granite, is a by-product of crushed syenite granite rock and has been successfully used in asphalt concrete mixes, construction of road base and subbase courses, airport runways, and concrete bridge restoration (Waltham 1994). The addition of this type of granite filler, improves Marshall stability, % VMA, shear values, film thickness of asphalt on the aggregates, reduces rutting and improves load-carrying capacity of the pavement structure.

Usually, the effect of donna fill and other granites as compared to natural sands used as fines in asphalt mixtures demonstrated an increase in mixture stability, thicker film thickness retained and a reduction in rutting and stripping susceptibility. Modifications made to hot mix asphalt with limestone fillers might add years to its life, because these modifications can reduce stripping, rutting, cracking, and aging due to complicated chemical reactions. Limestone substantially improves each of these properties when used alone, and also works well in conjunction with polymer additives, helping to create pavement systems that will perform to the highest expectations for many years. Life cycle cost analysis demonstrated that limestone is also cost-effective.

Some properties of the above mentioned materials are presented in Table 1.

Table 1. Properties of fillers

Type of Filler	Donna Fill	Limestone	Granite
Specific Gravity	2.65	2.67	2.74
Plasticity Index	Non-plastic	Non-plastic	Non-plastic
Specific Surface Area (cm^2/g)	6307	7968	7206
Angularity Index	0.62	0.46	0.49
Bulk Density (kg/m^3)	1080	1116	1215
Modulus of Elasticity E (GPa)	56	62	75

All fillers were obtained by dry sieving fine aggregate parent rock over a 75 μm sieve and then analyzed with the Microtrac analyzer for particle size distribution. The results of the analysis (gradations) are presented in Figure 1. It can be seen that their gradations are very close and therefore the different results of mastics thus formed were mainly attributed to different material properties.

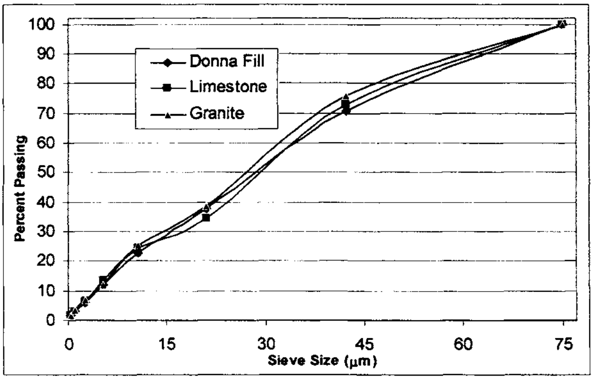

FIG. 1. Gradation of the Mineral Fillers

Asphalt binder

The asphalt binder used in this study was a PG64-22 unmodified base asphalt, primarily used in paving for both new construction and pavement rehabilitation and in both dense-graded and open graded Hot Mix Asphalt (HMA). It is also used for sealing of edges and cracks of asphalt pavements.

Mastics

Mixtures of asphalt binder and filler, called mastics in this paper, are often assumed to behave as simple viscoelastic materials or simply, binders stiffened by filler. Stiffening of asphalt binder is only one way in which the addition of mineral filler changes the properties of this material. In fact, mastics behave quite similarly to asphalt binders, in that, they flow with time and are temperature dependent. Thus, both loading time and test temperature must be taken into account when characterizing the flow behavior of mastics.

EXPERIMENTAL STUDY

Sample preparation

All mineral fillers were thoroughly mixed and dried for one hour in an oven at 160°C before being used in the testing. The asphalt mastics were prepared by mixing the binder with 3 types of filler having particle sizes smaller than the 0.075 (mm) sieve opening (#200 mesh). Measured quantities of 25 (g) of binder were heated at 150° C for 10 minutes and then mixed with the fillers in five volume fractions of 5, 10, 15, 20, and 30% of bulk material. After being heated, the binder was removed from the oven and the heated filler was added to it and was mixed until a homogeneous mixture was obtained; then the mixture was poured into silicon molds to make samples for the shear rheometer measurements - single and frequency sweep oscillation at either constant strain or constant stress.

DSR testing

The rheological properties of the binder and mastics were measured using an Automated Dynamic Shear Rheometer (ADSR), which can be used in stress and strain control modes. Two types of tests were conducted: single shear oscillation at constant strain (12%) and frequency sweep at constant stress (2500 Pa). The behavior of the materials was evaluated in terms of $|G^*|/\sin\delta$ as a function of temperature and loading time. Samples were tested at temperatures of 46° C, 55° C, and 64° C and loading frequencies ranging from 0.1 (Hz) to 100 (Hz).

Testing Procedures, Results and Discussion

DSR oscillation at constant strain (12%)

The dynamic shear rheometer (DSR) (AASHTO 2002) is currently being used by the DOTs for determination of the viscoelastic properties of asphalts following the recommendations of the Strategic Highway Research Program (SHRP) (Anderson et al. 2000, Stuart et al 2000). The Superpave specification parameter $|G^*|/\sin\delta$ was identified as the term to be used for medium to high temperature performance grading of asphalt binder for their rutting resistance (Bahia 1995, Gubler et al. 1999, Bahia et al. 2001).

In this study all the samples were tested in the strain mode, at a constant strain of 12% and a frequency of 10 (rad/s) or 1.592 (Hz), in accordance with SHRP specifications. The plates selected for testing the samples had 25 (mm) in diameter with a 1 (mm) gap between the plates. The shear complex modulus G* and phase angle δ were calculated automatically as part of the operation of the rheometer using proprietary computer software supplied by the equipment manufacturer.

It can be seen from Figure 2 that the mineral filler type influences the rheological properties of mastics, in that the moduli of mastics containing granite and limestone were larger than those containing donna fill. The graph shows the volume fractions of fillers without air voids. Volume fractions without air voids are presented in Table 2.

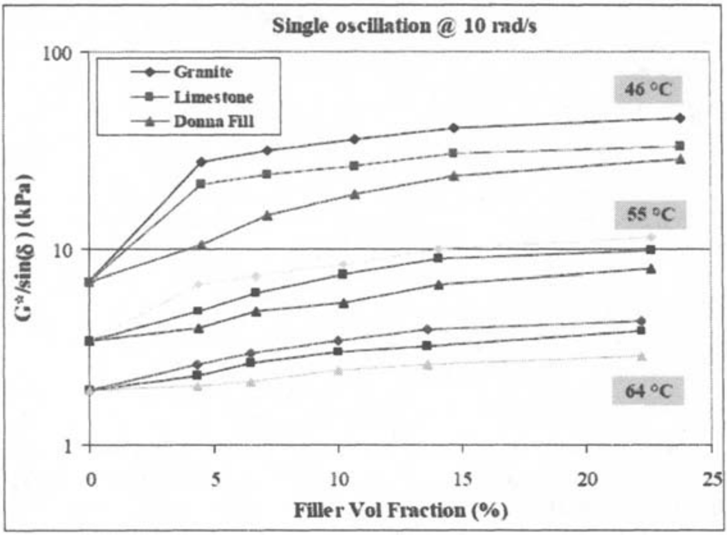

FIG. 2. Stiffening of Asphalt with the Addition of Various Filler Volume Fractions

The three types of filler had different effects on the same asphalt due to the filler properties and the physical-chemical reaction between fillers and asphalt (Shashidhar and Romero 1998). The increase in (|G*|/sinδ) for granite and limestone was due to the fact that both granite and limestone have larger moduli of elasticity than donna fill.

Table 2. Filler volume fractions by solid material

Filler type	Volume fraction (%)				
Donna fill	4.50	7.16	10.72	14.65	23.75
Limestone	4.37	6.75	10.26	14.07	22.62
Granite	4.35	6.48	10.01	13.61	22.23

Figure 2 shows the rut-controlling term (|G*|/sinδ) of the different mastics plotted against the volume fractions of the fillers. The values used in the graph, for the (|G*|/sinδ) term, represent the averages of two values obtained for each test. For each mixture, the complex modulus |G*| and the phase angle δ were measured twice by DSR at temperatures of 46°C, 55°C, and 64°C and at a frequency (f) of 1.596 (Hz). The values of the phase angle (δ) increased from 76 (deg) at 46°C, to 80 (deg) at 55°C, and to 84 (deg) at 64°C for both binder and mastics. This indicates that mastics behave similarly to pure binders for these temperatures and filler volume fractions.

DSR frequency sweep oscillation at constant stress

In general, multiple single frequencies or frequency sweep tests are used to construct the master curves relevant to the rheological properties of mastics and mixes. Complex moduli at different test temperatures and frequencies can then determined by using the time-temperature superposition principle. In constructing the master curves using the time-temperature superposition principle, data obtained from the DSR are first calculated in terms of stiffness or complex modulus G* over a range of temperatures and loading times and the results are compared to those at a reference temperature.

Typically, the stiffness modulus of asphalt binders (mastics) increases with decreasing temperature and increasing frequency (Roberts et al. 1996, Hoare and Hesp 2000). By shifting the stiffness modulus against the loading time relationship for various temperatures horizontally with respect to a chosen reference temperature, a complete modulus-time (loading frequency) behavior curve can be assembled. Hence, test data collected at any other temperatures can be shifted with respect to loading time (or frequency) so that the various curves can be aligned to form a single master curve.

In the frequency sweep test conducted on the asphalt binder and mastics, all the specimens were loaded at a constant shear stress of 2500 Pa. Figure 3 shows the frequency sweep test results at 46, 55, and 64 °C for binder and mastics (30% filler).

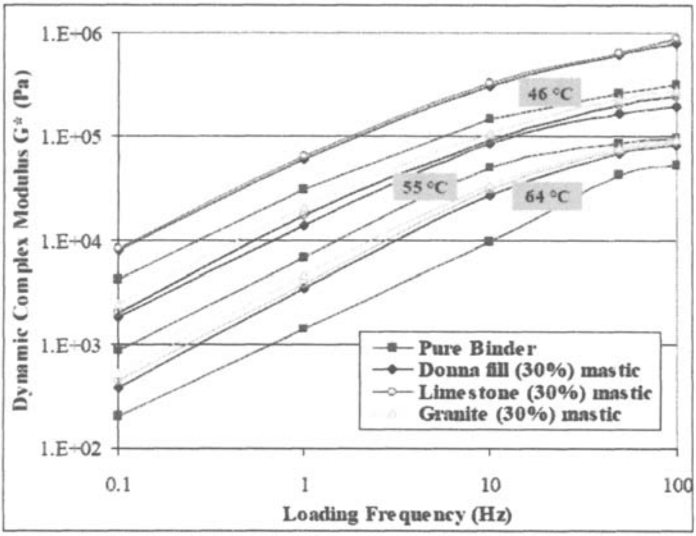

Figure 3. Frequency Sweep Results for Pure Binder and Mastics

In order for the testing data (dynamic modulus curves) to be shifted horizontally along the frequency axis, shift factors (a_T), whose logarithmic values represent the distances required to assemble the curves at different temperatures are calculated using the approaches by Anderson et al (2001). The shift factors a_T were obtained by using the Williams-Landel-Ferry equation and the data obtained from the oscillation frequency sweep test at constant stress for the three fillers at 30% bulk volume fractions. Table 3 presents a_T values calculated using temperature of 46 °C as the reference temperature (T_r). Similar values for the shift factors were obtained for mastics at lower volume fractions (Druta, 2006).

If the viscoelastic properties form an almost continuous function after shifting, then the time-temperature superposition principle is proved to be valid. Thus, for each curve determined at a particular test temperature, a horizontal shift factor a_T is produced. The shift factor a_T defines the required shift at a given temperature, i.e., a constant by which the frequency f(Hz) must be divided to get a reduced frequency f_r for the master curve:

$$f_r = f/a_T \qquad (1)$$

and it is only a function of temperature for a certain material. The Williams-Landel-Ferry (WLF) equation has been widely used to characterize the temperature shift factors for asphalt cement. This equation could accurately describe the shift factors for asphalt cement above a characteristic temperature, called the reference temperature T_r:

$$\log(f) - \log(f_r) = \log a_T = -C_1(T - T_r)/(C_2 + T - T_r) \qquad (2)$$

where,
a_T = horizontal shift factor
T = temperature, °C
T_r = reference temperature, °C
C_1, C_2 = empirical constants (9.5, 95)

Table 3. Shift factors for asphalt binder and mastics

Material	Shift factor a(T)		
	46 °C	55 °C	64 °C
Pure binder PG64-22	1.0037	0.822	1.517
Donna fill mastic	1.0042	0.795	1.528
Limestone mastic	1.0036	0.824	1.514
Granite mastic	1.0021	0.819	1.497

Figure 4 shows the master curves developed for the frequency sweeps of the samples presented above. The shifting was conducted using Williams-Landel-Ferry (WLF) equation, normalized to those at test temperature of 46 °C.

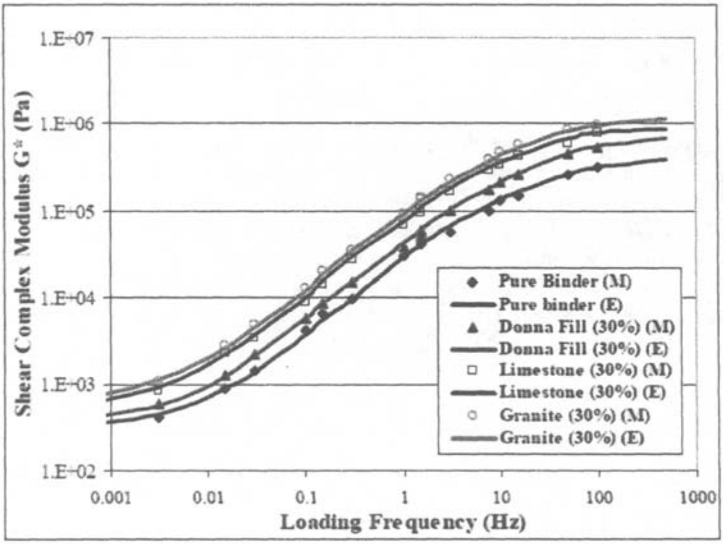

Figure 4. Master Curves for Pure Binder and Mastics (30% filler)

Hirsch model

One of the purposes of this paper was to adapt the Hirsch model (Christensen et al 2003) for estimating the complex shear modulus G* of asphalt concrete to estimating the complex shear modulus of mastics by using the binder complex modulus and volumetric composition of the mineral fillers. The following equation was employed for the estimation of the mastics complex modulus, in terms of the complex shear modulus, *G**, VFA, and VMA:

$$G^*_{mix} = P_c\{[E_a(1 - VMA/100) + G^*_{binder}[(VFA \cdot VMA)/10{,}000]\} + (1 - P_c)[(1 - VMA/100)/E_a + VMA/VFA \cdot G^*_{binder}]^{-1} \quad (3)$$

where: P_c is the contact factor

E_a is the filler modulus back-calculated from the data at 5% filler fraction (Pa)

G^*_{mix} is the complex shear modulus for the mixture (mastic) (Pa)

G^*_{binder} is the complex shear modulus for the binder (Pa)

VFA is voids filled with asphalt (%)

VMA is voids in mineral aggregate (%)

Expression for P_c is given by:

$$P_c = [3 + (VFA \cdot G^*_{binder})/VMA]^{0.678} / [396 + (VFA \cdot G^*_{binder})/VMA]^{0.678} \quad (4)$$

Values for G^*_{binder} were determined experimentally using the DSR oscillation at constant strain test.

Regarding the Hirsch model adapted for estimating the complex shear modulus of mastics G* by using the binder complex modulus and volume fractions of the mineral fillers, Figures 5 through 7 show that there is a good correlation between the predicted values and the measured values (all R^2 being around 0.8 or higher). For this study VFA was taken as 100% and VMA was replaced by the filler volume fraction and calculated without any air voids (see Table 2).

Summary and Conclusions

In order to properly characterize the resilient response of asphalt mastics the dynamic shear rheometer was employed for testing the mastics at different temperatures and mineral filler volume fractions. The stiffening effect of the fillers in the asphalt binder was evaluated through micromechanical (Hirsch model) and rheological (time-temperature principle) methods. Limestone and granite mastics showed higher shear moduli than donna fill mastics due to their higher moduli of elasticity.

Time-temperature superposition theory used for constructing the master curves of asphalt mixtures proved applicable to the characterization of the rheological properties of asphalt mastics.

Estimated shear moduli of mastics by using Hirsch model were in good agreement (R^2 values were around 0.8 or higher) with those obtained by measurements with the dynamic shear rheometer.

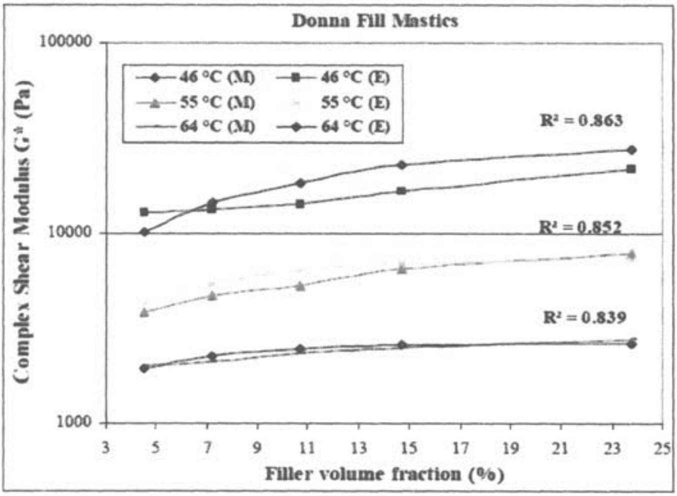

Figure 5. Estimated and Measured Values of G* for Donna Fill mastics

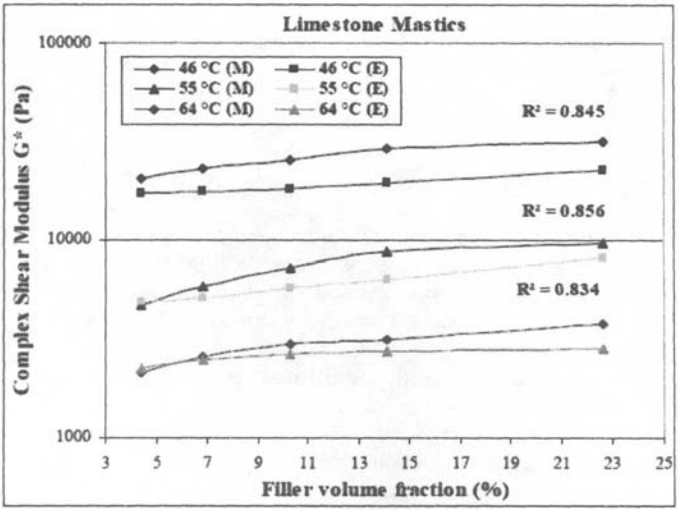

Figure 6. Estimated and Measured Values of G* for Limestone Mastics

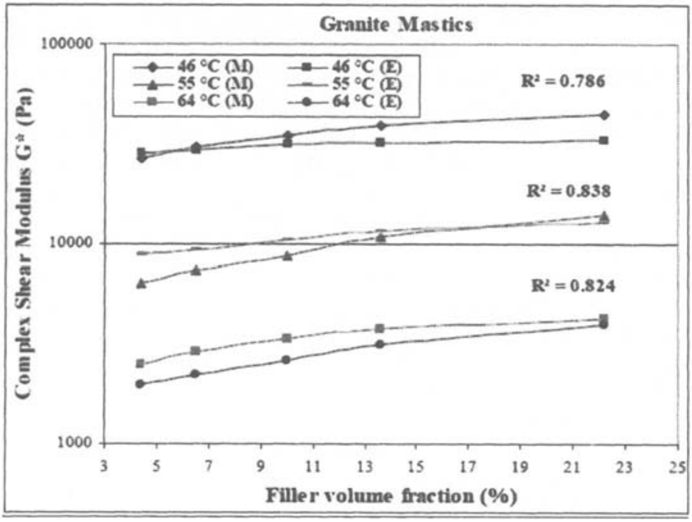

Figure 7. Estimated and Measured Values of G* for Granite Mastics

References

AASHTO Standard T315-02 (2002). "Standard Test Method for Determining the Rheological Properties of Asphalt Binder Using a Dynamic Shear Rheometer (DSR)."

Anderson, D. A., and. Chrismer, S. M. (1984). "Evaluation of tests for characterizing the stiffening potential of baghouse dust in asphalt mixes." TRR *968*, TRB, National Research Council, Washington, D.C., 31–37.

Anderson, D. A. and Marasteanu, M.O. (1999). "Physical hardening of asphalt binders relative to their glass transition temperatures." TRR 1661 (1547), National Research Council, Washington, D.C., 27-35.

Anderson, D.A., Christensen, D.W., and Bahia, H. (1991). "Physical properties of asphalt cement and the development of performance related specifications." AAPT Proceedings, 60, 437-475.

Anderson et al. (2000). "Factors affecting variability in strategic highway research program binder tests." TRR 1728 (1360), 28-36.

Bahia, H.U. (1995). "Critical evaluation of asphalt modification using the SHRP concepts" TRR 1488, 82-88.

Bahia, H.U. et al. (2001). "Characterization of modified asphalt binders in Superpave mix design." TRR, NCHRP Report 459, 124-128.

Buttlar et al. (1999). "Understanding asphalt mastic behavior through micromechanics" TRR, 1681, 157-169.

Chen, J.S. (1996). "Analysis of tensile failure properties of asphalt-mineral filler mastics." Journal of Materials in Civil Engineering, 10(4), 256-262.

Christensen, D.W., Pellinen, T., and Bonaquist, R.F. (2003). “Hirsch model for estimating the modulus of asphalt concrete.” AAPT, 72, 184-204.

Druta, C. (2006). “A micromechanical approach for predicting the complex shear modulus and accumulated shear strain of asphalt mixtures from binder and mastics.” Dissertation, Louisiana State University, Baton Rouge, Louisiana.

Gubler, R. et al. (1999). “Investigation of the system filler and asphalt binders by rheological means.” AAPT, 68, 284-304.

Hoare, T.R. and Hesp, S.A.(2000). “Low temperature fracture testing of asphalt binders.” TRR, 1728(1234), 36-42.

Ishai, I. and Craus, J. (1996). ”Effects of some aggregate and filler characteristics on behavior and durability of asphalt paving mixtures.” TRR 1530, National Research Council, Washington, D.C., 75-85.

Jiang, R.-B., Lin, J.D., and Lin, D.F. (1997). “Rheology of asphaltic binders and their effects on asphalt concrete.” TRR, 1535, 74-81.

Jo, D., Kim, R., and Lee, H. (1998). “Effects of aging on viscoelastic properties of asphalt-aggregate mixtures.” TRR, 1630(0334), 21-27.

Jo, D. and Kim, R. (2001). ”Laboratory evaluation of fatigue damage growth and healing of asphalt concrete mixtures using the impact resonance method”, ASCE Journal of Materials in Civil Eng., 13(6), 434-440.

Roberts, F.L. et al. (1996). “Hot-mix asphalt materials, mixture design, and construction.” NAPA Research and Education Foundation, Second Ed., 76-84.

Shashidhar, N. and Romero, P. (1998). “Factors affecting the stiffening potential of mineral fillers.” TRR, 1638(0989), 94-100.

Smith, B.J. and Hesp, S.A.M. (2000). “Crack pinning in asphalt mastic and concrete: regular fatigue studies.” TRR, 1728(1233), 75-81.

Stuart, K.D., Mogawer, W. S., and Romero, P. (2000). “Evaluation of the Superpave asphalt binder specification for high-temperature pavement performance.” AAPT, 69, 148-176.

Uddin, W. (1999). “A micromechanical model for prediction of creep compliance and viscoelastic analysis of asphalt pavements.” TRB, 78th Annual Meeting, Washington, D.C., CD Version.

Vacin, O.J., Stastna, J., and Zanzotto, L. (1997). ”Creep compliance of polymer modified asphalt, asphalt mastic and hot mix asphalt.” TRB, 82nd Annual Meeting, Washington, D.C., CD Version.

Waltham, T.(2003). “Foundations of engineering geology.” First Ed.,E & FN Spon, 44-50.

FUNDAMENTAL MECHANICS OF ASPHALT COMPACTION THROUGH FEM AND DEM MODELING

Linbing Wang[1], Bing Zhang[2] and Dong Wang[3] and Zhongqi Yue[4]

ABSTRACT

The compaction of asphalt concrete is the last step in controlling the quality of pavement. Tremendous information on the mixture's characteristics, segregation, and fundamental properties of asphalt concrete demonstrates itself in the compaction process. An understanding of the fundamental mechanisms of compaction will help better control the quality of asphalt concrete pavement. This paper presents the investigation of the compaction mechanics using both Finite Element Method (FEM) and Discrete Element Method (DEM). The FEM simulation adopted a porous viscoplasticity model, which considers the compaction in the view of its air void reduction resulted from the squeezing of aggregates and mastics. The DEM simulations provide a view of considering the compaction a process in which aggregate particles translate and rotate to positions forming denser packing. By this approach, particle shape and binder stiffness factors can be considered. The simulation results indicate that both approaches can describe the compaction phenomena consistently with field observations and empirical experience.

INTRODUCTION

Compaction of asphalt concrete is one of the most important steps in controlling the quality of pavement construction. More importantly, many problems demonstrate themselves during compaction: some mixes (may indicate a good mix) may not be easy to compact compared to others; too thin layer thickness may prevent effective compaction; a weaker mastic may make compaction too easy but it doesn't mean good quality; a soft base or subbase may cause difficulties for compaction (compaction energy is absorbed by the base or subbase); the non-uniformity of the base or subbase support causes non-uniform compaction if operation parameters do not vary correspondingly; and a change of environmental conditions such as temperature and wind speed results in change of viscosity and therefore compaction

---

[1] Associate Professor, Virginia Tech, Blacksburg VA 24061, email: wangl@vt.edu
[2] Ph.D. Candidate, Virginia Tech, Blacksburg, VA 24061
[3] Graduate Research Assistant, Virginia Tech, Blacksburg, VA 24061
[4] Associate Professor, University of Hong Kong, Hong Kong

effectiveness. An understanding of how these factors affect compaction in the point of view of fundamental mechanics will certainly help achieve better compaction, optimize layer thickness and other factors that affect compaction.

Factors that affect compaction can be generally classified into three categories: Properties of the Materials, Environmental Variables and Boundary Conditions, and Compaction Equipment and Operation Control. The properties of the materials include the gradation, shape, angularity and texture of aggregate, and the grade, the amount and the temperature sensitivity of the binder. The environmental variables and boundary conditions include air and base temperatures, the humidity, sunshine or cloudiness and wind velocity, layer thickness, stiffness of the underlying layer, and mix laydown temperature. Layer thickness is one of the most important variables that affect other influencing factors such as the rate of cooling of the asphalt mixtures, and the particle movement during compaction. Compaction equipment and operation control include types of roller, rolling patterns, number of passes, and rolling speed. These factors can be adjusted during the compaction. An understanding of the compaction mechanism plus the intelligent compactor technique will certainly enhance the compaction quality significantly (intelligent compaction requires a fundamental understanding of the compaction mechanism to make it wise; wrong understanding would make it unwise). The factors in the three categories are listed as follows (see Figure 1 for an illustration as well):

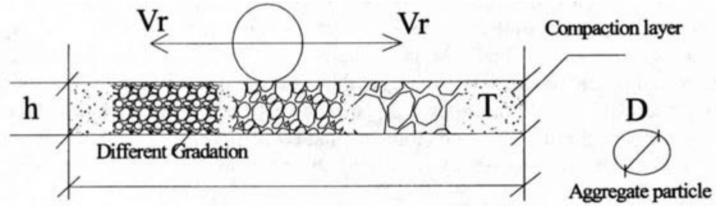

Temperature, Stress/Strain, Force/Displacement Boundary Conditions, and Initial Conditions.

FIG. 1 Illustration of the Compaction Model

Properties of the Materials: aggregate gradation (filler percentage as well), maximum size of aggregate (or the dominant aggregate size) D, aggregate shape, angularity and texture, asphalt content, asphalt type and temperature sensitivity.

Environmental Variables and Boundary Conditions: mixture temperature when laid T_l, Air temperature T_a, base temperature T_b, wind velocity V_w, other weather conditions (sunshine, cloudiness, humidity), layer thickness h, stiffness of the lower course S

Compaction Equipment and Operation Control: type of compactor, rolling pattern, number of roller passes N_r, rolling speed V_r, compaction time t

Obviously, a thorough investigation to explore how these factors affect compaction independently or in a coupled manner would require a huge experimental factorial and tremendous costs. Identification of the critical factors would help reduce the efforts while still enabling solving the essential problems in achieving effective compaction. In addition, environmental conditions are much more difficult to control and fundamental mechanisms at the materials scale (material properties are sensitive to the environmental conditions) cannot be properly investigated if an experimental method is adopted because of the difficulties in controlling the environmental conditions. Therefore, an advanced modeling and computational simulation approach is proposed for this study. The Discrete Element Method (DEM) has the advantage to deal with the components' properties separately (aggregate, binder and void) while the Finite Element Method (FEM) with continuum type of modeling using porosity as an internal variable can model the reduction of air voids in the compaction process. Both methods will be used for this investigation.

OBJECTIVE

The objective of this research is to investigate how different influencing factors affect compaction through modeling using both FEM and DEM.

DOMINATING FACTORS AND SIGNIFICANCE OF MODELING

A preliminary literature review indicates that critical factors include layer thickness, gradation, dominant aggregate particle size (the size that constitutes the largest percentage in the gradation), aggregate shape and angularity, temperature (binder viscosity), base/subbase support, and the number of passes (the compaction system is assumed to be fixed).

The mechanics based understandings of the compaction mechanisms can be compared with empirical observations accumulated through field-testing and experimental studies qualitatively to verify the rationality of the models on one hand and to use the simulations to guide field work on the other hand.

THEORETICAL COMPACTION MECHANICS

Numerical Approaches

There are several approaches in mechanics to model the compaction of asphalt concrete. Fundamentally there are two major groups of approach, those in the continuum mechanics branch and those in the micromechanics branch. The numerical method in the continuum approach uses mainly the FEM while the micromechanics approach uses the DEM. Analytical approach, although can offer some general guides in understanding the force and displacement relations, it cannot model the compaction process quantitatively and the deforming process as asphalt concrete is not a linear elastic/viscoelastic material.

Analytical Solution

The compaction problem can be theoretically modeled as a rolling contact problem (for example, the deforming behavior at the end of compaction). There are quite few analytical solutions in the elasticity domain and viscoelasticity domain to solve the contact problem. Examples include the Hertz solution and the Mindlin solution. These are elasticity solutions but cannot be converted into viscoelasticity solutions through the correspondence theory as conveniently because the contacting area is changing.

Both Hertz and Mindlin solutions indicate that a stiff material would deform (elastic deformation) less or more difficult to compact. The Mindlin solution also indicates that the surface adhesion or cohesion play a role in the deformation of the material (allowing for tangent forces applied on the surfaces). Nevertheless none of them can explain the mechanism of compaction well enough as they are elastic solutions and the displacements/ deformations will be completely recovered if the forces are removed. The viscoelasticity solution can explain the time-dependent deformation mechanisms to certain degree. It, however, still cannot explain the internal change of the material during the compaction, the unrecoverable deformations, the reduction of air voids and so on.

SOIL MECHANICS ANALOGY

During the compaction, the air void content is being reduced to form a densely packed structure, where aggregate particles may form direct contacts. When the structure is dense enough the reaction from the contacting aggregates will be strong enough to resist the compaction force and no voids can be further reduced. On the other hand, when temperature becomes lower during the compaction process, the material also becomes stiffer, gaining more resistance against the compaction force. If temperature drop effect is secondary (for example, due to the short period of compaction, and the potential application of heat compensation), compaction process may be compared to the consolidation process when pore water (air voids) were driven out of the mixture. With this understanding, at certain pressure level, the end porosity or air void content will be a highly non-linear function of the pressures. This phenomenon is common to many consolidation processes. It is also qualitatively consistent with the compaction process of asphalt concrete: it is relatively easier to reduce the air void content from 15% to 6%; it requires much more efforts to compact it from 6% to 4% air void content.

GENERAL MODELING PHILOSOPHY

There are two fundamentally different methods to interpret the compaction process. Method one is the particle view; method two is the void view. In the particle view, particles will translate and rotate to move to positions originally occupied by voids to form denser packing. The void view just considers compaction as a process when air voids are driven out of the mixture. Either view can explain the compaction mechanisms but have their advantages and disadvantages. The DEM approach falls into the aggregate view while the FEM may take the void view more conveniently.

FEM Modeling

There are few studies in the continuum regime for investigating the compaction mechanisms. The use of mixture theory, to certain degree explains the void reduction during the compaction process.

One of the more popular methods is using a viscoplasticity model in conjunction with FEM numerical simulations. Henny and Huerne (2002) studied the simulation of compaction process with an analogy between hot asphalt mixtures and wet soils. A "Critical State" material model based on soil mechanics was used as a fundamental model to describe the behavior of asphalt mixture in his study. He analyzed the influence of the compaction rate on mechanical properties of asphalt mixtures with the help of FEM simulation. A non-standard FEM approach, the Arbitrary Lagrangian Eulerian (ALE) method, was used to simulate the behavior of mixture during compaction considering the fact that the behavior of the material during this stage is between a solid and a liquid. In this paper we will use a continuum type of porous viscoplasticity model to simulate the compaction process. Improvement may be made through incorporation of microstructures (Hu et al, 2005;Zhang et al., 2006).

Porous Viscoplasticity Model

The model is based on the theory proposed by Gurson (1977) and modified by Tvergaard (1981). Rather than assuming plastic incompressibility, the porous plastic model considers hydrostatic components of stresses and strains. It takes the effect of void nucleation and growth into account. It shows the importance of plastic dilatation. Guler *et al.* (2002) used this Gurson-Tvergaard model in compaction simulation trying to calibrate the material parameters using experimental results.

The material model includes the following components:

- Linear elasticity:

$$\varepsilon_{ij}^{el} = C_{ijkl}^{el}\sigma_{kl}$$

- Yield function:

$$F = \left(\frac{q}{\sigma_y}\right) + 2q_1 f \cosh\left(-q_2 \frac{3p}{2\sigma_y}\right) - \left(1 + q_3 f^2\right) = 0$$

- Plastic flow:

$$\dot{\varepsilon}_{ij}^{pl} = \dot{\lambda}\frac{\partial F}{\partial \sigma_{ij}}$$

- Strain hardening:

Matrix material (fully dense):

$$\sigma_y = \sigma_y\left(\bar{\varepsilon}_m^{pl}\right)$$

The evolution of the equivalent plastic strain:

$$\left(1 - f\right)\sigma_y \dot{\bar{\varepsilon}}_m^{pl} = \sigma_{ij}\dot{\varepsilon}_{ij}^{pl}$$

The evolution of the volume fraction, f:

$$\dot{f} = \left(1 - f\right)\dot{\varepsilon}_{ii}^{pl} + A\dot{\bar{\varepsilon}}_m^{pl}$$

Rate dependent yielding can be modeled in ABAQUS and the failure can be modeled in ABAQUS explicit. Temperature dependent material parameters can be defined as a tabular function of temperature. The model gives reasonable results for $f < 10\%$.

Notation

σ_{ij}, ε_{ij}	The total stress and strain tensor

ε_{ij}^{el}	The elastic strain stress tensor
D_{ijkl}	The elasticity tensor
p	The hydrostatic pressure, $p = -\frac{1}{3}\sigma_{ij}\delta_{ij}$
S_{ij}	The deviatoric stress tensor, $S_{ij} = \sigma_{ij} + p\delta_{ij}$
q	The effective Mises stress, $q = \sqrt{\frac{3}{2}S_{ij}S_{ij}}$
σ_y	The yield stress of the fully dense material ($f = 0$), $\sigma_y = \sigma_y\left(\bar{\varepsilon}_m^{pl}\right)$
$\bar{\varepsilon}_m^{pl}$	The equivalent plastic strain in matrix $\bar{\varepsilon}_m^{pl} = \sqrt{\frac{2}{3}\varepsilon_{ij}^{pl}\varepsilon_{ij}^{pl}}$
f	The void volume fraction
q_1, q_2, q_3	Material parameters
A	$A = \frac{f_N}{s_N\sqrt{2\pi}}\exp\left[-\frac{1}{2}\left(\frac{\bar{\varepsilon}_m^{pl} - \varepsilon_N}{s_N}\right)^2\right]$
ε_N	The mean value of nucleation strain
s_N	The standard deviation of nucleation strain
f_N	The volume fraction of the nucleated voids (in tension)
EVOL	Element volume
VVF	Void volume fraction

FEM Simulations

Model

In the compaction simulation model (FIG. 2), the roller was assumed to be rigid and the porous plasticity model was used for Asphalt Concrete (AC). Besides the constant loading applied on the roller, a vibration force with smaller magnitude was also applied on the roller. The simulation was conducted using ABAQUS [1995].

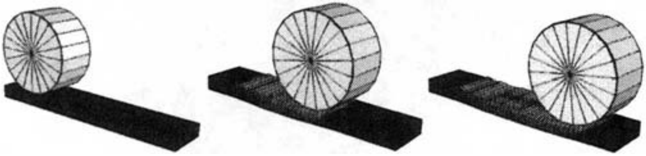

FIG. 2 Finite element model for compaction simulation

The asphalt concrete section being compacted was fixed at one end and other edges are free to move. So extension of the material was allowed during the compaction process. The initial Void Volume Fraction (VVF) was set to be 15% in the simulation. This study will quantitatively study the effects of compaction pressure and asphalt concrete thickness, base/subbase support on the compaction results. A yielding stress σ_y=15MPa was assumed for fully dense asphalt concrete under compaction loading. The evolution of Element Volume (EVOL) and VVF were used to evaluate the compaction. Material constants are the typical values used in Guler et al (2002).

Variables

Force applied on the roller: 1F, 2F, 3F, 4F
Vibration of the roller: 0.02F*sin (62.8T)
Thickness of the AC section: 1.0t, 1.5t, 2.0t, 2.5t
Where F=5000N, t=30mm, and T is the loading time.

Results-Compaction Pressure, Number of Passages and Layer Thickness Effect

Four levels of roller forces were applied to investigate the effect of pressure or compaction forces on the compaction effectiveness. The change of EVOL at a typical section was obtained and plotted against the number of passages of the roller in FIG. 3. It can be seen that under larger compaction forces, the lower layers of the asphalt concrete were compacted more uniformly. Increase of compaction pressure will increase the volume change (compaction) of the asphalt concrete. However, the increase of the compaction of the asphalt concrete is not proportional to the increase of the compaction pressure (FIG. 4).

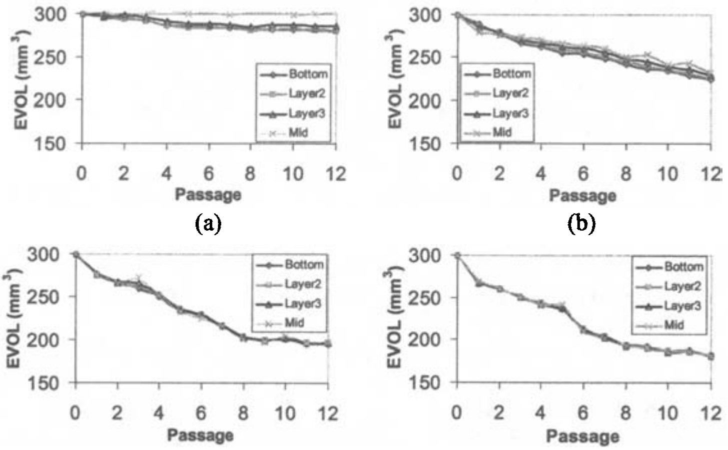

(a) (b)

(c) (d)

FIG. 3 Element volume change for different roller forces: (a) 1F, (b) 2F, (c) 3F and (d) 4F. The volume change was obtained at the bottom, the mid height and other two points between them

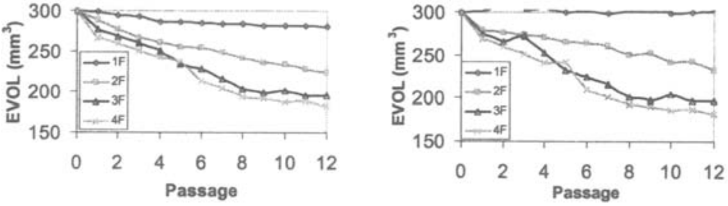

(a) (b)

FIG. 4 Change of element volume under different roller pressures at (a) bottom and (b) mid height of a typical section

Besides the reduction of the volume of asphalt concrete, the VVF was also obtained for the same asphalt layers, i.e. lower portion of the asphalt concrete in compaction. FIG. 5 shows the evolution of the VVF under different levels of compaction pressure. In general, larger compaction force will make the VVF reduce quickly. However, at certain level, e.g. 3F and 4F, the effect of the increased compaction force is not so obvious. We may also conclude from the plot that the compaction pressure should be between 2F and 3F for compaction processes with 12 passages. It may require less passages if the compaction forces are larger.

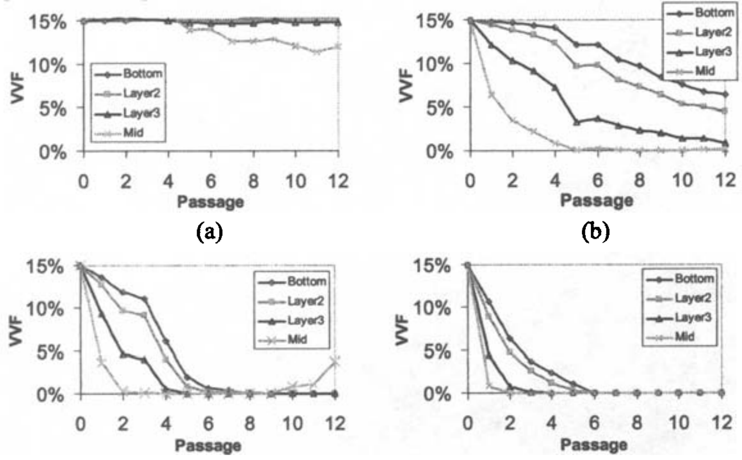

(a) (b)

(c) (d)

FIG. 5 Change of VVF for different roller forces: (a) 1F, (b) 2F, (c) 3F and (d) 4F. The VVF was obtained at the bottom, the mid height and other two points between

The changes of VVF at bottom and mid height of the AC section against the roller passage were plotted in FIG. 6. It can be seen that the targeted compaction air void content (or density) can be achieved much earlier (4-6 passages) for forces 3F and/or above in this case.

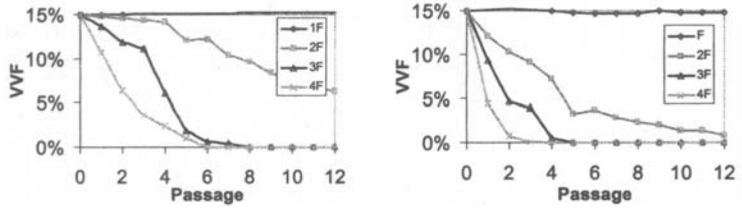

(a) (b)

FIG. 6 Change of VVF under different roller pressures at (a) bottom and (b) mid height

FIG. 7 shows the final EVOL and VVF (when additional passages would not further reduce the air void or increase the density) under different compaction pressures. For both the EVOL and VVF, the increase of the compaction pressure will lead to minimal difference in air void reduction if the pressure reached 3F.

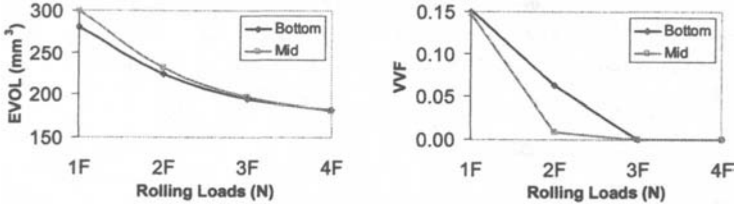

(a) (b)

FIG. 7 Final EVOL and VVF under different compaction pressure

FIG. 8(a) shows the change of EVOL at the bottom of the AC section for different thickness. Generally, the volume decreases of asphalt concrete are in a similar manner for different thickness. At mid height (FIG. 8(b)), changes of air void volume vary more largely, indicating a potential of less compaction efficiency for the middle layer of asphalt concrete. It should be noted that the values in this plot are not from the same depth (absolute values) to the surfaces. This simulation can help determine the optimal layer thickness for compaction. For example, from Figure 8b, it may be concluded that 2t-2.5t (60mm-75mm) are too high for effective compaction.

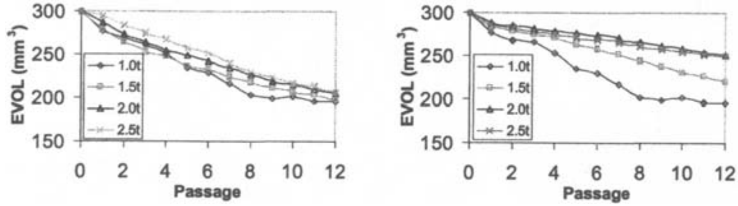

(a) (b)

FIG. 8 Change of EVOL for asphalt concrete with different thickness at: (a) bottom and (b) mid height of the compaction section

The evolution of VVF shown in FIG. 9 also indicates that the compaction becomes difficult when the thickness of the asphalt concrete layer increases. At the bottom of the asphalt concrete section, the VVF had almost no change for thickness 2.0t and 2.5t (60mm-75mm), indicating too larger thickness. At the mid height, the compaction pressure applied can meet the compaction requirement for thickness less than 2.0t.

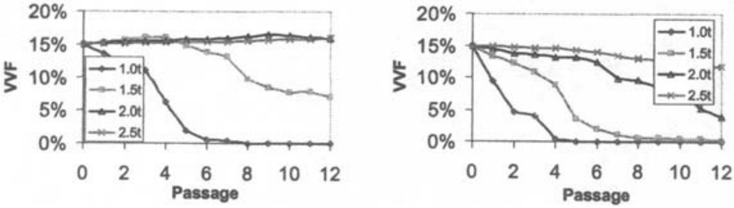

(a) (b)

FIG. 9 Change of VVF for asphalt concrete with different thickness at: (a) bottom and (b) mid height of the compaction section

FIG. 10 shows the deformation profile of the centerline. For different thickness, due to the lateral extension of the AC section in both directions (transversely and longitudinally), the evolution of the deformation profile and the maximum deformation at the compaction center are not proportional to the thickness. The maximum deformation is for thickness around 2.0t (FIG.11), indicating the optimal layer thickness for the compaction in terms of effectiveness and costs.

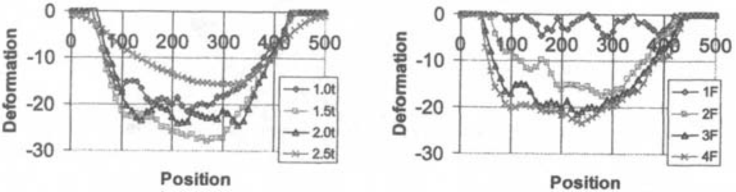

(a) (b)

FIG. 10 Deformation profiles: (a) different thickness of the compaction section at compaction pressure 3F, and (b) different compaction pressures (thickness 1.0t)

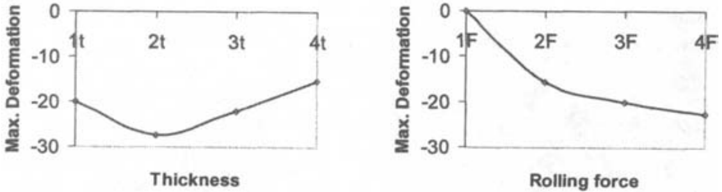

(a) (b)

FIG.11Center maximum deformations versus (a) thickness and (b) compaction pressure

Results-Base/Subbase Stiffness Effect

In order to study the effect of base/subbase stiffness on compaction, a base/subbase layer with finite and infinite element was added into the model. The elastic material model was used for the base/subbase. The elastic modulus varies from 5E to 0.5E (E is the elastic modulus of the asphalt concrete layer), representing hard and soft base/subbase respectively.

It can be seen from FIG. 12 that the effect of base/subbase stiffness on compaction is greater at lower part of the asphalt concrete layer than that at the upper part.

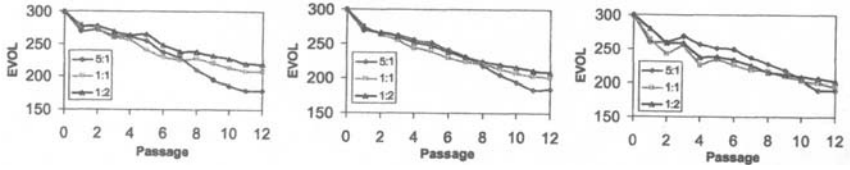

(a) (b) (c)

FIG. 12 change of EVOL along passages for different stiffness ratio at (a) bottom, (b) mid height and (c) top of the asphalt concrete layer

From the evolution of the VVF (Figure 13), the stiffness of the base/subbase seems to have similar effects on the change of VVF.

If we compare the evolution of EVOL at bottom, mid height and top of the asphalt concrete layer, the same trend was obtained for all the stiffness ratio variations (FIG. 14).

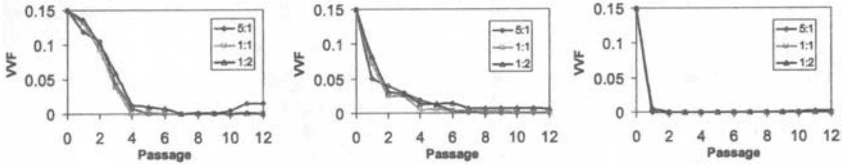

(a) (b) (c)

FIG. 13 change of VVF along passages for different stiffness ratios at (a) bottom, (b) mid height and (c) top of the asphalt concrete layer

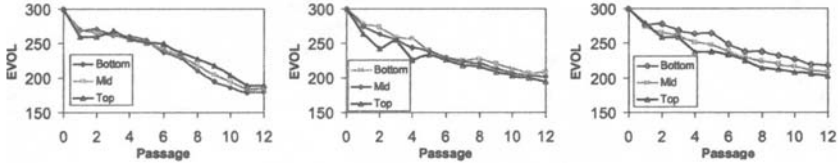

(a) (b) (c)

FIG. 14 change of EVOL along the thickness of the asphalt concrete layer for stiffness ratio: (a) 5:1, (b) 1:1 and (c) 1:2

This also can be seen from comparison of the VVF along the thickness of the asphalt concrete layer (FIG. 15).

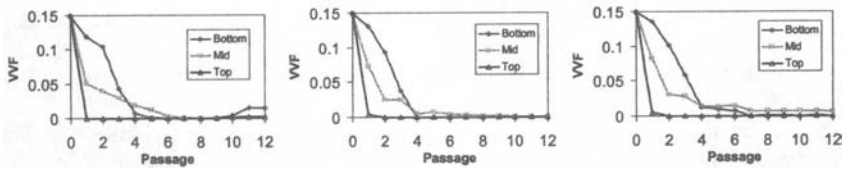

(a) (b) (c)

FIG. 15 change of VVF along the thickness of the asphalt concrete layer for stiffness ratio: (a) 5:1, (b) 1:1 and (c) 1:2

It is interesting to see that deformation at top of the asphalt concrete layer is smallest for the least stiff subbase (FIG. 16). From the EVOL and the VVF evolution, it has least volume change and void reduction. We may conclude that this is due to the deformation of the base/subbase, which causes difficulties the compaction of asphalt concrete layer.

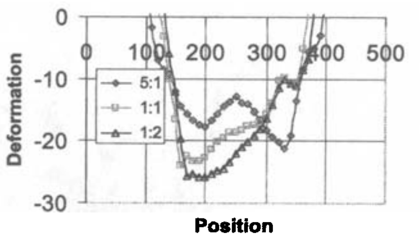

FIG. 16 final deformation profiles at top of the asphalt concrete layer for stiffness ratio: (a) 5:1, (b) 1:1 and (c) 1:2

The deformation increases dramatically when the stiffness ratio of base/subbase to asphalt concrete layer is smaller than 1 (FIG. 17). But the reduction of volume and voids is always smaller in these situations (FIG. 12 through FIG. 15), which means compaction is more difficult for soft base/subbase.

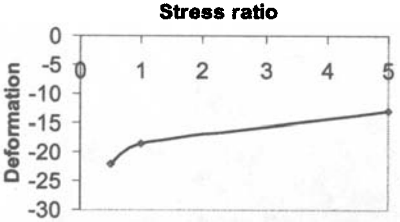

FIG. 17 maximum deformation of the asphalt concrete layer at center of the compaction versus stiffness ration between subbase material and the asphalt layer

The FEM simulation discoveries can be summarized as follows.

- Optimal compaction result depends on both compaction pressure and the layer thickness of asphalt concrete. This interrelationship can be determined from the simulation.
- Number of passages required in the compaction could be determined from the EVOL and VVF evolution curves.
- The required compaction pressure or the thickness of the compaction layer could be determined based on compaction procedure, i.e. compaction passages.
- Stiffer subbase material will lead to easy compaction of the asphalt concrete layer above.
- The effect of the stiffness of the base/subbase on the compaction is greater at bottom of the asphalt concrete layer than at the top.
- If the stiffness of the base/subbase material is smaller than the stiffness of the asphalt concrete layer during compaction, it may cause compaction problems.
- Finite element simulation of compaction can be used to evaluate factors affecting the compaction.

DEM MECHANISMS

Discrete Element Method (DEM) is one of the numerical simulation techniques utilized by the researchers to gain further insight into the interaction among the distinct constituents of mixed materials. Originally, it was developed to investigate the validity of various continuum models so that the appropriate model can be identified and incorporated into the FEM analysis to solve engineering problems (Cundall and Strack, 1979; Oda and Iwashita, 1999; Thornton and Antony, 1998). Then it was increasingly used in the study of the behavior of granular materials because of its ability to investigate granular material systems at the microscopic level. The method becomes more powerful when the internal structure of the pavement materials can be properly represented through the use of image analysis techniques in recent years (Fu, 2005).

Generally speaking, the DEM is a discontinuum analysis technique. It is distinguished from a continuous medium by its inheriting capability in considering the existence of interfaces or contacts between the discrete bodies that form the system. A model based on DEM is able to model the behavior of the constituents of distinguished properties such as aggregate and mastics, the contacts or interfaces between the discrete bodies, and represent the behavior of the solid material that constitutes the particles or sections in the discontinuous system.

Compared with FEM, DEM has its own characteristics and advantages. For example, after applying the image technique (Fu, 2005), a realistic representation of the internal structure allows modeling the deformation of composite materials more accurately. FEM, as a continuum method, can successfully capture the stress-strain distribution within the asphalt mixtures and its effect on the stiffness anisotropy (Abbas, 2004). However, it lacks the ability to account for the slippage between the aggregate particles, which has been cited as one of the most important mechanisms resulting in permanent deformation or rutting. Such a limitation can be overcome by DEM, which could consider the movement and behavior of those individual particles.

Computer programs based upon a continuum mechanics formulation (e.g., finite element and Lagrangian finite-difference programs) can simulate the variability in material types and nonlinear constitutive behavior typically associated with a rock mass, but the representation of discontinuities requires a discontinuum-based formulation (Itasca, 2003). There are several finite element, boundary element and finite difference programs available which have interface elements or "slide lines" that enable them to model a discontinuous material to some extent. However, their formulation is usually restricted in one or more of the following ways. First, the logic may break down when many intersecting interfaces are used; second, there may not be an automatic scheme for recognizing new contacts; and, third, the formulation may be limited to small displacements and/or rotations.

For these reasons, continuum codes with interface elements are restrictive in their applicability. A class of computer programs collectively described as discrete element codes provides the capability to represent the motion of multiple, intersecting discontinuities explicitly. Cundall and Hart (Cundall and Hart, 1992) provided the following definition of a discrete element method: the name "discrete element" applies to a computer program only if it: (a) allows finite displacements and rotations of discrete bodies, including complete detachment; and (b) recognizes new contacts automatically as the calculation progresses. Typically, an efficient algorithm for detecting and classifying contacts will be embodied in a discrete element code. The code will also maintain a data structure and memory allocation scheme that can handle many hundreds or thousands of discontinuities. Cundall and Hart (1992) identified the following four main classes of codes that conform to the definition of a discrete element method.

1. ***Distinct element programs*** use an explicit time-marching scheme to solve the equations of motion directly. Bodies may be rigid or deformable (by subdivision into elements); contacts are deformable. "Static relaxation" is a variation. Representative codes are TRUBAL, UDEC, 3DEC, DIBS, 3DSHEAR and PFC.

2. ***Modal methods*** are similar to the distinct element method in the case of rigid blocks but, for deformable bodies, modal superposition is used. This method appears to be better-suited for loosely-packed discontinua; in dynamic simulation of dense packing. Eigenmodes are apparently not revised to account for additional contact constraints by this approach. A representative code is CICE.

3. ***Discontinuous deformation analysis*** assumes contacts are rigid bodies, and bodies may be rigid or deformable. The condition of no-penetration is achieved by an iterative scheme; the deformability comes from superposition of strain modes. The relevant computer program is DDA.

4. ***Momentum-exchange methods*** assume both the contacts and bodies to be rigid: momentum is exchanged between two contacting bodies during an instantaneous collision. Friction sliding can be represented.

DEM SIMULATIONS

With the descriptions in the previous section, we can see the differences between FEM and DEM approaches. We can also appreciate the unique capability of the DEM approach, where the material structure can be better incorporated into simulations.

In investigating how important factors influence the compaction of pavement materials, the 3-Dimentional Particle Flow Code (PFC3D), which is based on the Discrete Element Method, is used as the simulation tool. The investigation includes:

1. Particle shape effect;
2. Particle contact property effect; and
3. Temperature effect;

Figure 18 illustrates the DEM model for investigating the compaction mechanism. Figures 18a and 18b show the roller's moving while Figure 18c illustrates the boundary walls. In the following explanations, Figure 18c may be referred in the next sections for the wall locations where different boundary conditions can be applied.

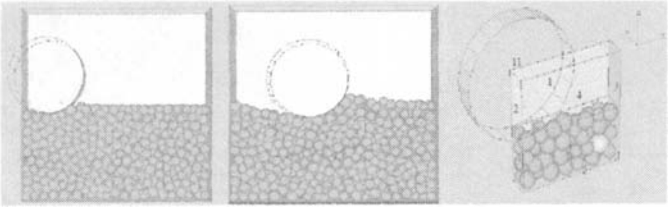

a. b. c.

FIG. 18 Illustration of the DEM Model

Results-Particle Shape Effect

In this section, the aggregate view of the compaction process is investigated. The particle shape effect is evaluated through clustering small balls together. Case 1 (Figure 19) is the simplest case or individual ball case. Case 2 clusters two balls into a rectangular while Case 3 clusters three balls into a triangle. If the ratio between the largest dimension and the smallest dimension is considered as a shape factor, then Case 1, Case 2 and Case 3 would have a shape factor equal to 1, 2 and 1.07 respectively. During compaction the particle rotation is one of the important kinematics that affects the compaction of the mixture. It may be intuitively interpreted that the more easily a particle can be rotated the less difficult to move the particle into a denser configuration. Figures 20a, 20b and 20c illustrate the rotations along the x, y, and z directions (Figure 18c) of the three particles, whose mass centers are located in the same place. It can be seen that the ball is easiest to rotate, followed by the triangle and the rectangular. If this simulation observation can be extended, one of the rational guesses is that particles of cubical shapes are easier to compact than flat or elongated particles.

FIG. 19 Particle Shape Effect

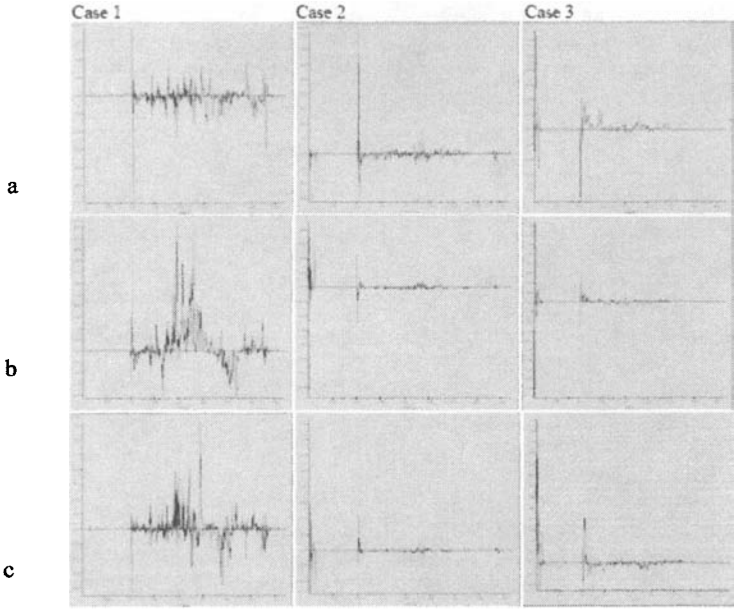

FIG. 20 Particle Rotations: a) against X-axis; b) against Y-axis; and c) against Z –axis (the first 1000 steps are ball-generation process while the compaction starts at step 1001).

Results-Particle Contact Property Effect
For two particles of the same materials, it is understood that the contact normal stiffness of the two particles would be larger for rougher particles. The contact normal stiffness could also be larger if the mastics between the two particles are stiffer. By assigning a larger normal stiffness to the contact pair, we may investigate how rougher aggregates or stiffer mastics/binder would affect compaction.

In this evaluation, we chose to keep the ks (shear stiffness) value of the model a constant and change the kn (normal stiffness) value, and monitor the peak forces in the z direction against the roller wall (Id=11, Figure 18c) in the same compaction process, where the roller is gradually rolling into the pavement through a displacement controlled algorithm.

Figure 21 plots the peak forces for three cases when the contact normal stiffness increases. It may be concluded from Figure 21 that as the normal stiffness of the contacting particles increases, the peak z-forces on the roller increases. This means more efforts are needed if the same compaction is to achieve. It should be noted that the original porosity or air void content for each of the three cases is kept the same.

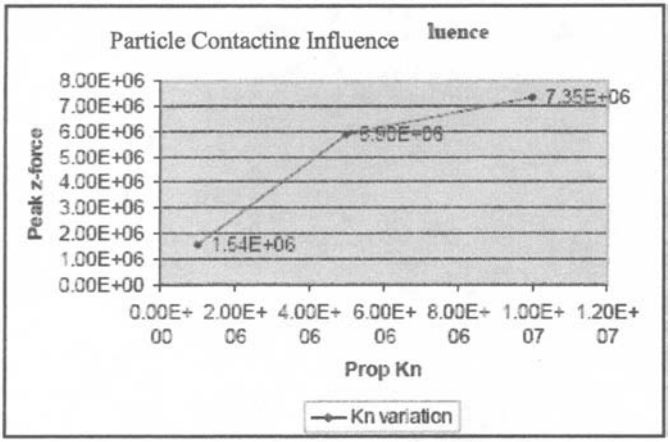

FIG. 21 Peak forces required to press the roller into pavement for the same rolling process

Results-Temperature Effect

Obviously, when the mixture temperature drops during transportation, the stiffness of the binder/mastics will increase resulting in an increase of the normal contact stiffness. From Figure 21, it may be inducted that the lower the temperature the more difficult to compact. Another situation that involves the temperature effect is when the surface temperature drops during the compaction, forming a relatively stiffer layer at the surface. It is anticipated the larger the temperature drop, the thicker and stiffer the surface hard layer.

The surface temperature drop effect is investigated through the simulation of the same compaction process in the particle contact property investigation, keeping the others the same while changing the stiffness of the top layer. Two cases are considered: case one considers a smaller top hard layer (1/5 of the asphalt layer) while case two considers the relatively larger thickness (2/5 of the asphalt layer) of the top colder/harder layer. The normal contact stiffness change is also related to the degree of temperature drop. The monitored peak z-forces (for parallel bonding) are presented in Figure 22. From Figure 22, it may be concluded that the peak z-force decreases as the stiffness of the top layer becomes larger and as time goes longer, which means the stiffer layer becomes thicker, the compaction effort will increase; larger compaction load/effort may be needed.

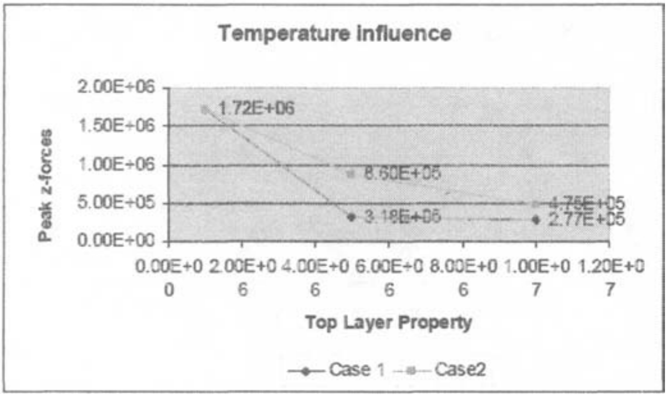

FIG. 22 Colder layer (temperature drop) effect

The DEM simulation discoveries can be summarized as follows.

- Mixtures with aggregates of elongated and flat particles, larger roughness and coarse textures are more difficult to compact.
- Temperature drop will make compaction more difficult due to the larger stiffness for particle contacts and/or stiffer top layer.

SUMMARY AND CONCLUSIONS

Both FEM and DEM simulations of the compaction process have been conducted for understanding the mechanics of compaction. Both approaches have demonstrated their uniqueness in the interpretation of the fundamental kinematics of compaction. The FEM approach can model the air void reduction process with reasonable accuracy. The DEM approach on the other hand can provide a fundamental understanding of the particle kinematics, and relative binder/mastics to aggregate stiffness. The simulation results indicate that both methods, if appropriately calibrated, can serve as guide for selection of compaction parameters such as layer thickness, compactor weight/vibration, number of passages and temperature. These methods can also be used to evaluate the compaction effectiveness.

REFERENCES

ABAQUS (1995). User's Manual. Hibbitt, Karlsson & Sorensen, Inc.,Pawtucket, R.I.

Abbas, Alar (2004). Simulation of the micromechanical behavior of asphalt mixture using the discrete element method, Washington State University

Cundall, P.A. and Strack, O.D.L. (1979). A distinct element model for granular assemblies. *Geotechnique*, 29: 47-65.

Cundall P.A and Roger D. Hart (1992). Numerical modeling of discontinua, Engineering Computations, 9: 101-113.

Fu, Yanrong (2005). Experimental Quantification and DEM Simulation of Micro-Macro behavior of Granular Materials using X-ray tomography Imaging. Ph.D. Dissertation, Louisiana State University.

Guler, M., Bosscher, P. J. and Plesha, M. E. (2002). A porous elastoplastic compaction model for asphalt mixtures with parameter estimation algorithm. 15th ASCE Engineering Mechanics Conference. June 2-5, 2002, Columbia University, New York, NY.

Gurson, A. L. (1977). Continuum Theory of Ductile Rupture by Void Nucleation and Growth: Part I - Yield Criteria and Flow Rules for Porous Ductile Media. Journal of Engineering Materials and Technology, 99: 2-15

Henny ter Huerne (2002). Possibilities for material characterization and FEM simulation of compaction process of asphalt pavement. Heron, 45.

Hu, RL, Yue, ZQ, Tham, LG, and Wang, LC, (2005). Digital image analysis of dynamic compaction effects on clayey fills, Journal of Geotechnical and Geoenvironmental Engineering, ASCE, 131(11): 1411-1422.

Itasca (2003). 3 Dimensional Distinct Element Code manual, Itasca Consulting Group, Inc.

Oda, M. and K. Iwashita, Editors (1999). An Introduction, Mechanics of Granular Materials. Elsevier.

Thornton, C. and Antony, S.J. (1998). Quasi-static deformation of compact granular assemblies. Acta Mechanica, 64: 45-61.

Tvergaard, V. (1981). Influence of Voids on Shear Band Instabilities under Plane Strain Condition. International Journal of Fracture Mechanics, 17: 389-407.

Zhang, B., Wang, LB., and Tumay, M. (2006) "An Evaluation of the Stress Non-uniformity due to the Heterogeneity of AC in the Indirect Tensile Test", ASCE Geotechnical Special Publication, 146: 29–43.

ANALYSIS OF NONLINEAR VISCOELASTIC PROPERTIES OF ASPHALT MIXTURES

Chien-Wei Huang[1], Eyad Masad[2], Anastasia H. Muliana[3] and Hussain Bahia[4]

ABSTRACT

This study presents characterization of the nonlinear viscoelastic behavior of hot mix asphalt (HMA) at different temperatures and strain levels using the Schapery nonlinear viscoelastic model. This model is employed to describe experimental measurements of two asphalt mixes under several combined temperatures and strain levels. The master curve is created for each strain level using time temperature superposition principle (TTSP) with a reference temperature of 40°C. The measurements at strain levels higher than 0.01% are used to determine the nonlinear viscoelastic parameters in the model. The FE model with the calibrated time-dependent and nonlinear material parameters is used to simulate the creep experimental tests, and good predictions are shown.

KEY WORDS: nonlinear viscoelasticity, hot mix asphalt, Schapery theory, finite element

1 INTRODUCTION

The nonlinear behavior of asphalt mixtures can be caused by the rotation and slippage of aggregates and the localized high strains in the binder phase (Kose et al., 2000). Abbas et al. (2004) developed an incremental nonlinear viscoelastic model to simulate the behavior of asphalt binders within the asphalt mix microstructure using finite element (FE) analysis. The results confirmed that the high strains in the binder phase can cause nonlinear viscoelastic response of the mix.

---

[1] *Graduate Research Assistant, Department of Civil Engineering, Texas A&M University, College Station, TX 77845-3136, Tel:979 845 8308, Fax: 979 845 0278 , Email :stanhuang917@tamu.edu*

[2] Associate Professor, Department of Civil Engineering, Texas A&M University, College Station, TX 77845-3136, Tel: 979 845 8308, Fax: 979 845 0278 , Email: *emasad@civil.tamu.edu*.

[3] Assistant Professor, Department of Mechanical Engineering, Texas A&M University, College Station, TX 77845-3123, Tel: 979 458 3579, Fax: 979 845 3081, Email: *amuliana@neo.tamu.edu*

[4] *Professor, Department of Civil Engineering, University of Wisconsin-Madison, Madison, WI 53706-1691, Tel.: 608 265 448 1Fax: 608 262 5199 Email:bahia@engr.wisc.edu*

In spite of the experimental evidence showing the nonlinear response of asphalt mixes, there has not been a systematic approach to model this response. The Schapery single integral model is one of the most popular models and has been applied to the characterization of the influence of the nonlinear constitutive behavior of engineering materials (Christensen, 1968; Schapery, 1969; Schapery, 2000). This study presents an implementation of the numerical representation of the Schapery integral equations in the ABAQUS finite element package for modeling the nonlinear viscoelastic behavior of asphalt mixtures at different temperatures and strain levels.

2. NUMERICAL IMPLEMENTATION OF THE SCHAPERY NONLINEAR VISCOELASTIC MATERIAL MODEL

The Schapery's nonlinear viscoelastic model can be expressed as follows (Schapery 1969):

$$\varepsilon(t) = g_0 D_0 \sigma^t + g_1 \int_0^t \Delta D\left(\psi^t - \psi^\tau\right) \frac{d\left(g_2 \sigma^\tau\right)}{d\tau} d\tau \tag{1}$$

where ε is the strain response due to a stress, D_0 is the instantaneous elastic compliance, ΔD is the transient compliance, ψ^t is the reduced time and it is given by:

$$\psi^t = \int_0^t \frac{d\xi}{a_T a_s} \tag{2}$$

g_0, g_1 and g_2 are the nonlinear parameters related to stress or strain status, a_T is the temperature shift factor and a_s is the strain or stress shift factor. The Prony series is used to represent the transient compliance ΔD as follows:

$$\Delta D^{\psi^T} = \sum_{n=1}^{N} D_n \left(1 - \exp\left(-\lambda_n \psi^t\right)\right) \tag{3}$$

where D_n is the n^{th} coefficient of Prony series and λ_n is the n^{th} retardation time.

In this paper, the recursive-iterative integration approach developed by Haj-Ali and Muliana (2004) is used to implement the Schapery nonlinear viscoelastic model. The recurrence formula allows bypassing the need to store entire strain histories at the material levels. The linear strain formulation is used within the recursive approach to give the trial solutions. The stress corrector scheme is added to minimize error arising from the linearization. This will enhance convergence and divergence. Furthermore, the recursive-iterative approach permits using a larger time increment, while giving accurate solution.

The strain response for isotropic materials can be decoupled into deviatoric and volumetric parts and it can be presented as:

$$\varepsilon_{ij} = \frac{1}{2G} S_{ij} + \frac{\sigma_{kk}}{9K} \delta_{ij} = \frac{1}{2} J S_{ij} + \frac{1}{3} B \sigma_{kk} \delta_{ij} \tag{4}$$

where G and K are shear modulus and bulk modulus, respectively. J and B are shear compliance and bulk compliance, respectively. S_{ij} is the deviatoric stress and σ_{kk} is the volumetric stress. Applying the Schapery integral constitutive model, the deviatoric and volumetric strain can be expressed as:

$$e_{ij}^{t} = \frac{1}{2} g_0^t J_0 S_{ij}^t + \frac{1}{2} g_1^t \int_0^t \Delta J^{(\psi^t - \psi^\tau)} \frac{d(g_2^\tau S_{ij}^\tau)}{d\tau} d\tau \tag{5}$$

$$\varepsilon_{kk}^{t} = \frac{1}{3} g_0^t B_0 \sigma_{kk}^t + \frac{1}{3} g_1^t \int_0^t \Delta B^{(\psi^t - \psi^\tau)} \frac{d(g_2^\tau \sigma_{kk}^\tau)}{d\tau} d\tau \tag{6}$$

where e_{ij} is the deviatoric strain and ε_{kk} is the volumetric strain. J_0 and B_0 are instantaneous elastic shear compliance and instantaneous elastic bulk compliance, respectively. ΔJ and ΔB are transient shear compliance and transient bulk compliance, respectively.

Assuming the Poisson's ratio υ to be time independent, the instantaneous elastic shear compliance, instantaneous elastic bulk compliances, transient shear and bulk compliances can be represented as:

$$\begin{aligned} &J_0 = 2(1+\upsilon)D_0 && B_0 = 3(1-2\upsilon)D_0 \\ &\Delta J(\psi) = 2(1+\upsilon)\Delta D(\psi) && \Delta B(\psi) = 3(1-2\upsilon)\Delta D(\psi) \end{aligned} \tag{7}$$

Substituting Eqs. (3) and (7) into (5) and (6), the deviatoric and volumetric can be written in terms of hereditary integral formulation and as follows:

$$\begin{aligned} e_{ij}^{t} = {} & \frac{1}{2}\left[g_0^t J_0 + g_1^t g_2^t \sum_{n=1}^{N} J_n - g_1^t g_2^t \sum_{n=1}^{N} J_n \frac{1-\exp(-\lambda_n \Delta\psi^t)}{\lambda_n \Delta\psi^t} \right] S_{ij}^t - \\ & \frac{1}{2} g_1^t \sum_{n=1}^{N} J_n \left[\exp(-\lambda_n \Delta\psi^t) q_{ij,n}^{t-\Delta t} - g_2^{t-\Delta t} \frac{(1-\exp(-\lambda_n \Delta\psi^t))}{\lambda_n \Delta\psi^t} S_{ij}^{t-\Delta t} \right] \end{aligned} \tag{8}$$

$$\begin{aligned} \varepsilon_{kk}^{t} = {} & \frac{1}{3}\left[g_0^t B_0 + g_1^t g_2^t \sum_{n=1}^{N} B_n - g_1^t g_2^t \sum_{n=1}^{N} B_n \frac{1-\exp(-\lambda_n \Delta\psi^t)}{\lambda_n \Delta\psi^t} \right] \sigma_{kk}^t - \\ & \frac{1}{3} g_1^t \sum_{n=1}^{N} B_n \left[\exp(-\lambda_n \Delta\psi^t) q_{kk,n}^{t-\Delta t} - g_2^{t-\Delta t} \frac{(1-\exp(-\lambda_n \Delta\psi^t))}{\lambda_n \Delta\psi^t} \sigma_{kk}^{t-\Delta t} \right] \end{aligned} \tag{9}$$

For implementation in finite element method, the incremental shear and bulk strains are derived and shown as:

$$\begin{aligned} \Delta e_{ij}^{t} &= e_{ij}^{t} - e_{ij}^{t-\Delta t} \\ &= \overline{J}^t S_{ij}^t - \overline{J}^{t-\Delta t} S_{ij}^{t-\Delta t} - \frac{1}{2} \sum_{n=1}^{N} J_n \left[g_1^t \exp(-\lambda_n \Delta\psi^t) - g_1^{t-\Delta t} \right] q_{ij,n}^{t-\Delta t} - \\ & \quad \frac{1}{2} g_2^{t-\Delta t} \sum_{n=1}^{N} J_n \left\{ g_1^{t-\Delta t} \left[\frac{1-\exp(-\lambda_n \Delta\psi^{t-\Delta t})}{\lambda_n \Delta\psi^{t-\Delta t}} \right] - g_1^t \left[\frac{1-\exp(-\lambda_n \Delta\psi^t)}{\lambda_n \Delta\psi^t} \right] \right\} S_{ij}^{t-\Delta t} \end{aligned} \tag{10}$$

$$\begin{aligned} \Delta \varepsilon_{kk}^{t} &= \varepsilon_{kk}^{t} - \varepsilon_{kk}^{t-\Delta t} \\ &= \overline{B}^t \sigma_{kk}^t - \overline{B}^{t-\Delta t} \sigma_{kk}^{t-\Delta t} - \frac{1}{2} \sum_{n=1}^{N} B_n \left[g_1^t \exp(-\lambda_n \Delta\psi^t) - g_1^{t-\Delta t} \right] q_{kk,n}^{t-\Delta t} - \\ & \quad \frac{1}{3} g_2^{t-\Delta t} \sum_{n=1}^{N} B_n \left\{ g_1^{t-\Delta t} \left[\frac{1-\exp(-\lambda_n \Delta\psi^{t-\Delta t})}{\lambda_n \Delta\psi^{t-\Delta t}} \right] - g_1^t \left[\frac{1-\exp(-\lambda_n \Delta\psi^t)}{\lambda_n \Delta\psi^t} \right] \right\} \sigma_{kk}^{t-\Delta t} \end{aligned} \tag{11}$$

where $\overline{J}^t$ and $\overline{B}^t$ can be expressed as:

$$\overline{J}^t = \frac{1}{2}\left[g_0^t J_0 + g_1^t g_2^t \sum_{n=1}^{N} J_n - g_1^t g_2^t \sum_{n=1}^{N} J_n \frac{1-\exp(-\lambda_n \Delta\psi^t)}{\lambda_n \Delta\psi^t} \right] \tag{12}$$

$$\overline{B}^t = \frac{1}{3}\left[g_0^t B_0 + g_1^t g_2^t \sum_{n=1}^{N} B_n - g_1^t g_2^t \sum_{n=1}^{N} B_n \frac{1-\exp(-\lambda_n \Delta\psi^t)}{\lambda_n \Delta\psi^t}\right] \tag{13}$$

The variables $q_{ij,n}^{t-\Delta t}$ and $q_{kk,n}^{t-\Delta t}$ are the shear and volumetric hereditary integrals, respectively for every Prony series term n at previous time $t-\Delta t$. The hereditary integrals are updated at the end of every converged time increment, which will be used for the next time increment. The formulation of shear and volumetric hereditary integrals are:

$$q_{ij,n}^t = \exp(-\lambda_n \Delta\psi^t) q_{ij,n}^{t-\Delta t} + (g_2^t S_{ij}^t - g_2^{t-\Delta t} S_{ij}^{t-\Delta t}) \frac{1-\exp(-\lambda_n \Delta\psi^t)}{\lambda_n \Delta\psi^t} \tag{14}$$

$$q_{kk,n}^t = \exp(-\lambda_n \Delta\psi^t) q_{kk,n}^{t-\Delta t} + (g_2^t \sigma_{kk}^t - g_2^{t-\Delta t} \sigma_{kk}^{t-\Delta t}) \frac{1-\exp(-\lambda_n \Delta\psi^t)}{\lambda_n \Delta\psi^t} \tag{15}$$

The shear and volumetric strain increments can be determined from Eqs. (10) and (11) provided that the stresses are given. This algorithm will be implemented in the displacement based FE framework, in which strains are the given variables. The current shear and volumetric stresses and the current nonlinear parameters can not be determined directly, because the nonlinear parameters are dependent on the current stress and vise versa. Hence, the iterative algorithm is added to solve for the current stress state, in which the nonlinear parameters are assumed at the beginning of each time increment

$g_\alpha^t = g_\alpha^{t-\Delta t} \quad ; \alpha = 0,1,2 \quad and \quad \Delta\psi^t = \Delta\psi^{t-\Delta t}$

Then, the trial stresses can be determined as follows:

$$\Delta S_{ij}^{t,tr} = \frac{1}{\overline{J}^{t,tr}}\left\{\Delta e_{ij}^t + \frac{1}{2} g_1^{t,tr} \sum_{n=1}^{N} J_n \left[\exp(-\lambda_n \Delta\psi^t) - 1\right] q_{ij,n}^{t-\Delta t}\right\} \tag{16}$$

$$\Delta \sigma_{kk}^{t,tr} = \frac{1}{\overline{B}^{t,tr}}\left\{\Delta \varepsilon_{kk}^t + \frac{1}{2} g_1^{t,tr} \sum_{n=1}^{N} B_n \left[\exp(-\lambda_n \Delta\psi^t) - 1\right] q_{kk,n}^{t-\Delta t}\right\} \tag{17}$$

where $\overline{J}^{t,tr}$ and $\overline{B}^{t,tr}$ have the same forms as Eqs. (12) and (13), respectively, but the nonlinear parameters are assumed to be functions of the last converged stress state.

In this paper, the iterative scheme is used to calculate the correct stress state from the current strain increment. In the iterative scheme algorithm, the residual strain should be defined and it can be determined by calculating the current strain. The residual strain equation can be written as:

$$R_{ij}^t = \Delta e_{ij}^t + \frac{1}{3} \Delta \varepsilon_{kk}^t \delta_{ij} - \Delta \varepsilon_{ij}^t \tag{18}$$

where $\Delta \varepsilon_{ij}^t$ is provided from the structural level. The Newton-Raphson typed iterative algorithm is used to minimize the strain residual in Eq. (18).

3. EXPERIMENTAL MEASUREMENTS

The dynamic frequency sweep test was used to characterize the linear viscoelastic coefficients and nonlinear parameters. This test applies repeated shear loading on the upper surface of a HMA specimen with a height of approximately 50 mm and a diameter of about 150 mm. This test was conducted under several temperatures and strain levels. The temperatures, frequencies and strain levels were as follows:

Temperature: 52, 46, 40, 27 °C
Frequency: 0.01, 0.02, 0.05, 0.1, 0.2, 0.5, 1.0, 2.0, 5.0, 10.0, 30.0 Hz
Strain: 0.01, 0.04, 0.07, 0.1 %

Two HMA mixes were tested in this study. The first one will be referred to as a fine mix, while the other one will be referred to as a coarse mix (Masad and Niranjanan 2002). These mixes differ in their aggregate size distributions. The dynamic compliance $|J^*|$ (stress amplitude/strain amplitude) and phase angles δ which is the lag between the stress and strain functions are converted to the compliance function in the time domain, which is expressed as follows:

$$J(t) = J_0 + \sum_{n=1}^{N} J_n \left(1 - \exp\left(\frac{-t}{\tau_n}\right)\right) \tag{22}$$

The time-temperature shifting is used to obtain the master curve at each of the strain levels and a reference temperature of 40°C. Figures 1 and 2 show the relationship between temperature and time-temperature factor a_T for the fine and coarse mixes, respectively. The nonlinear parameters (g_1g_2) are obtained by vertical shifting of the master curves at all strain levels to a reference strain of 0.01%. Figure 3 shows the relationship between g_1g_2 and strain levels for the fine mix. As expected, the nonlinear parameter g_1g_2 increases with an increase in strain level. The master curves at the different strain levels are also shifted horizontally to the reference strain of 0.01% in order to determine the time-strain shift factors (a_s) and obtain the long-term HMA behavior. The long-term linear viscoelastic Prony coefficients are obtained by fitting all the data shifted horizontally to the 0.01% strain. Figure 4 presents the long-term master curves for the fine mix. The results show that the Prony series can fit the temperature-strain master curve very well.

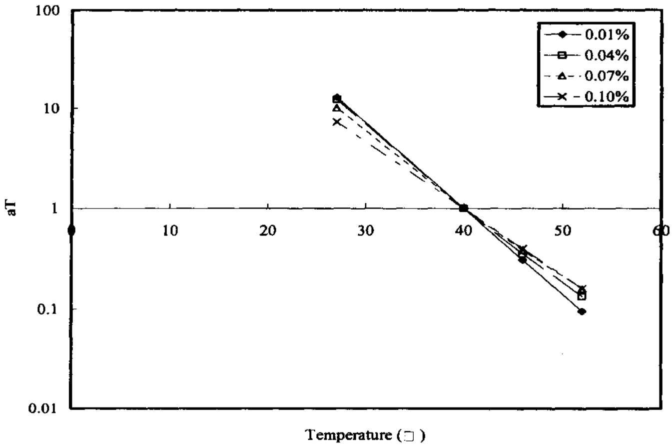

FIG. 1. **The relationship between time-temperature shift factor and temperature for the fine HMA mix.**

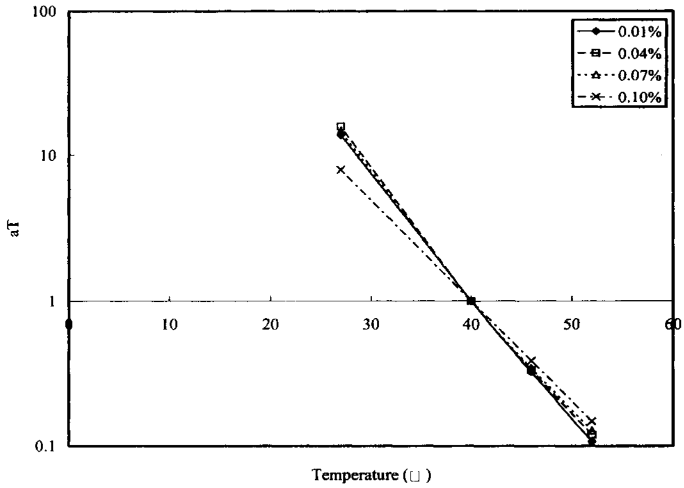

FIG. 2. The relationship between time-temperature shift factor and temperature for the Coarse HMA mix.

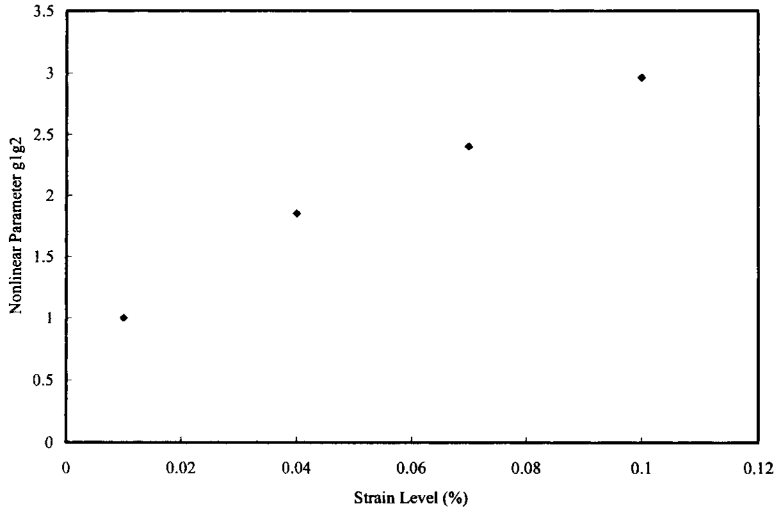

FIG. 3. THE RELATIONSHIP BETWEEN NONLINEAR PARAMETER AND STRAIN LEVEL FOR THE FINE HMA MIX.

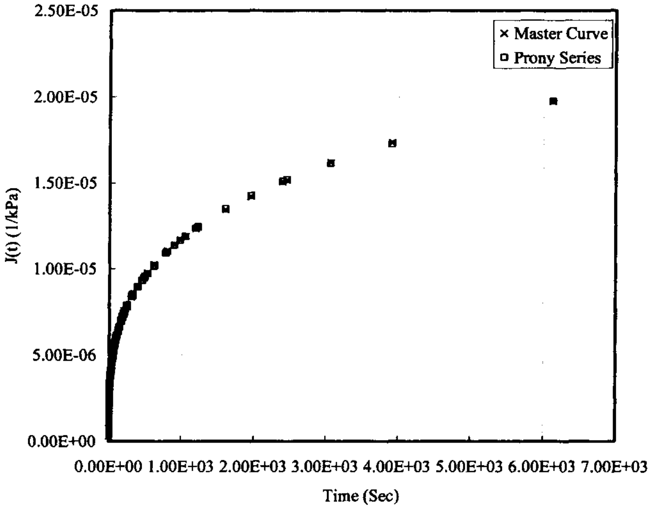

FIG. 4. The long-term master curve of strain level 0.01% for fine HMA mixes.

4. MODEL VERIFICATION

Inverse analysis is conducted to determine the ability of the parameters obtained in establishing the master curve and used in FE analysis to match the experimental measurements at different combinations of temperatures and strain levels. The time-temperature shift factors, nonlinear viscoelastic parameters and the long-term linear viscoelastic coefficients obtained from the analysis of the experimental tests are used as input parameters to the material subroutine of the finite element. Examples of the results for the fine and coarse mixtures are shown in Figures 5 and 6. In general, the numerical results have very good agreement with the experimental measurements. The differences between the model and measurements are attributed to the inherent errors in determining the model parameters. For example, a_T in Figures 1 and 2 vary slightly as a function of strain, while a_T is taken as the average of all strain levels in the FE model.

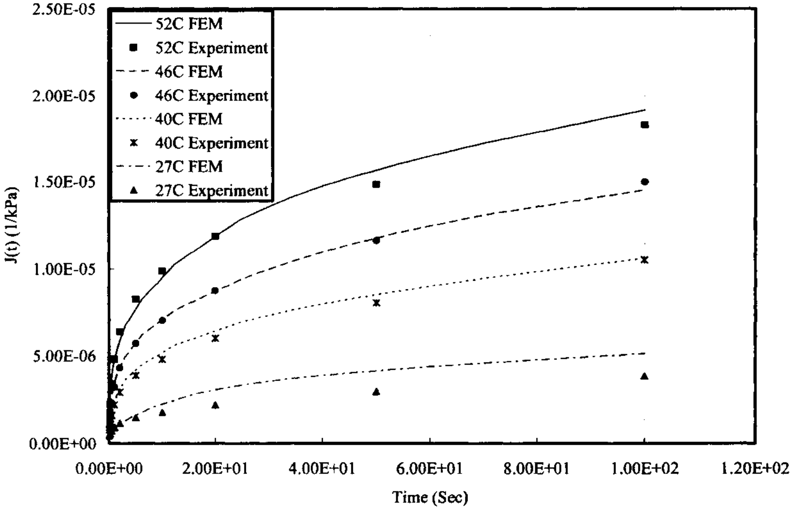

FIG. 5. The verification of strain level 0.04% for fine HMA mixes.

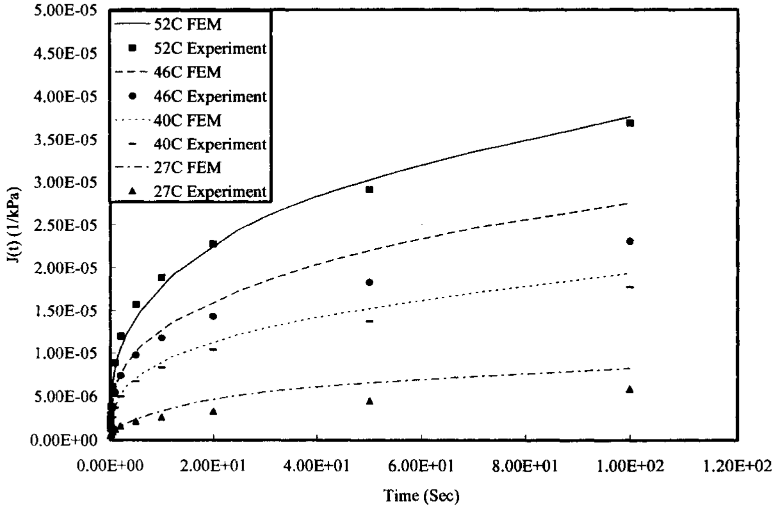

FIG. 6. The verification of strain level 0.04% for coarse HMA mixes.

5. SUMMARY OF FINDINGS

The nonlinear viscoelastic response of asphalt mixtures is described in this study using the Schapery's single integral model. The model parameters were obtained by analyzing the nonlinear viscoelastic response of two asphalt mixes tested at different temperatures, frequencies and strain levels. The time-strain shift factors were obtained by shifting the master curves at the different strain levels horizontally to the reference strain within the linear range. The nonlinear parameters were obtained by vertical shifting of the master curves at all strain levels to the same reference strain. The long-term linear viscoelastic coefficients were determined by fitting the Prony series to the data shifted horizontally at the reference strain. The time-temperature shift factors were determined and found to vary only slightly as a function of strain level.

Finite element analysis was conducted to simulate the experimental measurements. The analysis showed that the FE model matched the experimental measurements at different combinations of temperatures and strain levels. The nonlinear viscoelastic material subroutine implemented in finite element can be used to model the time dependent and stress dependent response of asphalt pavements under different environmental and loading conditions. In addition, research is currently underway to use the model in representing the nonlinear viscoelastic response of asphalt binders.

6. REFERENCES

Abbas, A., Papagiannakis, T., and Masad, E. (2004). "Linear and Non-Linear Viscoelastic Analysis of the Microstructure of Asphalt Concretes," *Journal of Materials in Civil Engineering, ASCE,* Vol. 16, No. 2, pp. 133 - 139.

Christensen, R.M. (1968). "On Obtaining Solutions in Nonlinear Viscoelasticity." *Journal of Applied Mechanics,* Vol. 35, pp. 129—133.

Haj-Ali, R.M. and Muliana, A.H. (2004). "Numerical Finite Element Formulation of the Schapery Nonlinear Viscoelastic Material Model." *International Journal for Numerical Methods in Engineering,* Vol. 59, pp. 25-45

Kose, S., Guler, M., Bahia H., and Masad, E. (2000). "Distribution of Strains within Hot-Mix Asphalt Binders." *Journal of the Transportation Research Board* No. 1728, pp. 21-27.

Masad, E. and Niranjanan, S. (2002). "Microstructural Finite Element Analysis of the Influence of Localized Strain Distribution on Asphalt Mix Properties," *Journal of Engineering Mechanics, ASCE,* Vol. 129, No. 10, pp. 1105-1114.

Schapery, R.A. (1969). "On the Characterization of Nonlinear Viscoelastic Materials." *Polymer Engineering and Science, Vol.* 9, pp. 295-310.

Schapery R. A. (2000). "Nonlinear Viscoelastic Solids." *International Journal of Solids and Structures*, pp. 359-366.

THE TEMPERATURE DEPENDENT GENERALIZED KUHN MODEL FOR ASPHALT CONCRETE

Vassilis P. Panoskaltsis[1]

ABSTRACT

An internal variable formulation for the introduction of the effects of temperature in viscoelastic models is presented. A new model, the temperature-dependent generalized Kuhn model of viscoelasticity, is developed by using this powerful and novel approach. An alternative formulation, through the use of the creep function and the time-temperature superposition principle, is also presented. The new model's predictions are compared to experimental data.

INTRODUCTION

In this paper we develop a new temperature-dependent viscoelastic model for the description and prediction of the behavior of asphalt concrete. The new model can be also used for the analysis of pavements in cases in which the influence of temperature is important. Furthermore, the incorporation of temperature is essential for modeling the fatigue behavior of the material. The temperature-dependent viscoelastic model developed here, is based on a viscoelastic model recently proposed by Panoskaltsis and co-workers (Panoskaltsis et al. 2006), named by them "The generalized Kuhn model of viscoelasticity". In order to incorporate temperature effects in the model, the classical approach, having been referred to in the literature as "the time-temperature superposition principle", is used in this work. Moreover, a novel approach for the incorporation of temperature is presented. This approach is based on the concept of internal variables of inelasticity and as it will be shown here it is very powerful. The paper is organized as follows: In the first section a brief overview of the generalized Kuhn model is presented. In the second section the new temperature-

---

[1] Associate Professor, Case Western Reserve University
Department of Civil Engineering
10900 Euclid Avenue
Cleveland, OH, 44106-7201, U.S.A.
E-mail:vpp@nestor.cwru.edu

dependent model is developed. In the third section the internal variable approach for the introduction of temperature in viscoelastic models is developed. In the last section the capabilities of the new model to predict experimental results are shown.

THE GENERALIZED KUHN MODEL

The generalized Kuhn model (GKM) (Panoskaltsis et al. 2006) is based on a generalization of the modified Kuhn model (MKM) proposed by Lubliner and Panoskaltsis (1992) and has been developed within the linear and nonlinear viscoelastic domains. The modified Kuhn model has been given three equivalent representations: a functional, a rheological and an internal variable one. It has been very successful in the description of concrete materials (Panoskaltsis et al. 1999). Although the modified Kuhn model predicts correctly the frequency dependence of the loss-tangent of concrete materials, it is not very successful in predicting the loss tangent of highly dissipative materials like asphalt concrete. This is achieved by the generalized Kuhn model. As with the MKM the GKM has been developed in three equivalent representations: a functional, a rheological and an internal variable one. The creep function of the GKM, written in a retardation-time superposition form, is given by Eq. (1),

$$J(t) = A + B\int_{1/C}^{\infty}\left(1 - e^{-t/\tau}\right)\frac{d\tau}{\tau^{1-\alpha}}, \qquad (1)$$

where A, B, C and α are parameters and $0 \le \alpha \le 1$. For $\alpha = 0$ the modified Kuhn model is obtained. The creep compliance of the discrete generalized Kuhn model (rheological representation) is given by the following truncated Dirichlet (or, as alternatively called, Prony) series

$$J_N(t) = A + \frac{B\ln r}{C^{\alpha}}\sum_{m=0}^{N} r^{\alpha m}\left(1 - e^{-Ct/r^m}\right). \qquad (2)$$

The creep function $J_N(t)$ has as a limit the function $J(t)$ for $N \to \infty$. Observe that $J_N(t)$ is the creep function of a generalized Kelvin-Voigt model, shown in Fig. 1, consisting of a spring with compliance A in series with $N+1$ Kelvin-Voigt units. In the discrete GKM the stiffnesses of the springs are not constant, unlike the discrete modified Kuhn model. The stiffness of the spring and the viscosity coefficient of the dashpot in the m^{th} Kelvin-Voigt element, denoted by E_m and η_m respectively, are

$$E_m = \frac{r^{-\alpha m}C^{\alpha}}{B\ln r} \qquad (3)$$

and

$$\eta_m = \frac{r^{m(1-\alpha)}}{C^{(1-\alpha)}B\ln r}. \qquad (4)$$

The retardation time in each Kelvin-Voigt unit is $\tau_m = \frac{\eta_m}{E_m} = \frac{r^m}{C}$. We will call these Kelvin-Voigt units with the special properties, Kuhn units.

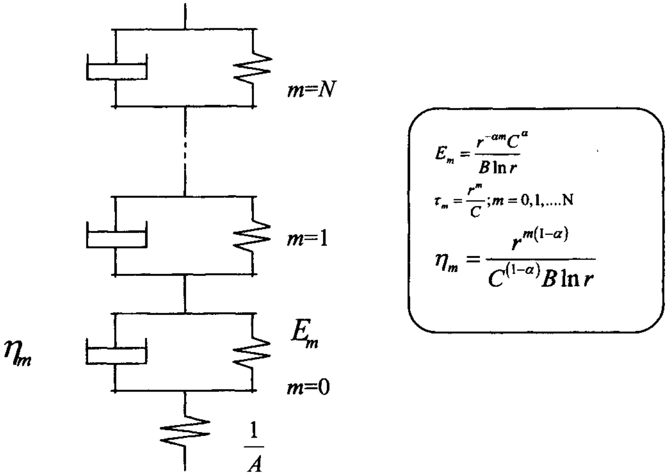

$$E_m = \frac{r^{-\alpha m} C^{\alpha}}{B \ln r}$$

$$\tau_m = \frac{r^m}{C}; m = 0, 1, \ldots. \mathrm{N}$$

$$\eta_m = \frac{r^{m(1-\alpha)}}{C^{(1-\alpha)} B \ln r}$$

Figure 1. Rheological representation of generalized modified Kuhn model.

The generalized Kuhn model shares the remarkable property of the MKM, i.e. that no matter how many Kuhn elements are used the number of parameters remains the same. The internal variable representation of the discrete GKM is given by Eqs. (5) and (6), which represent the evolution equations of the internal variables (interpreted here as the inelastic strains) in multi dimensions.

$$\dot{\boldsymbol{q}}_m^d + \frac{\boldsymbol{q}_m^d}{\tau_m} = \frac{\boldsymbol{s}}{\eta_m} = \frac{C^{(1-\alpha)} B \ln r}{r^{m(1-\alpha)}} \boldsymbol{s}, \tag{5}$$

$$\dot{\theta}_m + \frac{\theta_m}{\tau_m} = \frac{C}{r^m} \frac{1}{A} tr \boldsymbol{\sigma}, \tag{6}$$

where $\boldsymbol{q}_m^d$ and θ_m are the deviatoric and volumetric components respectively of the viscous strain tensor $\boldsymbol{q}_m$ of the m^{th} Kuhn element, i.e.

$$\boldsymbol{q}_m = \boldsymbol{q}_m^d + \frac{1}{3}\left(tr \boldsymbol{q}_m\right) \mathbf{1}, \tag{7}$$

$$\theta_m = tr\boldsymbol{q}_m, \tag{8}$$

where **1** is the identity tensor of rank 2, $\boldsymbol{s}$ is the deviator of the stress tensor $\boldsymbol{\sigma}$ and *tr* stands for the trace operator. The superimposed dot in Eqs. (5) and (6) indicates time derivative. The total viscous strain tensor $\boldsymbol{\varepsilon}^v$ for the discrete GKM is

$$\boldsymbol{\varepsilon}^v = \sum_{m=0}^{N} \boldsymbol{q}_m . \tag{9}$$

The total strain tensor is the sum of elastic and viscous strain tensors, i.e.

$$\boldsymbol{\varepsilon} = \boldsymbol{\varepsilon}^{el} + \boldsymbol{\varepsilon}^v . \tag{10}$$

This decomposition is well justified in the small strain framework, which is used in this work. Eqs. (5) to (10) give a complete characterization of the GKM in an internal variable form. Both the rheological representation of the discrete GKM, described by Eq. (2), and its internal variable representation are equivalent forms of the model. However, it should be noted that the internal variable form is advantageous because it can be also expressed in multi-dimensions and it can be extended into the nonlinear domain in a relatively easy manner.

The loss tangent –which is a measure of energy dissipation in viscoelasticity- of the discrete generalized Kuhn model is given by the following relation (Panoskaltsis et al. 2006)

$$\tan\delta = \frac{\dfrac{\omega}{C}\displaystyle\sum_{m=0}^{N}\frac{r^{(1+\alpha)m}}{1+\dfrac{\omega^2 r^{2m}}{C^2}}}{\dfrac{AC^\alpha}{B\ln r}+\displaystyle\sum_{m=0}^{N}\frac{r^{\alpha m}}{1+\dfrac{\omega^2 r^{2m}}{C^2}}}, \tag{11}$$

where ω is the frequency of excitation. For the derivation of the expression for the loss tangent the creep function and its Fourier transform are used. The discrete generalized Kuhn model's loss tangent predictions of experimental results of asphalt concrete are very good (Panoskaltsis et al. 2006).

THE TEMPERATURE DEPENDENT GENERALIZED KUHN MODEL

It is a well known fact that asphalt concrete is a temperature sensitive material; see e.g. Pagen (1965), FHWA (1978). The experimental observations for asphalt concrete, as well as other materials such as polymers and ceramics at high temperatures, are depicted on a qualitative plot of creep compliances versus time on a log-log scale in Fig. 2. From the plot it can be observed that at a given time, the creep compliance at a lower temperature is smaller than that at a higher temperature.

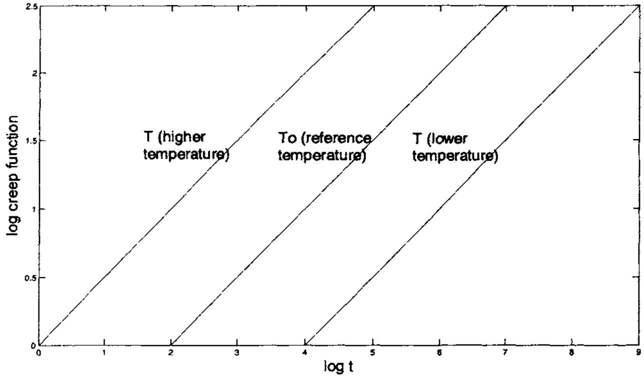

Figure 2. Schematic representation of creep functions versus time at different temperatures.

Crucial for the quantitative description of the creep function's temperature dependence is the introduction of the so called time-temperature shift factor a_T, which was first introduced for polymers (Williams, Landel and Ferry 1952). The shift factor for asphalt concrete may be defined as

$$a_T = \frac{t_T}{t_{T_o}}, \tag{12}$$

where t_T is the time to obtain a value of the creep function at temperature T, and t_{T_o} is the time to obtain the same value of the creep function at temperature T_o (the reference temperature). For asphalt concrete, based on numerous experiments, the logarithm of the shift factor a_T is observed to be varying linearly with temperature, as shown in Fig. 3 (see e.g. FHWA 1978, Huang 1993). The slope of the curve is given by

$$\beta = \frac{\log(a_T)}{T - T_o} = \frac{\log\left(\frac{t_T}{t_{T_o}}\right)}{T - T_o} \; . \tag{13}$$

From this equation it follows that

$$t_T = t_{T_o} \exp\left(2.3026\beta\left(T - T_o\right)\right), \tag{14}$$

where $2.3026 = \ln 10$; note that β is negative.

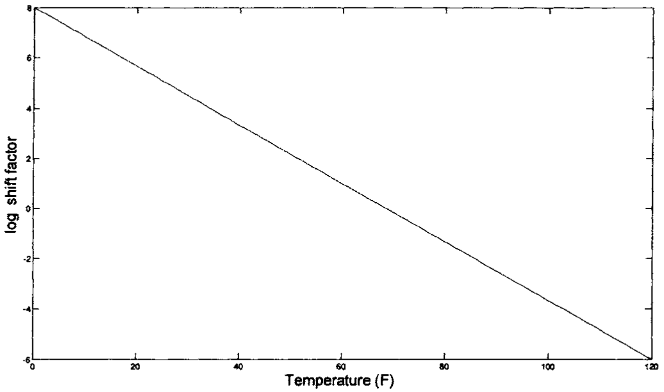

Figure 3. Logarithm of shift factor versus temperature.

A qualitative plot of creep functions with time on a linear scale, for asphalt concrete, is given in Fig. 4. In the figure, T_0 represents the reference temperature, T_h a higher than the reference temperature and T_l a lower than the reference temperature.

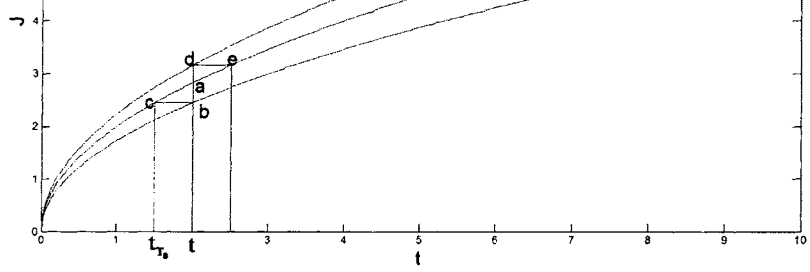

Figure 4. Qualitative representation of creep functions at different temperatures.

We assume that the creep function of the discrete generalized Kuhn model, given by Eq. (2), is valid at the reference temperature T_0, we denote it as $J(t;T_o)$ and we rewrite Eq. (2) as

$$J(t;T_0) = A + \frac{B \ln r}{C^{\alpha}} \sum_{m=0}^{N} r^{\alpha m} \left(1 - e^{-Ct/r^m}\right). \tag{15}$$

The problem at hand is to find the expression for the creep function at any other temperature *T*. For this, we proceed as follows: Let us assume that at the current time *t* –at which the creep value at the reference temperature is '*a*' (Fig. 4) - we want to find the creep value at a lower temperature T_l. From Fig. 4 we see that this is equal to '*b*' (on the creep curve corresponding to temperature T_l). This value is equal to the value '*c*' on the creep curve for the reference temperature T_0. The value '*c*' occurred at an earlier time equal to t_{T_0}. Therefore, the value '*c*' can be obtained from Eq. (15) if we substitute for time the value t_{T_0}. The relation between *t* and t_{T_0} is given in Eq. (14) (t_T in Eq. (14) is equal to *t*). By solving for t_{T_0} we obtain from Eq. (14):

$$t_{T_0} = t \exp\left(-2.3026\beta\left(T - T_o\right)\right). \tag{16}$$

Substituting this value in Eq. (15) we obtain the value '*c*' and therefore the value '*b*'. The same exactly arguments hold if we want to obtain the creep value '*d*' at a higher temperature T_h. Therefore, the creep function at any temperature *T*, denoted as $J(t;T)$, is obtained if we substitute Eq. (16) in Eq. (15), i.e.

$$J(t;T) = A + \frac{B_1 \ln r}{C_1^{\alpha}} \sum_{m=0}^{N} r^{\alpha m} \left(1 - e^{-C_1 t/r^m}\right), \tag{17}$$

where

$$C_1 = C \exp\left(-2.3026\beta\left(T - T_o\right)\right), \tag{18}$$

and

$$B_1 = B \exp\left(-2.3026\beta\left(T - T_o\right)\alpha\right). \tag{19}$$

As it is seen from the above equations the parameters B_1 and C_1 are temperature dependent.

Since we assumed that the creep function given by Eq. (2) or equivalently by Eq. (15) holds at the reference temperature T_0, the expression for the loss tangent in Eq. (11), which was derived by using Eq. (2), will also hold at the reference temperature T_0. In order to obtain the loss tangent at any temperature *T* we should use Eq. (17). Since Eq. (17) has the same exactly form as Eq. (2) the expression for the loss tangent at any temperature T will have the same form as Eq. (11) with the parameters B and C replaced by the temperature dependent parameters B_1 and C_1, which are determined from Eqs. (19) and (18) respectively. Therefore, the loss tangent at any temperature T will be

$$\tan\delta(T)=\frac{\dfrac{\omega}{C_1}\displaystyle\sum_{m=0}^{N}\frac{r^{(1+\alpha)m}}{1+\dfrac{\omega^2 r^{2m}}{C_1^2}}}{\dfrac{AC_1^{\alpha}}{B_1\ln r}+\displaystyle\sum_{m=0}^{N}\frac{r^{\alpha m}}{1+\dfrac{\omega^2 r^{2m}}{C_1^2}}}. \tag{20}$$

The temperature dependence of the viscosity coefficient can be shown as follows. Let η_m^* and η_m be the viscosity parameters for the m^{th} Kuhn element at temperature T and reference temperature T_0 respectively. Recalling Eq. (4), and using Eqs. (18) and (19), the following relation between the viscosity parameters at temperatures T and T_0 is established,

$$\frac{\eta_m^*}{\eta_m}=\frac{r^{m(1-\alpha)}}{C_1^{(1-\alpha)}B_1\ln r}\Bigg/\frac{r^{m(1-\alpha)}}{C^{(1-\alpha)}B\ln r}=\exp\left(2.3026\beta\left(T-T_o\right)\right). \tag{21}$$

From this expression it is seen that when the temperature increases the viscosity coefficient decreases, which is in accordance to experimental results. It is assumed that the stiffnesses of the springs remain independent of the temperature. The relation between the relaxation times at temperatures T and T_0 will be

$$\frac{\tau_m^*}{\tau_m}=\frac{\eta_m^*/E_m}{\eta_m/E_m}=\frac{\eta_m^*}{\eta_m}=\exp\left(2.3026\beta\left(T-T_o\right)\right). \tag{22}$$

So far, the temperature dependence of the parameters of the discrete generalized Kuhn model has been established for the one-dimensional case. The same relations between the parameters will be established for general three-dimensional cases, using a novel approach to incorporate the temperature into the model through an internal variable formulation. This approach provides a powerful way of extending the time temperature superposition principle into multi-dimensional and nonlinear formulations and is presented in the next session.

INTERNAL VARIABLE FORMULATION

As it was mentioned earlier the internal variable formulation of the discrete GKM is equivalent to its description via the creep function (Panoskaltsis et al. 2006).

The evolution equations of the internal variables, given by Eqs. (5) and (6), can be written as follows at the reference temperature T_o

$$\eta_m \frac{d\boldsymbol{q}_m^d}{dt} + E_m \boldsymbol{q}_m^d = \boldsymbol{s}, \tag{23}$$

$$\tau_m \frac{d\theta_m}{dt} + \theta_m = \frac{1}{A} tr\boldsymbol{\sigma}. \tag{24}$$

The evolution equations at any temperature T will be

$$\eta_m \frac{d\boldsymbol{q}_m^d}{dt_{T_0}} + E_m \boldsymbol{q}_m^d = \boldsymbol{s}, \tag{25}$$

$$\tau_m \frac{d\theta_m}{dt_{T_0}} + \theta_m = \frac{1}{A} tr\boldsymbol{\sigma}. \tag{26}$$

Since the internal variable formulation is equivalent to the description by means of the creep function and since –as it was explained earlier- in order to obtain the creep function at any temperature T we use the time t_{T_0}, the time derivatives are now taken with respect to t_{T_0}. By using the chain rule Eqs. (25) and (26) can be rewritten as

$$\eta_m \frac{d\boldsymbol{q}_m^d}{dt}\frac{dt}{dt_{T_0}} + E_m \boldsymbol{q}_m^d = \boldsymbol{s}, \tag{27}$$

$$\tau_m \frac{d\theta_m}{dt}\frac{dt}{dt_{T_0}} + \theta_m = \frac{1}{A} tr\boldsymbol{\sigma}. \tag{28}$$

Eq. (14), by differentiating it with respect to t_{T_o}, yields

$$\frac{dt_T}{dt_{T_o}} = \exp\left(2.3026\beta\left(T - T_o\right)\right). \tag{29}$$

Using Eq. (29) in Eqs. (27) and (28) the following equations are obtained,

$$\eta_m^* \frac{d\boldsymbol{q}_m^d}{dt} + E_m \boldsymbol{q}_m^d = \boldsymbol{s}, \tag{30}$$

$$\tau_m^* \frac{d\theta_m}{dt} + \theta_m = \frac{1}{A} tr\boldsymbol{\sigma}, \tag{31}$$

where η_m^* and τ_m^* represent the viscous parameter and relaxation time respectively at temperature T and they are given by Eqs. (32) and (33).

$$\eta_m^* = \eta_m \frac{dt}{dt_{T_0}} = \eta_m \exp\left(2.3026\beta\left(T - T_o\right)\right), \tag{32}$$

$$\tau_m^* = \tau_m \frac{dt}{dt_{T_0}} = \tau_m \exp\left(2.3026\beta\left(T - T_o\right)\right). \tag{33}$$

Eq. (32) shows the relation between the viscosity coefficient of the m^{th} Kuhn element at temperature T and its value at the reference temperature T_0. This is identical to the relationship obtained in Eq. (21). Similarly, Eq. (33) shows the relation between the relaxation time of the m^{th} Kuhn element at temperature T and its value at the reference temperature T_0 and this is identical to the relationship obtained in Eq. (22). Eqs. (30), (31), (32) and (33) constitute the internal variable formulation of the discrete generalized Kuhn model at any temperature T. The internal variable formulation is more general than the formulation based on the creep function, since it also holds in the multidimensional spaces of stress and strain tensors. Moreover, it does not depend on the existence of a closed form for the creep function and it can be used in cases of nonlinearities. It should be also mentioned that the internal variable formulation is amenable to a finite element implementation of the model.

RESULTS

The loss tangent given by Eq. (20) is used to fit the experimental results reported by Cerni (2001). Bitumen specimens are subjected to frequency sweep experiments at various temperatures and the plots of phase angle δ (in degrees) versus frequency (in Hz) at temperatures 6°C, 15°C and 25°C are obtained and shown in Fig. 5. Log scale has been used in the frequency axis. The parameters are estimated from model fit of the experimental results. The parameter estimation is done by nonlinear optimization techniques and programming is done in MATLAB. The objective function used for the parameter estimation is given by Eq. (34),

$$f = \sum_{i=0}^{M} \left(\frac{lt_{m,i} - lt_{\mathrm{expt},i}}{lt_{\mathrm{expt},i}} \right)^2, \tag{34}$$

where $lt_{m,i}$ and $lt_{\mathrm{expt},i}$ are i^{th} model and experimental loss tangent values and M is the total number of experimental data points. Fig. 5 shows the model fit at 6°C, 15°C, and 25°C. The values of the parameters are listed in Table 1. Fifteen Kuhn elements were used. It is noted that the values of the parameters A, α and r are temperature independent as they should.

Table 1. List of parameters for various temperatures fit.

Temperature	*A*	*B*	*C*	α	*r*
$T_1=6^0C$	1.15	$B_1=25.10$	$C_1=0.0196$	0.43	1.01
$T_2=15^0C$	1.15	$B_2=34.30$	$C_2=0.0404$	0.43	1.01
$T_3=25^0C$	1.15	$B_3=48.52$	$C_3=0.0907$	0.43	1.01

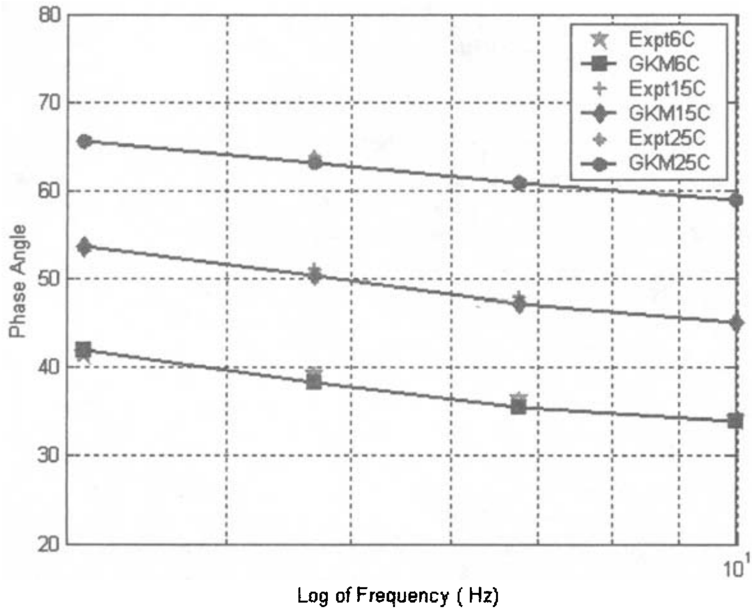

Figure 5. Loss tangent versus frequency; model fit to experimental data. The experimental data is from Cerni (2001).

For the validation of the model the following procedure is followed. Using the values of the parameters obtained for temperatures 6^0C and 15^0C, the values for the temperature dependent parameters *B* and *C* corresponding to 25°C are calculated. These calculated values are compared with the parameter values which have been obtained by the fitting process. For this, the slope β of the variation of the log of the shift factor a_T with temperature is calculated from Eq. (18) (treating T_1 as the reference temperature), i.e.

$$C_2 = C_1 \exp\left(-2.3026\beta\left(T_2 - T_1\right)\right), \tag{35}$$

where T_1, T_2, C_1 and C_2 are given in Table 1. From Eq. (35), the value of the slope β is calculated as $\beta = -0.035$. Clearly, instead of Eq. (18), Eq. (19) could have been used.

The values of the parameters B and C for 25^0C are calculated from the following equations, using the obtained value for β.

$$C_3 = C_1 \exp\left(-2.3026\beta\left(T_3 - T_1\right)\right) = 0.0906, \tag{36}$$

$$B_3 = B_1 \exp\left(-2.3026\beta\left(T_3 - T_1\right)\alpha\right) = 48.49. \tag{37}$$

These calculated (predicted) values are almost equal to the fitted values B_3 and C_3 given in Table 1. This provides an excellent validation of the model, since the predicted values match the fitted ones. Therefore, the model is able to predict the variation of the loss tangent with the frequency of excitation at different temperatures by computing the corresponding to the temperatures parameters B and C, following the procedure just shown, and then using Eq. (20). We note that as is seen in Fig. 5, the loss tangent values are increasing with temperature, which means that the dissipated energy is higher at higher temperatures.

The model is validated against a second set of experiments reported by Corte (2001). In this case, dynamic shear tests were conducted at various temperatures on four different asphalt concrete mixes with penetration grades (PG) 10/20, 25/35, 35/50, and 50/70. Phase angle variation (in degrees) with temperature at 7.8 Hz has been recorded. In this case for each concrete mix Eq. (20) is expressed as a function of the temperature, and the parameters A, B, C, α, r, β, with the help of Eqs. (18) and (19). B and C are the values of the parameters at the reference temperature, taken here to be 0^0C. The objective function is given by Eq. (34). The parameters are tabulated in Table 2 and the number of Kuhn elements used for the fitting is 15. Fig. 6 shows the experimental results and the model's fit to the experimental data. It is evident from the figure that the generalized Kuhn model fits phase angle variation with respect to temperature with very good accuracy. The values of the parameters B_1 and C_1 at any other temperature can be obtained by using Eqs. (19) and (18) respectively and thus the phase angle value at this temperature is computed with the use of Eq. (20), for any of those four asphalt mixes and for frequency equal to 7.8 Hz.

Table 2. List of parameters for phase angle versus temperature fit.

Parameters	PG 10/20	PG25/35	PG35/50	PG50/70
A	108.72	63.68	19.62	21.12
B	1722.3	8392.4	18431	6320.3
C	0.2099	0.0378	0.0057	0.008
α	0.3472	0.0511	0.0467	0.5388
r	1.05	1.05	1.05	1.05
β	-0.0149	-0.0196	-0.0196	-1.0302

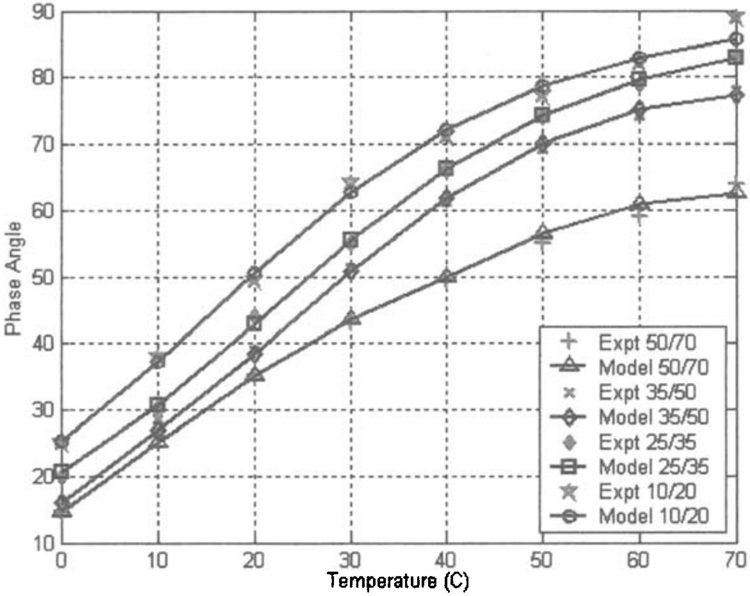

Figure 6. Model fit for phase angle versus temperature at 7.8 Hz. Experimental data is from Corte (2001).

Again, we observe from Fig. 6 that for all asphalt concrete mixes the phase angle (and hence the dissipated energy) increases with temperature, as it is expected.

CONCLUSIONS

In this paper we developed a new temperature-dependent viscoelastic model for asphalt concrete. The new model has been presented in both a rheological form as well as in an internal variable one and has a small number of parameters. The creep function and the loss tangent of the model have been derived as functions of temperature. The model's comparisons to experimental data are very favorable. One of the contributions of this work is that a general methodology has been developed by which any viscoelastic model, which is expressed in terms of a creep function or in an internal variable form, can be made temperature-dependent. The advantages of the internal variable formulation have been discussed in the paper.

REFERENCES

Cerni, G. (2001). "Influence of the conditioning time on the rheological properties of bituminous at intermediate temperatures: Loading time-temperature-conditioning time superposition principle." *Road Materials and Pavement Design*, 2(4), 379- 401.

Corte, J. F. (2001). "Development and uses of hard-grade asphalt and of high-modulus asphalt mixes in France." *Transportation Research Circular*, Transportation Research Board, 503, 12-31.

FHWA. (1978). "Predictive design procedures". *VESYS Users Manual, Report No. FHWA-RD-77-154*, Federal Highway Administration.

Huang, Y. H. (1993). *Pavement analysis and design*, Prentice Hall, Englewood Cliffs, New Jersey.

Lubliner, J., and Panoskaltsis, V. P. (1992). "The modified Kuhn model of linear viscoelasticity." *International Journal of Solids and Structures*, 29 (24), 3099-3112.

Pagen, C. A.. (1965). "Rheological response of bituminous concrete." *Highway Research Record,* 67, Highway Research Board, 1-26.

Panoskaltsis, V. P., Papoulia, K. D., Bahuguna, S., and Korovajchuk, I. (2006). "The generalized Kuhn model of linear viscoelasticity." *In review.*

Panoskaltsis, V. P., Bahuguna, S., Papoulia, K. D., and Lubliner, J. (1999). "Finite element analysis of rate dependence and failure of concrete." *Proceedings of the European Conference on Computational Methods,* H.A. Mang et al. eds., 31 August - 3 September, 1999, Munich, Germany.

Williams, M. L., Landel, R. F., and Ferry, J. D. (1952). "Time temperature dependence of linear viscoelastic behavior." *Journal of Applied Physics*, 23, 838-843.

LABORATORY VALIDATION OF VISCOELASTIC INTERCONVERSION FOR HOT MIX ASPHALT

Myung Goo Jeong[1], Amara Loulizi[2], P.E., and Gerardo W. Flintsch[3], M. ASCE

ABSTRACT: Various research efforts have proven that it is possible to interconvert the various linear viscoelastic material properties (i.e., the creep compliance, relaxation modulus, complex compliance, and dynamic modulus) of asphalt concrete materials. The interconversion makes it possible to predict one viscoelastic property from another and therefore eliminates the need to do more than one test to calculate all needed viscoelastic properties. This paper presents a laboratory validation of the interconversion between dynamic moduli and creep compliances obtained from two typical mixes used in the Commonwealth of Virginia. The measured dynamic modulus was successfully converted into creep compliance, and the measured creep compliance was successfully converted into dynamic modulus. Both converted properties were compared to the actual measured data. It was found that in most cases the converted properties were similar to the measured properties. However, the dynamic modulus predicted smaller creep compliance than was measured while the creep compliance predicted smaller dynamic modulus than was measured. This is attributed to the fact that the creep tests were performed at high, constant stress without confinement, which might have brought the material outside its linear viscoelastic range. More testing is therefore needed to confirm the promising results obtained with the existing conversion methods.

---

[1] Graduate Research Assistant (Former GRA at Virginia Tech, 2003~2005), Arizona State University, Department of Civil and Environmental Eng., PO Box 875306, Tempe, AZ 85287-5306, mgjeong@asu.edu

[2] Assistant Professor, Ecole Nationale d'ingénieur de Tunis, ENIT Département Génie Civil B.P. 37 Le Belvédère, 1002 Tunis, Tunisia, amlouliz@vt.edu

[3] Associate Professor, Charles Via, JR. Department of Civil and Environmental Engineering and , Director, Center for Sustainable Transportation Infrastructure, Virginia Tech Transportation Institute, 3500 Transportation Research Plaza, Blacksburg, VA 24061-0105, flintsch@vt.edu

INTRODUCTION

Determining the viscoelastic properties of hot mix asphalt (HMA) is important for several applications, including modeling flexible pavement response to truck and environmental loadings, predicting the performance of the material in terms of specific distress types (e.g., low-temperature cracking and rutting), and for specifications as quality control measures (e.g., limiting a function of the dynamic modulus and the phase angle to a specified passing value).

Rheologists have studied the viscoelastic properties of polymers for many years, and the theory governing viscoelastic behavior of these materials is well established *(1)*. Among the tests used by rheologists to determine viscoelastic parameters are static creep compliance and dynamic modulus tests. These tests are now gaining wide acceptance among highway agencies to measure viscoelastic properties of HMA. Asphalt material researchers have proven that the interconversion between those viscoelastic properties measured on asphalt mixtures using the theory worker relatively well at low temperatures (i.e., linear condition) *(2)*.

In 2005, the Virginia Department of Transportation (VDOT) and the Virginia Tech Transportation Institute reviewed existing methods for determining the moduli of HMA and identified simple laboratory tests that accurately describe the constitutive behavior of HMA used in the Commonwealth of Virginia *(3)*. The performed tests evaluated included uniaxial static creep compliance and dynamic modulus. The results from that study presented an opportunity to verify whether existing interconversion methods between viscoelastic properties could be applied to the HMA at wider temperature ranges. This would eliminate the need to perform one of the two tests as the results from one test could be used to calculate the properties obtained from the other. This paper presents the measured data on both mixes, the procedure used to convert from one property to another and a comparison of the converted property with the measured data.

EXPERIMENTAL PROGRAM

Two typical HMA mixtures used in Virginia, SM-9.5A and BM-25.0, were used in this study. The SM-9.5A mix is a surface mix with a 12.5-mm maximum nominal aggregate size and a PG64-22 binder. The BM-25.0 is a base mix with a 25.0-mm maximum nominal aggregate size and a PG64-22 binder. The mixes were designed according to VDOT specifications *(4)*, which follow the SUPERPAVE procedures with some minor odifications. Table 1 shows the job mix formula with the source of the aggregates for both mixes. Table 2 presents the average aggregate gradation for both mixes.

All specimens prepared for testing were compacted using a Gyratory Compactor. The specimens were compacted to achieve approximately 4% ± 1% voids in total mix (VTM) for the molded specimen. Therefore, the specimens were compacted by fixing the height rather than fixing the number of required gyrations. Once a specimen was extracted from the TGC, its bulk density (G_{mb}) was measured using the AASHTO T166 procedure *(5)*, and then it was cored and cut to the final specimen dimensions of 102 mm by 152 mm. Another bulk density was then performed on the final specimen since it is known that there is a slight difference in the measured VTM between the compacted mold specimen and the final cored and cut specimen.

TABLE 1. Job mix formula for both mixes

Type (1)	Percentage (%) (2)	Source (3)	Location (4)
BM-25.0			
# 357 Limestone	18	ACCO STONE	Blacksburg, VA
#68 Limestone	30	ACCO STONE	Blacksburg, VA
#10 Limestone	27	ACCO STONE	Blacksburg, VA
Concrete Sand	10	WYTHE STONE	Wytheville, VA
Processed RAP	15	ADAMS Construction	Blacksburg, VA
PG 64-22	4.7	Associated Asphalt	Roanoke, VA
Adhere HP+	0.5	ARR-MAZ Products	Winter Haven, FL
SM-9.5A			
# 8 Quartzite	45	Salem Stone	Sylvatus, VA
#10 Quartzite	25	Salem Stone	Sylvatus, VA
Concrete Sand	15	Wythe Stone	Wytheville, VA
Processed RAP	15	ADAMS Construction	Blacksburg, VA
PG 64-22	5.5	Associated Asphalt	Roanoke, VA
Adhere HP+	0.5	ARR-MAZ Products	Winter Haven, FL

TABLE 2. Aggregate gradation for both mixes

Sieve Open. (mm) (1)	Sieve # (2)	% Passing (3)	
37.5	1.5	-	100.0
25	1	-	92.8
19	3/4	-	84.9
12.5	1/2	100.0	77.7
9.5	3/8	91.4	70.1
4.75	#4	56.3	48.4
2.36	#8	39.9	25.4
1.18	#16	31.2	17.4
0.6	#30	23.1	13.2
0.3	#50	14.2	8.0
0.15	#100	9.7	5.3
0.075	#200	7.4	4.3

Table 3 presents the G_{mb} and VTM values for all prepared specimens after extraction from the TGC and after coring and cutting. For the SM-9.5A mix, the average VTM for the dynamic modulus specimens were 4.2% and 2.7% right after extraction from the TGC and after coring and cutting, respectively. The static creep test specimens had 4.3% and 3.1% VTM after extraction from the TGC and after coring and cutting, respectively. For the BM-25.0 mix, on average, the VTM for the dynamic modulus specimens were 5.0% and 3.7% right after extraction from the TGC and after coring and cutting, respectively. The static creep test specimens had 5.0% and 3.6% VTM after extraction from the TGC and after coring and cutting, respectively.

TABLE 3. G_{mb} and VTM for all prepared specimens

	Dynamic Modulus					Static Creep				
		Extracted Specimen		Final Specimen			Extracted Specimen		Final Specimen	
	Label (1)	G_{mb} (2)	VTM (%) (3)	G_{mb} (4)	VTM (%) (5)	Label (6)	G_{mb} (7)	VTM (%) (8)	G_{mb} (9)	VTM (%) (10)
SM-9.5A	S93	2.365	4.1	2.402	2.6	S109	2.363	4.2	2.400	2.7
	S94	2.366	4.1	2.402	2.6	S110	2.364	4.2	2.405	2.5
	S95	2.365	4.1	2.398	2.8	S111	2.361	4.3	2.396	2.9
	S96	2.367	4.1	2.403	2.6	S112	2.358	4.4	2.393	3.0
	S97	2.368	4.0	2.427	1.6	S113	2.370	3.9	2.406	2.5
	S98	2.363	4.2	2.392	3.0	S114	2.365	4.1	2.395	2.9
	S101	2.364	4.2	2.399	2.7	S115	2.356	4.5	2.392	3.1
	S102	2.360	4.3	2.388	3.2	S116	2.362	4.3	2.387	3.2
	S105	2.366	4.1	2.392	3.1	S117	2.356	4.5	2.362	4.2
	S107	2.362	4.3	2.388	3.2	S119	2.362	4.3	2.368	4.0
	Average	**2.365**	**4.2**	**2.399**	**2.7**	**Average**	**2.362**	**4.3**	**2.390**	**3.1**
BM-25.0	B56	2.473	4.9	2.510	3.5	B55	2.464	5.2	2.510	3.5
	B62	2.473	4.9	2.511	3.4	B58	2.467	5.1	2.509	3.5
	B63	2.470	5.0	2.517	3.2	B60	2.463	5.3	2.493	4.2
	B64	2.473	4.9	2.496	4.0	B61	2.474	4.9	2.499	3.9
	B65	2.465	5.2	2.511	3.5	B78	2.478	4.7	2.517	3.2
	B67	2.473	4.9	2.497	4.0	B79	2.471	5.0	2.518	3.2
	B68	2.471	5.0	2.502	3.8	B80	2.462	5.3	2.498	4.0
	B69	2.471	5.0	2.508	3.6	B81	2.466	5.2	2.514	3.3
	B76	2.470	5.0	2.488	4.3	B84	2.470	5.0	2.500	3.9
	B77	2.474	4.9	2.513	3.4	B85	2.476	4.8	2.509	3.5
	Average	**2.471**	**5.0**	**2.505**	**3.7**	**Average**	**2.469**	**5.0**	**2.507**	**3.6**

The dynamic modulus and static creep tests were performed with the same servo-hydraulic machine and using the same extensometers to measure the vertical deformations. Five temperatures were used: -15°C, 5°C, 20°C, 30°C, and 40°C. For the static creep test, the applied load was sustained for 1,000 seconds, while for the dynamic modulus test, six frequencies were used: 0.1 Hz, 0.5 Hz, 1 Hz, 5 Hz, 10 Hz, and 25 Hz. In both tests, two specimens were tested per temperature; therefore, 10 specimens per mix and per test were tested in total, as is presented in Table 3.

DYNAMIC MODULUS

Table 4 presents the average measured dynamic modulus and the phase angle for both mixes. As expected, under a constant loading frequency, the magnitude of the dynamic modulus decreases with an increase in temperature; and under a constant testing temperature, the magnitude of the dynamic modulus increases with an increase in frequency. On the other hand, the phase angle decreases as the frequency increases at testing temperatures of -15°C, 5°C, and 20°C. However, at testing temperatures of 30°C and 40°C, the behavior of the phase angle as a function of frequency is more complex, which is attributed to the aggregate interlock that controls the response of the specimen at high temperatures and low frequencies as reported by other researchers *(6)*.

The average measured data were used to construct a master curve for the dynamic modulus at a reference temperature of 20°C. The method developed by Pellinen and Witczak was used in this study to construct the master curve *(7)*. The method consists of fitting a sigmoidal curve to the measured dynamic modulus test data using nonlinear least-square regression techniques. The shift factors at each temperature are determined simultaneously with the other coefficients of the sigmoidal function. The calculated shift factors for the SM-9.5A mix and the BM-25.0 mix are shown in Figures 1a and 1b, respectively. The best-fit sigmoidal functions for the SM-9.5 mix and BM-25.0 mix are given by Equations 1 and 2, respectively.

$$\log\left|E^*\right| = 1.8762 + \frac{2.41534}{1+e^{-1.28301-0.59499\log f_r}} \tag{1}$$

$$\log\left|E^*\right| = 2.1358 + \frac{2.26117}{1+e^{-1.11630-0.62793\log f_r}} \tag{2}$$

TABLE 4. Average dynamic modulus (MPa) and phase angle (°) results

		-15°C		5°C		20°C		30°C		40°C	
		|E*| (1)	δ (2)	|E*| (3)	δ (4)	|E*| (5)	δ (6)	|E*| (7)	δ (8)	|E*| (9)	δ (10)
SM-9.5A											
Frequency (Hz)	25	19,563	1.2	13,833	6.0	11,312	15.1	6,722	24.3	3,484	32.1
	10	19,117	2.4	12,058	7.9	9,787	17.3	5,432	25.2	2,521	29.8
	5	18,750	3.0	11,313	8.7	8,609	19.2	4,384	27.1	1,985	28.6
	1	18,285	3.4	10,118	10.9	5,953	24.2	2,635	28.8	1,226	23.9
	0.5	17,528	3.7	8,804	12.8	4,734	29.8	2,054	31.5	709	28.3
	0.1	15,940	5.1	7,432	16.3	2,890	33.4	1,316	28.2	532	19.6
BM-25.0											
Frequency (Hz)	25	24,483	1.3	18,687	8.0	13,395	15.1	7,978	23.1	4,029	30.7
	10	24,243	2.8	17,431	7.8	11,549	17.1	6,568	24.4	3,122	28.5
	5	23,867	3.0	16,485	9.1	10,104	19.1	5,366	26.1	2,843	26.5
	1	22,484	3.9	13,993	11.1	6,952	23.9	3,246	29.5	1,708	23.0
	0.5	21,428	4.7	12,426	13.5	5,534	29.2	2,132	36.9	956	27.8
	0.1	19,991	5.8	10,408	16.6	3,419	33.6	1,316	35.1	725	20.5

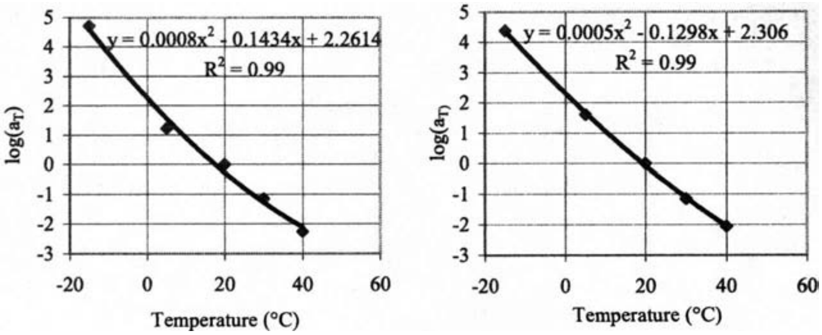

(a) (b)

FIG. 1. Shift factors versus temperature: (a) SM-9.5A and (b) BM-25.0

CREEP COMPLIANCE

Figure 2 shows the measured creep compliances over the 1,000-s loading time at each of the five tested temperatures for mixes SM-9.5A and BM-25.0. Each curve represents the average of the two tested specimens at that temperature. A master curve of the creep compliance was constructed for a reference temperature of 20°C for both mixes. A visual method with the Excel spreadsheet software was used to find the shift factors needed to construct the master curve.

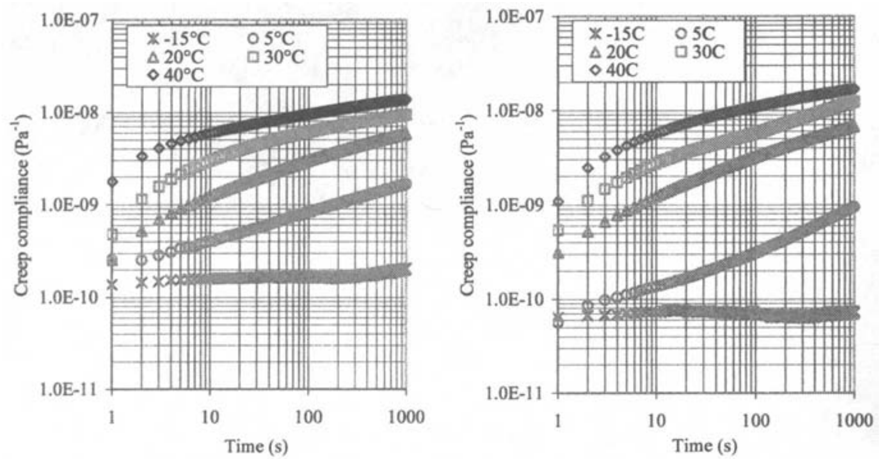

(a) (b)

FIG. 2. Creep compliance for both mixes (a) SM-9.5A and (b) BM-25.0

This visual method was adopted because it produced appropriate results, and other researchers had not found any significant differences between shift factors determined manually and those determined by a computer program *(8)*. The shift factors used to construct the creep compliance master curve are presented in Table 5. The table presents for comparison the shift factors used for the dynamic modulus data. It is known that simple rheological material should have the same shift factor for all viscoelastic properties. However, there are some differences between the shift factors used for the dynamic modulus data and those used for the creep compliance data. These differences could be due to experimental errors in both tests, errors with the nonlinear regression procedure used for the dynamic modulus data, or a departure of the mix behavior from the linear viscoelastic theory.

TABLE 5. Shift factors for both mixes

Parameters (1)	**Creep compliance**		**Dynamic modulus**	
	SM-9.5A (2)	BM-25.0 (3)	SM-9.5A (4)	BM-25.0 (5)
Log(a_T at -15°C)	4.5588	4.9746	4.7052	4.3842
Log(a_T at 5°C)	2.0439	2.2016	1.2174	1.6088
Log(a_T at 20°C)	0	0	0	0
Log(a_T at 30°C)	-1.0425	-0.8589	-1.1502	-1.1517
Log(a_T at 40°C)	-1.9780	-1.7479	-2.2625	-2.0583

Once the creep compliance master curve was constructed, a Prony series model was fit to the curve. This was performed because this type of fitting is needed in order to convert the creep data into dynamic modulus data as will be explained in the next section. The model is given by the following equation:

$$D(t_r) = D_g + \sum_{i=1}^{n} D_i(1 - e^{-t_r/\tau_i}) \tag{3}$$

where

$D(t_r)$ = creep compliance at reduced time t_r,

$D_g = \lim_{t_r \to 0} D(t_r)$ is the equilibrium (glassy) creep compliance,

D_i and τ_i = Prony series parameters, and

n = the number of terms used in the series.

A five-term Prony series was found to be suitable to fit the data though there is a relatively poor agreement in shorter time region. The use of additional terms to the series would likely improve the fitting. Figure 3 shows the creep compliance master curve with the Prony series fit for the SM-9.5A mix. Table 6 shows the calculated parameters for both mixes. It can be observed that the model does not fit the experimental data very well at the very short times, where it levels out more than the experimental model.

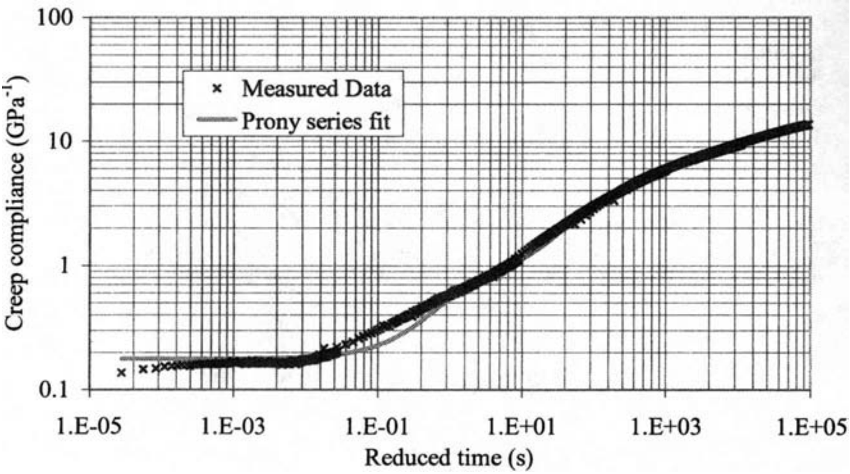

FIG. 3. Master curve and Prony series fit for the SM-9.5A mix

TABLE 6. Prony series parameters for the creep compliance master curve

Parameter (1)	SM-9.5A (2)	BM-25.0 (3)
Dg	0.1779	0.0695
D_1	0.5667	0.3534
τ_1	1.1788	1.0739
D_2	2.2899	1.32
τ_2	62.7561	17.6127
D_3	3.3976	2.8247
τ_3	779.3	184.1
D_4	3.3472	6.9871
τ_4	9977.3	3100.9
D_5	4.7423	8.2219
τ_5	55521.0	52695.4

CONVERSION OF CREEP COMPLIANCE INTO DYNAMIC MODULUS

If the creep compliance is expressed as a Prony series, as shown by Equation 3, then the complex compliance can be easily derived analytically. The real and imaginary part of the complex compliance is given by Equation 4 and Equation 5, respectively *(9)*.

$$D'(\omega) = D_g + \sum_{j=1}^{n} \frac{D_j}{\omega^2 \tau_j^{\,2} + 1} \tag{4}$$

$$D''(\omega) = \sum_{j=1}^{n} \frac{\omega \tau_j D_j}{\omega^2 \tau_j^2 + 1} \tag{5}$$

where
ω = angular frequency

The complex compliance is then determined using Equation 6, and the dynamic modulus can be calculated as the inverse of the complex compliance as shown by Equation 7 *(9)*.

$$|D^*(\omega)| = \sqrt{(D'(\omega))^2 + (D''(\omega))^2} \tag{6}$$

$$E^*(\omega) = \frac{1}{D^*(\omega)} \tag{7}$$

Figure 4 shows the calculated dynamic modulus for the SM-9.5A mix using the procedure described above. The figure also shows the measured dynamic modulus data for the same mix with the 95% confidence interval at each measurement point. It was assumed that at each testing temperature and frequency, the measured dynamic modulus followed a normal distribution with a mean equal to the average of the tested specimens and a standard deviation equal to the calculated standard deviation between those specimens. It must be noted that the wide confidence intervals are partially due to the small number of specimens tested. In other words, the intervals would have been more accurate if they were computed by a standard deviation of enough number of replicates; however only limited replicates were available. The figure shows that the calculated dynamic modulus from the creep compliance data is within the measured 95% confidence interval at some frequencies but out of this interval at most frequencies. In most cases, the calculated dynamic modulus was smaller than the measured one. In addition, the calculated dynamic modulus from the creep data reached the E_∞ modulus value (dynamic modulus value at infinite frequency) at a frequency of around only 10 Hz. The calculated E_∞ for the SM-9.5A mix was 5.6 GPa.

The same findings were observed for the BM-25.0 mix as shown in Figure 5. The calculated E_∞ for the BM-25.0 mix was 14.4 GPa. This means that creep data predicted a mix with weaker dynamic modulus than what was measured. This might be due to the fact that the creep compliance was performed using a high constant load of 690 kPa without any confinement. This stress might have caused the material to be outside its linear viscoelastic region, making the predicted dynamic modulus smaller than what was measured.

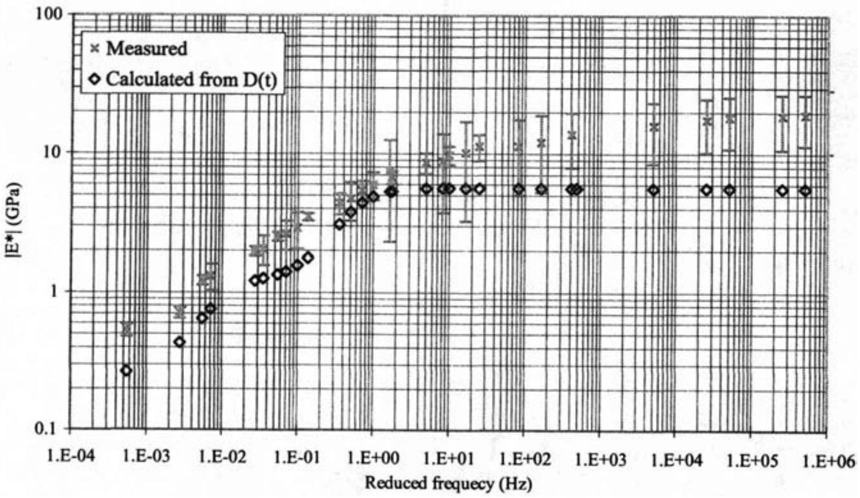

FIG. 4. Measured and calculated dynamic modulus from creep compliance (SM-9.5A)

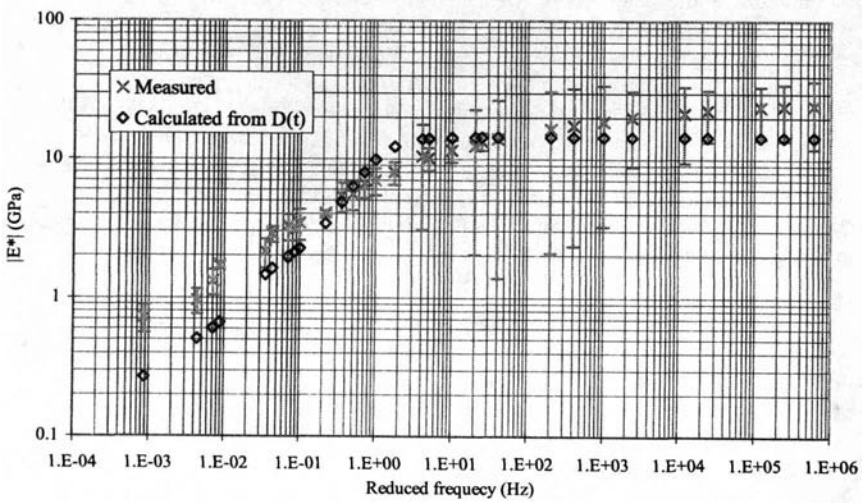

FIG. 5. Measured and calculated dynamic modulus from creep compliance (BM-25.0)

CONVERSION OF DYNAMIC MODULUS INTO CREEP COMPLIANCE

Calculating the creep compliance from the dynamic modulus requires two steps: first the dynamic modulus is converted into relaxation modulus, and then the relaxation modulus is converted into creep compliance.

Conversion of Dynamic Modulus into Relaxation Modulus

Schapery and Park proposed an approximate interconversion method to convert dynamic modulus data into relaxation modulus and verified this method using polymeric material *(10)*. Equations 8 and 9 show the formulas proposed by these researchers to convert the dynamic modulus into relaxation modulus. Equation 8 makes use of the real part of the dynamic modulus, while Equation 9 makes use of the imaginary part of the dynamic modulus.

$$E(t) \cong \frac{1}{\lambda'} E'(\omega)\bigg|_{\omega=(1/t)} \tag{8}$$

$$E(t) \cong \frac{1}{\lambda''} E''(\omega)\bigg|_{\omega=(1/t)} \tag{9}$$

where

λ' = adjust function ($\Gamma(1-n)\cos(n\pi/2)$),

λ'' = adjust function ($\Gamma(1-n)\sin(n\pi/2)$),

Γ = gamma function ($\Gamma(n) = \int_0^\infty u^{n-1}e^{-u}du$), and

n = the local log-log slope of the storage modulus $\left(\left|\frac{d\log E'(\omega)}{d\log\omega}\right|\right)$.

For this study, the storage modulus data was used to calculate the relaxation modulus. The storage modulus (E") was calculated using the dynamic modulus and phase angle (E" = |E*| cosδ) and then plotted on a logarithmic scale. A sigmoidal function was fitted to the storage modulus data using curve-fitting software. The regressed analytical function was used to compute the local logarithmic slope of the storage modulus (n) over the specified frequency range. The relaxation modulus at each time was then computed. Figure 6, for example, shows the computed relaxation modulus for the SM-9.5A mix.

Conversion of Relaxation Modulus into Creep Compliance

An exact relationship between the creep compliance and relaxation modulus exists by using the convolution integral in Equation 10 *(1)*.

$$\int_0^t E(t-\tau)D(\tau)d\tau = t \tag{10}$$

where
$E(t)$ = relaxation modulus
$D(t)$ = creep compliance,
t = time, and
τ = an integral variable.

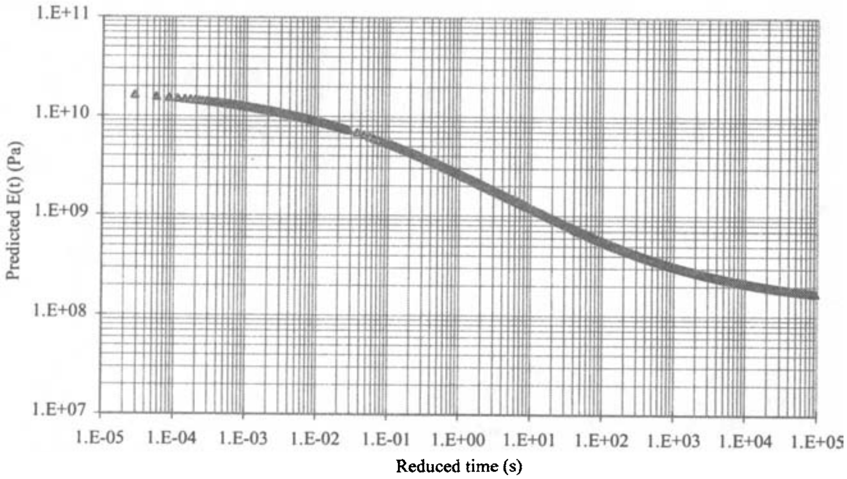

FIG. 6. Computed relaxation modulus from the dynamic modulus (SM-9.5A)

When an analytical form of a viscoelastic material is not available—for example, when only data points determined in the laboratory exist—the integral can be solved numerically *(11)*. However, the numerical method requires significantly tedious and cumbersome work. Leaderman showed that if both the creep compliance and relaxation modulus are modeled using a power law, then Equation 11 could be used to relate the relaxation modulus and the creep compliance *(12)*.

$$E(t)D(t) = \frac{\sin n\pi}{n\pi} \tag{11}$$

where
$E(t) = E_1 t^{-n}$ and
$D(t) = D_1 t^{n}$.

Practically, lab-determined data are not exactly represented by the power law function. However, if the data do not perfectly follow a power model but the functions behave smoothly, Equation 11 still works well. In this case, the local slope of the power model can be determined using Equation 12 *(11)*.

$$n = \left| \frac{d \log E(t)}{d \log t} \right| \tag{12}$$

Therefore, for this study, the determined relaxation modulus was fitted with a sigmoidal function, whose derivative was used to find the values of n, and then the creep compliance was calculated using Equation 11.

Figures 7 and 8 show the computed creep compliances for mixes SM-9.5A and BM-25.0, respectively. The figures also show the measured creep compliance with a 95% confidence interval. For both mixes, the computed creep compliance was smaller than the average measured one at almost all loading times. This may confirm what was previously explained for the predicted dynamic modulus from the creep compliance.

The measured dynamic modulus predicted smaller creep compliance (stronger mix) than what was measured. One possible reason is that the creep test was performed using a high constant stress of 690 kPa, which might have caused the material to be outside its linear viscoelastic region.

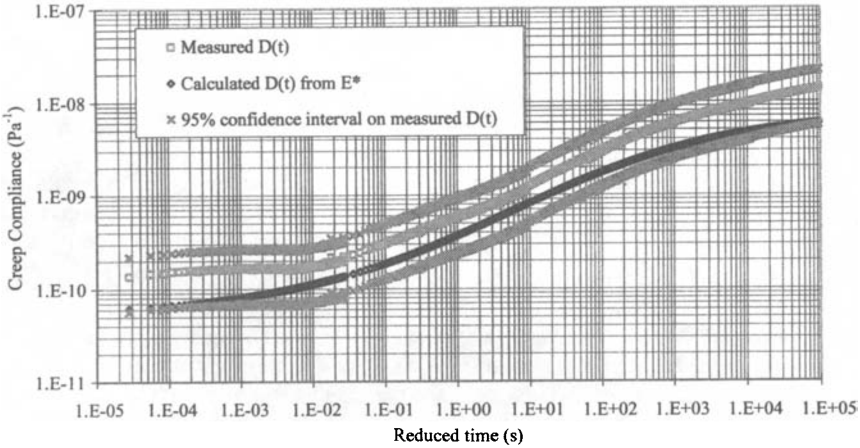

FIG. 7. Measured and calculated, from dynamic modulus, creep compliance (SM-9.5A)

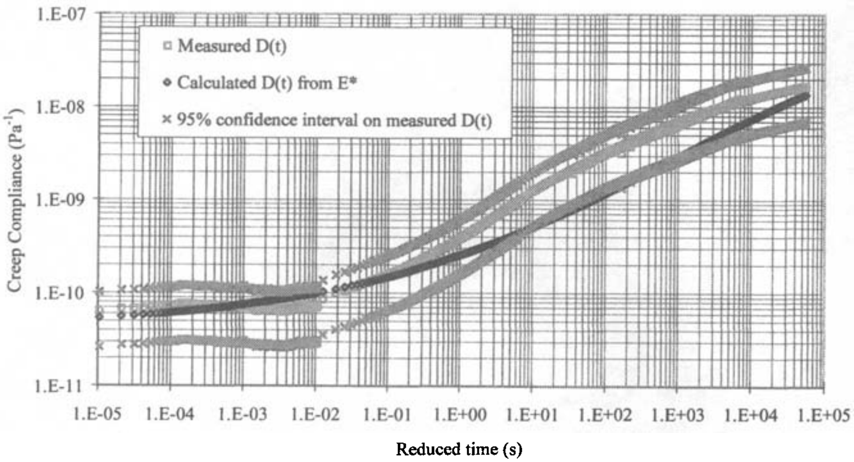

FIG. 8. Measured and calculated, from dynamic modulus, creep compliance (BM-25.0)

CONCLUSIONS

The results from creep compliance and dynamic modulus testing of two HMA mixes were used to verify whether existing interconversion methods between viscoelastic properties could be used on HMA. This would eliminate the need to perform one of the two tests as the results from one test could be used to calculate the properties obtained from the other. The uniaxial creep compliance and dynamic modulus of two typical mixes used in Virginia were measured at various temperatures and creep compliance master curves, and dynamic modulus master curves were constructed using the time-temperature superposition principle. The creep compliance data were used to compute the dynamic modulus and vice versa using existing interconversion procedures.

The investigation found that the converted properties did fall in most cases within the 95% confidence interval of the measured data. The discrepancy between the measured and calculated properties are mainly attributed to the fact that the creep test was performed using a high, constant stress, which might have brought the material outside its linear viscoelastic region. The interconversion between the viscoelastic properties showed very promising results, but more testing with other mixes is needed to confirm these findings.

REFERENCES

1. Ferry, J.D., Viscoelastic properties of polymers, 3rd ed., Wiley, New York, 1980.
2. Kim, Y.R. and Y. Lee, "Interrelationships Among Stiffnesses of Asphalt-Aggregate Mixtures," Journal of the Association of Asphalt Paving Technologists, Vol. 64, 1995, pp. 575-606.
3. Flintsch, G.W., I.L. Al-Qadi, A. Loulizi, and D. Mokarem, "Laboratory Tests for Hot-Mix Asphalt Characterization in Virginia," VTRC Report 05-CR22, Charlottesville, VA, 2005.
4. Virginia Department of Transportation, Road and Bridge Specifications, 2002.
5. American Association of State Highways and Transportation Officials. AASHTO T166-00, Specific Gravity of Compacted Bituminous Mixtures Using Saturated Surface-Dry Specimens, Standard Specifications for Transportation Materials and Methods of Sampling and Testing, Part2 - Tests, 20th Edition, Washington, DC, 2000, pp. 514–516.
6. Clyne, T. R., Li, X., Marasteanu, M. O., and Skok, E. L. Dynamic and Resilient Modulus of MN DOT Asphalt Mixtures, Report No. MN/RC-2003-09, 2003, Minnesota Department of Transportation, Minneapolis, MN.
7. Pellinen, T.K., and M.W. Witczak, "Stress Dependent Master Curve Construction for Dynamic Modulus," *Journal of the Association of Asphalt Paving Technologists*, Vol. 71, 2002, pp. 281–309.
8. Witczak, M.W., R. Roque, D.R. Hiltunen, and W.G. Buttlar, "Modification and Re-Calibration of Superpave Thermal Cracking Model," NCHRP 9-19 Project Report, Arizona State University Department of Civil and Environmental Engineering, Tempe, Arizona, December 2000.
9. Park, S.W. and R.A. Schapery, "Methods of interconversion between linear viscoelastic material functions. Part I—A numerical method based on Prony series," International Journal of Solids and Structures, Vol. 36, pp. 1653-1675, 1999.
10. Schapery, R.A. and S.W. Park, "Methods of interconversion between linear viscoelastic material functions. Part II—An approximate analytical method," International Journal of Solids and Structures, Vol. 36, pp. 1677–1699, 1999.
11. Park. S.W. and Y.R. Kim, "Interconversion Between Relaxation Modulus and Creep Compliance for Viscoelastic Solids," ASCE Journal of Materials in Civil Engineering, Vol. 11, No. 1, pp. 76–82, 1999.
12. Leaderman, H., "Viscoelasticity phenomena in amorphous high polymeric systems," Rheology, Vol. II, F.R. Eirich, Ed., Academic Press, NY, 1958.

A LABORATORY STUDY ON CRACKING POTENTIAL OF BINDER COURSE ASPHALT MIXTURES USED IN SEMI-RIGID PAVEMENTS

Fujian Ni[1], Zhong Wu[2], P.E., Member, ASCE,
Rongsheng Chen[1], Xingyu Gu[3] and Qiao Dong[4]

Abstract: Surface cracking is one of major early distresses in newly constructed semi-rigid pavements in China. Such semi-rigid pavements usually consist of three layers of hot mix asphalt (HMA) mixtures on top of a cement-treated aggregate (CTA) base over lime treated subgrade. To control the CTA base cracks reflected to the surface, a HMA binder course mixture is desired to be not only anti-reflective cracking but also fatigue resistant. This study was in an effort to investigate the reflective cracking problem on semi-rigid pavements through a proper binder course mixture design and laboratory characterization of the fatigue and anti-cracking properties of binder course mixtures used in China.

INTRODUCTION

High-volume roads in China often use semi-rigid pavement structures. A typical semi-rigid pavement structure consists of three layers of hot mix asphalt (HMA) mixtures (total thickness about 180-mm) on top of a cement-treated aggregate (CTA) base (usually 350-mm thick) over a lime treated subgrade. Note that the mixture design specifications (RIHMC 2000; RIHMC 2005) for the three HMA layers are different in China. In general, the top and intermediate HMA layers are required to use high rut-resistant asphalt binders (e.g. polymer-modified binders) and finer aggregate gradations. On the other hand, the bottom HMA layer (hereafter termed as the binder course) is usually specified to use a regular non-modified binder with coarser aggregate gradations.

---

[1] Professor, College of Transportation Engineering, Southeast Univ., Nanjing, China. nifujian@jsmail.com.cn.

[2] Accelerated Pavement Research Program Manager, Louisiana Transportation Research Center, 4101 Gourrier Ave., Baton Rouge, LA. zhongwu@ltrc.lsu.edu.

[3] Associate Professor, College of Transportation Engineering, Southeast Univ., Nanjing, China.

[4] Formal Graduate Student, College of Transportation Engineering, Southeast Univ., Nanjing, China.

Reflective cracking is one of the major early distresses commonly found in newly constructed semi-rigid pavements. Research on how to improve a HMA mix design to control such reflective cracking problems is urgently needed. Results from a finite element simulation (Ni et al. 2006) indicate that, when the CTA base course is under intact condition (no cracks), the overall stress state at the bottom of the binder course is in compression. However, once the CTA base course develops cracks primarily due to shrinkage, significantly high tensile stresses and strains will be generated in the vicinity of the base cracks at the bottom of the HMA binder course. Under such a tension state, repeated traffic loads will first cause fatigue cracking at the bottom of the binder course. Fatigue cracks will then gradually propagate to the pavement surface, and finally result in failure for a surface HMA layer due to the reflective cracking.

Therefore, to control the CTA cracks reflected to the surface, a HMA binder course mixture is desired to be not only anti-reflective cracking but also fatigue cracking resistant. This study was in an effort to control the reflective cracking problem on semi-rigid pavements through a proper binder course mixture design and laboratory characterization of the fatigue and anti-cracking properties of binder course mixtures evaluated.

OBJECTIVE AND SCOPE

The main objective of this study was to evaluate the fatigue and anti-cracking properties of the binder course mixtures using different asphalt binders and aggregate gradations. This knowledge will eventually be used to develop a proper binder course mixture design to improve the reflective cracking problem commonly found in semi-rigid pavements in China.

To achieve the objective, three asphalt binder types and four aggregate gradations were selected in this study. HMA mixture characterization was accomplished by conducting three cracking-related laboratory tests – reflective cracking simulation test, impact ductility test, and beam fatigue test.

MIXTURE DESIGN

Asphalt Binders

Two conventional non-modified and one styrene-butadiene (SB) elastomeric polymer-modified asphalt binders were selected for use in this study. Table 1 presents the related asphalt binder specifications and binder test results. As shown in Table 1, the three binders, termed as A1, A2 and A3, respectively, can be further grouped (or graded) into different elasticity grades based on the penetration test results. High penetration values are corresponding to high ductility values for the three binder evaluated, indicating high elastic stiffness at an intermediate temperature. In general, all binders were satisfied to the current asphalt binder specification used in China (RIHMC 2000). The binder A3 has the highest elasticity grade, followed by A2, and then by A1.

TABLE 1. Asphalt Binder Test Results and Specifications

Binder Type	**A1**		**A2**		**A3**	
Test	**Results**	**Specification**	**Results**	**Specification**	**Results**	**Specification**
Penetration at 25°C	51	40~60	63.8	60~80	92	80~100
Flash point, °C	325	260+	295	260+	290	260+
Solubility, %	99.88	99.5	99.89	99.5	—	—
Viscosity, 60°C, Pa.s	—	—	222.4	180	272	—
Ductility at 15°C, cm	>150	80+	>150	100+	—	—
Ductility at 10°C, cm	26	15+	50	20+	—	—
Ductility at 5°C, cm	—	—	—	—	21.2	18+
Ductility at 15°C, after thin-film oven test, cm	47	10+	94.2	15+	—	—
Ductility at 10°C, after thin-film oven test, cm	12	4+	19	6+	—	—
Ductility at 5°C, after thin-film oven test, cm	—	—	—	—	16.8	10+

Aggregate Gradations

Four aggregate gradations with different nominal maximum aggregate size (NMAS) were included in this study. Table 2 presents the percent passing of each gradation. Typical crushed limestone aggregates, currently used in a highway construction project, were selected for this study, which included crushed coarse and fine limestone aggregates as well as limestone fines. The name of each gradation in Table 2 is associated with its NMAS. For example, AG-25 has a NMAS of 25 mm. It is noted that only gradation AG-19 was fine-graded (the gradation curve is above the Superpave restricted zone), the remaining gradations passed through the restricted zone.

TABLE 2. Aggregate Gradations

Sieve Size(mm)	Gradation Type			
	AG-25	AG-19	AG-16	AG-13
31.5	100	100	100	100
25.0	97	100	100	100
19.0	79	98	100	100
16	70	88	95	100
13.2	63	79	84	95
9.5	53	67	70	76.5
4.75	41	53	48	53
2.36	31	40	34	37
1.18	23	29	24.5	26.5
0.6	17	21	17.5	19
0.3	12	14	12.5	13.5
0.15	9	7.5	9.5	10
0.075	5	5.7	6	6

Mix Design

Marshall mix design was used to determine the optimum asphalt content. The optimum asphalt cement content for all mix designs was determined from asphalt concrete mixtures compacted with the Marshall Hammer at 75 blows per face and an air voids between 3 ~ 5 percent. Table 3 presents the Marshall mix design results. It is noted that, in terms of the Stability, mix containing AG-19 gradation was the lowest; in terms of the Flow, mix with AG-25 was the highest.

TABLE 3. Marshall Mix Design Results

Mixtures Grouped by Gradation	% AC	Gmb	VTM(%)	% Saturation	Stability (kN)	Flow (0.1mm)
AG-25	3.6	2.452	4.2	65.6	12.7	41.2
AG-19	4.0	2.453	3.8	69.9	10.5	38.1
AG-16	4.2	2.453	3.5	72.5	13.6	31.6
AG-13	4.5	2.462	3.2	79.3	14.1	34.6

Test Factorial and Specimen Preparation

As stated earlier, three cracking related tests were conducted in this study. Testing temperature for the reflective cracking simulation test and impact ductility test was set to be 20 °C, while the beam fatigue test was conducted at 15 °C. The testing temperature of 15 °C for the beam fatigue test was based on the current China asphalt pavement construction specification (RIHMC 2005), where a fatigue resistance parameter (i.e. the allowable tensile stress at the bottom of a HMA layer) is required to be tested at this temperature. Table 4 presents the test factorial of this study.

TABLE 4. Test Factorial

Mixture Designation	NMAS (mm)	Binder	Engineering Property Tests and Testing Temperatures		
			Reflective Cracking Simulation, 20°C	Impact Ductility, 20°C	Beam Fatigue, 15°C
BM^{A1}_{AG-19}	19	A1	3	3	4
BM^{A2}_{AG-13}	13	A2	3	3	4
BM^{A2}_{AG-16}	16	A2	3	3	4
BM^{A2}_{AG-19}	19	A2	3	3	4
BM^{A2}_{AG-25}	25	A2	3	3	4
BM^{A3}_{AG-19}	19	A3	3	3	4

Rectangle beam samples were used in all three cracking tests. The beam sample sizes for the reflective cracking simulation, impact ductility test and beam fatigue test were 240-mm (long) x 70-mm (wide) x 50-mm (high), 250-mm x 35-mm x 35-mm, and 381-mm x 63.5-mm x 50-mm, respectively. All test specimens were compacted using a kneading compactor. In general, a larger slab was first compacted at a target air void of 5.0 ± 1.0 percent (similar to the initial roadway air voids found for the binder course layer) and then cut into the proper test sample size using a diamond saw machine.

TEST DESCRIPTION

Reflective Cracking Simulation (RCS) Test

The schematic representation of a RCS test is presented in Figure 1. As shown in Figure 1, a RCS sample consists of three layers in order to simulate the reflective cracking development on a semi-rigid pavement. To prepare a testing sample, a rubber pad is first placed at bottom of a steel test mold. A cement concrete slab with a dimension of 240-mm x 70-mm x 80-mm is then placed on top of the rubber pad with a 10-mm wide crack cutting through the middle of the slab. The cracked concrete slab is used to simulate a shrinkage crack on a CTA base. Next, a hot tack coat layer (using the binder A2 in this study) is applied on top of the concrete slab with an application rate of 1.0 L/m^2. Finally, the asphalt mixture slab is immediately placed on top of the applied hot tack coat layer to form a RCS test sample.

The RCS test was designed to perform on a MTS-810 loading system. During a test, a sinusoidal (haversine) axial compressive load was applied through a small steel plate (with rubber at the interface) to the center of the asphalt beam specimen at a loading frequency of 10Hz. The amplitude of applied load was 2.4 kN. The number of load repetitions versus the measured crack lengths was continuously recorded. The test results from a RCS test include the average cracking rate, the initial cracking number and the final cracking number. The final cracking number was determined at a time when a reflective crack reaches to the beam surface, or the length of the crack was about 40 ~ 45mm long after a significantly high load repetitions (usually higher than 300,000 repetitions).

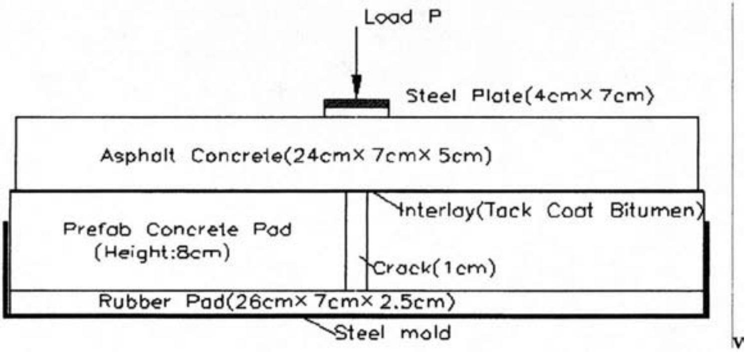

FIG. 1. RCS Test Setup

Impact Ductility Test

Note that performing a RCS test is not only relatively complicated in sample preparation, but also time-consuming. It may be not suitable for the routine lab use. Several researches (Huang et al. 1994; Baburamani and Porter 1996; Van Dijk 1975) indicated that, when a vehicle load passes through a pavement surface on top of a base crack, due to the high vehicle speed (small loading time), such wheel loading is similar to an impact load to asphalt materials. Based on this observation, an impact load based test was also selected for characterizing the anti-reflective cracking property for the binder course mixtures in this study.

The test setup of Impact Ductility test is showed in Figure 2. The Impact Ductility test was a displacement-controlled loading test, designed to perform on a MTS-810 loading system with a three-point loading setup. During a test, the beam specimen was loaded monotonically till fracture failure under a constant cross-head deformation rate of 500 mm/min at a test temperature of 20 °C. The load and vertical deformation were continuously recorded and a load-vertical displacement curve was plotted. An impact ductility value is defined as the area under the loading portion in a load-vertical deflection curve, up to the maximum applied load. According to the literature (Huang et al. 1994; Baburamani and Porter 1996), the impact ductility value represents the total stored energy in a HMA mixture before its fracture failure. The higher an impact ductility value, the better a HMA mixture resists to the reflective cracking.

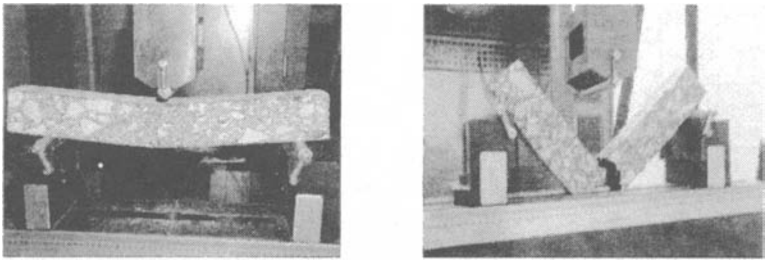

FIG. 2. Impact Ductility Test Setup

Beam Fatigue Test

The Beam Fatigue test was conducted according to SHRP M009 protocol at 15°C. It was a strain-controlled type of test where a beam 318 mm (15 in) long by 63.5 mm (2.5 in) wide by 50.8 mm (2.0 in) height is subjected to 4-point bending. Different strain levels are required in the beam fatigue test to generate a range of load repetitions at failure. The center deflection of the beam was continuously measured and used in the computation of the stiffness. Failure is defined as the load cycle at which the specimen exhibits a 50 percent reduction in stiffness. Figure 3 presents the test setup for the Beam Fatigue test. In this study, this test was conducted using a UTM machine with a temperature control chamber.

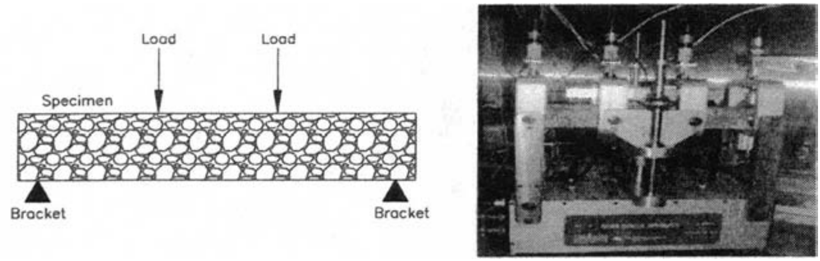

FIG. 3. Beam Fatigue Test Setup

DISCUSSION OF RESULTS

RCS Test Results

As stated earlier, three parameters can be obtained from a RCS test result: the average cracking rate, initial cracking number, and final cracking number. The initial cracking number is defined as the number of repetitions when the beam starts to crack. The final cracking number is the number of load repetitions when the beam fails. The average cracking rate is the ratio between the average crack length measured from two side walls of a beam sample and the difference of the final and the initial cracking numbers.

Figure 4 shows reflective cracking development photos for HMA mixtures evaluated under a RCS test. Note that side walls of asphalt beams were painted into a white color in order to better trace the development of cracking. As shown in Figure 4, under the repeated compressive load, all cracks propagated in a zigzag manner, moving across those weak links inside an asphalt-aggregate structure. In addition, the crack initiation point does not necessarily start in the middle of a base crack.

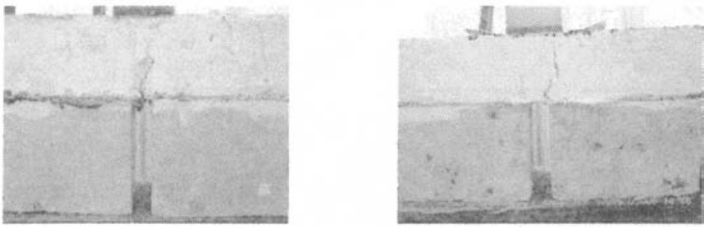

(a) Mix $BM^{A1}_{AG\text{-}19}$ at 164,955 cycles (b) Mix $BM^{A2}_{AG\text{-}13}$ at 397,520 cycles

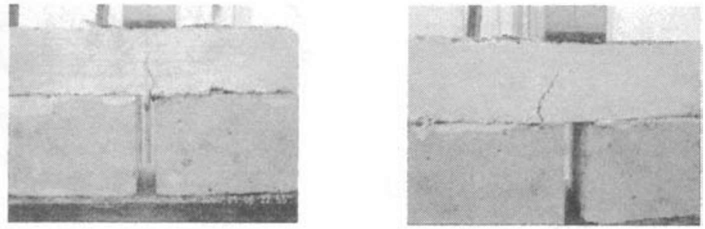

(c) Mix $BM^{A2}_{AG\text{-}19}$ at 149,842 cycles

(d) Mix $BM^{A2}_{AG\text{-}16}$ at 211,835 cycles

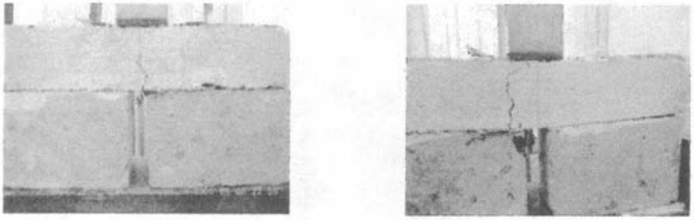

(e) Mix $BM^{A3}_{AG\text{-}19}$ at 314,814 cycles

(f) Mix $BM^{A2}_{AG\text{-}25}$ at 184,960 cycles

FIG. 4. Photos of Reflective Cracking

Figure 5 presents the average RCS results grouped for HMA mixtures using different binder types but with a same AG-19 gradation. As shown in Figure 5, as the binder elasticity grade increases, the average cracking rate decreases, and the final cracking number increases. This indicates that using a high elasticity grade binder in a HMA mixture generally can delay the reflective cracking propagation rate significantly.

Figure 6 presents the average RCS results grouped for HMA mixtures in different gradation groups but with a same A2 binder. Figure 6 illustrates that as the NMAS increases, the average cracking rate increases, and the initial cracking number decreases with an exception for the mixture containing the AG-25 gradation. As shown in Figure 6, even though the mixture with AG-25 gradation had the highest average crack propagation rate, it also had the highest initial cracking number among the four mixtures evaluated. This implies that with a large NMAS of 25-mm, a HMA mixture (e.g. Mix $BM^{A2}_{AG\text{-}25}$ in Figure 4(f)) tends to form a better interlock in the aggregate structure to resist an initial cracking. On the other hand, due to its low asphalt content (Table 3), it lacks of binder cohesion. As a result, when an initial crack is developed, it will propagate at a rapid rate. Overall, by considering the effects from both the binder content and aggregate structure, a smaller NMAS HMA mixture tends to have a higher anti-reflective cracking property than a larger NMAS HMA mixture.

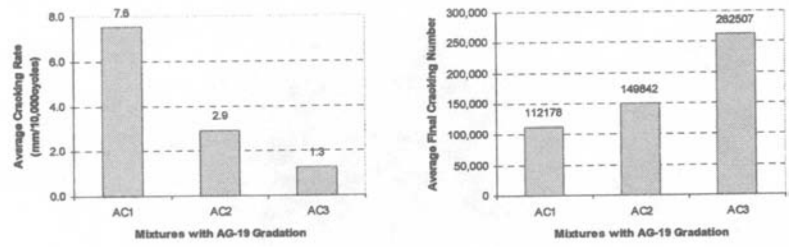

(a) (b)

FIG. 5. Average RCS results for Mixtures with Different Asphalt Binders

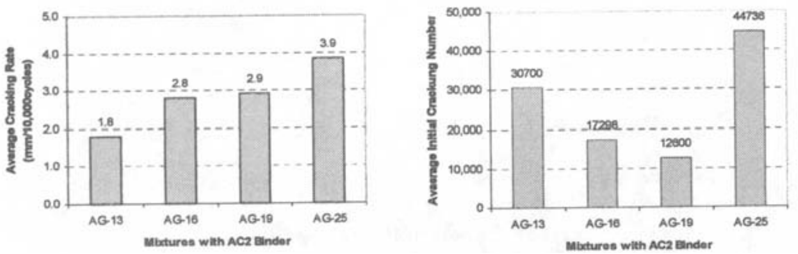

(a) (b)

FIG. 6. Average RCS results for Mixtures with Different Aggregate Gradations

Impact Ductility Test

Figure 7 presents the impact ductility results for HMA mixtures evaluated in this study. A high impact ductility value is desired for a crack-resistant mixture. As the NMAS increases, the impact ductility value decreases, Figure 7(a). Similarly, as the binder elasticity grade increases, the impact ductility of a mixture tends to increase, Figure 7(b). Overall, the impact ductility test results confirmed the results obtained from the RCS tests as described above.

Figure 8 presents the relationship between the impact ductility and the average cracking rate of six kinds of mixtures. A fairly good polynomial relationship was observed. This observation indicates that, in general, the impact ductility test can be used as a good alternative test to characterize the anti-reflective cracking property for a HMA mixture.

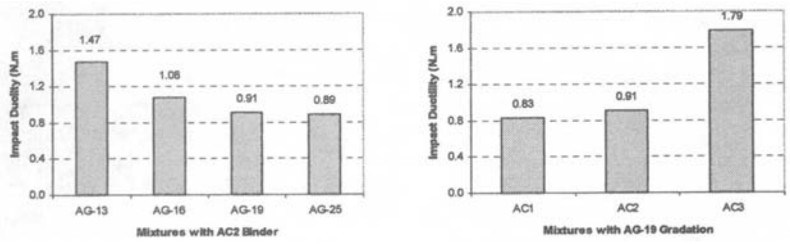

(a) (b)

FIG. 7. Average Impact Ductility Test Results

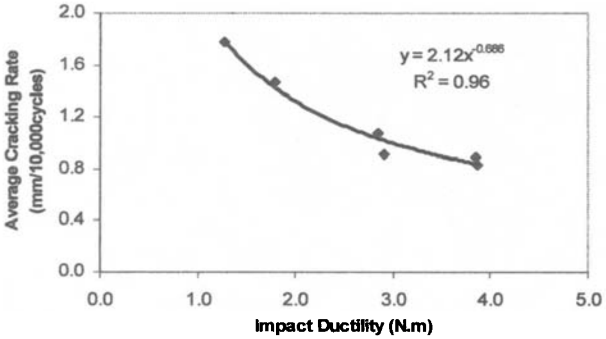

FIG. 8. Relationships between RCS and Impact Ductility Test Results

Beam Fatigue Test

Figures 9(a) and (b) present the beam fatigue test results for mixtures containing various binders and different aggregate gradations, respectively. As shown in Figure 9(a), the mixtures containing the highest elasticity grade, polymer-modified binder (A3) displayed a significantly higher fatigue life than mixtures with other two non-modified, lower elasticity grade binders. This indicates that the polymer modified binder used in this study can significantly improve a mixture's fatigue cracking resistance. On the other hand, the fatigue curves for mixtures containing A1 and A2 binders were found to cross-link with each other. At a lower tensile strain (smaller than 400 micro-strains), mixtures with A1 binder had a slightly higher fatigue life; whereas, at a higher tensile strain (higher than 400 micro-strains), the fatigue life for mixtures containing A2 binder were higher. One possible reason for this inconsistency may be attributed to sample preparation and handling. However, as shown in Figure 9(a), the fatigue resistance for mixtures containing A1 and A2 binders were not significantly different from each other under a normal traffic loading.

For mixtures containing a same binder type but with different NMAS gradations, those with a smaller NMAS tended to have a higher fatigue resistance. As shown in Figure 9(b), except the mixture with AG-19, as the NMAS decreases, the fatigue resistance of a mixture increases. The reason why the mixture with AG-19 appeared to have a lower fatigue resistance than mixtures with AG-25 will be further discussed in the following sections. But it should be noted here that AG-19 was the only fine-graded gradation used in this study.

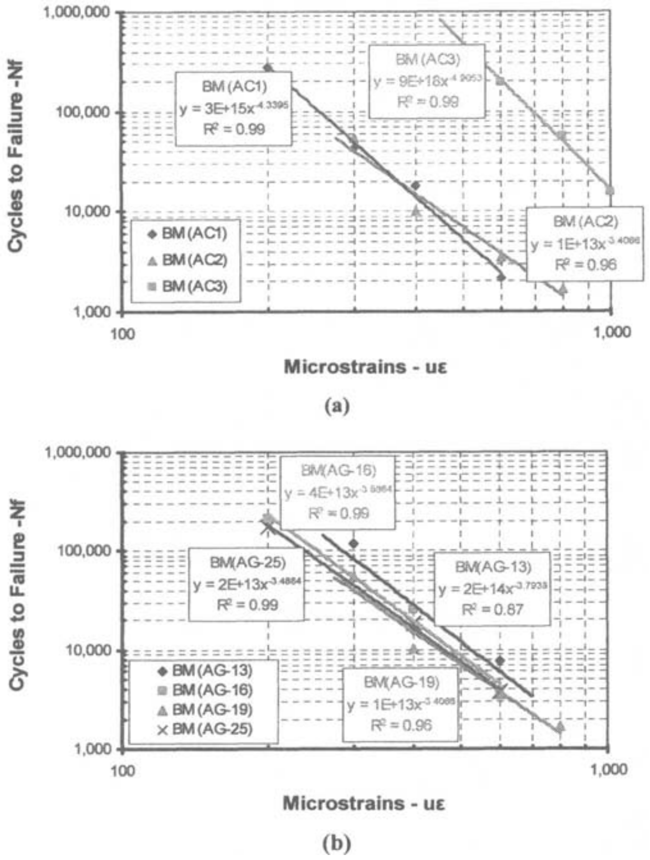

(a)

(b)

FIG. 9. Beam Fatigue Test Results (a) Mixtures with Different Binders; (b) Mixtures with various Aggregate Gradations

Binder Effect on Cracking Resistance

The reason for high elasticity grade binder performed better than low elasticity grade binder in both fatigue and reflective cracking resistance may be explained by the binder's fatigue factor, G*sin(δ), where G* is dynamic shear modulus of asphalt binder and δ is phase angle. A dynamic shear rheometer, DSR, was used to investigate the rheological behavior of the PAV-aged binders. The DSR tests were performed at 25 °C. The G*sin(δ) values for A1, A2, and A3 binders were found to be 9,663-, 7,362-, and 2,005-kPa, respectively. According to Superpave specification, G*sin(δ) for a certain binder at its fatigue temperature should be less than 5,000-kPa. Note that only A3 had a G*sin(δ) value lower than 5,000-kPa. This illustrates that the polymer-modified binder, A3, had significantly better fatigue cracking resistance than the two non-modified binders (A1 and A2). In addition, it is interesting to note that the G*sin(δ) values had a fairly good relationship to both RCS and impact ductility test results, which are shown in Figure 10. As the G*sin(δ) value increases, the average cracking rate increases and the impact ductility value decreases. In summary, binder DSR test results indicate that G*sin(δ) obtained at a fatigue temperature is indicative to both fatigue resistance and anti-cracking property for a HMA mixture.

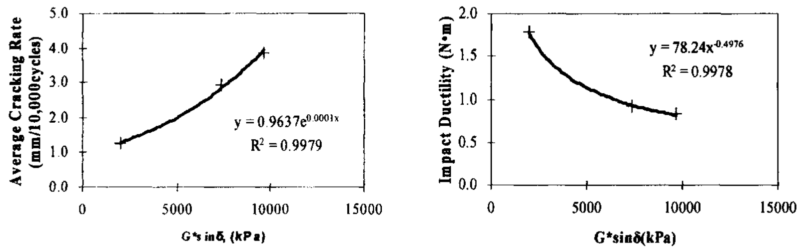

(a) (b)

FIG. 10. (a) Relationship between binder G*sin(δ) values and RCS Test Results; (b) Relationship between binder G*sin(δ) values and Impact Ductility Test Results

Gradation Effect on Cracking Resistance

To evaluate the influence of the aggregate gradation on mixture's cracking performance, a power-law gradation analysis (Ruth et al. 2002) was used. The power-law gradation analysis divides a gradation curve into coarse aggregate (CA) and fine aggregate (FA) two portions and uses the following power law regressions to characterize the slope and intercept constants for two corresponding gradation curves:

$$P_{CA} = a_{CA}(d)^{n_{CA}}, \qquad \text{and} \qquad P_{FA} = a_{FA}(d)^{n_{FA}} \qquad (1)$$

where,

P_{CA} or P_{FA} = percent by weight passing a given sieve have opening of width d
a_{CA} = intercept constant for the coarse aggregate
a_{FA} = intercept constant for the fine aggregate
d = sieve opening width, mm
n_{CA} = slope (exponent) for the coarse aggregate
n_{FA} = slope (exponent) for the fine aggregate

In this study, the sieve size of 2.36 mm was selected as a divider for the CA and the FA portions in the regression analysis. In general, both intercepts of a_{CA} and a_{FA} represent the total percent passing on a sieve size of 1mm. The slopes of n_{CA} and n_{FA} are indicative of the shapes of a gradation curve and can be either greater or smaller than 0.45. The greater an n_{CA} value, the coarser the CA portion gradation (i.e. more distances below the 0.45 maximum density line). On the other hand, the higher an n_{FA} value, the finer the FA portion gradation (i.e. more distances above the 0.45 maximum density line) (Mohammad et al. 2004).

Table 5 presents the gradation analysis results for the four gradations selected in this study. As shown in Table 5, all regression analyses received a high R^2-value, indicating that Eq.1 fits those gradation curves very well. In general, the a_{CA} and a_{FA} results (% passing on 1mm sieve size) agreed well with those percentage values passing on 1.18mm sieve size listed in Table 2, both illustrating that the AG-19 gradation had the highest fine aggregate percentage among the four gradations evaluated. It is interesting to note that the n_{CA} values in Table 5 provide an exactly same ranking as those fatigue test results shown in Figure 9(b). A lower n_{CA} value was found to be associated with a lower fatigue resistance for a mixture. This observation implies that a coarser CA portion (i.e. higher n_{CA} value) is desired for a fatigue resistance mixture. On the other hand, Mohammad et al. (2004) reported that n_{FA} values were found to have good correlation with the rut-resistance of a HMA mixture. Although rutting was not the topic of this research, however, it may be pointed out here that laboratory rut resistance test did observe the lowest average rut depth for mixtures containing the AG-19 gradation (with the highest n_{FA} in Table 5), followed by mixtures with the AG-25 gradation (with the second highest n_{FA} in Table 5) (Ni et al. 2006).

TABLE 5. Results of Power Law Regression Analyses for four Gradation Types

Gradation Type	Coarse Aggregate Portion > =2.36 mm			Fine Aggregate Portion <2.36 mm		
	a_{CA}	n_{CA}	R^2	a_{FA}	n_{FA}	R^2
AG-13	23.3	0.531	0.998	24.9	0.524	0.991
AG-16	21.4	0.529	0.999	22.8	0.497	0.994
AG-19	28.3	0.401	0.988	28.1	0.633	0.988
AG-25	19.9	0.464	0.989	21.8	0.524	0.998

In summary, the gradation analysis of this study yields two main observations: (1) to obtain a fatigue resistant mixture, the CA portion of a gradation should be the coarser the better (i.e. high n_{CA} values); (2) to obtain a rut resistant mixture, the FA portion of a gradation should be the coarser the better (i.e. high n_{FA} values). Therefore, how to balance both n_{CA} and n_{FA} values in a gradation design is the key to obtain a HMA mixture with both rutting and fatigue cracking resistance.

CONCLUSIONS

To improve anti-reflective cracking properties, a binder course HMA mixture is recommended to use a smaller NMAS gradation but with a higher elasticity grade (i.e. polymer modified) asphalt binder. However, to obtain a fatigue-resistant binder mixture, a coarse CA portion gradation shall be selected with a high n_{CA} value (higher than 0.45).

Both RCS and impact ductility tests provided a similar ranking for different groups of binder course mixtures considered in this study. This indicates that the Impact Ductility test can be used in place of the RCS test in characterizing the anti-reflective cracking properties of asphalt mixtures. Since the maximum tensile strength for a HMA mixture under a compressive or impact load is different from that under a repeated load, it is concluded that, for characterizing the anti-reflective cracking problem in a semi-rigid pavement, both the impact ductility test and beam fatigue test shall be performed.

REFERENCES

Baburamani, P. S., and Porter, D. W. (1996). "Dissipated Energy Approach to Fatigue Characterisation of Asphalt Mixes." *Proc. combined 18th ARRB TR Conference Transit New Zealand Symposium*, 327-347.

Huang, W., Deng, X., and Monismith, C.L. (1994). "An Energy-Based Approach to Characterize the Fatigue Properties of Asphalt Mixtures." *J. of China Highway*, 7(3):23-28.

Mohammad, L.N., Wu, Z., Raghavendra, R., and Abadie, C. (2004). "Comparison of Aggregate Gradation and Mixture Physical Properties to Performance Tests of Coarse-Grade Superpave Mixtures in Louisiana." *J. of the Association of Asphalt Paving Technologists*, Vol. 73, 261-285.

Ni, F., Gu, X., Chen, R., and Qiao, D. (2006). "Performance Requirements of Structural Layers on Asphalt Pavements and High Performance Asphalt Concrete Mixtures." *Research Report*, College of Transportation Engineering, Southeast University, Nanjing, China.

Research Institute of Highway Ministry of Communications (RIHMC 2000). "*Testing Specifications for Asphalt Binders and Mixtures Used in Highway Engineering (JTJ 052-2000).*" Beijing, China.

Research Institute of Highway Ministry of Communications (RIHMC 2005). "*Technical Specifications for Asphalt Pavement Construction (JTG F40-2004).*" Beijing, China.

Ruth, B. E., Roque, R., and Nukunya, B. (2002). "Aggregate Gradation Characterization Factors and Their Relationships to Fracture Energy and Failure Strain of Asphalt Mixtures", *J. of the Association of Asphalt Paving Technologists*, Vol. 71, 2002, 310-344.

Van Dijk, W. Practical Fatigue Characterization of Bituminous Mixes (1975). *Proc., Association of Asphalt Paving Technologists*, Phoenix, Arizona, Vol. 44.

EFFECT OF THE RELATIVE ROOT-MEAN-SQUARE ERROR ON PAVEMENT RESPONSE

Wael Alkasawneh[1], P.E., Ernie Pan[2], Roger Green[3], P.E.

ABSTRACT: Analysis of flexible pavements using the multilayered elastic theory involves the use of elastic moduli backcalculated from deflection basins measured utilizing the Falling Weight Deflectometer (FWD). Uncertainties associated with the thickness of the elastic layers, seed moduli, and the backcalculation algorithms have been studied to increase the reliability and accuracy of the backcalculated deflection basin by minimizing the relative root-mean-square error (RMSE). Therefore, the RMSE of the backcalculated deflection basin has been used always to assess the validity of the backcalculated set of elastic moduli of the pavement. In this study, the sensitivity of the pavement response to the RMSE is investigated by comparing the response of a pavement section using the exact set of moduli with that using the backcalculated set of pavement moduli with a RMSE less than 1%. The results showed that even when the RMSE in deflections is as low as 0.22%, the pavement response (strain, stress, and therefore fatigue and rutting predictions) using the backcalculated set of moduli can largely be different than that using the exact set of moduli, suggesting more uncertainties to the backcalculated set of moduli.

INTRODUCTION

Elastic modulus is an important property of pavement materials. Different methods have been proposed by researchers to estimate the elastic modulus based on laboratory bending tests and empirical equations (Bonnaure et *al.*, 1997), wave propagation methods (Cho and Lin, 2001), and the Falling Weight Deflectometer (FWD).

---

[1] Graduate Student, The University of Akron, Department of Civil Engineering, Akron, OH 44325-3905, wael@uakron.edu
[2] Associate Professor, The University of Akron, Department of Civil Engineering, Akron, OH 44325-3905, pan2@uakron.edu
[3] Pavement Research Engineer, Ohio Department of Transportation, 1980 West Broad Street, Columbus, Ohio 43223, Roger.Green@dot.state.oh.us

The elastic modulus in pavements cannot be determined accurately based on empirical equations since actual field conditions, loading conditions, and traffic conditions vary. In addition, some of the input parameters in the empirical equations cannot be determined for an existing pavement. Therefore, for practical purposes, elastic moduli need to be determined using in-situ methods to include the effect of different field factors.

The FWD test is currently the most widely used nondestructive method in pavement engineering. The test involves applying impact loads (impulse forces) to a loading plate and measuring the vertical displacement of the pavement surface at different locations using velocity sensors. The FWD system normally uses seven to nine geophones within a distance less than 2 meters with the first sensor below the center of the loading plate. The measured deflections from the FWD test along the pavement surface are then utilized to backcalculate the modulus of elasticity in each layer. This method, however, suffers from different limitations since backcalculating the modulus of elasticity does not always ensure an accurate estimate of the modulus where a seed modulus is required for each layer in the backcalculation procedure. Therefore, the backcalculation of the elastic moduli does not provide a unique solution and in many cases is user-dependent. It is common to assess the accuracy of the backcalculated elasticity moduli by assessing the accuracy between the measured deflection from FWD and the calculated deflection using the backcalculated set of elastic modului.

In this study we investigate the current practice of rejecting and accepting the backcalculated elasticity moduli based on a tolerance value between the measured and calculated deflections.

ERROR TOLERANCE IN BACKCALCULATION PROCEDURE

Backcalculation of elasticity moduli is commonly carried out by assuming a set of pavement-layer moduli (seed moduli) that can produce a deflection basin similar to the measured one from the FWD test. In order to minimize the error between the measured and calculated deflections, the relative root-mean-square error (RMSE) is used to control the convergence of the backcalculated deflections and to assess the acceptance and rejection of the final set of pavement moduli. The RMSE is computed by:

$$RMSE = \sqrt{\frac{1}{n}\sum_{i=1}^{n}\left(\frac{d_i - D_i}{D_i}\right)^2} \times 100\% \tag{1}$$

where, *RMSE* is the relative root-mean-square error, n is the total number of the deflection measurement points, d_i is the backcalculated deflection at point i, and D_i is the measured deflection at point i. When the RMSE value decreases, the accuracy of the backcalculated elasticity moduli is assumed to increase as the error between the measured and calculated deflections decreases.

In the LTPP test sections, a RMSE of 3% was used as an acceptable error (Von Quintus and Simpson, 2002). In addition, Von Quintus and Simpson (2002) showed that selection of a 2% RMSE does not necessarily result in convergence in the backcalculated elasticity moduli in all cases. In general, their results indicated (Von Quintus and Simpson, 2002) that RMSE values less than 3% have little effect on the average backcalculated elastic moduli. In practice, RMSE values larger than 1% can be achieved quickly (Harichandran et *al.* 2000). Therefore, the most commonly used value for the RMSE is between 1% and 3%. However, it is believed that achieving lower RMSE will always enhance the backcalculated elastic moduli and therefore more accurate results can be obtained.

BACKCALCULATION STUDY

The majority of the available research investigates the difference between the RMSE values from different backcalculation programs (Fwa et *al.* 1997), the effect of other factors on the quality of the deflection data (Mehta and Roque 2003), the effect of the seed generation on the RMSE values (Fwa and Rani 2005), and the effect of other factors on the FWD data. To the best of the authors' knowledge, however, the effect of the backcalculated elastic moduli and the associated RMSE on the strain and stress responses of flexible pavements has not been discussed so far.

In this paper, to study the effect of the RMSE on the strains and stresses in flexible pavements, a three-layer pavement section was selected. The flexible pavement section and the backcalculated elastic moduli were reported by Anderson (1988) and were shown in **Tables 1** and **2**. Responses at a total of 11 points (as shown in **Table 4**) were calculated for each case: responses along the ground surface at common locations of the velocity sensors used in the FWD test along the pavement profile (points 1 through 7), at the middle of the AC layer (point 8), at the bottom of the AC layer (point 9), at the middle of the base layer (point 10), and at the top of the subgrade (point 11). For all cases, responses were calculated for a circular load with a radius of 150 mm and a pressure of 690 kPa. The Poisson's ratio for all layers was equal to 0.35.

The pavement response was calculated using the ***MultiSmart3D*** program. The ***MultiSmart3D*** program is a fast and accurate software tool developed by the Computer Modeling and Simulation Group at the University of Akron, and it is based on the innovative computational and mathematical techniques for multilayered elastic systems (Pan 1989a,b; Pan 1990; Pan 1997). The program is capable of analyzing any pavement system regardless of the number of layers, the thickness of each layer, the number of response points, and the shape of the applied pressure at the surface of the pavement.

The RMSE for each case was calculated using **Eq. 1** and shown in **Table 3**. In addition, **Table 3** shows the relative errors using the exact and backcalculated elastic moduli. The relative error is defined as:

$$RE = \left|\frac{Exact - Calculated}{Exact}\right| x100\% \qquad \textbf{(2)}$$

This definition of the relative error is also used to compare the calculated strains and stresses based on the exact and backcalculated models. In other words, *Calculated* is the response using the backcalculated elastic moduli, and *Exact* is the response using the exact elastic moduli.

Pavement responses from the exact and backcalculated elastic moduli (Cases 1 through 5) are shown in **Tables 5** through **10**. In addition, **Tables 5** through **10** show the relative error associated with each response.

TABLE 1. Parameters of the Original (Exact) Layers

Case (1)	AC Thickness (mm) (2)	Base Thickness (mm) (3)	Exact Modulus (MPa)		
			AC (4)	Base (5)	Subgrade (6)
Case 1	381.0	152.4	3447.3785	13789.5140	68.9476
Case 2	381.0	152.4			
Case 3	381.0	152.4			
Case 4	381.0	152.4			
Case 5	381.0	152.4			

TABLE 2. Parameters of the Backcalculated Layers

Case (1)	Backcalculated Modulus (MPa)		
	AC (2)	Base (3)	Subgrade (4)
Case 1	3506.1839	13507.0427	69.0096
Case 2	3359.2980	15717.2743	68.6304
Case 3	3656.5723	12088.8670	69.4302
Case 4	3410.8018	13371.5676	68.7063
Case 5	3657.1101	12017.7062	69.6715

TABLE 3. Relative Errors in Moduli and RMSEs in Deflections between the Exact (TABLE 1) and Backcalculated (TABLE 2) Moduli

Case (1)	AC (%) (2)	Base (%) (3)	Subgrade (%) (4)	RMSE (%) (5)
1	1.71	2.05	0.09	0.24
2	2.55	13.98	0.46	0.22
3	6.07	12.33	0.70	0.65
4	1.06	3.03	0.35	0.69
5	6.08	12.85	1.05	0.85

TABLE 4. Coordinates and Locations of the Response Points

Point (1)	x (mm) (2)	y (mm) (3)	Z (mm) (4)	Location (5)
1	0.0	0.0	0.0	AC Surface
2	304.8	0.0	0.0	
3	609.6	0.0	0.0	
4	914.4	0.0	0.0	
5	1219.2	0.0	0.0	
6	1524.0	0.0	0.0	
7	1828.8	0.0	0.0	
8	0.0	0.0	190.5	Middle of AC Layer
9	0.0	0.0	380.9	Bottom of AC Layer
10	0.0	0.0	457.2	Middle of Base Layer
11	0.0	0.0	533.5	Top of Subgrade Layer

TABLE 5. Exact Responses from the Original (Exact) Pavement Profile

Point (1)	ε_x (μm/m) (2)	ε_y (μm/m) (3)	ε_z (μm/m) (4)	σ_x (kPa) (5)	σ_y (kPa) (6)	σ_z (kPa) (7)	u_z (mm) (8)
1	-57.77	-57.7	-62.49	-677.95	-677.95	-690.00	0.21
2	-7.00	-27.08	18.35	-64.75	-116.02	0.00	0.17
3	-8.44	-18.22	14.35	-58.21	-83.17	0.00	0.16
4	-3.32	-14.08	9.37	-32.39	-59.87	0.00	0.15
5	-0.04	-10.94	5.91	-15.20	-43.02	0.00	0.13
6	1.74	-8.56	3.67	-4.93	-31.24	0.00	0.12
7	2.70	-6.76	2.18	1.32	-22.83	0.00	0.11
8	22.57	22.57	-88.36	-71.10	-71.10	-354.37	0.19
9	1.60	1.59	-21.33	-49.96	-49.97	-108.51	0.18
10	10.32	10.32	-12.91	197.33	197.33	-39.95	0.18
11	21.43	21.43	-85.56	-1.45	-1.45	-6.91	0.18

TABLE 6. Response (Top Row) and Relative Error (Bottom Row in Parenthesis) Using Case 1 Backcalculated Layer Model

Point (1)	ε_x (μm/m) (2)	ε_y (μm/m) (3)	ε_z (μm/m) (4)	σ_x (kPa) (5)	σ_y (kPa) (6)	σ_z (kPa) (7)	u_z (mm) (8)
1	-57.10	-57.10	-61.13	-679.52	-679.52	-690.00	0.21
	(1.173)	(1.173)	(2.179)	(0.232)	(0.232)	(0.000)	(0.465)
2	-7.04	-26.87	18.26	-65.72	-117.21	0.00	0.17
	(0.592)	(0.788)	(0.505)	(1.501)	(1.021)	(0.000)	(0.223)
3	-8.34	-18.07	14.22	-58.59	-83.88	0.00	0.16
	(1.233)	(0.777)	(0.922)	(0.651)	(0.851)	(0.000)	(0.197)
4	-3.27	-13.96	9.28	-32.59	-60.34	0.00	0.15
	(1.408)	(0.854)	(0.960)	(0.610)	(0.794)	(0.000)	(0.186)
5	-0.04	-10.84	5.86	-15.32	-43.37	0.00	0.13
	(7.515)	(0.876)	(0.901)	(0.742)	(0.806)	(0.000)	(0.171)
6	1.72	-8.49	3.64	-4.99	-31.50	0.00	0.12
	(1.039)	(0.875)	(0.833)	(1.047)	(0.829)	(0.000)	(0.158)
7	2.67	-6.70	2.17	1.31	-23.03	0.00	0.11
	(1.054)	(0.865)	(0.739)	(0.722)	(0.858)	(0.000)	(0.146)
8	22.16	22.16	-86.76	-71.03	-71.03	-353.91	0.19
	(1.823)	(1.823)	(1.808)	(0.099)	(0.099)	(0.129)	(0.317)
9	**1.91**	**1.91**	-21.17	-47.60	-47.60	-107.55	0.18
	(19.686)	**(19.686)**	(0.742)	(4.722)	(4.722)	(0.879)	(0.241)
10	10.51	10.51	-13.14	197.19	197.19	-39.50	0.18
	(1.910)	(1.910)	(1.777)	(0.074)	(0.074)	(1.118)	(0.255)
11	21.56	21.56	-85.49	-1.42	-1.42	-6.90	0.18
	(0.611)	(0.611)	(0.089)	(1.720)	(1.720)	(0.248)	(0.264)

TABLE 7. Response (Top Row) and Relative Error (Bottom Row in Parenthesis) Using Case 2 Backcalculated Layer Model

Point (1)	ε_x (μm/m) (2)	ε_y (μm/m) (3)	ε_z (μm/m) (4)	σ_x (kPa) (5)	σ_y (kPa) (6)	σ_z (kPa) (7)	u_z (mm) (8)
1	-58.31 (0.930)	-58.31 (0.930)	-65.18 (4.306)	-672.90 (0.745)	-672.90 (0.745)	-690.00 (0.000)	0.21 (0.035)
2	-6.75 (3.632)	-27.02 (0.227)	18.18 (0.926)	-62.04 (4.186)	-112.48 (3.051)	0.00 (0.000)	0.17 (0.407)
3	-8.70 (3.091)	-18.23 (0.088)	14.50 (1.039)	-57.74 (0.802)	-81.45 (2.061)	0.00 (0.000)	0.16 (0.307)
4	-3.52 (6.211)	-14.17 (0.660)	9.53 (1.719)	-32.48 (0.265)	-58.97 (1.500)	0.00 (0.000)	0.15 (0.175)
5	**-0.17** **(300.543)**	-11.05 (1.009)	6.04 (2.154)	-15.45 (1.594)	-42.52 (1.180)	0.00 (0.000)	0.13 (0.052)
6	1.66 (4.465)	-8.67 (1.265)	3.77 (2.728)	-5.25 (6.419)	-30.96 (0.894)	0.00 (0.000)	0.12 (0.066)
7	2.66 (1.604)	-6.86 (1.484)	2.26 (3.539)	**0.98** **(25.332)**	-22.69 (0.620)	0.00 (0.000)	0.11 (0.180)
8	23.21 (2.829)	23.21 (2.829)	-91.06 (3.060)	-71.82 (1.021)	-71.82 (1.021)	-356.17 (0.509)	0.19 (0.302)
9	**0.30** **(81.365)**	**0.30** **(81.365)**	-21.15 (0.831)	**-58.94** **(17.970)**	**-58.94** **(17.970)**	-112.31 (3.509)	0.18 (0.468)
10	**9.17** **(11.155)**	**9.17** **(11.155)**	**-11.52** **(10.792)**	199.20 (0.945)	199.20 (0.945)	-41.63 (4.217)	0.18 (0.405)
11	20.15 (5.994)	20.15 (5.994)	-83.18 (2.781)	-1.52 (4.868)	-1.52 (4.868)	-6.77 (2.037)	0.18 (0.350)

TABLE 8. Response (Top Row) and Relative Error (Bottom Row in Parenthesis) Using Case 3 Backcalculated Layer Model

Point (1)	ε_x (μm/m) (2)	ε_y (μm/m) (3)	ε_z (μm/m) (4)	σ_x (kPa) (5)	σ_y (kPa) (6)	σ_z (kPa) (7)	u_z (mm) (8)
1	-55.76	-55.76	-57.53	-685.22	-685.22	-690.00	0.21
	(3.484)	(3.484)	(7.948)	(1.072)	(1.072)	(0.000)	(1.228)
2	-7.24	-26.58	18.21	-68.93	-121.30	0.00	0.17
	(3.401)	(1.870)	(0.787)	(6.460)	(4.548)	(0.000)	(0.380)
3	-8.02	-17.84	13.92	-59.42	-86.03	0.00	0.16
	(5.037)	(2.058)	(3.001)	(2.085)	(3.444)	(0.000)	(0.391)
4	-3.07	-13.71	9.04	-32.78	-61.61	0.00	0.15
	(7.473)	(2.602)	(3.532)	(1.229)	(2.914)	(0.000)	(0.457)
5	**-0.05**	-10.62	5.91/5.69	-15.28	-44.19	0.00	0.13
	(219.214)	(2.883)	(3.709)	(0.522)	(2.703)	(0.000)	(0.513)
6	1.75	-8.30	3.53	-4.81	-32.04	0.00	0.12
	(0.508)	(3.054)	(3.963)	(2.409)	(2.539)	(0.000)	(0.568)
7	2.66	-6.54	2.09	**1.55**	-23.38	0.00	0.11
	(1.470)	(3.182)	(4.322)	**(17.314)**	(2.398)	(0.000)	(0.621)
8	21.21	21.21	-82.83	-70.20	-70.20	-352.01	0.19
	(6.017)	(6.017)	(6.256)	(1.260)	(1.260)	(0.665)	(0.669)
9	**3.29**	**3.29**	-21.23	**-37.34**	**-37.34**	-103.77	0.18
	(106.255)	**(106.255)**	(0.479)	**(25.253)**	**(25.253)**	(4.370)	(0.394)
10	**11.58**	**11.58**	**-14.42**	195.01	195.01	-37.85	0.18
	(12.266)	**(12.266)**	**(11.683)**	(1.178)	(1.178)	(5.251)	(0.473)
11	22.58	22.58	-86.86	-1.34	-1.34	-6.97	0.18
	(5.388)	(5.388)	(1.516)	(7.540)	(7.540)	(0.797)	(0.533)

TABLE 9. Response (Top Row) and Relative Error (Bottom Row in Parenthesis) Using Case 4 Backcalculated Layer Model

Point (1)	ε_x (μm/m) (2)	ε_y (μm/m) (3)	ε_z (μm/m) (4)	σ_x (kPa) (5)	σ_y (kPa) (6)	σ_z (kPa) (7)	u_z (mm) (8)
1	-58.46 (1.195)	-58.46 (1.195)	-63.09 (0.951)	-678.32 (0.055)	-678.32 (0.055)	-690.00 (0.000)	0.22 (0.860)
2	-7.08 (1.125)	-27.42 (1.238)	18.58 (1.215)	-67.82 (0.116)	-116.20 (0.155)	0.00 (0.000)	0.17 (0.790)
3	-8.48 (0.480)	-18.42 (1.114)	14.48 (0.913)	-58.02 (0.316)	-83.13 (0.046)	0.00 (0.000)	0.16 (0.730)
4	-3.30 (0.460)	-14.22 (0.985)	9.43 (0.709)	-32.18 (0.662)	-59.75 (0.196)	0.00 (0.000)	0.15 (0.671)
5	**0.00** **(100.104)**	-11.03 (0.881)	5.94 (0.495)	-15.01 (1.273)	-42.89 (0.324)	0.00 (0.000)	0.13 (0.614)
6	1.79 (3.007)	-8.63 (0.788)	3.68 (0.221)	-4.77 (3.326)	-31.10 (0.450)	0.00 (0.000)	0.12 (0.557)
7	2.75 (1.993)	-6.80 (0.700)	2.18 (0.161)	1.45 (9.928)	-22.70 (0.577)	0.00 (0.000)	0.11 (0.504)
8	22.84 (1.163)	22.84 (1.163)	-89.29 (1.051)	-70.86 (0.327)	-70.86 (0.327)	-354.14 (0.064)	0.20 (0.841)
9	**1.79** **(12.346)**	**1.79** **(12.346)**	-21.67 (1.604)	-48.76 (2.392)	-48.76 (2.392)	-108.05 (0.417)	0.19 (0.826)
10	10.60 (2.766)	10.60 (2.766)	-13.27 (2.757)	196.66 (0.342)	196.66 (0.342)	-39.78 (0.415)	0.18 (0.816)
11	21.88 (2.097)	21.88 (2.097)	-86.87 (1.524)	-1.45 (0.222)	-1.45 (0.222)	-6.98 (0.968)	0.18 (0.805)

TABLE 10. Response (Top Row) and Relative Error (Bottom Row in Parenthesis) Using Case 5 Backcalculated Layer Model

Point (1)	ε_x (μm/m) (2)	ε_y (μm/m) (3)	ε_z (μm/m) (4)	σ_x (kPa) (5)	σ_y (kPa) (6)	σ_z (kPa) (7)	u_z (mm) (8)
1	-55.77 (3.472)	-55.77 (3.472)	-57.50 (7.988)	-685.30 (1.085)	-685.30 (1.085)	-690.00 (0.000)	0.21 (1.367)
2	-7.23 (3.321)	-26.58 (1.857)	18.21 (0.793)	-68.92 (6.448)	-121.33 (4.570)	0.00 (0.000)	0.17 (0.553)
3	-7.99 (5.284)	-17.83 (2.091)	13.91 (3.102)	-59.33 (1.936)	-85.99 (3.394)	0.00 (0.000)	0.16 (0.588)
4	-3.05 (8.057)	-13.70 (2.679)	9.02 (3.705)	-32.70 (0.946)	-61.55 (2.807)	0.00 (0.000)	0.14 (0.677)
5	**0.07** **(256.180)**	-10.61 (2.996)	5.68 (3.964)	-15.20 (0.007)	-44.12 (2.545)	0.00 (0.000)	0.13 (0.755)
6	1.76 (1.183)	-8.29 (3.202)	3.51 (4.321)	-4.75 (3.761)	-31.97 (2.331)	0.00 (0.000)	0.12 (0.832)
7	2.67 (1.168)	-6.53 (3.363)	2.08 (4.825)	**1.60** **(21.260)**	-23.32 (2.138)	0.00 (0.000)	0.11 (0.906)
8	21.22 (5.981)	21.22 (5.981)	-82.82 (6.270)	-70.10 (1.401)	-70.10 (1.401)	-351.94 (0.685)	0.19 (0.820)
9	**3.35** **(109.897)**	**3.35** **(109.897)**	-21.27 (0.299)	**-36.94** **(26.065)**	**-36.94** **(26.065)**	-103.63 (4.495)	0.18 (0.554)
10	**11.63** **(12.772)**	**11.63** **(12.772)**	**-14.49** **(12.191)**	194.73 (1.320)	194.73 (1.320)	-37.81 (5.352)	0.18 (0.636)
11	22.64 (5.667)	22.64 (5.667)	-86.94 (1.614)	-1.34 (7.575)	-1.34 (7.575)	-7.00 (1.180)	0.18 (0.700)

In **Tables 5** through **10**, values without parentheses are the pavement responses using the backcalculated moduli in **Table 2** (Cases 1 to 5) while values in parentheses are the relative errors compared to responses using the original (exact) pavement profile. Cells that are highlighted with gray show the response with a relative error higher than 2% whilst values in bold show the response with a relative error higher than 10%.

The results in **Tables 3**, and **5** through **9** show that even if the RMSE value is kept less than 1%, the resulting response of strains and stresses can largely differ than the exact response. Cases 1 and 2 (**Tables 6** and **7**, respectively) have relatively the same RMSE in deflection but have different relative errors in strains and stresses. In addition, the magnitude and location of the relative errors vary randomly between Cases 1 and 2. Case 1 showed a relative error of 19.686% in the horizontal strain (ε_x, or ε_y) at the bottom of the AC layer (point 9) while Case 2 showed a higher relative error of 81.365% in the horizontal strain at the same point. On the other hand, at the ground surface (point 5), Case 2 showed a relative error of 300.543% in the horizontal strain which is approximately 40 times the relative error of the horizontal strain at the same point in Case 5 (7.515%). The relative error in Case 1 was higher than 2% in 9.1% of the response points and higher than 10% in 3% of the response points; in Case 2 the relative error was higher than 2% in 48.9% of the response points and higher than 10% in 13.6% of the response points, all indicating a random variation in the error. This high variation in the strain and stress errors can be explained by high relative error of the backcalculated elastic moduli in Case 2 as compared to that in Case 1 (**Table 3**).

Similar random variation in the relative error can be also observed at a higher RMSE for Cases 3 and 4 as shown in **Tables 8** and **9** respectively where the RMSE was almost the same (less than 1%). However, the relative error in Case 3 was higher than 2% in 65.2% of the response points and higher than 10% in 13.6% of the response points while in Case 4 the relative error was higher than 2% in 19.7% of the response points and higher than 10% in 4.5% of the response points, indicating again a random variation in the error. Similarly, the high variation in the strain and stress errors was attributed to the high variation in the relative error of the backcalculated elastic moduli rather than the RMSE values.

Comparing Cases 3 and 5 (**Tables 8** and **10**) one can observe different RMSE values but similar relative errors in the backcalculated elastic moduli. Furthermore, in both cases the magnitude and location of the relative error in the strains and stresses were nearly identical. This finding shows that controlling the RMSE does not necessarily reduce the relative error associated with the pavement response (strains and stresses) at either the surface or along the pavement profile. This would require a better control of the backcalculated moduli. However, controlling the error associated with the backcalculated elastic modulus is not an easy task since the exact modulus is not known. Even with known elastic moduli from lab testing, the variation between the backcalculated and exact moduli can be high. The difference between backcalculated subgrade elastic moduli from the FWD and laboratory elastic moduli has been studied by many researchers (Daleiden et *al.* 1994; Von Quintus and Killingworth 1997). It was found that there is no unique relation between the backcalculated and laboratory measured resilient moduli. The ASSHTO Guide (1993) suggested that the backcalculated modulus is three times the laboratory modulus, whilst Von Quintus and Killingworth (1997) suggested that one could use some correction factors calculated from any multilayered elastic program to match the backcalculated and laboratory moduli. However, the suggested factors are highly dependent on the backcalculation program and should be used with caution. On the other hand, Stolle (2002) showed that the moduli of the base and subgrade layers have the largest contribution to the measured FWD deflection.

It should be noted that in all cases the effect of the backcalculated moduli on the vertical stress (σ_z) was relatively small as compared to their effect on the horizontal strains, vertical strains, and horizontal stresses.

PAVEMENT FATIGUE PREDICTION

The damage of flexible pavements can be assessed by predicting the number of loads needed to initiate cracks (fatigue cracking). The Shell Model (Bonnaure et *al.* 1980) and the Asphalt Institute Model (Shook et *al.* 1982) are frequently used for fatigue cracking in flexible pavements.

The Shell Model is based on two different loading modes, as given by **Eqs. 3** and **4**, below:

Shell Constant Strain Model:

$$N_{\epsilon} = 13909 A_f K \left(\frac{1}{\epsilon_t}\right)^5 E_s^{-1.8} \tag{3}$$

and Shell Constant Stress Model:

$$N_{\sigma} = A_f K \left(\frac{1}{\epsilon_t}\right)^5 E_s^{-1.4} \tag{4}$$

where N_ε and N_σ are the number of load repetitions to fatigue cracking using the constant strain and constant stress analysis, respectively, A_f and K are material constants, ε_t is the tensile strain at the critical location and E_s is the stiffness of the material (i.e. elastic modulus). The constant strain model is applicable to thin AC layers usually less than 51 mm, whilst the constant stress model is applicable to thick AC layers usually more than 203 mm. The Shell Model was calibrated and generalized for any thickness as given below (MEPDG, 2004):

$$N_f = A_f K F'' \left(\frac{1}{\epsilon_t}\right)^5 E_s^{-1.4} \tag{5}$$

where N_f is the number of load repetitions to fatigue cracking, and F'' is a constant that depends on the layer thickness and the material stiffness.

The Asphalt Institute Model is given below:

$$N_f = 0.00432 C \left(\frac{1}{\epsilon_t}\right)^{3.291} \left(\frac{1}{E_s}\right)^{0.854} \tag{6}$$

where, similarly, N_f is the number of load repetitions to fatigue cracking, C is a material constant, ε_t is the tensile strain at the critical location, and again E_s is the material stiffness. The Asphalt Institute Model can be used for any thickness.

It can be seen from the above equations that the critical tensile strain and the stiffness of the AC layer are the main factors affecting the number of load repetitions needed to initiate fatigue failure. The effect of the backcalculated set of elastic moduli on the fatigue in flexible pavements can be studied by finding the ratio between the estimated number of repeated loads (N_f) using the backcalculated set of elastic moduli and that using the exact set of elastic moduli. In other words, the ratio is equal to N_{fb} (backcalculated set of elastic moduli) over N_{fe} (exact set of elastic moduli).

RUTTING DAMAGE

Rutting in flexible pavement is considered as a functional deterioration. Rutting is mainly predicted by calculating the vertical strains at the top of the subgrade and then estimating the allowable load repetitions until a certain rutting threshold is met. For example, Shook et *al.* (1982) assumed a rutting depth of 10 mm in their method, while Potter and Donald (1985) assumed 20-30 mm rutting depth.

Recently, the results from the test sections at MnROAD were used to develop a method to predict the number of allowable load repetitions until rutting failure using a rut depth of 13 mm as shown in the following relation (Skok et *al.*, 2003):

$$N_r = (5.5).10^{15}\left(\frac{1}{\epsilon_v}\right)^{3.929} \tag{7}$$

where N_r is the number of allowable load repetitions until rutting failure, and ε_v is the maximum compressive strain at the top of the subgrade layer.

It can be seen, from the above equation, that the vertical strain at the top of the subgrade layer is very important to predict the lifetime of the pavement due to rutting. Similar to the fatigue case, the effect of the backcalculated elastic moduli on the rutting can be studied by finding the ratio between the estimated number of repeated loads (N_r) using the backcalculated set of elastic moduli and that using the exact set of elastic moduli. In other words, the ratio is equal to N_{rb} (backcalculated set of elastic moduli) over N_{re} (exact set of elastic moduli).

FATIGUE AND RUTTING PREDICTION

The fatigue and rutting of the pavement are studied for the five cases as summarized in **Tables 1** and **2**, and the results are listed in **Table 11**. It is observed from **Table 11** that, for all cases except Case 2, using either the Shell Model or the Asphalt Institute Model, the fatigue life will be largely underestimated based on the backcalculated moduli as compared to those based on the exact moduli. Furthermore, comparing Case 2 to Case 1 it can be seen that even for the same RMSE the predicted number of repeated loads for fatigue can be largely overestimated rather than underestimated. The fatigue prediction results in **Table 11** also show that even for a small relative error (less than 2.1% in Case 1) in the backcalculated set of elastic moduli the fatigue life of the pavement can be underestimated by 60% using the Shell model and by 45% using the Asphalt Institute Model, indicating a very high sensitivity of the fatigue life to the relative error in elastic moduli rather than the RMSE.

TABLE 11. Comparison of Fatigue Life Using Backcalculated and Exact Pavement Moduli

Case (1)	N_{fb}/N_{fe} Shell (2)	N_{fb}/N_{fe} Asphalt Institute (3)	RMSE (%) (4)
Case 1	0.407	0.554	0.24
Case 2	4449.469	251.951	0.22
Case 3	0.027	0.092	0.65
Case 4	0.559	0.682	0.69
Case 5	0.025	0.087	0.85

The effect of the RMSE value and the relative error in pavement moduli on rutting can be observed from **Table 12**. It can be seen that even for a very small RMSE (Cases 1 and 2 where the RMSE is 0.22% and 0.24%, respectively), the rutting failure prediction based on the backcalculated moduli was overestimated by 11.7% in Case 2 while it was overestimated by 0.3% in Case 1, indicating a high sensitivity of the rutting life on the relative error in moduli. In addition, the results show that as the RMSE (error) increases, the underestimation of the rutting increases, as can be observed by comparing the rutting results in **Table 12** for Cases 2 to 5.

TABLE 12. Comparison of Rutting Failure Using Backcalculated and Exact Pavement Moduli

Case (1)	N_{rb}/N_{re} (2)	RMSE (%) (3)
Case 1	1.003	0.24
Case 2	1.117	0.22
Case 3	0.943	0.65
Case 4	0.942	0.69
Case 5	0.939	0.85

CONCLUSIONS

This study shows that the use of the RMSE is not enough to secure an accurate backcalculation of the pavement elastic moduli. Large discrepancies can exist in the predicted pavement strains and stresses using the backcalculated and exact elastic moduli. As a result, even a RMSE value less than 1% can significantly affects the fatigue and rutting predictions in flexible pavements.

The effect of the RMSE is suitable for controlling the fitness of the backcalculated deflection basin to that measured in the field while the use of the relative error in the elastic moduli is more appropriate. However, the availability of laboratory measured elastic moduli does not guarantee more appropriate backcalculated elastic moduli. This variation adds more uncertainty when dealing with data from the FWD test, and should be the future endeavor in pavement engineering.

ACKNOWLEDGEMENT

We are grateful for the support by ODOT/FHWA under grant ODOT 20943.

REFERENCES

Anderson, M. (1988). "Backcalculation of composite pavement layer moduli." PhD dissertation, The University of Kentucky, Kentucky.

Bonnaure, F., Gest, G., Gravois, A. and Uge, P. (1977). "A new method of predicting the stiffness of asphalt paving mixtures." *Proceedings of the Association of Asphalt Paving Technologists*, 46, 64–100.

Bonnaure, F., Gravois, A., and Udron, J. (1980). "A new method of predicting the fatigue life of bituminous mixes." *Journal of the Association of Asphalt Paving Technologist*, 49, 499-529.

Cho, Y.S., and Lin, F.B. (2001). "Spectral analysis of surface wave response of multi-layer thin cement mortar slab structures with finite thickness." *NDT and E International*, 34, 115–122.

Daleiden, J.F., Killingsworth, B.M., Simpson, A.L., and Zamora, R.A. (1994). "Analysis of procedures for establishing in situ subgrade moduli." *Transportation Research Record 1462,* TRB, National Research Council, Washington, D.C., 102-107.

Fwa, T.F., and Rani, T.S. (2005). "Seed modulus generation algorithm for backcalculation of flexible pavement moduli." *Transportation Research Record 1905*, TRB, National Research Council, Washington, D.C., 117-127.

Fwa, T.F., C. Y. Tan, and Chan, W. T. (1997). "Backcalculation analysis of pavement-layer moduli using genetic algorithms." *Transportation Research Record 1905*, TRB, National Research Council, Washington, D.C., 134-142.

Harichandran, R. S., Ramon, C. M., and Baladi, G. Y. (1994). "MICHBACK user's manual." Department of Civil and Environmental Engineering, Michigan State University, East Lansing, Michigan.

Mehta, Y., and Roque, R. (2003). "Evaluation of FWD data for determination of layer moduli of pavements." *Journal of Materials in Civil Engineering* ,ASCE, 15(1), 25-31.

MEPDG, National Research Council (2004). "Guide for mechanistic-empirical design (MEPDG)." National Cooperative Highway Research Program (NCHRP).

Pan, E. (1989a). "Static response of a transversely isotropic and layered half-space to general dislocation sources." *Phys. Earth Planet. Inter.*, 58, 103-117.

Pan, E. (1989b). "Response of a transversely isotropic and layered half-space to general surface loads." *Phys. Earth Planet. Inter.*, 54, 353-363.

Pan, E. (1990). "Thermoelastic deformation of a transversely isotropic and layered half-space by surface loads and internal sources." *Phys. Earth Planet. Inter.*, 60, 254-264.

Pan, E. (1997). "Static Green's functions in multilayered half-spaces." *Applied Mathematical Modeling*, 21, 509-521.

Potter, D.W, and Donald, G.S. (1985). "Revision of the NAASRA interim guide to pavement thickness design." *Australian Road Research,* Technical Note 2, 15(2).

Skok, E.L., Clyne, T.R., Johnson, E., Timm, D.H., and Brown, M.L. (2003). "Best practices for the design and construction of low volume roads revised." *Report No. MN/RC-2002-17REV*, Minnesota Department of Transportation Research Services Section, Minnesota.

Shook, J. F., Finn, F. N., Witczak, M. W., and Monismith, C. L. (1982). "Thickness design of asphalt pavements – the asphalt institute method." *Fifth International Conference on the Structural Design of Asphalt Pavements*, 1, 17-44.

Stolle, D. (2002). "Pavement displacement sensitivity to layer moduli." *Canadian Geotechnical Journal*, 39, 1395-1398.

Von Quintus, H.L. and Killingsworth, B. (1997). "Design pamphlet for the backcalculation of pavement layer moduli in support of the 1993 AASHTO Guide for the Design of Pavement Structures." *Publication No. FHWA-RD-97-076*, Federal Highway Administration, Washington, D.C.

Von Quintus, H.L., and Simpson, A.,L. (2002). "Backcalculation of layer parameters for LTPP test sections volume II: layered elastic analysis for flexible and rigid pavements." *Report No. FHWA-RD-01-113*, Federal Highway Administration, Washington, D.C.

Considerations for Nonlinear Analyses of Pavement Foundation Geomaterials in the Finite Element Modeling of Flexible Pavements

Erol Tutumluer[1], Member, ASCE and Minkwan Kim[2]

ABSTACT: Flexible pavements are commonly used for low to high volume roads subjected to many wheel load applications and also for airfields subjected to rather heavy aircraft gear/wheel loads. As the demand for applied wheel loads and number of load applications increase, it becomes very important to properly characterize the behavior of unbound aggregate layers and subgrade soils as the pavement foundation geomaterials. Laboratory studies have shown that resilient responses for these geomaterials follow nonlinear, stress-dependent behavior under repeated loading. Therefore, a finite element (FE) type layered elastic analysis is needed to employ nonlinear resilient material models to predict accurate pavement responses for mechanistic based pavement design. In this study, modulus models well proven over the years to adequately describe the nonlinear pavement geomaterial behavior were programmed in a user material subroutine (UMAT) to perform axisymmetric and three-dimensional (3D) analyses using the general-purpose ABAQUS FE program. The results indicated that modulus characterizations of the nonlinear, stress-dependent base and subgrade layers were essentially needed to reliably predict accurate pavement responses both in axisymmetric and 3D analyses.

Introduction

The various layers of pavement structure have different properties to affect pavement response and overall performance. As the demand for heavier wheel loads and number of load applications increase, nowadays, it becomes even more important to properly characterize the mechanistic response behavior of the unbound granular and subgrade soil layers as the foundation geomaterials of the pavement structure. As properly documented in numerous studies, pavement foundation geomaterials follow nonlinear, stress-dependent modulus characteristics under repeated traffic loading (Brown and Pappin 1981, Thompson and Elliot 1985). Unbound aggregates often

---

[1] Associate Professor, PH (217) 333-8637; email: tutumlue@uiuc.edu
[2] Graduate Research Assistant, PH (217) 333-6973; email: mkim8@uiuc.edu
Department of Civil and Environmental Engineering, University of Illinois, 205 N. Mathews, Urbana, IL 61801, USA; FAX (217) 333-1924.

used in base/subbase layers exhibit stress-hardening, whereas, fine-grained soils for subgrade show stress-softening type behavior. The pavement stiffness characterized by resilient modulus (M_R) is therefore not a constant but a function of the applied stresses in that layer.

Due to its ability to incorporate advanced material characterization models to predict more accurately the load induced responses, finite element (FE) based structural analysis has been the main mechanistic approach for analyzing flexible pavements. Several well known axisymmetric pavement FE analysis programs already consider the nonlinear pavement foundation geomaterial behavior such as ILLI-PAVE (Raad and Figueroa 1980) and GT-PAVE (Tutumluer 1995). General-purpose FE programs, such as ABAQUS and ADINA, have also been used for analyzing pavements (Chen et al. 1995, Cho et al. 1996, Taciroglu 1998, and Saad et al. 2005). However, most of these FE solutions by general-purpose FE programs did not properly consider such stress-dependencies of the pavement layer moduli.

The objective of this study is to develop a way to employ proper material characterizations in general-purpose FE analyses and examine effects of geomaterial nonlinearity on pavement response predictions. Results obtained from both axisymmetric and three-dimensional (3D) nonlinear analyses are compared. Implications of the nonlinear, stress-dependent geomaterial modulus characterizations are also investigated in relation to 3D considerations in pavement analysis.

Nonlinear Stress-dependent Models

After construction and shakedown of pavement materials with initial traffic loading, the permanent deformation accumulation per each cycle decreases to a minimum. Under the repeated application of wheel loads, most of the pavement deformations are then recoverable and thus considered elastic. It has been customary to use resilient modulus for the elastic stiffness of the pavement materials. This stiffness associated with the resilient response is the resilient modulus (M_R) defined by

$$M_R = \frac{\sigma_d}{\epsilon_r} \tag{1}$$

where deviator stress $\sigma_d = \sigma_1 - \sigma_3$ and ϵ_r is recoverable strain.

For unbound aggregate layers, M_R is mainly dependent on the bulk and dynamic wheel load (deviator) stresses. The following Uzan (1985) model properly captures this dependency of the modulus on stress states as follows:

$$M_R = K_1 \left(\frac{\theta}{p_o}\right)^{K_2} \left(\frac{\sigma_d}{p_o}\right)^{K_3} \tag{2}$$

where bulk stress $\theta = \sigma_1 + \sigma_2 + \sigma_3 = \sigma_1 + 2\sigma_3$ (when $\sigma_2 = \sigma_3$), p_0 is a unit pressure (1 kPa or psi), and K_1, K_2, and K_3 are model parameters obtained from triaxial test data.

For both the nonlinear axisymmetric and 3D FE analyses performed in this study, stress states applied in the laboratory triaxial conditions ($\sigma_2 = \sigma_3$) were essentially used to determine model parameters.

For fine-grained subgrade soils, the resilient modulus is also dependent upon the applied stress state. Typically, soil moduli follow a stress-softening type behavior and the bilinear model proposed by Thompson and Robnett (1979) is one of the most commonly used M_R models to simply capture this behavior. The bilinear M_R model which is primarily a function of the deviator stress is given as follows:

$$\begin{aligned} M_R &= K_1 + K_3 \times (K_2 - \sigma_d) \text{ when } \sigma_d \leq K_2 \\ M_R &= K_1 - K_4 \times (\sigma_d - K_2) \text{ when } \sigma_d \geq K_2 \end{aligned} \tag{3}$$

where K_1, K_2, K_3, and K_4 are model parameters obtained from triaxial test data. Representing the bilinear behavior, parameter K_1 is referred to as the breakpoint modulus E_{Ri}, which is a characteristic soil property.

Pavement Section Domain Study for FE Models

The pavement structure extends to infinity in the horizontal and vertical direction. For this reason, it is important to choose a domain size that gives the most accurate pavement responses in FE analysis. According to Duncan et al. (1968), to obtain the reasonable responses of FE analysis, it was necessary to move the fixed boundary to a depth of 50-times radius of circular loading area (R) and move the roller boundary at the horizontal distance of 12-times R from center.

In this study, an axisymmetric FE model was generated to determine an appropriate domain size for predicting accurate pavement responses. This pavement section domain was modeled using axisymmetric finite elements truncated far away from the centerline of loading to get favorable results of the KENLAYER program (Huang, 2004). The three-layered pavement geometry and the material properties used are shown in Table 1 and Figure 1(a).

Table 1. Material Properties used in the Axisymmetric FE Modeling

Layer	Element	Thickness (mm)	E, M_R (MPa)	ν	Material Properties
AC	8-noded quadrilateral	76	2,758	0.35	Isotropic and Linear Elastic
Base	8-noded quadrilateral	305	207	0.40	Isotropic and Linear Elastic
Subgrade	8-noded quadrilateral	20,955	41	0.45	Isotropic and Linear Elastic

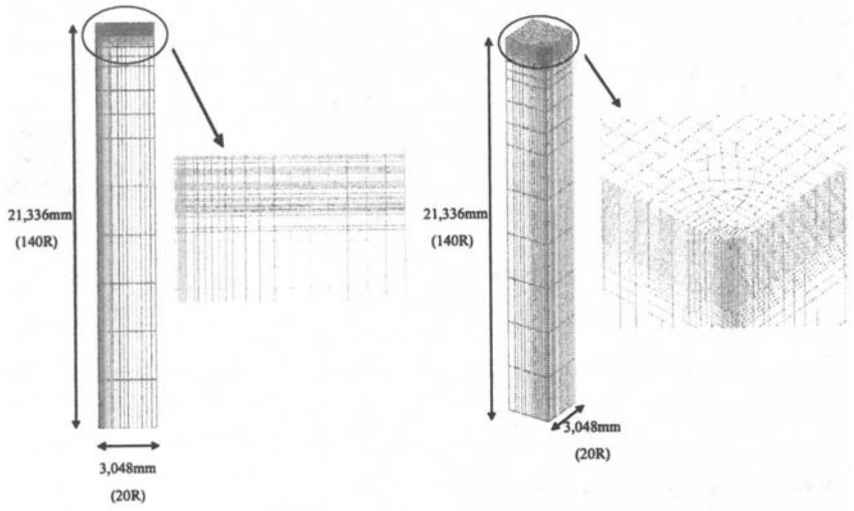

(a) Axisymmetric model (b) 3D model

Figure 1. Axisymmetric and 3D FE Models

The load was applied as a uniform pressure of 0.55 MPa over a circular area of 152 mm radius. Figure 1(a) shows the axisymmetric FE mesh for the selected domain size of 20-times R in the horizontal direction and 140-times R in the vertical direction. Using this mesh, the predicted pavement responses were in very good agreement with those of the KENLAYER closed form solutions as listed in Table 2.

Table 2. Predicted Critical Pavement Responses for the Analysis Domain Study

	Linear Elastic Analysis	
Pavement response	KENLAYER	ABAQUS with 8-noded quadrilateral elements
δ_{surface} (mm)	-0.927	-0.930
$\sigma_{r\ \text{bottom of AC}}$ (MPa)	0.777	0.773
$\sigma_{v\ \text{top of subgrade}}$ (MPa)	-0.041	-0.041
$\varepsilon_{v\ \text{top of subgrade}}$ ($\mu\varepsilon$)	-936	-933

For the 3D FE model, the same pavement geometry and the input properties listed in Table 1 were again considered this time using the 20-noded solid element instead of 8-noded quadrilateral elements. The developed 3D FE mesh is shown in Figure 1(b) for the same domain size of 20-times R in the horizontal direction and 140-times R in the vertical direction. The boundary conditions at the vertical boundary and symmetry planes were assigned zero horizontal displacements together with a restraint condition of zero horizontal and vertical displacements on the bottom plane. A fine FE mesh was generated in the vicinity of wheel loading to apply an accurate representation of the circular shape loading and capture the steep stress and strain gradients.

Before performing nonlinear FE analysis, the linear elastic solutions were compared from the ABAQUS axisymmetric and 3D models to evaluate differences between the two pavement models. Table 3 lists predicted critical pavement responses from the two analyses. Overall, the differences were negligible and the largest difference was not more than 3% for the surface deflection. The other responses, such as tensile stresses at bottom of asphalt concrete (AC) and vertical stresses on top of subgrade, had differences less than 1%. Generally, these comparisons between the axisymmetric and the 3D analyses are quite acceptable especially when considering the assumptions for the axisymmetric FE formulations and the circular shaped mesh discretization representing the wheel loading. Therefore, the developed 3D pavement FE model was considered accurate enough to study next the nonlinear pavement foundation considerations.

Table 3. Predicted Pavement Responses between Axisymmetric and 3D Analyses

Pavement response	Linear Elastic Analysis*		
	Axisymmetric model	3D model	Difference (%)
δ_{surface} (mm)	-0.930	-0.909	2.26
$\sigma_{r\ \text{bottom of AC}}$ (MPa)	0.773	0.770	0.39
$\sigma_{v\ \text{top of subgrade}}$(MPa)	-0.041	-0.040	2.44
$\varepsilon_{v\ \text{top of subgrade}}$ ($\mu\varepsilon$)	-933	-930	0.32

* Negative is compression

Previous Pavement Studies using General-purpose FE Programs

ABAQUS, ANSYS, and ADINA are the most commonly used general-purpose FE programs which can provide proper analyses for various engineering problems. Several researchers have already performed linear and/or nonlinear pavement analyses using these general-purpose FE programs. Chen et al. (1995) and Cho et al. (1996) conducted a comprehensive study of various FE pavement analyses. The results from ABAQUS were comparable to those from other pavement analysis programs, such as ILLI-PAVE (Raad and Figueroa 1980), GT-PAVE (Tutumluer 1995), and KENLAYER (Huang 2004), and the results yielded the lowest tensile strains for the linear analysis case. Three types of ABAQUS FE models, i.e., plane strain, axisymmetric, and 3D, were evaluated to facilitate the selection of appropriate modeling and corresponding element types for simulating traffic loading effects. They concluded that the axisymmetric and 3D FE models yielded different results for pavement responses.

Taciroglu (1998) solved for the pavement responses using 3D ABAQUS analysis and adopted the K-θ model (Hicks and Monismith 1971) and the Uzan (1985) model as the nonlinear unbound granular material M_R models. The ABAQUS user material (UMAT) subroutine was formulated to incorporate mainly strain dependent modulus models for the unbound aggregates. The nonlinear resilient behavior of granular materials were adequately modeled and but the solutions often predicted high asphalt bending stresses, and substantially different granular base stresses and strains were obtained from the nonlinear model.

The ABAQUS FE program was also used for pavement analysis by Schwartz (2002) who employed the K-θ model (Hicks and Monismith 1971) in the base course by using this time the "*HYPOELASTIC material model" inputs in the ABAQUS 3D modeling framework. The secant resilient modulus values could not be directly used in nonlinear solutions but were numerically converted to tangent moduli for input as a function of the first stress invariant, I_1. A tension cut-off was also imposed by specifying a very small modulus for tensile I_1 values. Comparing the linear and nonlinear solutions, Schwartz (2002) reported that there were up to 25% and 20% differences between the maximum asphalt tensile stresses and strains, respectively, for the most extreme case and less than 5% differences of stresses and strains at the top of the subgrade and surface deflection. He also noted that these differences would seem acceptable for practical design.

Recently, Saad et al. (2005) examined the dynamic responses of flexible pavement structures to single wheel traffic loads using the 3D FE analysis program ADINA. Their study focused on elastoplastic analyses different than the pavement resilient behavior. The base material was dealt with elastoplastic Drucker-Prager model as a strong or weak base and the subgrade was simulated by the modified CamClay model. Elastoplasticity of the base material caused an increase of 46% in the rutting strain, 28% in the maximum tensile fatigue strain on the bottom of the asphalt layer, and 30% in the maximum surface deflection. The subgrade nonlinearity had little impact on the fatigue strain which was less than 1%.

Nonlinear Material Subroutine for the ABAQUS Program

ABAQUS (2005) FE program allows for defining any complex constitutive model by specifying user customized material inputs via the user defined material subroutine (UMAT) interface. In this study, the UMAT subroutine was programmed to facilitate a direct secant modulus iterative approach for the nonlinear solution of the pavement foundation geomaterials using the computed stress states. In each iteration, this subroutine was the called at every material integration point to update the stresses and state variables. The material Jacobian matix (C) of the constitutive model is defined in the following form:

$$C = \frac{\partial \Delta \sigma}{\partial \Delta \varepsilon} \tag{4}$$

where $\Delta\sigma$ is the increment in Cauchy stress and $\Delta\varepsilon$ is the increment in strain.

The Young's modulus (E) was replaced by the resilient modulus (M_R) and the generalized Hooke's law was used for stress computation as follows:

$$\sigma_{ij} = \frac{vE}{(1+v)(1-2v)}\epsilon_{kk}\delta_{ij} + \frac{E}{1+v}\epsilon_{ij} = \frac{vM_R}{(1+v)(1-2v)}\epsilon_{kk}\delta_{ij} + \frac{M_R}{1+v}\epsilon_{ij} \tag{5}$$

where σ_{ij} is the stress tensor, v is Poisson's ratio, E is the Young's modulus, ϵ_{kk} is the volumetric strain, δ_{ij} is Kronecker delta, and ϵ_{ij} is the strain tensor.

Generally, when constitutive properties were updated at the integration points within each element, the element stiffness matrix, K^e, was computed using the constitutive relation matrix D.

$$K^e = \int B^T D B \, dv \tag{6}$$

where B is the strain-displacement matrix.

To properly account for the granular material and fine-grained soil types, the Uzan (1985) model and the bilinear model were used, respectively. The constitutive relation matrix D was varied throughout the element in accordance with the elastic stiffness formulation. In other words, matrix D was formed as follows:

$$D = \frac{M_R}{(1+v)(1-2v)} \begin{bmatrix} 1-v & v & v & 0 & 0 & 0 \\ v & 1-v & v & 0 & 0 & 0 \\ v & v & 1-v & 0 & 0 & 0 \\ 0 & 0 & 0 & \frac{1-2v}{2} & 0 & 0 \\ 0 & 0 & 0 & 0 & \frac{1-2v}{2} & 0 \\ 0 & 0 & 0 & 0 & 0 & \frac{1-2v}{2} \end{bmatrix} \tag{7}$$

The nonlinear iterations were performed using the appropriate M_R model to calculate the resilient modulus corresponding to the computed stress state at that integration point. Due to the nature of the stress-dependent M_R models used, an iterative procedure which considered a direct secant stiffness approach was found to be necessary in the analysis with an incremental loading scheme (Tutumluer, 1995). This method is less complicated than other nonlinear solution techniques, but it is sophisticated enough to give good convergence of the iterations to determine resilient modulus of pavement foundation geomaterials. In fact, this is the only approach that worked with guaranteed convergence using a modulus averaging scheme as follows:

$$M_R^j = (1-\lambda)M_R^{j-1} + \lambda M_{R\,model}^j \tag{8}$$

where M_R^j is the new M_R to be used at the end of iteration number j, λ is called an averaging or damping factor taking values between 0.0 and 1.0, M_R^{j-1} is M_R used at the end of iteration number (j-1), and $M_{R\,model}^j$ is M_R computed from the model at the end of iteration number j. To force convergence in the nonlinear iterations, the damping factor λ often needs to be assigned values less than 0.3. The cumulative error of 0.2% within two iterations and the maximum 5% difference between the old and new values of the resilient moduli usually controlled the convergence of nonlinear solutions. The developed UMAT material model subroutine was validated with the GT-PAVE axisymmetric FE program used specifically for pavement analysis (Kim and Tutumluer, 2006).

Nonlinear Pavement Analysis Results

Axisymmetric Nonlinear FE Analysis First the axisymmetric ABAQUS model was used to analyze the pavement section selected for the domain study (see Figure 1a) with nonlinear pavement geomaterial characterizations. The Uzan and the bilinear subgrade M_R models (Equations 2 and 3) were employed in the granular base and subgrade soil layers. Table 4 lists the pavement geometry and the assigned model parameters and material input properties. A uniform pressure of 0.55 MPa was applied over the circular area with a radius of 152 mm. Pavement responses were predicted for the following pavement layer material characterizations with the linear elastic AC layer: (1) nonlinear base and linear subgrade, (2) linear base and nonlinear subgrade, and (3) nonlinear base and nonlinear subgrade.

Table 4. Pavement Geometry and Material Properties for Nonlinear Analyses

<table>
<tr><th>Layer</th><th>Element</th><th>Thickness (mm)</th><th>E (MPa)</th><th>ν</th><th colspan="6">Material Properties</th></tr>
<tr><td>AC</td><td>8-noded quadrilateral /solid</td><td>76</td><td>2,758</td><td>0.35</td><td colspan="6">Isotropic and Linear Elastic</td></tr>
<tr><td rowspan="3">Base</td><td rowspan="3">8-noded quadrilateral /solid</td><td rowspan="3">305</td><td rowspan="3">207 (initial)</td><td rowspan="3">0.40</td><td colspan="6">Nonlinear: Uzan model (Equation 2)</td></tr>
<tr><td colspan="2">K_1 (MPa)</td><td colspan="2">K_2</td><td colspan="2">K_3</td></tr>
<tr><td colspan="2">4.1</td><td colspan="2">0.64</td><td colspan="2">0.065</td></tr>
<tr><td rowspan="3">Subgrade</td><td rowspan="3">8-noded quadrilateral /solid</td><td rowspan="3">20,955</td><td rowspan="3">41.4 (initial)</td><td rowspan="3">0.45</td><td colspan="6">Nonlinear: Bilinear model (Equation 3)</td></tr>
<tr><td>K_1 (MPa)</td><td>K_2 (MPa)</td><td>K_3 (MPa/ MPa)</td><td>K_4 (MPa/ MPa)</td><td>σ_{dll}^* (MPa)</td><td>σ_{dul}^* (MPa)</td></tr>
<tr><td>41.4</td><td>0.041</td><td>1,000</td><td>200</td><td>0.014</td><td>0.145</td></tr>
</table>

* σ_{dll} and σ_{dul} are for lower and upper limits of the applied deviator stress values.

Table 5 lists the critical pavement responses predicted by both linear and nonlinear axisymmetric analyses using the ABAQUS FE program. Figure 2 shows the vertical displacements predicted at the centerline of loading in the AC, base, and subgrade layers as obtained from the three different pavement layer material characterization cases. The nonlinear characterization of the base layer mainly caused increases in the predicted responses of up to 18% in the tensile strain at the bottom of the AC, 29% in the vertical strain on top of the subgrade, and 33% in the surface deflection. The nonlinearity of subgrade also affected the critical pavement responses; up to 21% decrease in the vertical strain on top of the subgrade and 23% decrease in the surface deflection. On the other hand, the nonlinearity of subgrade soils had little impact on the tensile strain at the bottom of the AC. As listed in Table 5, the combined nonlinear base and subgrade characterizations yielded the most accurate pavement response predictions quite different from the linear elastic case. Note that these differences, specific to the pavement geometries, layer material properties, and the loading conditions studied here, were given as examples to demonstrate the important effects of nonlinear pavement foundation behavior.

Table 5. Predicted Pavement Responses from Axisymmetric FE Analyses*

Pavement response	Linear base and linear subgrade	Nonlinear base and linear subgrade	Linear base and nonlinear subgrade	Nonlinear base and nonlinear subgrade
δ_{surface} (mm)	-0.93	-1.24	-0.76	-0.97
$\varepsilon_{r\ \text{bottom of AC}}$ ($\mu\varepsilon$)	227	267	227	257
$\varepsilon_{v\ \text{top of subgrade}}$ ($\mu\varepsilon$)	-932	-1,203	-772	-937

* Negative is compression

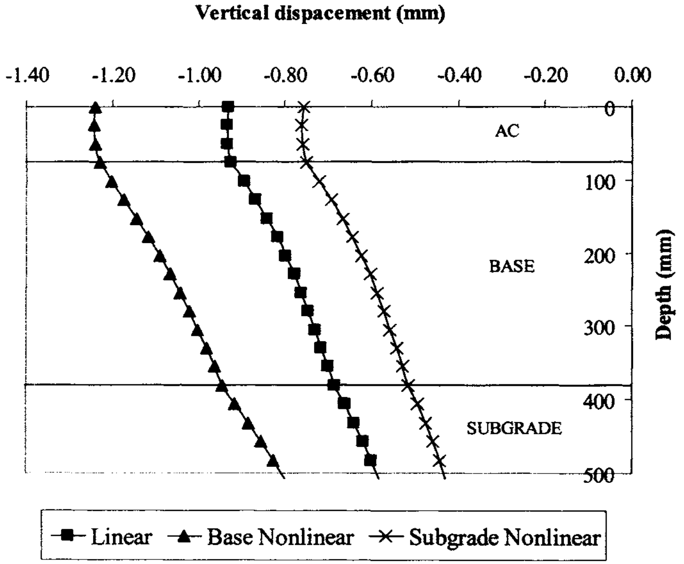

Figure 2. Predicted Vertical Displacements from Axisymmetric FE Analyses

3D Nonlinear FE Analysis The 3D axisymmetric ABAQUS model was next used to analyze the pavement section selected for the domain study (see Figure 1b) with nonlinear pavement geomaterial characterizations. The Uzan and the bilinear subgrade M_R models (Equations 2 and 3) were again employed in the granular base and subgrade soil layers. For comparison purposes, the same model parameters and material properties listed in Table 4 were also used in the 3D solutions except for the 8-noded solid element employed in the 3D FE mesh.

Table 6 lists the critical pavement responses predicted by both linear and nonlinear 3D analyses using the ABAQUS FE program with more responses presented here than listed in Table 5. The nonlinear FE analyses resulted in considerably different pavement response predictions when compared to those from the linear analyses. The largest difference was for the case of the nonlinear base and linear subgrade material. The nonlinear characterization of the base layer caused increases in the predicted responses of up to 29% in the tensile strain at the bottom of the AC, 30% in the vertical strain on top of the subgrade, and 36% in the surface deflection. The subgrade nonlinear characteristics resulted in 21% decrease in the vertical strain and 22% decrease in the surface deflection. Similar to the results of the axisymmetric FE analyses, the nonlinearity of subgrade soils had little impact on the tensile strain at bottom of the AC.

Table 6. Predicted Pavement Responses from 3D FE Analyses*

Pavement response	Linear base and linear subgrade	Nonlinear base and linear subgrade	Linear base and nonlinear subgrade	Nonlinear base and nonlinear subgrade
δ_{surface} (mm)	-0.91	-1.23	-0.74	-0.98
$\delta_{\text{top of subgrade}}$ (mm)	-0.66	-0.91	-0.50	-0.65
$\sigma_{\text{r bottom of AC}}$ (MPa)	0.77	1.00	0.77	0.97
$\varepsilon_{\text{r bottom of AC}}$ ($\mu\varepsilon$)	227	292	226	277
$\sigma_{\text{v top of subgrade}}$ (MPa)	-0.040	-0.067	-0.050	-0.075
$\varepsilon_{\text{v top of subgrade}}$ ($\mu\varepsilon$)	-930	-1,212	-770	-928

* Negative is compression

Although 3D nonlinear FE analysis of flexible pavements is currently the state-of-the-art structural analysis approach, the 3D analysis results in this study were not much different from those of the axisymmetric analyses. This is partly because the same material model that uses the triaxial conditions ($\sigma_2=\sigma_3$) and the axisymmetric assumption in base layer was used in both the axisymmetric and 3D analyses. This is actually good news indicating that axisymmetric analysis with nonlinear geomaterial layer characterizations can still be used confidently for predicting reasonably accurate responses under single wheel loading. However, before one can confidently make that statement, future research should closely investigate whether the use of a nonlinear geomaterial model developed from true triaxial tests that can fully apply and simulate the 3D stress states in material modeling (including an intermediate principal stress σ_2 different from σ_3) would bring any improvement in results from the 3D analyses of flexible pavements.

Summary and Conclusions

To properly characterize the resilient response of geomaterials, i.e., coarse-grained unbound aggregates and fine-grained subgrade soils, appropriate stress-dependent modulus characterization models were programmed in a user-defined material model subroutine (UMAT) in the general purpose ABAQUS™ finite element (FE) program. This way, stress-dependent characterizations of the base and subgrade layers were made part of the ABAQUS FE nonlinear solutions for flexible pavement response analysis. To converge smoothly in each loading, a direct secant stiffness approach was adopted in nonlinear analysis to work suitably for both ABAQUS axisymmetric and three-dimensional (3D) pavement analyses.

Both axisymmetric and 3D FE analyses were suitably conducted with the developed ABAQUS material subroutine (UMAT) considering the effects of nonlinear pavement base and subgrade behavior. Compared to the linear elastic solutions, significantly different critical pavement responses, i.e., tensile strain at bottom of AC related to fatigue cracking and vertical strain on top of subgrade related to rutting, were predicted when nonlinear analyses were performed in the base and subgrade layers.

The comparisons between the axisymmetric and 3D nonlinear ABAQUS predictions did not indicate any major differences partly because the same material models obtained from laboratory triaxial testing conditions were implemented in both axisymmetric and 3D analyses. Future studies dealing with 3D nonlinear FE analysis should focus on the effects of intermediate principal stress and how that would influence response predictions for various pavement geometries and loading conditions to investigate 3D effects such as multiple wheel loading and geosynthetic reinforcement of base courses.

References

Brown, S.F. and Pappin, J.W. (1981). "Analysis of Pavements with Granular Bases." *Transportation Research Record 810*, TRB, National Research Council, Washington, D.C., 17-23.

Chen, D.H., Zaman, M., Laguros, J., and Soltani, A. (1995). "Assessment of Computer Programs for Analysis of Flexible Pavement Structures." *Transportation Research Record 1482*, TRB, National Research Council, Washington, D.C., 123-133.

Cho, Y., McCullough, B.F., and Weissmann, J. (1996). "Considerations on Finite-element Method Application in Pavement Structural Analysis." *Transportation Research Record 1539*, TRB, National Research Council, Washington, D.C., 96-101.

Duncan, J.M., Monismith, C.L., and Wilson, E.L. (1968). "Finite Element Analyses of Pavements." *Highway Research Record 228*, TRB, National Research Council, Washington, D.C., 18-33.

Hibbit, Karlsson & Sorensen, Inc. (2005). *ABAQUS/standard User's Manual, Version 6.5.* Hibbit, Karlsson & Sorensen, Inc., Pawtucket, Rhode Island.

Hicks, R.G. and Monismith, C.L. (1971). "Factors Influencing the Resilient Properties of Granular Materials." *Transportation Research Record 345*, TRB, National Research Council, Washington, D.C., 15-31.

Huang, Y.H. (2004). Pavement Analysis and Design, 2nd Edition, Pearson Prentice Hall, Pearson Education Inc., Upper Saddle River, New Jersey

Kim, M. and Tutumluer, E. (2006). "Modeling Nonlinear, Stress-Dependent Pavement Foundation Behavior Using A General-Purpose Finite Element Program." In ASCE Geotechnical Special Publication 154, entitled, *Pavement Mechanics and Testing*, Edited by B. Huang, R. Meier, J. Prozzi, and E. Tutumluer, Proceedings Book of the ASCE Geo-Institute Geoshanghai Conference, Shanghai, P.R. of China.

Raad, L., and Figueroa, J.L. (1980). "Load Response of Transportation Support Systems." *Journal of Transportation Engineering*, ASCE, 106(1), 111-128.

Saad, B., Mitri, H., and Poorooshasb, H. (2005). "Three-dimensional Dynamic Analysis of Flexible Conventional Pavement Foundation." *Journal of Transportation Engineering*, ASCE, 131(6), 460-469.

Schwartz, C.W. (2002). Effect of Stress-dependent Base layer on the Superposition of Flexible Pavement Solutions, The International Journal of Geomechanics, 2(3), 331-352.

Taciroglu, E. (1998). "Constitutive Modeling of the Resilient Response of Granular Solids." Ph.D. thesis, University of Illinois at Urbana-Champaign, Urbana, IL.

Thompson, M.R. and Elliott, R.P. (1985). "ILLI-PAVE Based Response Algorithms for Design of Conventional Flexible Pavements." *Transportation Research Record 1043*, TRB, National Research Council, Washington, D.C., 50-57.

Thompson, M.R. and Robnett, Q.L. (1979). "Resilient Properites of Subgrade Soils." *Journal of Transportation Engineering*, ASCE, Vol. 105, No.TE1.

Tutumluer, E. (1995). *Predicting Behavior of Flexible Pavements with Granular Bases*. Ph.D. thesis, Georgia Institute of Technology, Atlanta.

Uzan, J. (1985). "Characterization of Granular Material," *Transportation Research Record 1022*, TRB, National Research Council, Washington D.C., 52-59.

EVALUATION OF GEOGRID BENEFITS USING MONOTONIC AND REPEATED LOAD TRIAXIAL TESTS

Munir D. Nazzal[1], Murad Abu-Farsakh[2], and Louay N. Mohammad[3]

ABSTRACT

A series of monotonic and repeated load resilient modulus triaxial tests were conducted on unreinforced and geogrid reinforced crushed limestone samples to evaluate the effects of the stiffness, location, and number of geogrid layer/s on the strength properties and stress strain response parameters of those samples. Five different types of geogrids were used, and for each geogrid type, four different cases were investigated. For each monotonic triaxial test, three response parameters were selected to assess the benefits of geogrid improvement namely, $E_{s1\%}$, $E_{s2\%}$, and USS. Statistical analyses were conducted on the results using ANOVA and post ANOVA LSM. The results of these analyses indicated that generally geogrid with higher stiffness moduli exhibited greater improvement. In addition, double layers had always the maximum improvement, while the minimum benefit was observed for single geogrid layer placed at the sample mid-height. The cyclic triaxial test results were used to determine resilient moduli for the different samples. These results showed that the geogrid reinforcement did not enhance the resilient properties of the reinforced samples.

INTRODUCTION

Geogrids are extruded sheets of polyethylene or polypropylene with apertures that interlock with soil particles in a regular pattern producing a stronger composite mass. Over the last decades geogrids have been used as reinforcement in flexible

---

[1] Research Associate, Louisiana Transportation Research Center, Louisiana State University, Baton Rouge,
LA 70808.

[2] Research Assistant Professor, Louisiana Transportation Research Center, Louisiana State University, Baton Rouge, LA 70808.

[3] Professor, Department of Civil and Environmental Engineering, Louisiana Transportation Research Center, Louisiana State University, Baton Rouge, LA 70808.

pavements, bridge abutments, and many other applications. Many studies have been conducted to characterize the behavior of reinforced soils in large-scale model experiments (Haas et al., 1988; Barksdale et al., 1989; Miura et al., 1990; Webster, 1993; Cancelli et al., 1996; Collin et al., 1996; and Perkins and Ismeik, 1997; Berg et al., 2000; Perkins, 2001). These studies showed that geogrids can mechanically improve the overall strength and stability of reinforced structures.

Few studies were conducted to study the reinforcement mechanisms in a small-scale controlled laboratory environment (Ashmawy et al., 1999; Moghaddas-Nejad and Small, 2003; Perkins et al., 2004). These studies investigated the effect of geogrid on deformation and strength behavior of reinforced material using monotonic and cyclic triaxial tests. In general, the results of these studies showed that the presence of geogrids significantly improved the strength of tested samples. In addition, the geogrid layer tended to reduce the accumulated plastic strains under cyclic loading. However, it did not have a significant effect on the resilient strain.

The objective of this study is to evaluate the influence of the number of geogrid layers and geogrid location and properties on the strength properties of reinforced crushed limestone samples. This was done by conducting a total of monotonic and cyclic triaxial tests on unreinforced and geogrid reinforced samples. Five different types of geogrids were used, and for each geogrid type, four different cases were investigated. The cases included varying the location and number of reinforcement layers placed in the tested samples. A statistical analysis was then carried out on the triaxial test results.

TESTING PROGRAM

The testing program for this study included conducting a series of drained montonic and repeated load triaxial tests on reinforced and unreinfoerced samples. All tests were performed using the MTS closed loop, servo hydraulic triaxial testing machine. The applied load was measured using a load cell installed inside the triaxial cell. This type of the set up reduces the equipment compliance errors and also alignment errors. The capacity of the load cell used was ± 5000 lbf. The axial displacement measurements were made using two Linearly Variable Differential Transducer's (LVDT) placed between the top platen and base of the cell to reduce the amount of extraneous axial deformation measured compared to external LDVTs. Air was used as the confining fluid to the specimens.

Materials

Crushed limestone

The tested material was taken from a selected crushed limestone sample typically used in construction of base course layers in Louisiana. The material has a nominal size of 25.4 mm, and a D_{10} and D_{60} sizes of 0.18 mm and 6 mm respectively, giving it a uniformity coefficient of 30. In addition, it is classified as A-1-a and GW-GC according to the American Association of State Highway and Transportation (AASHTO) classification system, and the Unified Soil Classification System (USCS).

The crushed limestone has a maximum dry unit weight 17.2 kN/m3 (139.2 lb/ft^3) and an optimum moisture content of 7.0%, as measured by the standard proctor test.

Geogrid

The reinforcement material in this study included five different types of Tensar Biaxial geogrids, namely, BX-1100, BX-1200, BX -1500, BX 6100, and BX 6200. These gegroids are used to reinforce base course layer in a pavement structure.

Sample Preparation

The dimension of the sample tested in triaxial experiment is based on the nominal maximum particle size of its material. Since the crushed limestone material used in this study had a nominal particle size greater than 19.0 mm, all samples were prepared with 152.4 mm (6 in) diameter and a length of 304 mm (12 in) using a split mold. All samples were mixed at optimum moisture content and compacted using a vibratory compaction device to achieve the maximum dry density measured by the standard proctor test. To achieve a uniform compaction throughout the specimen, samples were compacted in 50 mm (2 in) lift thickness. Each layer was compacted until the required density was obtained as indicated by measuring the distance from the top of the mold to the top of the compacted layer. The smooth surface on top of the lift was lightly scratched to achieve good bonding with the next lift. The dry density achieved was within ± 1 percent of target value. The water content achieved was within ± 0.5 percent of the target value.

Monotonic Triaxial Tests

Drained conventional triaxial tests were conducted on unreinforced and reinforced sample. The strain rate used in these tests was 0.00033 in/sec. This rate was chosen to ensure that no excess pore water was developed during testing. In each test the sample was loaded to strain level of 1%, then unloaded and reloaded to failure. Triaxial Tests were performed at 21 (kPa) confinement pressure on samples reinforced with each of the five geogrid types investigated in this study. For each reinforcement type, four cases were investigated. The first three cases included placing one reinforcement layer placed at the middle, one and two thirds of sample height from bottom, respectively. While in the fourth case, samples were reinforced with two geogrid layers placed at one and two thirds of the sample height from bottom. Three replicate samples were tested for each case to ensure repeatability of the tests.

Repeated Load Triaxial Tests

Repeated load triaxial tests were performed in accordance with AASHTO-T307 standard method for determining the resilient modulus of base course material. In this method a series of steps consisting of different levels of cyclic axial stress are followed such that the resilient modulus is measured at varying confinement and shear stress levels. The cyclic loading consists of repeated cycles of a haversine shaped load-pulse. These load pulses have a 0.1 sec load duration and 0.9 sec rest period. Cyclic triaxial tests were conducted on unreinofrced samples, and samples reinforced with one of the five geogrid types used in this study. Three different placement cases were investigated for each reinforcement type; namely, single layer placed at the sample mid-height, single layer placed at the one third of the sample height from top, and double layers placed at one and two thirds of the sample height from top. Three replicate samples were tested for each case.

RESULTS AND ANALYSIS

Monotonic Triaxial Tests

The stress-strain curves were obtained from the monotonic triaxial tests for unreinforced samples and samples reinforced with geogrid BX1100, BX1200, BX 6100, and BX 6200. To quantitively evaluate the improvement due to the reinforcement under monotonic loading; three response parameters were first determined for each triaxial test, namely, the secant elastic moduli at 1% strain level ($E_{s1\%}$), the secant elastic moduli at 2% strain level ($E_{s2\%}$), and the ultimate shear strength (USS). These response parameters were chosen to assess the reinforcement influence on the behavior of the tested material at different strain levels. An improvement factor (IM) of each of the three response parameters was then calculated for each reinforced sample as the ratio of that parameter to the corresponding average value of the unreinforced samples. Figures 1a to 1c present the average improvement factor of each reinforced case. It is clear that the improvement in all three parameters due to the inclusion of geogrid reinforcement increased with increasing the stiffness of the geogrid. However, this improvement was dependent on the location and number of geogrid layer/s. In addition, the improvement in the USS and $E_{s2\%}$ was more apparent than that in $E_{s1\%}$, with a maximum improvement in the ultimate shear strength values (a maximum value of IM-USS of 2.5 was observed).

An analysis of variance (ANOVA) was conducted using Statistical Analysis Software (SAS) software to detect the effects of geogrid layer location, number, and stiffness on the improvement in each of the three response parameter obtained from monotonic triaxial tests ($E_{s1\%}$, $E_{s2\%}$, USS). The ANOVA analyses were performed using MIXED procedure available in SAS. The linear model used in these analyses was a completely randomized design consisting of a four by five factorial (four cases and by five geogrid types), and is shown in Equation 1. The dependent variable in each of the analyses was the improvement factor of one of the response parameters.

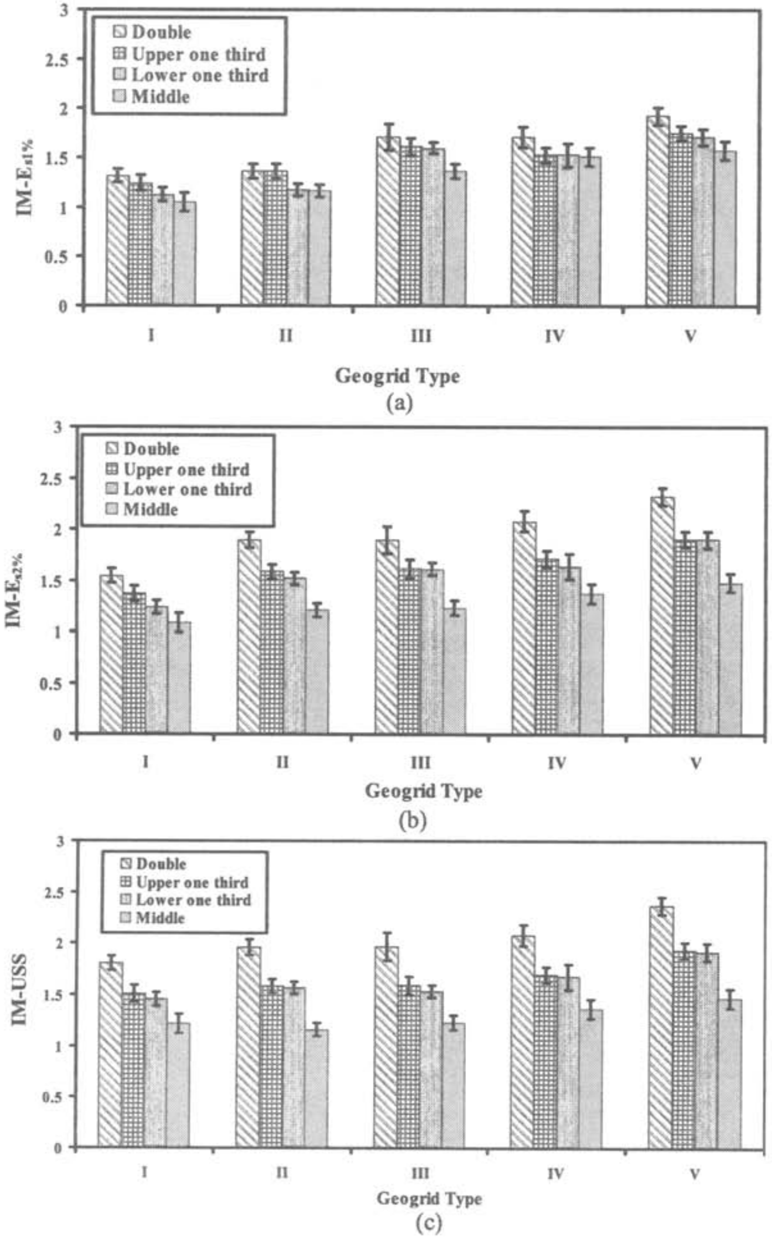

(a)

(b)

(c)

FIG. 1. Improvement in Response Factors:

a)E$_{s1\%}$ b) E$_{s2\%}$ c)USS

$$Y_{ijk} = \mu + \tau_{1i} + \tau_{2j} + \tau_1\tau_{2ij} + \epsilon_{ijk} \quad (1)$$

Where μ is the overall mean, τ_{1i} is the effect of location case with levels i, τ_{2j} is the effect of stiffness with level j, $\tau_1\tau_{2ij}$ is effect of the interaction between location and stiffness, and ϵ_{ijk} is the random sampling variation for observation k, with k ranging, at case and stiffness level ij. Y_{ijk}: is the dependent variable.

The Type III Tests of fixed effects output were used to determine the significance of the effects. The ANOVA results of the three analyses are presented Table 1. It can be seen that at a 95% confidence level the type of geogrid and geogrid placement case, had a significant effect on the improvement in $E_{s1\%}$, $E_{s2\%}$, USS. While the interaction between the geogrid type and placement case had a significant effect only on the improvement in the $E_{s2\%}$, USS. The significance of interaction indicates that the behaviors of the two main effects (placement case and stiffness) are inconsistent, which means that they do not increase and decrease by the same amount. However, a closer look at the F-value reveals that the influence of the interaction effect is small compared to the main effects.

Based on the ANOVA analyses result, Post ANOVA Least Square Means (LSM) analyses were conducted to compare all of the different geogrid type-location cases. Tukey adjustment was used in this analysis since it provides tests for all pairwise comparisons at a well balance of the type I and type II errors when compared to other adjustments available. Saxton's macro was conducted to convert the results of the Post ANOVA-LSM analyses to letter groupings. The results of this grouping are shown in Tables 2 and 3. Table 2 presents the grouping of the geogrid type effect on $E_{s1\%}$, $E_{s2\%}$, and USS. It is observed that the maximum and minimum improvement in all of the three response parameters was achieved when using geogrids BX-1500 and BX-6100 respectively. While, the improvement in $E_{s1\%}$ due to geogrid types BX-1200 and BX-6200 was statistically indistinguishable from each other. However, the effect of geogrid type BX-6200 on the improvement in $Es_{2\%}$ and USS were distinguishable from BX-1200 but indistinguishable from BX-1100. In addition Table 3 shows that the effect of the placement case on the improvement in $Es_{1\%}$ values are significantly different from one another and rank from the highest to the lowest values as follows: double > upper one third > lower one third > middle. While the effect of the locations on the $Es_{2\%}$ USS had similar trend except that geogrids with locations at the upper and lower one third were statistically indistinguishable from each other.

TABLE 1. ANOVA Results for $E_{s1\%}$, $E_{s2\%}$ USS

Type III Tests of Fixed Effects for $E_{s1\%}$				
Effect	**Num DF**	**Den DF**	**F Value**	**Pr > F**
Geogrid Type	4	40	139.34	<.0001
Location	3	40	43.19	<.0001
Location* Geogrid Type	12	40	1.91	0.0625
Type III Tests of Fixed Effects for $E_{s2\%}$				
Effect	Num DF	Den DF	F Value	Pr > F
Geogrid Type	4	40	209.38	<.0001
Location	3	40	394.00	<.0001
Location* Geogrid Type	12	40	3.07	0.0038
Type III Tests of Fixed Effects for USS				
Effect	Num DF	Den DF	F Value	Pr > F
Geogrid Type	4	40	133.99	<.0001
Location	3	40	563.00	<.0001
Location* Geogrid Type	12	40	3.04	0.0040

TABLE 2. Grouping of Geogrid Type Effect

$E_{s1\%}$ Parameter			
Geogrid Type	**Estimate**	**Standard Error**	**Letter Group**
BX-1500	1.7413	0.01978	A
BX-6200	1.5705	0.01978	B
BX-1200	1.5681	0.01978	B
BX-1100	1.2658	0.01978	C
BX-6100	1.1817	0.01978	D
$E_{s2\%}$ Parameter			
BX-1500	1.9013	0.01532	A
BX-1200	1.6640	0.01532	B
BX-6200	1.5888	0.01532	C
BX-1100	1.5526	0.01532	C
BX-6100	1.2847	0.01532	D
USS Parameter			
BX-1500	1.9215	0.01438	A
BX-1200	1.7038	0.01438	B
BX-6200	1.5810	0.01438	C
BX-1100	1.5682	0.01438	C
BX-6100	1.4986	0.01438	D

TABLE 3. Grouping of Location Case Effect

$E_{s1\%}$ Parameter			
Location	**Estimate**	**Standard Error**	**Letter Group**
Double Layers	1.6049	0.01769	A
Upper one third	1.4993	0.01769	B
Lower one third	1.4286	0.01769	C
Middle	1.3291	0.01769	D
$E_{s2\%}$ Parameter			
Double Layers	1.9187	0.01371	A
Upper one third	1.6378	0.01371	B
Lower one third	1.5813	0.01371	C
Middle	1.2554	0.01371	D
USS Parameter			
Double Layers	2.0358	0.01286	A
Upper one third	1.6633	0.01286	B
Lower one third	1.6302	0.01286	B
Middle	1.2892	0.01286	C

Repeated Load Triaxial Tests Results

Resilient modulus tests were also conducted on the unreinforced and reinforced samples. For each test the resilient modulus was first calculated as the cyclic axial stress divided by the resilient (recoverable) strain for the last 10 cycles of each step. A regression analysis was then carried out to fit the test data using the generalized constitutive model (Equation 2) that has been adopted by the 2002 new mechanistic-empirical Design Guide (NCHRP, 2004).

$$M_R = p_a k_1 \left(\frac{\theta}{p_a}\right)^{k_2} \left(\frac{\tau_{oct}}{p_a} + 1\right)^{k_3}$$

(2)

Where

M_R : is the resilient modulus; p_a: is the atmospheric pressure (101.3 kPa); θ : is the bulk stress and equal to $\sigma_1 + 2\sigma_3$, τ_{oct}: is the octahedral shear stress and equal to $\sqrt{2}/3\,(\sigma_1 - \sigma 3)$, and k_1, k_2, and k_3: are the material properties.

The resilient modulus was then calculated for the different unreinforced and reinforced samples at stress state that was selected based on previous finite element study (Nazzal et al., 2006). Figure 2 presents the results of this calculation. It is noticed that for samples reinforced with one layer a slight improvement in the resilient modulus calculated at the selected stress state was detected for all tests. However, no conclusion can be drawn since this improvement lies within the margin of error of the calculated value.

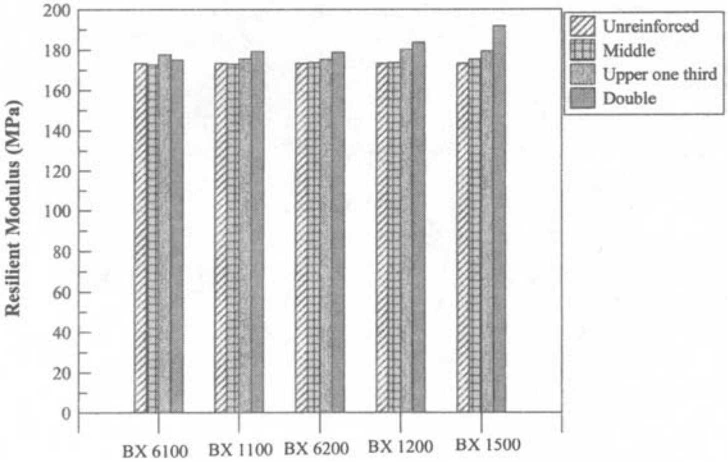

FIG. 2. Resilient Modulus Values at Stress State Obtained From Finite Element Analysis

ANOVA analysis was also conducted to compare the resilient modulus calculated at the selected stress state for each reinforced case with unreinforced case. A single factor Completely Randomized Design (CRD) with 17 effect levels (16 reinforced cases unreinforced case) was used in this analysis. Post ANOVA Least Square Means (LSM) analyses were conducted. Duntte's adjustment was used to compare LSM of the reinforced samples with unreinforced sample. It was observed that at 95% confidence level only the resilient modulus values of samples reinforced with double layers of geogrid BX-1500 were higher than those of unreinforced samples. This suggests that the reinforcement did not have a significant effect on the resilient modulus properties of crushed limestone. These results are consistent with the recent works reported by Moghaddas-Nejad and Small (2003) and Perkins (2004) where similar tests were reported using different granular materials and a single layer of geogrid reinforcement.

CONCLUSIONS

A series of monotonic and cyclic triaxial tests were conducted on unreinforced and geogrid reinforced crushed limestone samples to evaluate the effects of location and properties of the geogrid reinforcement layer on the strength properties and stress strain response parameters of reinforced samples. Three response parameters were determined from monotonic triaxial test results and were used to evaluate the benefits of the geogrid. While the cyclic triaxial test results were used to determine the resilient modulus values at stress state determined using a finite element model. Based on the results of this study the following conclusion can be drawn:

- The inclusion of geogrid reinforcement layer/s improves the strength/stiffness of crushed limestone material substantially under montonic loading. The improvement was more pronounced in the ultimate shear strength and $E_{s2\%}$ values than that in $E_{s1\%}$, with a maximum improvement in the ultimate shear strength values.
- Under monotonic loading the improvement in the stiffness parameter of crushed limestone was found to be a function of the location, stiffness, number of geogrid layer/s.
- For a certain placement location stiffer geogrid exhibited higher improvement in the monotonic triaxial response parameters.
- For a specific geogrid type the maximum improvement was achieved when two geogrid layers were used. While the minimum improvement was found for samples reinforced with single geogrid layer at the middle. In addition, the upper and lower third geogrid location had statistically indistinguishable effect on the improvement in the $E_{s2\%}$ and USS.
- The results of the resilient modulus showed that the reinforcement did not have a significant effect on the resilient modulus values of crushed limestone samples.

REFERENCES

Ashmawy, A.K, Bourdeau, P.L., Drnevich, V.P., Dysli, M., (1999) "Cyclic Response of Geotextile- Reinforced Soil," *Journal of Soils and Foundations*, Vol. 39, No. 1, February, pp.

Barksdale, R.D., Brown, S. F., and Chan, F., 1989, "Potential benefits of geosynthetics in flexible pavement systems", *National Cooperative Highway research Program Report* No. 315, Transportation Research Board, National Research Council, Washington, DC, USA, 56 p.

Berg, R. R., Christopher, B.R., and Perkins, S.W., 2000, "Geosynthetic reinforcement of the aggregate base course of flexible pavement structures", GMA White paper II, Geosynthetic material Assoiation, Roseville, MN, USA, 130 p.

Cancelli, A., and Montanelli, F., 1996, "In-ground test for geosynthetic reinforced flexible paved roads", Proc. Of the Conference Geosynthetics '99, Boston, MA, USA, Vol. 2, pp. 863-878.

Cancelli, A., Montanelli, F., Rimoldi, P., and Zhao, A, 1996, "Full scale laboratory testing on geosynthetics reinforced paved roads", Earth reinforcement, Ochiai, H., Yasufuku, N., and Omine, K., Editors, Balkema, Proceedings of the International Symposium on Earth Reinforcement, Fukuoka, Kyushu, Japan, November, 1996, pp.

573-578.

Haas, R., Walls, J. and Carroll, R.G. (1988). "Geogrid Reinforcement of Granular Bases in Flexible Pavements," *Transportation Research Record 1188*, pp. 19-27.

Miura, N., Sakai, A., Taesiri, Y., Yamanouchi, T., and Yasuhara, K., 1990, "Polymer grid reinforced pavement on soft clay grounds", *geotextiles and geomembranes*, Vol. 9, No. 1, pp. 99-123.

Moghaddas-Nejad, F. and Small, J.C. (1996). "Effects of Geogrid Reinforcement in Model Track Tests on Pavements", *Journal of Transportation Engineering*, Vol. 122, No. 6, pp. 468-474.

Moghaddas-Nejad, F. and Small, J.C. (2003), "Resilient and Permanent Characteristics ofReinforced Granular Materials by Repeated Load Triaxial Tests", *ASTM Geotechnical Testing Journal,* Vol. 26, No. 2, pp. 152-166.

Nazzal M., Abu-Farsakh, M. Y., and Mohammad, L. (2006). Numerical Analyses of Geogrid Reinforced Flexible Pavements. *Proc., GeoCongress Conference*, Atlanta,

NCHRP (2004), NCHRP Project 1-37A, *Development of NCHRP 1-37A Design Guide, Using Mechanistic Principles to Improve Pavement Design*, http://www.NCHRP 1-37A Designdesignguide.com/.

Perkins, S.W. and Ismeik, M. (1997a). "A Synthesis and Evaluation of Geosynthetic

Reinforced Base Layers in Flexible Pavements: Part I," *Geosynthetics International*, Vol. 4, No. 6, pp. 549- 605.

Perkins, S.W. and Ismeik, M. (1997b). "A Synthesis and Evaluation of Geosynthetic

Reinforced Base Layers in Flexible Pavements: Part II," *Geosynthetics International*, Vol. 4, No. 6, pp. 549- 605.

Perkins, S.W., Christopher, B., Cuelho, E.L., Eiksund, G.R., Hoff, I., Schwartz, C.W., Svano, G., and Want, A. (2004). "Development of design methods for geosynthetic reinforced flexible pavements". A report prepared for the U.S. Department of transportation, Federal Highway Administration, FHWA/DTFH61-01-X-00068.

PERMANENT DEFORMATION OF SUBGRADE SOILS

Zhong-yin Guo [1], Hong-liang Zhang[2], Lin Cong [3]and Qi-ju Gao[4]

ABSTRACT: Few research projects have been conducted on the permanent deformation of subgrade soils in China. Based on a comprehensive literature review, a testing procedure to evaluate permanent deformation in subgrade soils is developed and presented in this paper. The parameters in the permanent deformation test include confining pressure, deviator stress, load shape, load duration, load rest period, moisture content and dry density. Using the procedure, the authors conducted repeated load tests for three subgrade soils. The test results are in good agreement with the relationships between the permanent strain and the number of load applications proposed by Tseng and Lytton. The regression models for sand, silty clay and clay have been developed from these results.

INTRODUCTION

The major function of the subgrade is to provide support to pavement structures. It has been well documented that the subgrade soil plays a critical role in the initiation and propagation of permanent deformation in pavements and directly influences pavement performance (Huang, 1993). Most of the asphalt pavements constructed in China include semi-rigid base courses. Reflection cracks often occur in these

---

1 Professor, Key Laboratory for Road Traffic Engineering of Ministry of Education, Shanghai, 200092, China.
zhongyin@mail.tongji.edu.cn.
2 PhD, Key Laboratory for Special Area Highway Engineering of Ministry of Education, Highway College of Chang'an University, Xi'an, Shaanxi, 710064, China; Key Laboratory for Road Traffic Engineering of Ministry of Education, Shanghai 200092, China.
3 PhD, Key Laboratory for Road Traffic Engineering of Ministry of Education, Shanghai 200092, China.
4.Doctor candidate, Key Laboratory for Road Traffic Engineering of Ministry of Education, Shanghai 200092, China; Shandong Communications Science Research Institute, Jinan, Shandong, 250031, China

pavements and water will infiltrate the subgrade easily. However, few research projects on permanent deformation in the subgrade soils have been conducted in China. Test procedures and prediction models for permanent deformation with the consideration of the specific conditions of China have not been established. Because asphalt pavement properties, axle loads and soil properties in China may be different from those elsewhere, the procedures and models developed in other countries may not be used directly in China. As a result, permanent deformation of subgrade soils has not been incorporated into the design of asphalt pavements in China.

The testing procedure for permanent deformation in subgrade soils has to be established before a predicting model is developed. Based on a comprehensive literature review, the testing procedure is established in this paper according to the specific condition in China. With this procedure, repeated load tests are conducted for three subgrade soils and regression models for permanent deformation are developed.

REVIEW ON PERMANENT DEFORMATION IN SUBGRADE SOILS

Review on Predicting Models of Permanent Deformation

The pioneering research work in the area of permanent deformation was credited to the efforts of Monismith et al (1975). The power model proposed by Monismith is well accepted in predicting the amount of rutting contributed by the subgrade. It is expressed as

$$\varepsilon_p = AN^b \tag{1}$$

where

ε_p = permanent or plastic strain;

N = number of load repetitions;

A, b = material parameters (regression coefficients from test data)

Besides Monismith, many researchers have proposed models to predict the permanent deformation of soils. These include a hyperbolic curve model (Barksdale,1972), a polynomial model (Allen and Deen, 1986), a VESYS model (Kenis, 1978), an incremental model (Bonaquist and Witczak, 1996) and a shakedown model (Muhanna et al, 1998; Werkmeister et al, 2001). Zhao et al (2004) found that the power model proposed by Monismith (1975) can be used to predict the permanent deformation of most soils and established the regression formula for the coefficients in the power model through repeated load tests for eight soils.

Models developed by Tseng and Lytton (1989) were used as the starting point in MEPDG 2002 Design Guide to estimate the permanent deformation of unbound materials. The basic relationship is given by

$$\frac{\varepsilon_p(N)}{\varepsilon_r} = \beta_{r1}\left(\frac{\varepsilon_0}{\varepsilon_r}\right)e^{-\left(\frac{\rho}{N}\right)^{\beta}} \tag{2}$$

where

ϵ_0, β and ρ, material constants.

ϵ_r, resilient strain imposed in laboratory tests to obtain material properties ϵ_0, β and ρ.

β_{r1}, calibration factor.

The models for subgrade soils developed by Tseng and Lytton (1989) were given by

$$\log(\frac{\varepsilon_0}{\varepsilon_r}) = -1.69867 + 0.09121W_c - 0.0172893\sigma_d + 0.91219\log(E_r/6.895) \tag{3a}$$

$$\log\beta = -0.9730 - 0.0000040319072W_c^2\sigma_d + 0.0024894851\sigma_d - 0.000004902103W_c^2\sigma_\theta \tag{3b}$$

$$\log\rho = 11.009 + 0.00009862219W_c^2\sigma_d - 0.0583901\sigma_d + 0.0000079042785W_c^2\sigma_\theta \tag{3c}$$

where

W_c = Water content (%)
σ_d = Deviator stress (kPa)
σ_θ = Bulk stress (kPa)
E_r = Resilient modulus of the layer/sub-layer (kPa)

Ayres(1997) provided a modified version of these models. They were given by

$$\log(\frac{\varepsilon_0}{\varepsilon_r}) = 0.74168 + 0.08109W_c - 0.0000017631617E_r \tag{4a}$$

$$\log\beta = -0.61119 - 0.017638W_c \tag{4b}$$

$$\log\rho = 0.622685 + 0.541524W_c \tag{4c}$$

Extensive studies of the Ayres's modified models in the calibration process also resulted in several unfavorable conditions. Through modifications, the final form of the permanent deformation model for unbound materials used in the 2002 Design Guide is given by

$$\log(\frac{\varepsilon_0}{\varepsilon_r})\pounds\tfrac{1}{2}\frac{0.15\times e^{\rho^\beta} + 20\times e^{(\frac{\rho}{10^9})^\beta}}{2} \tag{5a}$$

$$\log\beta = -0.61119 - 0.017638W_c \tag{5b}$$

$$\rho = 10^9\left[\frac{-4.89285}{1-(10^9)^\beta}\right]^{\frac{1}{\beta}} \tag{5c}$$

Review on the Testing Procedure for the Permanent Deformation of Subgrade Soils

The testing procedures adopted by researchers are presented in Table 1. Uzan (1998) conducted a survey on the moisture content of the subgrade in Israel. He found that most of the moisture contents were 1.2 to 1.3 times of plastic limits (PL). So the moisture content he adopted in permanent deformation tests was 1.22 times of the plastic limit. The survey conducted by Elliott (1992) showed that the moisture contents were about 100 to 120 percent of the optimum moisture contents (OMC) in most cases. Few other researchers have made efforts to discuss the determination of the test procedure. Puppala (1999) pointed out that the procedure for permanent deformation tests of subgrade soils need to be studied further according to the specific condition of highways.

The testing program for measuring the resilient modulus of subgrade soils can be referred when the program of permanent deformation test is determined. The major specifications about the test of the resilient modulus include T307-99, LTPP P46-96, NCHRP 1-28, and NCHRP 1-28A. The test configurations in the four specifications are presented in Table 2.

PERMANENT DEFORMATION TESTING PROGRAM FOR SUBGRADE SOILS

Determination of Key Test Configurations

Moisture Content

Table 1 shows that in some research the moisture contents adopted are all greater than the OMC. But in other research the moisture contents of less than, greater than and equal to the OMC are adopted at the same time. Surveys have shown that the moisture contents of subgrade soils in China, which have been kept in balance, are often greater than the OMC. To make the design of asphalt pavement safer, the moisture contents used by Elliott et al (1998), 105% and 110% and 120% of OMC are adopted.

Dry Density

The Technical Standard of Highway Engineering of China requires that the ratio of the dry density to the maximum dry density (MDD) should be 94% to 96% and 93% to 96% for the soils which are 0 to 80 cm and 80 to 150 cm from the top of the subgrade, respectively. But the ratio may be less than 93% in the construction of subgrades, so 91% and 96% are recommended to be used.

TABLE 1. Summary of the Test Procedures byr Various Permanent Deformation Studies

Configurations	Monismith et al (1975)	Behzadi Yandell (1996)	Muhann et al (1998)	Uzan (1998)	Puppala (1999)	Suppakit (2003)	Zhao (2004)
Load Shape		Rectangle	Half sine	Half sine	Half sine	Half sine	Half sine
Load duration (second)	0.1	0.5	0.1	0.1	0.1	0.1	0.1
Rest Period (second)	2.9	1	0.9	0.9	0.9	0.9	0.9
No. of Applications (in thousands)	10 or 100	10	10	10 or 100	3 or 2.5	10	10 or 100
Confining Pressure (kPa)	34.5	15 to 50	20.7	0 and 20	a	b	21
Deviator Stress (kPa)	34.5 to 138	34.5 to 345	25 to 90% of strength	40 and 75	c	0.2, 0.4 and 0.6 times of strength	14 to166
Soil Tested	Silty clay	Silty clay	A-5 and A-6			Fine and coarse grained soils	Eight soils
Dry Density (% of MMC)	90 to 95	90 to 100		90		95	95
Moisture Content	16 to 20%	16%	OMC, OMC±2.5%	1.22PL			105, 110 and 120% of OMC

where a=the confining pressure is 21, 35, 70, 105, 140 kPa for a sand and 0, 21, 42 kPa for a clay;
b=the confining pressure is 0, 21, 42 kPa for a clay and a silty clay and 21, 48, 97 kPa for a sand and coarse-grained soils;
c = the deviator stress is 21, 35, 52.5, 70, 105, 140, 210, 280 kPa for a sand and 14, 28, 42, 56, 70 kPa for a clay.

TABLE 2. Configurations for Resilient Modulus Tests in Specifications

Configurations		T307-99	LTPP P46-96	NCHRP 1-28	NCHRP 1-28A
Load shape		Half sine	Half sine	Half sine	Half sine
Load duration (second)		0.1	0.1	0.1	0.2
Rest Period (second)		0.9 3	0.9	0.9	0.8
Confining Pressure (kPa)	Fine-grained soils	41.4, 27.6, 13.8	41.4, 27.6, 13.8	0	55.2, 41.4, 27.6, 13.8
	Coarse-grained soils	41.4, 27.6, 13.8	41.4, 27.6, 13.8	13.8, 20.7, 27.6, 41.4	13.8, 27.6, 41.4, 55.2, 82.8
Deviator Stress (kPa)	Fine-grained soils	12.4, 24.8, 37.3, 49.7, 62.1	12.4, 24.8, 37.3, 49.7, 62.1	13.8, 27.6, 41.4, 55.2, 69	27.6, 48.3, 69, 96.6
	Coarse-grained soils	12.4, 24.8, 37.3, 49.7, 62.1	12.4, 24.8, 37.3, 49.7, 62.1	13.8, 20.7, 27.6, 41.4, 55.2	6.9, 13.8, 20.7, 27.6, 41.4, 55.2, 82.8, 110.4, 124.2, 165.6, 248.4

Deviator Stress

The compressive stress at the top of the subgrade has been calculated for many asphalt pavements used in China. Results show that the compressive stresses are 10 to 180 kPa, with typical values of 10 to 30 kPa in most cases.

The field test conducted in an expressway by Zhang et al (2005) showed that when the axle load was 17.4 kN, the compressive stress at 30 cm below the top of the subgrade was 12 kPa.

To determine the upper limit of the deviator stress, the compressive stress at the top of the subgrade is calculated for the pavement shown in Table 3, which may represent the weakest pavement used in China. The compressive stress is 45 kPa under the standard axle load of 10 kN. If the axle load is 50% greater than the standard axle load it becomes 68 kPa, which can represent the largest compressive stress in the subgrade in China.

Based on the discussion above, referring to the deviator stresses in NCHRP 1-28A, three deviator stress levels are selected. They are 28, 48 and 69 kPa for fine-grained soils and 28, 55 and 83 kPa for coarse-grained soils.

Confining Pressure

Several researchers (Allen and Thompson, 1974; Brown and Hyde, 1975) explored the effect of variable (cyclic) confining pressures on the deformation of subgrade soils. Similar results for resilient and permanent strain were obtained from cyclic and constant confining pressures. This suggests that a fixed confining pressure could be used in repeated loading tests to get deformation data. Elliott el al (1998) and Zhao et al (2004) found that the confining pressure was not a critical factor influencing permanent deformation. It can also be seen from Table 1 that the fixed confining pressure of 21 kPa is used by about half of the researchers.

The confining pressure in the subgrade is calculated for many asphalt pavements used in China. Results show that, whether subgrade is made up of fine or coarse grained soils, the range of the confining pressure is from 0 to 60 kPa. In most cases, it is 10 to 30 kPa.

Table 2 also presents the confining pressures adopted in some major specifications for the resilient modulus test in USA. Table 2 shows that the confining pressure of 27.6 kPa is adopted in all of the four specifications. 27.6 kPa lies between 10 to 30 kPa and is close to 21 kPa. So the confining pressure of 28 kPa, which is the integer being most close to 27.6 kPa, is adopted in this study.

TABLE 3. The Weakest Pavement Selected in China

Structural Layers	Material	Thickness cm	Resilient modulus MPa	Poisson's ratio
Friction course	asphalt macadam mixture	3	600	0.25
Base course	Graded crushed stone	20	300	0.25
Sub base course	sand	20	200	0.25
subgrade			30	0.35

Load Frequency, Load Duration and Rest Period

Table 1 shows that a repeated load frequency of 1 HZ, a rest period of 0.9 second and a load duration of 0.1 second are adopted by all of the researchers after 1998. This stress pulse is produced by the vehicle running at the velocity of 80 km/h. But in NCHRP 1-28A they are considered to be only adapted to pavement materials. The subgrade is under the pavement, thus the duration of the stress pulse caused by vehicles will be closer to 0.2 second in the subgrade as compared to 0.1 second in the pavement. So a repeated load frequency of 1 HZ, a rest period of 0.8 second and a load duration of 0.2 second are adopted in NCHRP 1-28A.

Zhang et al (2005) measured the compressive stress distribution in the subgrade of an expressway under moving vehicles. When the weight of the rear axle was 9.8 kN and the moving velocity was 60 km/h, the compressive stress distribution in subgrade was shown in Fig. 1. The higher and lower peaks in Fig.1 are caused by the rear axle and front axle, respectively. It can be calculated that the load duration in the subgrade is about 0.3 to 0.4 second. If the velocity of the vehicle is 80 km/h the load duration will be 0.2 to 0.3 second.

Based on the discussions above, a repeated load frequency of 1 HZ, a rest period of

0.8 second and a load duration of 0.2 second are adopted in this study.

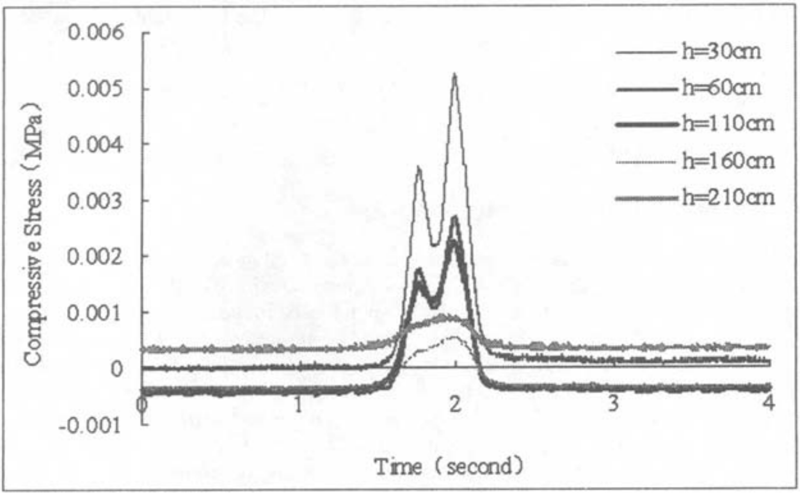

FIG. 1. Compressive Stress in Subgrade versus Time

Recommended Testing Program

Finally, the following procedure parameters are selected for the permanent deformation test of subgrade soils:

(1) Testing Configuration
Load Frequency: 1HZ.
Load Duration: 0.2 second.
Rest Period: 0.8 second.
Confining Pressure: 28 kPa.
Deviator Stress: 28, 48 and 69 kPa for fine-grained soils; 28, 55and 83 kPa for coarse-grained soils.
Number of Load Application: 10,000
(2) Compaction Specification
Compaction Method: Static compactor.
Compacted Dry Density: 91 and 96% of MDD.
Compacted Moisture Content: 105, 110 and 120% of OMC.

TEST RESULTS

Basic Properties of Soils Tested

Repeated load tests are conducted for sand, silty clay and clay in UTM. Test specimens are 200 mm in height and 100 mm in diameter. The basic properties of the soils are listed in Table 4.

TABLE 4. Basic Properties of Soils Tested

Soil	MDD (g/cm^3)	OMC (%)	Specific Gravity	Liquid Limit (%)	Plastic Limit (%)	Plastic index
Sand	2.00	11.1	2 .658	20.64	16.09	10.55
Clay	2.04	9.4	2. 736	27. 00	17.37	9.62
Silty clay	1.80	15.8	2 .690	33.40	21.63	11.83

Results of Repeated Load Tests

When the deviator stress is equal to 28 kPa, the permanent deformation increases with time at first and then decreases for some tests. Obviously this situation doesn't exist in reality. Therefore, these test results are not used in the analysis.

Elliott (1998) found that the initial data points couldn't completely represent soils' behavior because the loading system was being tuned to apply for the correct deviator stress during the first 10 to 30 cycles of load. Test results given by the authors show that an excessively large portion of the total permanent deformation is developed during the first 10 to 20 cycles of load. In the construction of highways, after the sugrade is completed, it will be compacted further by the rollers and trucks during the construction of the pavement. So the first 20 cycles of load can be included in this further compaction and the permanent deformation produced in these cycles will not contribute to the rut on the surface of the pavement.

For the reasons above, permanent deformation produced in the first 20 cycles of load are ignored. Some test results are plotted in Appendix II.

It should be noted that, the work condition with the moisture content of 105% of OMC and the confining pressure of 28 kPa is named "105-28". In the figures in Appendix II, this work condition is noted as 1. Similarly, the work condition "105-48" is noted as 2, "105-68" is noted as 3, "110-28" is noted as 4, "110-48" is noted as 5, "110-69" is noted as 6, "120-28" is noted as 7, "120-48" is noted as 8 and "120-69" is noted as 9.

Analysis of the test results shows that the relationship between the permanent strain and the number of load applications is close to the function given in Equation 2. The correlation coefficient R^2 in any work condition is greater than 0.99. This proves that the basic relationship shown in Equation 2 can be used to predict the permanent deformation of subgrade soils. However the test results are not in accordance with the results calculated from any one of the models used by Tseng and Lytton, Ayre et al, or MEPDG Design guide.

According to the test results, the coefficients in the formula are given as

(1) for sand:

$$\log(\frac{\varepsilon_0}{\varepsilon_r}) = 2.18784 - 0.11229W_c - 0.005427E_r \quad R^2=0.37 \qquad (6a)$$

$$\log\rho = 23.18288 - 1.41508W_c - 0.04981E_r \quad R^2=0.46 \qquad (6b)$$
$$\log\beta = -3.03719 + 0.15938W_c + 0.009936E_r \quad R^2=0.54 \qquad (6c)$$

(2) for clay:

$$\log(\frac{\varepsilon_0}{\varepsilon_r}) = -8.88415 + 0.79949W_c + 0.012675E_r \quad R^2=0.71 \qquad (7a)$$
$$\log\rho = -34.40419 + 3.36489W_c + 0.04869E_r \quad R^2=0.67 \qquad (7b)$$
$$\log\beta = 3.99682 - 0.39393W_c - 0.006643E_r \quad R^2=0.72 \qquad (7c)$$

(3) for silty clay:

$$\log(\frac{\varepsilon_0}{\varepsilon_r}) = 0.36702 + 0.028W_c - 0.002467E_r \quad R^2=0.36 \qquad (8a)$$
$$\log\rho = 12.07558 - 0.43565W_c - 0.014249E_r \quad R^2=0.48 \qquad (8b)$$
$$\log\beta = -2.31889 + 0.0739W_c + 0.009104E_r \quad R^2=0.52 \qquad (8c)$$

The regression coefficient R^2 in these formulas is all greater than critical values.

APPLICATION OF THE PERMANENT DEFORMATION MODEL FOR SUBGRADE SOILS

There are two major methods to prevent excessive permanent deformation of asphalt pavement in design: to control the allowable compressive strain on the top of the subgrade, or to calculate the total permanent deformation of the pavement directly. The total permanent deformation, which includes the permanent deformation of asphalt mixtures, aggregates and subgrade soils, can be calculated through layer wise summation method. Obviously, the permanent deformation predicting model of subgrade soils has to be used to calculate the total permanent deformation.

The method to calculate the total permanent deformation through layerwise summation method is very complicated and difficult to be used in the routine design of pavements. So the allowable compressive strain on the top of the subgrade is recommended to prevent rutting in China (Yao et al, 2003).

Because asphalt pavements, axle loads, material properties and the climate in China may be different from those in other countries, the design equations of the allowable compressive strain on the top of the subgrade must be established separately. The following are the steps:

(1) Selecting typical pavements in China.

(2)Establishing the permanent deformation predicting models for asphalt mixtures, aggregates and subgrade soils through tests in laboratories.

(3)Calculating the compressive strain on the top of the subgrade.

(4)Calculating the total permanent deformation through layerwise summation method.

(5)Calculating the allowable number of the load applications after the determination of the rut criterion.
(6)Performing regression analysis relating the compressive strain on the top of the subgrade and the number of the load applications and establishing the design equation for the allowable compressive strain on the top of the subgrade.

SUMMARY AND CONCLUSION

Subgrade soils play a critical role in the initiation and propagation of permanent deformation of pavements and directly influence the pavement performance. Based on comprehensive literature review, the basic configurations of permanent deformation tests for subgrade soils have been established according to the specific condition in China. The results of repeated load tests conducted to three soils are in well accordance with the basic relationships between the permanent strain and the number of load applications proposed by Tseng and Lytton. The regression models for sand, silty clay and clay are found.

APPENDIX I. NOTATION

The following symbols are used in this paper:

A =material parameters (regression coefficients from test data);
b =material parameters (regression coefficients from test data);
E_r = resilient modulus of the layer/sub-layer;
MDD =maximum dry density;
N =number of load repetitions;
OMC = optimum moisture content;
PL =plastic limit;
W_c = water content;
B =material properties;
β_{r1} =calibration factor;
ϵ_0 =material properties;
ε_p =permanent or plastic strain;
ϵ_r = resilient strain imposed in laboratory tests to obtain material properties ϵ_0, β and ρ;
ρ =material properties;
σ_d = deviator stress, and
σ_θ = bulk stress.

APPENDIX II. PLOTS OF TESTING RESULTS

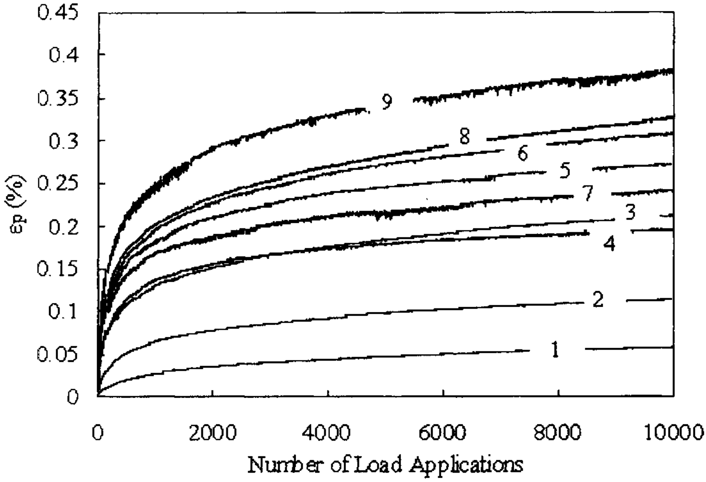

FIG. II-1. Development of Permanent Deformation (sand with dry density of 96% of MDD)

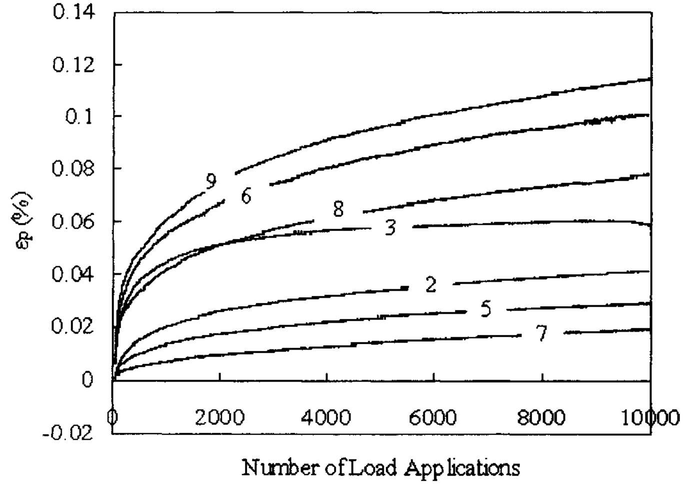

FIG. II-2. Development of Permanent Deformation (clay with dry density of 96% of MDD)

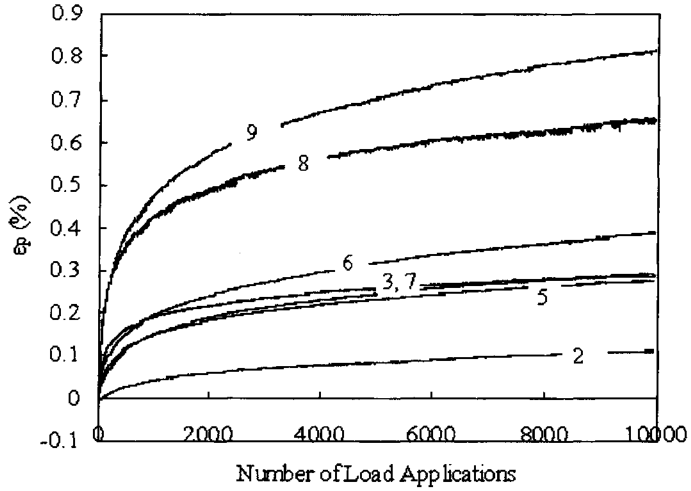

FIG. II-3. Development of Permanent Deformation (silty clay with dry density of 96% of MDD)

REFERENCES:

Allen, D. L., Deen, R. C. (1986). "A computerized analysis of rutting behavior of flexible pavement." *Transp. Res. Record., 1095*, 1-10.

Allen J. J., Thompson, M. R. (1974). "Resilient response of granular materials subjected to time-dependent lateral stress." *HRR, 510,* HRB, Washingtong D. C., 1-13.

Ayres, M. Jr. (1997). "Development of a rational probabilistic approach for flexible pavement analysis." *Ph.D. thesis*, University of Maryland, College Park.

Barksdale, R. D. (1972). "Laboratory evaluation of rutting in base course materials." *Proc. 3rd International Conference on the Structural Design of Asphalt Pavements*, University of Michigan, 161- 174.

Behzadi, G., Yandell, W. O. (1996). "Determination of elastic and plastic subgrade soil parameters for asphalt cracking and rutting prediction." *Transp. Res. Record., 1540*, 97-104.

Bonaquist, R. and Witczak, M. W. (1996). "Plasticity modeling applied to the pavement deformation response of granular materials in flexible pavement systems." *Transp. Res. Record., 1540*, 7-14.

El-Basyouny M. M., Witczak M. and Kaloush K. (2005). "Development of the permanent deformation models for the 2002 design guide." Transportation Research Board, National Research Council, Washington D. C.

Elliott, R. P., and Dennis, N. D., and Qiu, Y. (1998). "Permanent deformation of subgrade soils, Phase I: A Test Protocol." *Research Report MBTC FR-1069*, Department of Civil Engineering, University of Arkansas.

Kenis, W. J. (1978). "Predictive design procedure, VESYS user's manual: an interim design method for flexible pavement using the VESYS structural subsystem." *Final Report No. FHWA-RD-77-154,* Federal Highway Administration, Department of Transportation, Washington, DC.

Huang, Y. H. (1993). "Pavement analysis and design." Prentice Hall.

Lentz, R. W. (1979). "Permanent deformation of a cohesionless subgrade material under cyclic loading." *Ph.D. thesis*, Michigan State University, East Lansing, USA.

Monismith, C. L., Ogawa, N., Freeme, C. R. (1975). "Permanent deformation characteristics of subgrade soils due to repeated loading." *Transp. Res. Record.*, *537*, 1-17.

Muhanna, A.S., Rahman, M.S., and Lambe, P.C. (1998),"Resilient modulus and permanent strain of subgrade soils." *Transp. Res. Record., 1619*, 85-93.

Poulsen, J and Stubstad, R. N. (1978). "Laboratory testing of cohesive subgrades: results and implications relative to structural pavement design and distress model." *Transp. Res. Record., 671*, 84-91.

Puppala, A.J., Mohammad, L.N., and Allen, A.(1999). "Permanent deformation characterization of subgrade soils from RLT test." *J. of Material in Civil Engrg.*, 111(4), 274-282.

Raad, L., and Zeid, B. A. (1990). "Repeated load model for subgrade soils: model development." *Transp. Res. Record., 1278*, 72-82.

Suppakit Chomitd. (2003). "Plastic deformation of potentials of subgrades soils from repeated load triaxial test." *Ph.D. thesis,* University of Texas, Arlington, Texas USA.

"Technical standard of highway engineering." Beijing: People's Communication Press, 2004. (in Chinese).

Tseng, K-H, and Lytton, R.L.(1989). "Prediction of permanent deformation in flexible pavement materials." *Implication of Aggregates in the Design, Construction, and Performance of Flexible Pavements*, ASTM STP 1016, ASTM, Philadephia, PA, 154-172.

Werkmeister, S., Dawson, A.R., and Wellner, F. (2001). "Permanent deformation behavior of granular material and the shakedown concept." *Transp. Res. Record.*, *1757*, 75-81.

Yao Zh. K. and Zhao H. D. (2003) "Design indexes of asphalt pavement." *Research Report*, Tongji University, Shanghai, China. (in Chinese).

Zhang, H.L., Hu Ch.Sh., and Gao J.P..(2005). "Measurement of compressive stress in subgrade of asphalt pavement under moving load." *Proc. of the 5th International Conference of Transportation Professsionals*, Xi'an, China, 131-139. (in Chinese).

Zhao Y. S., Dennis N. D., Elliott R. P. (2004). "Prediction of subgrade permanent strain using simple soil properties." *Geo. Trans.* ,1076 1085.

Subject Index

Page number refers to the first page of paper

This page intentionally left blank

Author Index

Page number refers to the first page of paper